STUDY OF NEUTRON YIELD FROM HEAVY-ION REACTIONS USING PRE-EQUILIBRIUM MODELS

By

SABYASACHI PAUL

(PHYS01201204009)

Bhabha Atomic Research Centre, Mumbai

A thesis submitted to the

Board of Studies in Physical Sciences

In partial fulfillment of requirements

for the Degree of

DOCTOR OF PHILOSOPHY

of

HOMI BHABHA NATIONAL INSTITUTE

March, 2018

Homi Bhabha National Institute

Recommendations of the Viva Voce Committee

As members of the Viva Voce Committee, we certify that we have read the dissertation prepared by Mr. Sabyasachi Paul entitled "Study of neutron yield from heavy-ion reactions using pre-equilibrium models" and recommend that it may be accepted as fulfilling the thesis requirement for the award of Degree of Doctor of Philosophy.

Chairman - **Prof. R. M. Tripathi**	**Date:** 16/3/2018
Guide / Convener - **Prof. A. K. Mohanty**	**Date:** 16-3-2018
Co-Guide - **Prof. Maitreyee nandy**	**Date:** 16-03-2018
Examiner - **Prof. Bivash Ranjan Behera**	**Date:** 16/03/2018
Member - **Prof. B. K. Nayak**	**Date:** 16/03/2018

Final approval and acceptance of this thesis is contingent upon the candidate's submission of the final copies of the thesis to HBNI.

I/We hereby certify that I/we have read this thesis prepared under my/our direction and recommend that it may be accepted as fulfilling the thesis requirement.

Date: 16.03.2018

Place: HBNI, Mumbai

Guide

Version approved during the meeting of Standing Committee of Deans held during 29-30 Nov 2013

STATEMENT BY AUTHOR

This dissertation has been submitted in partial fulfillment of requirements for an advanced degree at Homi Bhabha National Institute (HBNI) and is deposited in the Library to be made available to borrowers under rules of the HBNI.

Brief quotations from this dissertation are allowable without special permission, provided that accurate acknowledgement of source is made. Requests for permission for extended quotation from or reproduction of this manuscript in whole or in part may be granted by the Competent Authority of HBNI when in his or her judgment the proposed use of the material is in the interests of scholarship. In all other instances, however, permission must be obtained from the author.

Sabyasachi Paul

Sabyasachi Paul.

DECLARATION

I, hereby declare that the investigation presented in the thesis has been carried out by me. The work is original and has not been submitted earlier as a whole or in part for a degree/diploma at this or any other Institution / University.

Sabyasachi Paul.

DEDICATED TO

My Parents, Teachers, Family

& Friends...

List of Publications arising from the Thesis

Journal

1. Pre-equilibrium neutron emission in heavy ion reaction: Mean field effect and multiple emission;

   <u>Sabyasachi Paul</u>, Maitreyee Nandy, A. K. Mohanty and Y. K. Gambhir;

   Physical Review C, 94, 2016, 034607.

2. Pre-equilibrium Neutron Emission from O+Al at 7.5 MeV/A And 8.8 MeV/A;

   <u>Sabyasachi Paul</u>, C. Sunil, Sanjoy Pal, V. Nanal, V. Suman, G. S. Sahoo, A. A. Shanbhag, S. P. Tripathy, T. Bandyopadhyay, M. Nandy, A. K. Mohanty;

   Physical Review C, 96, 2017, 044607.

   Symposium

3. Influence of nucleon density distribution in nucleon emission probability;

   Sabyasachi Paul, Maitreyee Nandy, A. K. Mohanty, P. K. Sarkar and Y. K. Gambhir; Proc. of the DAE Symposium on Nuclear Physics 59, p. 488 (2014).

4. Effect of Nuclear Density Distribution on Neutron Emission;

   Sabyasachi Paul, Maitreyee Nandy, A. K. Mohanty, Y. K. Gambhir and P. K. Sarkar; Proc. of the DAE Symposium on Nuclear Physics 60, p. 348 (2015).

5. Comparison of neutron yield at 100 MeV/A 12C on a thick C target: A Pre-equilibrium approach;

   Sabyasachi Paul, Maitreyee Nandy; Proc. of the DAE Symposium on Nuclear Physics 61, p. 480 (2016).

Sabyasachi Paul

Sabyasachi Paul

ACKNOWLEDGEMENTS

Completion of this doctoral dissertation was possible with the support of several people. I would like to express my sincere gratitude to all of them.

At the outset, I wish to express my deepest and sincere gratitude to my guide, professor Ajit K. Mohanty, Director, Saha Institute of Nuclear Physics, Kolkata for his valuable guidance, constant encouragement and persistent motivation.

I am extremely grateful to my research guide, Dr. Maitreyee Nandy, Professor, Saha Institute of Nuclear Physics, for her valuable guidance, scholarly inputs and consistent encouragement, I received throughout the research work. This feat was possible only because of the unconditional support provided by madam. A person with an enormous amount of patience, amicable and positive disposition, she has always made herself available to clarify my doubts despite her busy schedules and I consider it as a great opportunity to do my doctoral programme under her guidance and to learn from her research expertise. I am thankful to her for sharing her knowledge and scientific understanding through the fruitful discussions with me throughout the work.

I convey my heartfelt gratitude to Dr. Pradip K. Sarkar, former Head, Health Physics Division, without whom this work would not have been initiated and for his tremendous support and encouragement till date. His advice and comments have been priceless and played a significant role in documenting my work. I remain grateful to him for introducing me into this field and thank him for showing keen interest in my work.

I take this opportunity to express my sincere regards to Dr. Tapas Bandyopadhyay for sharing his work experience and scientific knowledge with me during the experiments and calculations. His motivational words, enthusiasm and constant encouragement helped me to continue my work regarding the study of neutron spectrometry and dosimetry.

I would take this opportunity to thank the respected members of my doctoral committee Prof. R.M. Tripathi (Chairman), Prof. B.K. Nayak (member) and Prof. S. Basu (former Dean Academic, PMS) for their critical reviews and valuable suggestions during the annual progress reviews and pre-synopsis presentation.

It gives me a great pleasure to acknowledge my senior colleagues Shri D. S. Joshi for continuous support and motivation. I thank Dr. S. P. Tripathy, who consistently extended his research expertise throughout my work and I owe a lot to him for this achievement.

I am grateful to Dr. Sunil C, Shri Anil Shanbhag and Dr. (Smt.) Biju K. for their constant motivation and training necessary for working in a radiation field and spectrometry. I would also like to thank my colleagues Mrs. V. Suman and Shri G. S. Sahoo for sharing their experimental expertise and scientific knowledge with me, without their help it would not have been possible to carry out the neutron spectrometry studies.

I take this opportunity to express my sincere regards and appreciation to Dr. Vandana Nanal, Dr. Sanjoy Pal for their constant support during the course of experiment. I sincerely acknowledge Dr. P. Surendran, Shri S. C. Sharma, Shri J. P. Nair, NPD for fruitful discussions prior and during the course of work and all the staff members of TIFR-BARC pelletron facility and DNAP, TIFR for the beam line setup and timely help and support during the experiment.

I would also like to thank Dr. Ambar Chatterjee, Formed Head, Nuclear Physics Division for his invaluable suggestions for operating LAMPS software and Dr. K. Ramachandran for providing the instrument modules and key instructions during experimental setup of the high energy neutron measurement experiment at PLF. I would like to thank Dr. Y. K. Gambhir, IIT, Mumbai for the key discussions regarding the work on mean field theory and to allow me to use his code for nucleon density calculations.

I thank Dr. K. S. Pradeepkumar, Associate Director, Health Safety and Environment group and Dr. R. M. Tripathi, Head HPD for all the encouragement and help extended during the experiments. Their support was vital all throughout the course of this work.

I am thankful to all my friends for their encouragement and support. I greatly value their friendship and deeply appreciate their belief in me.

Most importantly, I owe a lot to my parents, who encouraged and helped me at every stage of my personal and academic life and longed to see this achievement come true. Their blessings and good wishes have helped me to achieve what I am today. Finally, I would like to express my endless thanks and appreciations to my wife for her support and care.

Sabyasachi Paul

March, 2018

Sabyasachi Paul

HPD, BARC, Mumbai.

CONTENTS

Chapter 3. Development of the PEQ Model and Validation with existing data

Chapter 4. Experimental Validation of PEQ estimates from HION code

Synopsis

The study of nuclear reactions is important to explore nuclear structure and properties of nuclei through the de-excitation process of the composite system. Decay of a hot nuclear system formed in the interaction of two heavy nuclei at low to intermediate energies constitutes an important field of study as several processes other than evaporation and non-equilibrium reactions participate. The energy carried away by individual particles depends on its mode of generation, i.e. at which stage of nuclear reaction, it is emitted from the excited nucleus. In the initial phases of energy exchange between the target and projectile, only some nucleons share the projectile energy. As a result the emitted particles carry large energy (direct or pre-equilibrium). Gradually energy gets shared amongst large number nucleons through nucleon-nucleon interaction and complete system reaches an equilibrium. Then emissions become evaporative in nature, with almost quasi-continuous distribution at lower energies. At low projectile energies, the evaporation is predominant process but as projectile energy increases, contribution from the pre-equilibrium (PEQ) process increases. Cross section for direct reactions is much smaller compared to the other two processes in the reaction regime considered. To understand the interaction processes taking place within a nuclei, careful analysis of relative contributions of different processes involved and the energy-angle distribution of the ejectile is necessary.

Distribution of fast particles emitted in these reactions could not yet be fully explained even with the several reaction models available to explain heavy ion reactions. Neutron emission in these reactions is still more important as this is one of the predominant channels in the energy domain discussed. Thus study of neutron distribution provides us with the insight into the reaction mechanism involved. Secondly, heavy ion reactions at low to intermediate energies are largely investigated in various accelerator facilities in the country. Neutrons constitute the major component of the prompt radiation field in these facilities. Knowledge of neutron energy distribution from these reactions provides us with the source term for radiation dose calculation, helps plan an experiment, ensure equipment and personnel protection around the accelerator. These studies also provide us with the input data for shield design and planning in similar facility.

Neutron interactions vary widely in their characteristics at various energies and in different interacting media. Neutrons also deliver energy through elastic or inelastic collisions (more probable with low Z elements), through nuclear reactions with the interacting medium etc., depositing a large amount of energy in proton rich/aqueous substances. Biological effect of neutrons to different human tissues and organs vary largely depending on the neutron energy and the aqueous fraction in the tissue. So, for the radiation workers, members of the public as well as for the environment very careful estimation of the neutron energy, yield and angular distribution is very important from radiological protection purposes. To address the energy dependent behavior of the neutrons, International Commission on Radiological Protection has proposed an energy dependent radiation weighting factor (ICRP-74) [1] for neutrons.

In an experiment for the study of atoms and nuclei, the primary requirement is to probe the system with energies of the order of few MeV to hundreds of MeV, primarily generated using particle accelerator facilities worldwide. Among many others, FOTIA, BARC-TIFR pelletron accelerator, Mumbai; pelletron at IUAC, New Delhi, K-130 and K-500 cyclotrons at VECC, Kolkata and INDUS-I and INDUS-II at RRCAT, Indore are the facilities available for academic and material science research in India using particle beams or synchrotron radiation. These generate a large neutron field during operation. Study of the energy-angle distribution within the shielded enclosure or in the control area is important for academic as well as for radiological safety interest. In these accelerator facilities, the energy of fast neutrons generated varies from keV to few tens / hundreds of MeV. Presently neutron dose equivalent (NDE) measuring instruments are conventionally used for protection purposes in the restricted or open access areas. But the conventional NDE measuring instruments do not produce reliable estimate of dose for neutrons beyond 20 MeV energy. So for higher projectile energies, dose due to higher energy neutrons cannot be estimated properly. Secondly, the NDE instruments are calibrated for dose estimations based on the neutron fluence-to-dose conversion coefficients provided by ICRP and gets modified over time based on different simulation studies, while the neutron energy-angle distribution remains invariant for a given combination of target, projectile and beam energy. So determination of the neutron spectrum is important. The evaporation component is well studied and can be estimated in the framework of Weisskopf-Ewing or Hauser Feshbach formalism. Keeping these facts in view a model has been developed in the present work to estimate the PEQ neutron fluence, using the basic exciton model framework with two body scattering **with a modified spatial nucleon density distributions**. This model has been validated using existing literature data and supported with experimentally observed data. The prime objective of the work is to estimate the yield and angular distribution for fast neutrons above 20 MeV emission energies, generated from heavy ion reactions in accelerator and analyse the effect of relativistic mean field and angular momentum of the composite system on neutron distributions. The thesis has been divided in six chapters and a brief description of each is as follows:

Chapter 1: Introduction

This chapter describes the significance and quantification of neutrons generated from different reactors, accelerator facilities and radioactive sources. The energy ranges of fission, spallation and heavy ion reaction neutrons, for different reaction mechanism like direct (DIR), pre-equilibrium (PEQ), evaporation and their importance are discussed. The chapter also provides a brief account of the conventional dosimetry involving as for example, thermal neutron detection and spectrometric techniques like pulse height, pulse shape discrimination or time of flight. The advantages as well as limitations of these conventional techniques have been discussed. The scope and aim of the work with respect to the need for an accurate estimation of the equivalent doses to the radiation workers, has also been discussed at the end of this chapter.

Chapter 2: Basic theoretical models

The details of the three neutron emission processes, DIR, PEQ and evaporation in terms of the nuclear reaction time scales, various available models for estimation of the yield and angular distributions from these processes are discussed in this chapter. A brief chronological advancement in the development of the models, their advantages and limitations in reproducing the experimental cross-section measurements or yield studies are also mentioned here. The details of the evaporation formalisms like Weisskopf-Ewing and Hauser-Feshbach theory and model codes for evaporation neutron yield estimations - PACE and EMPIRE have also been discussed. A brief discussion on the progressive development of the PEQ models using two-body scattering kinematics, starting from the Griffins [2] work in 1967 to the present day, using different models like exciton [3], hybrid, master equation models or quantum mechanical approaches [4] like multi-step direct or compound has also been presented in this chapter. For radiological protection and shielding calculations, the yield of neutrons from a stopping target, where the projectile deposit all its energy is an important aspect. At the end of this chapter, the basic mechanism and assumptions need to be incorporated to estimate the neutron yield from these stopping targets by superposition of the continuously degrading projectile energies is also discussed.

Chapter 3: Development of the PEQ Model and validation with existing data

This chapter discusses the formalism developed for estimation of the PEQ neutron yield and angular distribution incorporating the influence of relativistic mean field (RMF) and multiple PEQ emission. The assumptions used are discussed along with the basic physics framework. Influence of RMF on PEQ neutron emission is studied through the nucleon density distribution in the composite nucleus. Contribution of simultaneous and sequential PEQ processes in neutron emission has also been investigated. **In a few studies by earlier workers** PEQ nucleon emission from heavy ion reactions was studied through nucleon-nucleon (N-N) scattering using two body collision kinematics. The basic assumption used in the PEQ model heavy ion (HION) of Ghosh et. al. [5] considers the progressive energy sharing between the projectile and target nucleons through a series of two-body interactions at different exciton hierarchy. The effect of nuclear excitation was introduced by considering the fused system to consists of two different sub systems within the, viz. the hot and cold spots. The mutual interaction between the nucleons of hot spot or between a nucleon in the hot spot and one in the cold spot excites the nucleons when the emission channel may open up and particle emission becomes probable. If no emission channel opens, the nucleons enter into further two-body scattering resulting in further energy sharing. Energy-angle partition amongst the nucleons is calculated using the scattering kernels [6]. Particle emission probability is calculated from the ratio of the emission rate to the total interaction rate (collision and emission). **In the present work,** influence of relativistic mean field (RMF) in PEQ neutron emission has been studied. In order to do this nucleon-nucleon collision rate is calculated from the spatial variation of nucleon density in the composite system. Spatial nucleon density distribution is obtained from RMF theory [7] and a semiphenomenological approach. The final emission probabilities are calculated and compared with the existing literature data at energies between 10-30 MeV per nucleon. The comparisons are done for available neutron multiplicity data [8-10] from ^{20}Ne and ^{12}C induced reactions on ^{165}Ho target. Our comparisons showed that inclusion of the modified collision rates largely improved the agreement of the calculated distributions with the measured data at backward angles but an under-prediction compared to the experimental measurements at forward angles, intermediate emission energies existed for projectile energies beyond 15 MeV per nucleon. Multiple PEQ formalisms [11] -- simultaneous multi-particle emissions from a single exciton hierarchy and further PEQ emission from the residual nucleus after the first particle emission (sequential) have been proposed to improve the underprediction and reproduce the experimental neutron multiplicities. The multiple PEQ formalism reproduced the experimental observations and has been found to have significant contributions in the yield at projectile energies above 15 MeV/A. In the present study, it has also been found that at higher projectile energies, the relative contribution of the sequential emissions is more than the simultaneous one.

Chapter 4: Experimental validation of pre-equilibrium estimates with present model

This chapter discusses the experimentally obtained neutron distribution from heavy ion reaction at 7.5 and 8.8 MeV/A and compares the measured high energy emissions with the present model HION3 [12] using the single particle PEQ emission formalism. An experiment was carried out at the BARC-TIFR Pelletron LINAC facility (PLF), Mumbai using ^{16}O as projectile beam. The projectiles bombarded a thick stopping Al target at two different beam energies 120 and 142 MeV. The yield of neutrons from this reaction was measured using proton recoil scintillator detectors at five different angles using the time of flight technique. The measured neutron yield and angular distribution data corrected for detector efficiencies were further compared with the modified HION estimates. In this chapter, the basic experimental setup, detector efficiency and spectra measurement using the time-of-flight technique are also discussed. The n-γ separation from their pulse shape and energy spectra measurement from the time difference data were carried out in offline analysis using the linux advanced multi-parameter system (LAMPS) software [13]. The measured data are compared with the HION3 estimates. As the projectile energy was 7.5 and 8.8 MeV/A only single PEQ emission has been considered instead of multiple PEQ emission. HION3 estimates are found to have a good corroboration with the measured data at all five angles (0°, 30°, 60°, 90° and 120°) for the high energy emission neutrons beyond 20 MeV. This indicates that even at energies below 10 MeV per nucleon, modified HION has been able to reproduce the PEQ neutron yield from a heavy ion reaction. From the measured neutron spectra at different angles and energies, a dosimetric estimate has been evaluated using the ICRP-74 dose conversion coefficients (DCC). These are then compared with the experimentally obtained dose from neutron dose equivalent (NDE) meter. The result shows that the doses detected by the NDE meter, are 6-10% less than the total dose obtained from measured spectra at the forward angles for both the projectile energies. The under-prediction reduces to 3-6% at the backward angles (90° and 120°). This may be attributed to due to the fast neutrons beyond 20 MeV. The dose estimated from the measured spectra upto 20 MeV neutron energy agrees well with the NDE measurements. So, from the radiation protection perspective, the HION estimates can serve as an additional support over the NDE meter estimates to arrive at an accurate estimate of the equivalent doses for radiation workers.

Chapter 5: Estimation of Pre-equilibrium component for heavy ion reactions at large projectile energies

This chapter deals with the fast neutron emission above 20 MeV obtained from different target-projectile combinations using the code modified HION (HION3 and HION4) [12] at projectile energies between 10 MeV/A – 50 MeV/A. In this work, an estimate of the fast neutron contribution and the percentage contribution of the PEQ yield with respect to evaporation has been estimated. For this study, the most commonly used projectile beams for basic research and different applications have been chosen as projectiles. Major elements in the beam dump (Cu, Ta), shielding, construction material (Fe, C) in the accelerator and commonly used target materials such as Au, Ag have been chosen as the target elements. The five projectiles, ^{7}Li, ^{12}C, ^{16}O, ^{19}F and ^{28}Si are chosen in the present work based on the fact that these are the five most abundantly used beams in the PLF in last 25 years of operation. Evaporation estimates were calculated from the PACE4 code at projectile energies from 10 MeV per nucleon to 50 MeV per nucleon. The results show that, at lighter mass targets, the PEQ contribution is large compared to the high Z targets, where the PEQ contribution varies between 3-20% at projectile energies between 10-50 MeV per nucleon of the corresponding evaporation estimates. For the lowest mass fused system of ^{19}F (^{7}Li+^{12}C), the PEQ contribution is found to vary between 2.7% at 10 MeV per nucleon to 30% at 50 MeV per nucleon. For other low mass composite systems like ^{24}Mg (^{12}C+^{12}C), the PEQ estimates were found to be 8% of the evaporation contribution at 120 MeV projectile energy but significantly increases at 600 MeV. Apart from these systems, rest of the composite systems showed an average increase in the PEQ contributions varying from 3-20%. In this work, a simplified empirical relation has also been proposed to estimate the total energy integrated PEQ contributions for different target-projectile systems at various incident energies using multi-particle emissions. Based on the ICRP-74 DCC values, the total estimated dose from the fast neutrons were also found to vary similarly for the low mass composite systems. So this work will provide an additional safety factor for estimating the dose from the fast neutron components beyond energies of 20 MeV and incorporation of these dose components will ensure a better safety margin over the conventional NDE meter readings. At the end of this chapter, an estimate of the high energy neutrons in the range of few hundreds of MeV has also been carried out using the HION code, to compare the yield and angular distribution from a ^{12}C on ^{12}C system at 100 MeV per nucleon projectile energy, to check the higher energy regime of applicability of this model. The result showed a good match in the forward angle spectral yield but further modifications are needed to be incorporated to account for the angular distributions at backward angles of emission.

Chapter 6: Conclusion

The concluding chapter of the thesis provides the major conclusions of the present work which are summarized as follows:

1. The in house developed formalisms, modified HION (HION2, HION3 and HION4) provides an accurate estimate of the PEQ neutrons from heavy ion nuclear reactions at low to intermediate energies. Spatial density distribution of neutrons calculated from RMF theory and a semiphenomenological approach modifies the nucleon-nucleon collision rate at different impact parameter and subsequently the emission probabilities.
2. The modified emission probability produces a better agreement with the available experimental neutron multiplicity distribution in the projectile energy range between <10-30 MeV per nucleon.
3. At projectile energies of 20 MeV per nucleon and onwards, multiple emissions from the excited nucleus contribute to the PEQ neutron distribution.
4. Experimental measurements carried out at PLF, Mumbai showed that the model can estimate the fast neutron spectra and the associated angular distribution, in a large angular range of 0° to 120° even at energies below 10 MeV per nucleon. **Dosimetric estimates carried out**

using the ICRP-74 DCC values and NDE meter showed a considerable difference in the total doses, which can be supplemented using the HION code estimates.

5. An estimate of the PEQ neutron emission, in the framework of the code HION3 and HION4, for different target projectile combinations, commonly encountered in accelerator facilities shows that, neglecting the PEQ estimates at higher projectile energies can underestimate the neutron yield and the dose by 20- 30% at forward angles compared to the conventional NDE meter results. So to ensure an accurate equivalent dose estimate for radiological protections, the PEQ estimates need to be incorporated. An empirical expression for the total energy integrated PEQ yield as a function of the target and projectile masses and the projectile energy has also been proposed in the present work.

In conclusion, it can be stated that, this work can estimate the experimental PEQ yield from heavy ion nuclear reactions for the incident energy ranges of less than 10 MeV per nucleon to 30 MeV per nucleon. Estimations with the modified HION code till energies 50 MeV per nucleon have also been tried. At larger energies of 100 MeV per nucleon, the code estimates the forward angles neutron spectra significantly well. But at backward angles neutron emissions are overestimated and further modifications need to be incorporated for obtaining the proper angular distributions.

References

[1] ICRP, 1996. Conversion Coefficients for use in Radiological Protection against External Radiation. ICRP Publication 74. Ann. ICRP 26 (3-4)

[2] Griffin J J; Statistical Model of Intermediate Structure;Phys. Rev. Lett. 17, 478 (1966)

[3] Blann M; Hybrid Model for Pre-Equilibrium Decay in Nuclear Reactions;Phys. Rev. Lett. 27, 337 (1971)

[4] Feshbach H, Kerman A K and Koonin S; The statistical theory of multi-step compound and direct reactions; Ann. Phys., NY 125, 429 (1980)

[5] Maitreyee Nandy, Sudip Ghosh, and P.K. Sarkar; Angular distribution of preequilibrium neutron emissions from heavy-ion reactions; Phys. Rev. C 60, 044607 (1999)

[6] A. De, T. Shibata, and H. Ejiri; Angular distribution of fast protons from the pre-equilibrium process of the ^{165}Ho(α,p) reaction; Phys. Rev. C 45, 774 (1992)

[7] Relativistic mean field theory for finite nuclei; Y. K Gambhir, P. Ring, A. Thimet, Annals of Physics; 198, 132-179 (1990).

[8] D. Hilscher, H. Rossner, A. Gamp, U. Jahnke, et. al.; Energy and linear-momentum dissipation in the fusion reaction of ^{165}Ho + ^{20}Ne at 30 MeV/nucleon; Phys. Rev. C 36, 208 (1987).

[9] E. Holub, D. Hilscher, G. Ingold, U. Jahnke, H. Orf, and R. Rossner;Neutron emission in central heavy-ion collisions of ^{165}Ho + ^{20}Ne at 11, 14.6, and 20.1 MeV/nucleon; Phys. Rev. C 28, 252 (1983).

[10] E. Holub, D. Hilscher, G. Ingold, U. Jahnke, et. al. ; Preequilibrium neutron emission in fusion of ^{165}Ho + ^{12}C at 25 MeV per nucleon; Phys. Rev. C 33,143 (1986).

[11] M. Blann and H.K. Vonach; Global test of modified precompound decay models; Phys. Rev. C 28, 1475 (1983).

[12] S. Paul, M. Nandy, A. K. Mohanty, Y. K. Gambhir; Preequilibrium neutron emission in heavy ion reaction: Mean field effect and multiple emission; Phys. Rev. C 94, 034607 (2016).

[13] A. Chatterjee; http://www.tifr.res.in/~pell/lamps.html (Private communication); 2016

LIST OF FIGURES

LIST OF TABLES

Chapter 1

Introduction

Energy-angle distribution of particles emitted in a nuclear reaction provides information on the reaction mechanism and gives us the insight into the property of the nuclei. Both the nucleon- and heavy ion induced reactions have been studied in great detail starting from the beginning of last century. But the latter is not yet understood well over a large energy domain. Particle emission from a hot nucleus is characterized by its excitation energy and the probable mode of de-excitation pathways. At low excitation energy of the composite nucleus reaction proceeds mainly through evaporation from an equilibrated compound system. In the high energy domain, the system behaves as a free fluid favoring direct reaction and fragmentation. In the intermediate energy range non-equilibrium reaction mechanism pre-dominates and determines the double-differential particle distribution [1-4]. Analysis of the particle spectra endows one with the understanding of the de-excitation channels and the mechanism of the particular reaction [5-8]. Moreover, a nuclear reaction serves as the source term for numerous applications starting from the nuclear reactors to the production of medically important radioisotopes. In all these areas neutron emission is an interesting area of study for multiple reasons: it is the most favorable among all particle emission pathways considering its zero Coulomb barrier. Secondly, fast neutrons constitute one of the primary components of the prompt radiation field in positive ion accelerators [9-11]. Interaction of these neutrons with the human tissues and organs vary widely depending upon the composition of the interacting material, energy of the neutron and its mode of interaction [12-20]. The possible mode of interaction can vary between elastic collisions, inelastic collisions and different types of nuclear reactions including fission. Neutron dose delivered to the tissue is determined by the mode of interaction and the neutron energy besides other factors. So a very careful investigation of the production pathways for neutrons, the emission yields and an evaluation of energy spectra, angular distribution using both experimental and theoretical models is important. In the present work, the emphasis is to determine the energy-angle distribution of pre-equilibrium (PEQ) neutrons from heavy ion reactions for different kind of target projectile combinations with the help of a reaction model developed [21-22]. In order to do that a theoretical approach developed earlier has been modified, validated using measured data by other workers as well as measured in this work, PEQ neutrons estimated for different systems using this model and empirical formalism developed for neutron yield and dose distribution. In the next section we describe the relevance of estimating the energy-angle distribution of neutrons in order to have a proper estimate of the neutron yield and equivalent dose to the human organs and tissues. A proper understanding of the processes will help overcome the operational limitation of the conventional radiation meters to assess the neutron dose accurately and ensure better overall safety to radiation workers, member of the public and environment.

1.1 Necessity for Neutron yield Studies

The neutron sources can broadly be classified in three major categories: reactors (fission neutrons), particle accelerators including spallation sources and portable sources. The neutron spectrum from low-flux [23, 24] and high-flux [25 – 31] reactors are typical fission-evaporation neutron spectrum extending upto around 8 – 10 MeV. The pulsed proton driven neutron sources or spallation neutron (SNS) sources [32 – 36] use the high energy protons (~GeV) on a heavy mass target and is a recent technique for generation of high flux of high energy neutrons (~upto few hundreds of MeV). The high energy electron accelerators produce high energy photo neutrons. Neutron distribution from all the SNS sources and electron accelerators needs a careful estimation of the high energy component for both radiological protection and shielding calculations [12-15].

Apart from these, the conventional neutron sources (radioactive sources) involving radioactive decay provide energies up to around ~ 5 MeV. In the low to intermediate energy positive ion accelerators neutrons of energies up to few hundreds of MeV are obtained. These are used for basic research, medical applications, material studies etc. [37-41]. In all these cases, a knowledge of the neutron field is very important to understand the reaction mechanism, estimate the reaction product yield, the extent of the neutron damages to the materials, to properly plan the experiment and to protect the radiation workers, public and the environment as a whole.

The conventional dose measuring units available measures the dose or the neutron yield upto 20 MeV neutron energy only. Other neutron detection systems like Bonner spheres use thermal neutron detector along with a moderating material to measure neutrons mostly upto 20 MeV. Moreover the spectrum determination in these systems requires a prior idea of the neutron spectrum in a similar situation. In order to measure the neutron distribution over the entire energy spectrum in an accelerator facility neutron flight time measurement or pulse height unfolding is employed which provides a good estimate of the neutron spectra using different kind of unfolding techniques [42-54]. But these techniques require advanced instrumentation and good proton recoil scintillator detector [55-57] assembly etc. Moreover, in positive ion accelerator facilities the prompt radiation field consists of gamma radiation in addition to the neutrons. So neutron spectrum measurement requires good discrimination of the neutrons from the associated gamma rays and determination of the energy distribution. This does not offer a convenient choice for regular evaluation of neutron doses in these accelerator environments. Secondly, for numerous possible combinations of target-projectile and beam energy it is not feasible to carry out the neutron spectrum measurement. So, one of the preferred choices to understand the neutron energy-angle distribution in such accelerator facilities is the reaction model calculation. This will also provide a strong support to ensure radiological protection for neutron energies to hundreds of MeV.

The evaporation neutron yield and the corresponding angular distribution are accurately determined using the Weisskopf-Ewing theory [58-59] or the Hauser-Feshbach [60-61] approach. In high energy domain, the quantum molecular dynamics (QMD) approach [62-64], intra-nuclear cascade models [65-72], fluid dynamics models, viz. Vlasov or Vlasov-Uehling-Uhelnbeck (VUU) models [73-76] predict the particle emissions. But at intermediate energies, both characteristics co-exist and a hybridised model with proper optimization become necessary to estimate the emission yields. In the present work, a formalism based on nucleon scattering has been developed where the collision rates are determined from spatial distribution of neutrons. This model is used to calculate the neutron yield with emission energies beyond 20 MeV in heavy ion reaction. The low energy evaporation neutrons are calculated using the conventional evaporation codes PACE4 [77-78] and EMPIRE (ver. 3.2) [79]. Our interest is centered on the neutrons emitted from PEQ process in a heavy ion reaction in the energy range of few tens of MeV per nucleon. In the next section we shall briefly discuss about the production of neutrons in such reactions and the basic mechanisms involved.

1.2 Neutron production processes with basic mechanism

In an accelerator environment, the neutron production pathways are different for positive ion and electron accelerators. The electron accelerators produce neutron through photonuclear reaction induced by the high energy bremsstrahlung radiation. The detail of neutron production processes in electron accelerators will not be discussed here, as this directly does not come under the scope of this work. In the case of positive ion accelerators, neutrons are produced through different reaction channels. The basic mechanism of neutron production in heavy ion accelerators is similar to that for proton accelerators but other competing channels like deep inelastic scattering, quasi elastic transfer influence the particle yield. Particle emissions from heavy ion interactions at low to intermediate energies are assumed to proceed mainly through three different processes: emissions from a direct reaction involving a single interaction – here only a small part of the target nucleus is involved and most of the other nucleons behave as spectator. As the emissions take place from the first interaction the emitted neutron carries a large amount of energy and often leaves the residual nucleus in one of the discrete states. The angular distribution of such emissions is forward peaked. The second process consists of multiple interactions (mostly a few body scattering interaction involving small parts of both the target and the projectile nuclei) leading to energy sharing between the nucleons within the composite system known as the pre-equilibrium reactions. Finally all nucleons interact in a long-time evolution of the composite nucleus and energy sharing takes place among all the constituent nucleons. The composite system attains an equilibrated configuration and is called the compound nucleus. Particle emissions from this equilibrated compound nucleus are considered as compound nuclear emission or evaporation. These are low energy emissions as the energy available per particle is small and the angular distribution is symmetric around 90^{o} centre-of-mass angle. The energy distribution of the emitted particles follows a Maxwell-Boltzmann distribution. At the juncture of the direct and evaporation part of the neutron energy spectrum, there exists a gray energy region where the pre-equilibrium emissions are important and enhances the neutron yield. The direct reaction occurs within 10^{-22}s, evaporation neutron emission within 10^{-15}-10^{-18}s and the PEQ processes by $10^{-20-}10^{-21}$s. In a medium energy heavy ion accelerator with typical excitation energy ~ 10 MeV/A (Pelletron Linac facility, Mumbai or IUAC facility, New Delhi), the contribution of the direct component is small and the evaporation is the major contributing component in the total particle yield. There are a number of published works [80-83], both experimental and theoretical confirming the presence of PEQ emissions in this projectile energy region. The detail of a typical neutron energy spectra and the relative contribution of the components will be discussed in the next chapter.

In the next chapter we will also focus on the chronological advancements in the theoretical models and approximations made to estimate the PEQ particle emissions from heavy ion nuclear reactions. But before that, we would like to emphasize on the importance of such models in the next section.

1.3 Importance of fast neutrons-- challenges in the yield and energy estimations

In the previous section, we have discussed about the processes and typical orders of reaction time for direct, evaporation and PEQ processes. In all these cases, the most important aspect is the respective yields and angular distributions of the ejectiles from different reaction modes. While the compound nuclear and direct reactions are well understood there are still gray areas in understanding the PEQ emissions. The first model put forward to estimate the energy distribution of the emitted particles in this process is the exciton model [84]. This model proposes a stepwise attainment of the statistical equilibrium through a series of two-body interactions between a part of the target and projectile nucleus through a number of excited particle-hole pairs (known as excitons) within the nuclei. This brings the transition from the stage of potential overlap to the partial energy sharing between the parts of the fused nuclei.

Further different modifications on this theory were carried out by Blann [85], Gadioli et al [86] and others to predict a large number of experimental particle energy spectra and corresponding excitation functions successfully. The difficulty in estimating the PEQ yields and angular distributions stems from two reasons: firstly the cross-section for PEQ emissions is much smaller compared to that for compound nuclear emissions. Secondly, the PEQ reaction involves only a few nucleons in an unequilibrated system. As a result it can neither be described by the statistical model, nor by a quantum mechanical prescription. Researchers have shown that while describing the evolution of the composite system in the framework of two-body scattering, after four to five stages of scattering interactions the fused system reaches equilibrium [21]. This point is considered as the termination of the PEQ process and emissions at later stages should be dealt with using the evaporation models.

After the proposition of exciton model, in a very quick succession a number of different propositions like Fermi gas equilibration model [21-89]; hybrid model [85,90], the Master equation model [91], quantum molecular dynamics [62-64] etc were developed and tried to estimate the increased yield in the high energy particle emissions. A quantum mechanical prescription defining of the PEQ emission process, viz. a multi-step direct (MSD) and multi-step compound (MSC) is also proposed using the quantum mechanical theory [92]. These were considered to be the relaxation processes with at least one particle in the unbound states or with all particles in the bound state respectively within the fused systems. MSD is a more like direct reaction type approach and MSC with evaporation like behavior for describing the PEQ process. A brief discussion of these will be given in the next chapter. Similar quantum mechanical treatments proposed by Nishioka et al, Tamura et. al. [93-95]. estimated the angular distribution and yields from PEQ emissions with considerable accuracy. Along with these, some semiphenomenological and theoretical models, like Fermi jet model or the moving source parameterization using empirical relations with different arbitrary coefficients has been also tried to fit the increased neutron yield at higher emission energies.

1.4 The present work

In the earlier sections, a set of models to describe the PEQ emissions have been mentioned. Of these QMD, moving source, Fermi jet models are employed to assess nucleon emission from heavy ion reactions. But none of these models can explain the angular distribution of the emitted nucleons over a wide emission energy range. The moving source parameterization is based on fitting the experimental data by optimizing a set of arbitrary parameters and does not rigorously consider the physical properties of the reaction system. It shows good fit with the experimental measurements in some cases with a set of coefficients which vary quite strongly with the parameters of the system under study and fails for systems with halo nucleus or magic configuration. The physical basis for choosing the coefficients is not justified. The Fermi jet model predicts the high energy forward angle emissions in most of the systems but fails to predict the backward angle emissions. The model predictions have also been found to increasingly underestimate the experimental neutron yield at high projectile energies. In QMD approach, the nucleons are considered as the wave packets and the composite nucleus is represented as convolution of a large number of wave packets. It employs a Monte Carlo random sampling engine to trace the time evolution of nucleons through two-body collisions using the Newtonian equation of motion in a self-consistent mean field. The complex physical processes involved makes it very time consuming. Moreover the requirement of a large sample size to achieve an acceptable limit of uncertainty in the calculation restricts its usage for the heavy mass composite systems. Other dynamical models like the Boltzmann transport model or the fluid dynamics models like Vlasov or VUU formalisms predict the nucleon emissions at good accuracy for high excitation energies. So this creates an empty space for understanding the non-equilibrium emissions from a composite system at an excitation of few tens of MeV per nucleon. In order to cater to these requirements, the present work has been carried out to estimate the neutron emissions from heavy ion interactions at intermediate energies using a PEQ frame work.

The modified version of the pre-equilibrium reaction model heavy ion (HION) [96], namely HION2, HION3 and HION4 [97] to estimate the PEQ neutron emission is one of the prime focus of the present work. An elaborate discussion on the basic model can be found in some earlier work [21, 98-101], but for the sake of completeness the model will be briefly discussed in chapter 3. It uses a two-body scattering kinematics for estimating the PEQ emission yields and the corresponding angular distributions. During the progress towards equilibrium, the particle emissions are calculated in the basic exciton model framework. The number of excitons at the initial stage was calculated assuming a Fermi sphere of the composite system in momentum space. The evolution of the system at consecutive scatterings was calculated using the scattering kernels. The nucleon-nucleon (N-N) interactions within the fused system considers two subsystems, one represented by a finite temperature and the other by a zero temperature Fermi distribution. During the nucleon-nucleon scattering, the nucleons are excited from these two subsystems and exciton-hole pairs are created, annihilated or redistributed within the fused nucleus. Mathematical evaluation of the process is done using a set of recursion relations. The process continues till the system reaches a quasi-static condition for exciton number, i.e. attainment of the equilibrium stage. A brief discussion on mathematical formulation for the particle emission probabilities can be found in chapter 3. **The major modifications in the**

present work compared to the older versions are as follows: modification of the effective excitation of the composite system by considering the rotational energy at higher impact parameters and incorporation of the collision rate calculated from the spatial nucleon distribution to obtain a modified emission probability. The second modification provides a larger impact in the emission probability calculations. Two different formalisms, viz. semiphenomenological [102-103] and relativistic mean field (RMF) [104-105] approaches were used to estimate spatial variation in the nucleon distributions from the centre to skin of the nuclei. In this work, the spatial density distribution has been utilized to calculate the two body collision rates from nuclear mean free path (mfp) of interacting nucleons inside the nucleus. In the earlier version of the model, the collision rates were calculated based on empirical relation of Blann [85], which uses only the excitation energy of the composite system and the binding energy of the ejectile. This relation does not provide a true physical representation of the collision rates within the nucleus. The modified approach gives a realistic collision rate leading to significantly altered emission probabilities compared to that obtained from the empirical estimates. The variation in neutron emission probabilities for different systems using both empirical and mean field approaches are discussed in chapter 3.

With this modified physics core, the methodology has been validated using reported experimental data of earlier workers for heavy ion reactions (Ne and C as projectiles and Ho as the target at projectile energies between 10-30 MeV/A) [106-108]. A careful investigation at higher projectile energies showed that the density dependent collision rate helps to reduce the overprediction at backward angles but fails to reproduce the experimental observations and underestimates the emission yields at forward angles. Then a multiple pre-equilibrium (MPEQ) formalism [90] has been incorporated to consider simultaneous or sequential multiple PEQ neutron emission. Incorporation of MPEQ is found to reproduce the experimental data. Secondly, one experimental study has been carried out at TIFR Pelletron-Linac facility (PLF) to estimate the thick target neutron yields and PEQ contribution at energies below 10 MeV per nucleon. Neutron distribution from bombardment of ^{16}O beam on a thick Al target at two different projectile energy 120 and142 MeV at five different angles (0°, 30°, 60°, 90° and 120°) was measured using the time of flight (ToF) technique [97]. The experimental data were compared with the HION estimates at higher emission neutron energies and found to have a good match at both forward and backward angles. Along with the ToF measurements, a conventional neutron dose equivalent (NDE) meter was also used for measuring the doses at aforementioned angles. Finally the ToF measured values at different energy bins were folded with ICRP 74 dose conversion coefficients (DCC) [12] to estimate the equivalents doses and compared with the NDE meter readings.

Upon validation of the present model developed for the PEQ neutron emission a theoretical study of neutron yield distribution for different target-projectile combinations has been carried out at different projectile energies. Subsequently neutron dose distribution for these systems has been estimated. This study will help augment the database for radiological protection. PEQ contributions have been calculated for targets like ^{12}C, ^{56}Fe, $^{63/65}Cu$ to heavy mass element like ^{197}Au. In this part of the work projectile beams like ^{7}Li, ^{12}C, ^{16}O, ^{19}F and ^{28}Si are chosen, as these are the most frequently used particle beams in last 25 years in the PLF facility, Mumbai. An estimate of the PEQ contribution for different composite systems at varying projectile energies has been carried out using the modified HION code. A comparison of the neutron dose from the PEQ process and the evaporation contribution has been carried out. A simple empirical relation to estimate the total PEQ yields for different target-projectile combinations has also been formulated in the present work. Estimates based on this empirical relation can be used to improve the radiological safety factors against neutron dose in the accelerator environment. This will help us to correct the underestimation in the total dose registered by the conventional neutron dose equivalent meters for neutron energies above 17 MeV. In the next section we will discuss the need for improvements in the estimated doses due to the high energy neutron components and the contribution of PEQ neutrons at different projectile energies.

1.5 Improvements in the dosimetric estimates from PEQ emissions

Neutron spectrometry serves both academic studies and protection purposes in any radiation environment. Understanding of the energy-angle distribution provides insight into the reaction mechanism, energy levels of the participating nuclei and the interaction processes involved. From the radiological safety point of view, it becomes very important for estimation of the source terms, validation of shielding thicknesses, demonstration of the regulatory compliances and above all to meet the principle of as low as reasonably achievable (ALARA) during all operational conditions. This also provides a support for interpretation of the doses measured by the conventional radiation survey meters and personal dosimeters.

At lower energies the evaporation codes can well predict the neutron spectrum and the resultant dose distribution. NDE meters or REM meters provide a validation for the theoretical estimates of the total dose at low emission energies (upto 17-20 MeV). At higher emission energies, experimental measurement is not always feasible. So a theoretical model which can provide yield and angular distributions for non-equilibrium reactions and validated with experimental data can be used to estimates the equivalent doses. In this work a detailed analysis of the high energy emission estimates from the modified HION code indicates a contribution of

6-10% in the equivalent doses from the PEQ neutrons even at projectile energies below 10 MeV per nucleon when compared with the measured readings from a conventional NDE meter. Similar results have been found with the theoretical study at progressively higher projectile energies for heavy projectile-target interactions.

1.6 Organization of the thesis

In chapter 1, the motivation of the present work in view of the limitations of earlier work in the area of intermediate projectile energies has been briefly discussed. The requirement for the development of a new theoretical model in the presence of available PEQ models has also been discussed. Importance of neutron with energies beyond 20 MeV and its significance in the radiation protection purposes has been discussed briefly in this chapter.

The second chapter discusses the basic nuclear physics aspects like emission processes and underlying theory to estimate the yield and angular distributions with a brief description of the evaporation codes like PACE and EMPIRE. A brief review of the pre-equilibrium emission mechanisms and the process of estimating the thick target neutron yields from the corresponding thin target estimates by the principle of superimposition of the thin target yields have also been discussed here.

In chapter 3, the HION model (the basic model from earlier works and the modifications incorporated in this work) has been brief discussed. Validation of the code by comparing some earlier reported data with the older version of the HION code and modified one has been presented in this chapter. The emission probabilities of neutrons are calculated for different fused systems at various energies, considering the spatial nucleon distribution by both semiphenomenological and relativistic mean field (RMF) approaches. A further modification to reproduce the higher yields at forward angles - a multiple PEQ module have also been added and its requirement at projectile energies of 25 MeV per nucleon onwards has been demonstrated.

Chapter 4, describes the measurement of neutron distribution from a heavy ion reaction at 7.5 and 8.2 MeV per nucleon and validation of the modified HION code for these reactions. An effort has been made to estimate the PEQ neutron yields from bombardment of ^{16}O beam on a thick Al target at two projectile energies 120 and 142 MeV using the time-of-flight technique. The neutron yields and angular distributions at higher emission energies were compared with the HION estimates. Requirement of dose estimates for neutrons above 20 MeV for radiological protection has also been envisaged in this chapter. The measured yields were converted to equivalent neutron doses using ICRP-74 DCC's and compared with the conventional NDE meter readings to estimate the dose contributions from PEQ neutrons.

In chapter 5, a theoretical study of neutron yield and dose distribution has been carried for different projectile-target combinations at increasing projectile energies up to 50 MeV per nucleon. The target projectiles combinations were chosen based on the type of structural materials used in the accelerator environment and on the particle beams predominantly used during operation. The corresponding yield and angular distributions for evaporation (from PACE4 code) are also reported for those composite systems. The extent of underestimations expected in the doses estimated by NDE meter due to its limitation of operation beyond 20 MeV has been calculated. A theoretical estimate to show the progressive increase in the PEQ contributions at high projectile energies is discussed.

Chapter 6, concludes the thesis with an executive summary and list of conclusions obtained from this work and scopes for the future work in this area.

Chapter 2

Basic theoretical models

In nuclear reaction the emission of neutrons is more probable compared to other charged particles due to absence of the Coulomb barrier. In low to intermediate energy heavy ion reactions this emission process from the composite system can be classified in three different categories based on the interaction time, viz. the direct, pre-equilibrium and compound nuclear reactions. The basic characteristics of these processes and associated theoretical models for estimating the respective cross-sections or yields will be discussed briefly in the next subsections

2.1 Neutron emission processes at different reaction time scale

In a nuclear reaction as the two nuclei approach each other their potentials overlap. But if the two nuclei are not close enough, internal degrees of freedom are not excited. The projectile then interacts with the target as a whole through elastic scattering. The second possibility is, that due to potential overlap, the internal degrees of freedom are excited, a fused system is formed, inelastic reaction channels open up and particle emission can take place. In the third possibility nucleon-nucleon interaction takes place in the target+projectile composite system, energy of the incoming projectile is shared by the interacting nucleons and the system proceeds towards equilibrium. Eventually an equilibrated system is formed.

Depending upon the time taken for the reaction to take place, the nuclear reaction mechanisms can be classified in major three categories: reactions taking place from the first stage of target-projectile interaction are called the direct reactions ($\sim 10^{-22}$ sec), emissions from equilibrated compound nucleus are known as compound nuclear reaction ($\sim 10^{-18}$ sec) or evaporation. As the energy brought in by the projectile is being shared by the nucleons of the composite system taking it towards equilibrium, particle emission can take place from any stage of this relaxation process. This is called pre-equilibrium nuclear reaction ($\sim 10^{-19}$ sec).

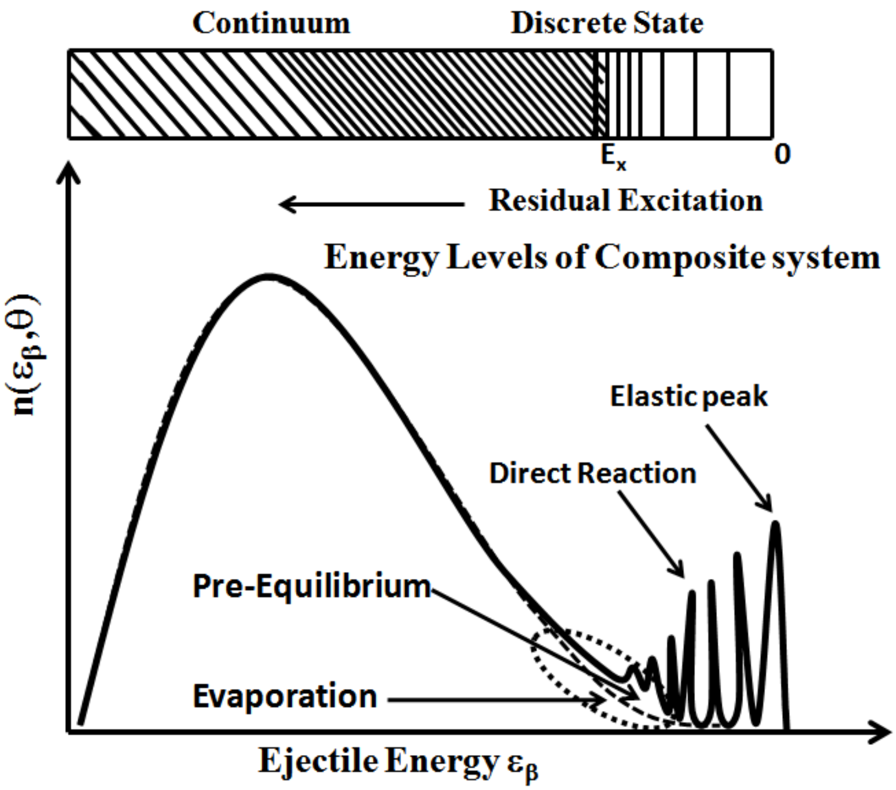

Figure2.1. A Typical neutron emission spectra from heavy ion nuclear reaction [109, p-310]

In the next subsections we will discuss about these three categories of nuclear reactions. Among these, the direct and compound nuclear reactions does not come into the direct purview of this work so an overview of the physical processes and models describing those will be presented here. A typical example of the neutron emission spectra from a heavy ion reaction is presented in Figure 2.1.

2.2 Direct Reactions

The nuclear reactions which are completed in a time frame similar to that required for the transit of the projectile through the target nuclei, are known as the direct reactions. Due to very short interaction time multiple interactions and sharing of energy amongst many nucleons are not possible. As a result a large amount of energy is transferred to a single nucleon or a small cluster of nucleons of the target nuclei. These energetic nucleon or the cluster escapes out of the composite system in different ways: knock on, stripping or transfer type of nuclear reactions as shown below.

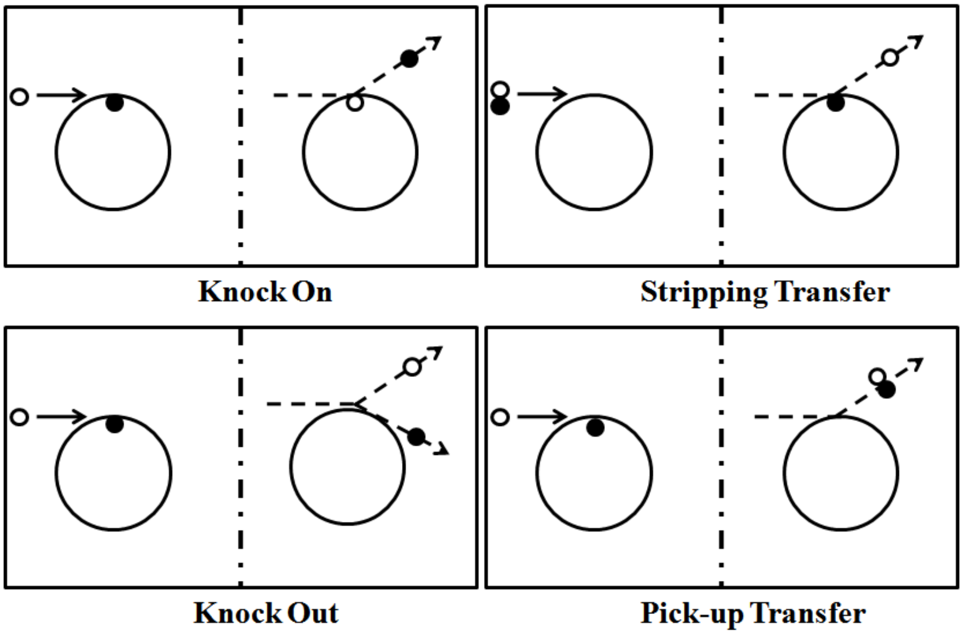

Figure2.2. Typical examples of different direct reactions [109]

The direct reactions have a number of common features:

a) The projectile interacts with a small part of the target nuclei.

b) A fraction of the projectile momentum is transferred to the ejectile which results in high emission energies predominantly in the forward direction.

c) This is a single step interaction between the projectile and the target nuclei. So the interaction can be studied by means of a standard one-body wave-equation, i.e., the Schrodinger equation.

d) The reaction time is short and is typically of the order of time taken by the projectile to pass through the target nucleus. So the reaction time is of the order of $\left(r_0 A^{1/3}/\sqrt{2E/m}\right)$ sec [109], r_0

being a constant ~ 1.2 fm, *A* the target mass number and *E* and *m* the projectile energy and mass respectively.

So, in summary we can say that reaction occurring in a time $\sim 10^{-22}$seconds and having the characteristic features of forward peaked angular distribution and high ejectile energies are called direct nuclear reactions. These are single-step interactions which often populate the residual nucleus in discrete states. The corresponding ejectile energy distribution is represented by the discrete peaks towards the right end of the energy axis in figure 2.1.

2.3 Compound Nuclear Reactions

The characteristics of nuclear reactions other than single-step processes are quite different from those discussed above – particularly with respect to the reaction time. After the first interaction between the projectile and the target nuclei, energy is gradually shared among increasing number of nucleons through nucleon-nucleon interactions and finally the composite (target + projectile) system reaches a statistical equilibrium. The equilibrated composite system is called a compound nucleus. The interactions among the nucleons lead to formation and decay of different configurations, but the average number of excited degrees of freedom remains unchanged after equilibration. During the process, due to statistical fluctuation sufficient energy may be concentrated on a single nucleon or a cluster and particle emission may take place. The large number of interactions involved in the energy sharing process results in the long reaction time of the order of 10^{-13} - 10^{-15} sec. This also ensures that the memory of the entrance channel is lost. As a result the ejectile angular distribution is found to be symmetric about 90° centre-of-mass angle on account of angular momentum conservation. Since the compound nucleus has lost the memory of the incident channel, its decay will be uncorrelated to its formation. This is known as the Bohr's independence hypothesis [110]. In contrary to the case of direct reactions, the energy per nucleon is small and emissions will carry relatively less amount of energy. Since, the compound nucleus may be in one of its collective states, the wave function of the excited compound nucleus is formed from a very complex configuration. So we use the methods of statistical mechanics to study compound nuclear reactions.

2.3.1 The compound nuclear reaction Cross-section

For a compound nuclear reaction

$$a + X \rightarrow C * \rightarrow Y + b$$

based on the independence hypothesis, the cross-section is given by,

$$\sigma(\alpha, \beta) = \sigma_{CN}(\alpha). P_\beta \tag{2.1}$$

where, $\sigma_{CN}(\alpha)$ is the formation cross-section of the excited compound nucleus, C^*, through the α-channel and P_β is the probability of C^* decaying through the β-channel.

The total reaction cross-section consists of three components, a direct reaction component $\sigma_{dir}(\alpha)$, a preequilibrium component $\sigma_{PEQ}(\alpha)$ and a compound nuclear component $\sigma_{CN}(\alpha)$. If we assume that $\sigma_{dir}(\alpha),\ \sigma_{PEQ}(\alpha) \ll \sigma_{CN}(\alpha)$, then we have

$$\sigma_{abs}(\alpha) = \sigma_{CN}(\alpha) = \pi {\lambda_\alpha}^2 \sum_{l=0}^{\infty} (2l + 1)\, T_l(\varepsilon_\alpha) \tag{2.2}$$

where T_l are the transmission coefficients for the partial wave l, λ_α is the de Broglie wavelength for the entrance channel. When this assumption $\sigma_{dir}(\alpha), \sigma_{PEQ}(\alpha) \ll \sigma_{CN}(\alpha)$ does not hold good, $\sigma_{CN}(\alpha)$ is to be obtained from (2.2) by separately estimating $\sigma_{dir}(\alpha)$ and $\sigma_{PEQ}(\alpha)$.

The aim of a nuclear reaction theory is to explain the observed ejectile spectrum and angular distribution, determined by the angular momentum carried away by the ejectile. There are two important models that describe the emission of ejectile from the excited compound nucleus. These are Weisskopf-Ewing formalism [59] and the Hauser-Feshbach formalism [60].

2.3.2 The Weisskopf-Ewing Formalism

At low energies, the excitation of compound nuclear states proceed via resonance through individual states and is described by Breit-Wigner theory [111] for absorption cross section for the process $\alpha \rightarrow \beta$ at the resonance energy E_r, with corresponding total width, partial width of formation and decay Γ, Γ_α, Γ_β respectively. The statistical factor g, includes the spin of particles forming the resonance and the total angular momentum J.

$$\sigma_{\alpha\beta}(E) = \frac{\pi}{k^2}\frac{g.\Gamma_\beta.\Gamma_\alpha}{(E-E_r)^2 + \Gamma^2/_4}; \quad g = \frac{(2J+1)}{(2s_\alpha+1)(2s_\beta+1)} \tag{2.3}$$

As the energy increases, the compound nucleus energy states overlap with no possibility to identify individual states. The reaction amplitude corresponds to the excitation of overlapping states leading to an energy averaged cross-section. From independence hypothesis, following eqn. (2.1) and considering the reaction $(\alpha \rightarrow \beta)$ proceed through the compound nucleus C, one can write

$$\sigma_{\alpha\beta} \sim \sigma_{CN}(C)\frac{\Gamma_\beta}{\Gamma}; \quad \Gamma = \sum_{\alpha} \Gamma_\alpha; \quad \Gamma_\alpha \propto g_\alpha k_\alpha^2 \sigma_{CN}(C) \tag{2.4}$$

So finally the cross-section can be written as; $\sigma_{\alpha\beta} = \sigma_{CN}(C)\frac{g_\beta k_\beta^2 \sigma_{CN}(\beta)}{\sum_\alpha g_\alpha k_\alpha^2 \sigma_{CN}(\alpha)}$. In the same system with compound nucleus energy and binding energy of the ejectile as E_{CN} and B_β respectively, if the energy of the ejectile range between E_β to $E_\beta + dE_\beta$ leaving the residual system in the energy range of U_β to $U_\beta + dU_\beta$, then $U_\beta = E_{CN} - B_\beta - E_\beta$. In this energy level, introducing the density of states $\omega(U_\beta)$, we get,

$$\sigma_{\alpha\beta} dE_\beta = \sigma_{CN}(C) \frac{g_\beta k_\beta^2 \sigma_{CN}(\beta)\omega(U_\beta)dU_\beta}{\sum_\alpha g_\alpha k_\alpha^2 \sigma_{CN}(\alpha)\,\omega(U_\alpha)dU_\alpha} \qquad (2.4a)$$

Since, $k^2 = 2\mu E$,

$$\sigma_{\alpha\beta}(E_\beta)dE_\beta = \sigma_{CN}(C) \frac{(2I_\beta + 1)\mu_\beta E_\beta \sigma_{CN}(\beta)\omega(U_\beta)dU_\beta}{\sum_c \int_0^{E_\alpha^{max}} (2I_\alpha + 1)\mu_\alpha E_\alpha \sigma_{CN}(\alpha)\omega(U_\alpha)dU_\alpha} \qquad (2.4b)$$

where, $\mu_\beta$is the reduced mass of ejectile. This is the Weisskopf-Ewing form of angle integrated cross-section. To a good approximation nuclear level densities, $\omega(U) \propto exp(U/T)$, where T is the nuclear temperature. So the ejectile spectrum from the Weisskopf-Ewing formalism [59] will be of Maxwellian type, promptly rises above the threshold energy and falls exponentially at higher emission energies.

2.3.3 The Hauser-Feshbach Formalism

The Hauser- Feshbach theory [60] in its simplest form, assuming that the projectile, target, residual and ejectile all have zero intrinsic spin and also that there is no relative orbital angular momentum in either the entrance channel or exit channel, can be written as:

$$\sigma(\alpha, \beta) = \pi {\lambda_\alpha}^2 \frac{T_\alpha T_\beta}{\sum_\beta T_\beta} \qquad (2.5)$$

The general form of the Hauser- Feshbach formalism includes the effects of angular momentum and spin of the compound nucleus. Considering the target to be in its ground state with spin $\vec{I}$ and the projectile with an intrinsic spin $\overrightarrow{S_a}$ having an orbital angular momentum $\vec{l}$ relative to the target, the reaction is represented as,

$$\begin{array}{ccccccc} a_{\alpha''} + & X_{\alpha'} & \xrightarrow{\vec{l}} C^* & \xrightarrow{\vec{l'}} & b_{\beta'} & + Y_{\beta''} \\ \overrightarrow{S_a} & \vec{I} & \vec{J} & & \overrightarrow{S_b} & \overrightarrow{I'} \end{array}$$

The compound nucleus angular momentum, $\vec{J}$ can be expressed as $\vec{l} + \overrightarrow{S_a} + \vec{I} = \vec{J}$. Similarly, the entrance channel spin $\vec{j} = \overrightarrow{S_a} + \vec{I}$ and

$$\vec{l} + \vec{j} = \vec{J} \tag{2.6}$$

This is the angular momentum conservation in the entrance channel. A similar approach will provide the angular momentum conservation condition in the exit channel as $\overrightarrow{l'} + \overrightarrow{j'} = \vec{J}$ with $\overrightarrow{j'} = \vec{S}_b + \overrightarrow{I'}$

The objective at this point is to obtain the compound nuclear double differential cross-section $\sigma(\alpha, \varepsilon_\beta, \theta)$, i.e., the cross section of the reaction channel (α, β) where the ejectile is emitted with energy ε_β in the direction θ with respect to a pre-determined Z-axis. The angular distribution is determined by the angular momentum couplings. We therefore, first evaluate the cross-section, $\sigma(\alpha, lm_l jm_j | J, M | \varepsilon_\beta, \theta, l'm_{l'} j'm_{j'})$ where, a transition takes place from the initial channel α, characterized by the angular momenta (l, m_l) and (j, m_j) through the compound nuclear state (J, M), to the exit channel defined by the ejectile energy ε_β, its direction of emission θ and the angular momenta $(l', m_{l'})$ and $(j', m_{j'})$. We begin by defining a few symbols [60].

$\sigma^{JM}(\varepsilon_\alpha, lm_l, jm_j)$: the formation cross-section of the compound nucleus with spin (J, M) from the entrance channel energy ε_α, orbital angular momentum (l, m_l) and channel spin (j, m_j).

$P(JM; l'm_{l'}, j'm_{j'})$: the probability of exit channel orbital angular momentum $(l', m_{l'})$ and channel spin $(j', m_{j'})$ coupling to give angular momentum (J, M)

$Y_{l',m_{l'}}(\theta,\phi)$: the eigen function of the exit channel orbital angular momentum$(l',m_{l'})$. $\left|Y_{l',m_{l'}}(\theta,\phi)\right|^2$ is the probability of the ejectile having orbital angular momentum$(l',m_{l'})$ moving in the direction (θ,ϕ).

P_β: the emission probability of *b* with energy ε_β in any direction with orbital angular momentum (magnitude) l'.

Thus we can write,

$$\sigma^{JM}\left(\alpha, lm_l jm_j|J,M|\varepsilon_\beta,\theta,l'm_{l'}j'm_{j'}\right)$$
$$= \sigma^{JM}\left(\varepsilon_\alpha, lm_l, jm_j\right).P\left(JM; l'm_{l'}j'm_{j'}\right).\left|Y_{l',m_{l'}}(\theta,\phi)\right|^2.P_\beta \tag{2.7}$$

A nuclear energy level can be assigned a well-defined spin, only when it is a discrete level – but in the continuum of states various levels overlap and an unambiguous spin assignment is not possible. For transitions to discrete levels the reciprocity relation, $\frac{\sigma(\alpha,\beta)}{\lambda_\alpha^2}=\frac{\sigma(\beta,\alpha)}{\lambda_\beta^2}$ is valid and P_β is given by, $P_\beta=\frac{T_{l'}(\varepsilon_\beta)}{\sum_\beta\sum_{l'}T_{l'}(\varepsilon_\beta)}$. Taking into account the orbital angular momentum l' in the exit channel the earlier can be written as,

$$\sigma^{JM}\left(\alpha, lm_l jm_j|J,M|\varepsilon_\beta,\theta,l'm_{l'}j'm_{j'}\right)$$
$$= \sigma^{JM}\left(\varepsilon_\alpha, lm_l, jm_j\right).P\left(JM; l'm_{l'}j'm_{j'}\right).\left|Y_{l',m_{l'}}(\theta,\phi)\right|^2.\frac{T_{l'}\left(\varepsilon_\beta\right)}{\sum_\beta\sum_{l'}T_{l'}\left(\varepsilon_\beta\right)} \tag{2.8}$$

Formation of the compound nucleus through the l^{th} partial wave with angular momentum coupling can be obtained as,

$$\sigma^{JM}\left(\alpha, lm_l jm_j\right) = \pi{\lambda_\alpha}^2(2l+1)T_l(\varepsilon_\alpha).P\left(lm_l jm_j; JM\right) \tag{2.9}$$

where, $P\left(lm_l jm_j; JM\right)$ is the probability that angular momenta (l,m_l) and $\left(j,m_j\right)$ couple together to give angular momentum (J,M). The probability of a given l and m_l combining with a given j and m_j to form the state (J, M) is the square of the Clebsch-Gordon co-efficient $\langle ljm_l m_\mathrm{j} \, | JM \rangle$. With proper constraints, it can be shown that,

$$P\big(lm_l jm_j; JM\big) = \frac{\left|\langle ljm_l m_\mathrm{j} \, | JM \rangle\right|^2}{(2l+1)(2I+1)(2S_a+1)} \tag{2.10}$$

Substituting (2.24) in (2.23), we have

$$\sigma^{JM}\big(\alpha, lm_l jm_j\big) = \pi {\lambda_\alpha}^2 T_l(\varepsilon_\alpha). \frac{\left|\langle ljm_l m_\mathrm{j} \, | JM \rangle\right|^2}{(2I+1)(2S_a+1)} \tag{2.11}$$

The probability $P\big(JM; l'm_{l'}, j'm_{j'}\big)$ can be evaluated in exactly the same way. The square of the Clebsch-Gordon co-efficient $\langle l'j'm_{l'}m_{\mathrm{j}'} \, | JM \rangle$ is the probability that angular momenta $(l', m_{l'})$ and $\big(j', m_{j'}\big)$ couple together to result in the angular momentum (J, M). The probability of M has already been defined by $P\big(lm_l jm_j; JM\big)$ and with $\left|Y_{l', m_{l'}}(\theta, \phi)\right|^2$ giving us the probability of $m_{j'}$. We than have, $P\big(JM; l'm_{l'}, j'm_{j'}\big) = \langle l'j'm_{l'}m_{\mathrm{j}'} \, | JM \rangle^2$. So finally

$$\sigma^{JM}\big(\alpha, lm_l jm_j | J, M | \varepsilon_\beta, \theta, l'm_{l'}j'm_{j'}\big)$$

$$= \frac{\pi {\lambda_\alpha}^2}{(2I+1)(2S_a+1)} T_l(\varepsilon_\alpha). \left|\langle ljm_l m_\mathrm{j} \, | JM \rangle\right|^2. \left|\langle l'j'm_{l'}m_{\mathrm{j}'} \, | JM \rangle\right|^2. \left|\chi_{l', m_{l'}}(\theta)\right|^2$$

$$\times \frac{T_{l'}\big(\varepsilon_\beta\big)}{\sum_\beta \sum_{l'} T_{l'}\big(\varepsilon_\beta\big)} \tag{2.12}$$

So far we have considered the formation of the state (J, M) through only given values of m_l and m_j and its decay also through given values of $m_{l'}$ and $m_{j'}$. But a given (J, M) can be formed from all values of $m_l = -l$ to $m_l = +l$ and the values of $m_j = M - m_l$. Similarly, (J, M) can decay through all values of $m_{l'} = -l'$ to $m_{l'} = +l'$ and values of $m_{j'} = M - m_{l'}$. If we sum (2.26) over m_l and m_j, we get the cross-section $\sigma\big(\alpha, lj | J, M | \varepsilon_\beta, \theta, l'j'\big)$ involving all the Z-component values of the four angular momentum relevant to the reaction. Note, that because of the constraints $m_l + m_j = M$ and $m_{l'} + m_{j'} = M$. There is no need to sum over m_j and $m_{j'}$ for a fixed M.

$$\sigma(\alpha, lj|J, M|\varepsilon_\beta, \theta, l'j')$$

$$= \frac{\pi {\lambda_\alpha}^2}{(2I+1)(2S_a+1)} \sum_{m_l} \sum_{m_{l'}} \left|\langle ljm_l m_\mathrm{j}\ |JM\rangle\right|^2 .\ \langle l'j'm_{l'}m_{\mathrm{j}'}\ |JM\rangle^2 .\left|\chi_{l',m_{l'}}(\theta)\right|^2$$

$$\times \frac{T_{l'}(\varepsilon_\beta) T_l(\varepsilon_\alpha)}{\sum_\beta \sum_{l'} T_{l'}(\varepsilon_\beta)} \qquad (2.13)$$

If we consider the projectile momentum to be parallel to the Z-axis we can write (2.27) as,

$$\sigma(\alpha, lj|J, M|\varepsilon_\beta, \theta, l'j')$$

$$= \frac{\pi {\lambda_\alpha}^2}{(2I+1)(2S_a+1)} \sum_{m'} |\langle ljM\ |JM\rangle|^2 .\ \langle l'j'm_{l'}m_{\mathrm{j}'}\ |JM\rangle^2 .\left|\chi_{l',m_{l'}}(\theta)\right|^2 \frac{T_{l'}(\varepsilon_\beta) T_l(\varepsilon_\alpha)}{\sum_\beta \sum_{l'} T_{l'}(\varepsilon_\beta)} \qquad (2.14)$$

Eqn. (2.14) is the cross-section of transition from α-channel to β-channel via the intermediate compound nuclear state with angular momentum (J, M). The effect of M, the spin orientation, is not observed in a nuclear reaction unless one is working with polarized projectiles or targets. So, summing eqn. (2.14) over M we get,

$$\sigma(\alpha, lj|J, M|\varepsilon_\beta, \theta, l'j') = \frac{\pi {\lambda_\alpha}^2}{(2I+1)(2S_a+1)} A_J(l, j|l', j'|\theta) \frac{T_{l'}(\varepsilon_\beta) T_l(\varepsilon_\alpha)}{\sum_\beta \sum_{l'} T_{l'}(\varepsilon_\beta)} \qquad (2.15)$$

where, $A_J(l, j|l', j'|\theta) = \sum_M \sum_{m'} |\langle ljM\ |JM\rangle|^2 .\ \langle l'j'm_{l'}m_{\mathrm{j}'}\ |JM\rangle^2 .\left|\chi_{l',m_{l'}}(\theta)\right|^2$ with the summation over m' is from $m' = -l'$ to $m' = l'$ and that over M from $M = -J\ to\ J$.

Eqn. (2.15) is the angular distribution for the transition from l and j spins to l' and j' spins through the intermediate state spin J. The observed angular distribution is obtained by summing (2.15) over l, j, J, j' and l'

$$\sigma(\alpha; \varepsilon_\beta, \theta) = \frac{\pi {\lambda_\alpha}^2}{(2I+1)(2S_a+1)} \sum_{l,j,J,j',l'} A_J(l,j|l',j'|\theta) \times \frac{T_{l'}(\varepsilon_\beta) T_l(\varepsilon_\alpha)}{\sum_\beta \sum_{l'} T_{l'}(\varepsilon_\beta)} \tag{2.16}$$

where the summation limits are,

$$\left.\begin{array}{c} 0 \leq l \leq \infty \\ |I - S_a| \leq j \leq I + S_a \\ |l - j| \leq J \leq l + j \\ |I' - S_b| \leq j' \leq I' + S_b \\ |J - j'| \leq j \leq J + j' \end{array}\right\} \tag{2.17}$$

Eqn. (2.16) is the standard expression for <u>Hauser-Feshbach formalism of compound nuclear reactions leading to population of discrete levels of the residual nucleus</u>.

The angle-integrated cross-section is obtained from (2.16) as, $\sigma(\alpha, \varepsilon_\beta) = \int \sigma(\alpha, \varepsilon_\beta, \theta) d\Omega$. The spherical harmonics, $Y_{l',m'}(\theta, \phi)$ are the normalized eigen functions of l'^2 and l'_Z. Hence,

$$\int \left|Y_{l',m'}(\theta, \phi)\right|^2 d\Omega = \int \left|\chi_{l',m'}(\theta)\right|^2 \, d\Omega = 1 \tag{2.18}$$

Again, the Clebsch-Gordon coefficients are normalized probability amplitudes. Therefore using limits and constraints over spin and angular momenta, we can achieve,

$$\sigma(\alpha, \varepsilon_\beta) = \frac{\pi {\lambda_\alpha}^2}{(2I+1)(2S_a+1)} . \sum_{l,j,J,j',l'} (2J+1) . \frac{T_{l'}(\varepsilon_\beta) T_l(\varepsilon_\alpha)}{\sum_\beta \sum_{l'} T_{l'}(\varepsilon_\beta)} \tag{2.19}$$

as the angle integrated Hauser-Feshbach equation for compound nuclear transition to discrete levels of the residual.

From Bohr’s independence hypothesis the angular distribution in compound nuclear reactions should be isotropic. The symmetry in angular distribution arises from the conservation of angular momentum and parity, first for the formation and then for the decay of intermediate state. If the observed angular distribution does not show symmetry about 90°, it is clear that no intermediate state is formed with well defined spin and parity and the reaction mechanism is not compound nuclear type.

The direct and compound nuclear reactions taken together accounts for the greater part of the nuclear reaction cross-sections. However, these are not the only mechanisms by which particle emission can occur in nuclear reactions. Particle emission is also possible while the composite nucleus is proceeding towards statistical equilibrium. Emissions taking place after the first projectile-target particle interaction are the direct emissions. Emissions from the second interaction onwards in the non-equilibrated system belong to the category of pre-equilibrium or pre-compound nuclear reactions.

2.4 Pre-equilibrium emission mechanism

The importance of the pre-compound mechanism in understanding nuclear reaction cross-sections is illustrated in Fig. 2.1. The high energy end shows discrete peaks corresponding to the excitation of discrete nuclear states. This part of the spectrum is dominated by the direct reaction mechanism. As the energy of the ejectile decreases, the excitation of the residual nucleus increases. At high excitation the residual nucleus is populated in the continuum of states and the ejectile spectrum is continuous. The broad peak on the low energy side is explained by the compound nucleus theory and can be described by a Maxwellian distribution (the broken line in Fig. 2.1). In between these two regions there is a portion of the continuous ejectile spectrum which cannot be accounted for either by direct reaction or by the compound nuclear process. This is the region dominated by pre-compound or pre-equilibrium (PEQ) emissions.

The characteristics of pre-compound reactions are midway between those exhibited by the direct and compound nuclear processes. As the composite nucleus proceeds towards statistical equilibrium the projectile energy and momentum are shared between more and more particles after each nucleon-nucleon interaction. So the particles emitted from the initial stages carry more energy than those emitted from the equilibrated compound nucleus. This qualitatively accounts for the high energy tail of the continuous energy spectrum in Fig. 2.1. Moreover, in the initial stages of the pre-compound process the composite nucleus retains the memory of the projectile direction. So the emission spectrum from these initial stages is preferentially forward peaked. However, in the later stages, as the number of excited degrees of freedom increases the memory of the projectile direction gets more and more diffused and the ejectile spectrum tends towards isotropy. As a result though the pre-compound emission shows forward peaking it also exhibits substantial cross-section in the backward angles as well.

There are a few different approaches proposed for quantitative estimation of pre-compound contribution in the particle emission spectra. Among these, exciton model is the earliest one for pre-compound nuclear reactions and was proposed by Griffin [84]. The model was developed to explain the emitted neutral spectrum in ^{117}Sn (p, n) ^{117}Sb reaction at 14 MeV proton energy. Subsequently the Fermi gas equilibration model [88, 112] (also known as Harp-Mi1ler-Berne (HMB) model) and the hybrid model [85, 90] were proposed. The hybrid model combined the approach of the exciton model to the HMB model. The original exciton model has been extended by a number of authors [113-119]. All these semi-classical models are fairly successful in explaining angle integrated spectra of pre-compound ejectiles but often fail to explain back-angle cross-sections, which through some modifications [120-121,98,101] removed the shortcoming to some extent.

In the early eighties some quantum mechanical theories have also been formulated [92,95] to explain pre-compound reactions. They reproduce the observed cross-sections quite well particularly for higher energy ejectiles. However, the semi-classical exciton and hybrid models are used extensively to describe both light and heavy particle induced reactions. Some features of the quantum mechanical theories have been incorporated in the exciton model later

[114,122-124]. In the following sub-sections, the models for angle integrated energy spectra and angular distributions will be described.

2.4.1 Exciton model

Exciton model considers that relaxation of the composite system proceeds through two-body scattering. Each stage of this process is characterized by the number of excited particles (p) and holes (h) which are called excitons (n: $n = p + h$).

The simple exciton model [84] is illustrated in Fig. 2.3 for nucleon induced reaction. The nuclear potential is shown with equally spaced single particle levels. Initially the target nucleus is in the ground state. A nucleon projectile with a given energy ε_p enters the target nucleus and forms a 1particle - 0hole ($1p - 0h$) state, i.e., $n = 1$.

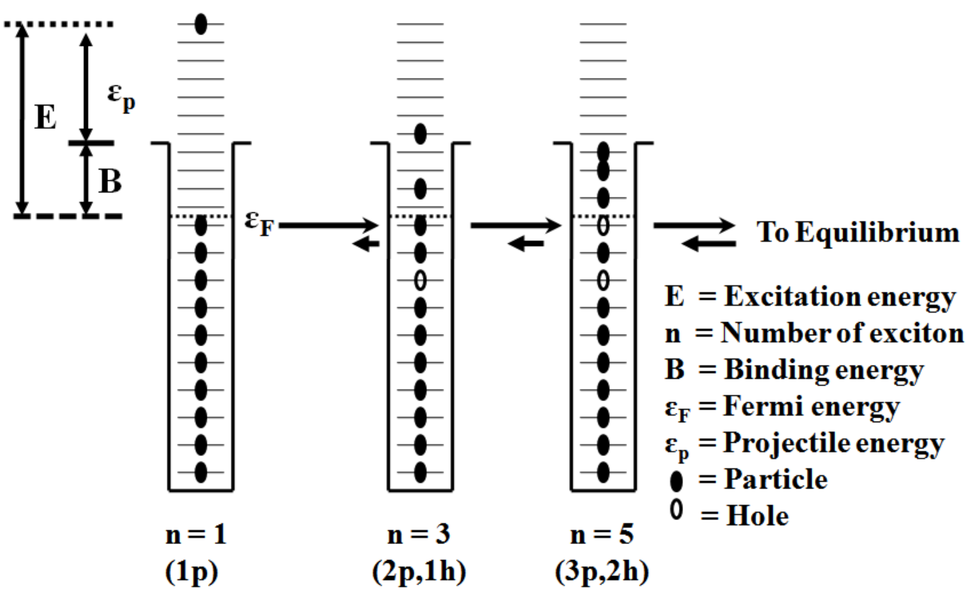

Figure 2.3 The schematic of equilibration process in the exciton model with relative probability and direction of transitions indicated by length and direction of the arrows [109, p-312].

In order to be absorbed and to initiate the reaction the projectile must interact with an individual target nucleon. Since all levels below the Fermi energy are filled the first interaction between the projectile and a target nucleon will raise the latter above the Fermi energy and leave a hole below. Thus a $2p - 1h$ or $n = 3$ state is formed. After formation of the $n = 3$ state either of the excited particles may be emitted if it has sufficient energy to escape. If, however, particle emission does not occur then there will be a further two-body interaction either between one of the two excited particles and a particle below the Fermi surface or between the two excited particles themselves. The first results in the formation of a $3p - 2h$ or $n = 5$ exciton state while the second would lead either to a new $2p - 1h$ state (with different energy configurations of the particles and holes) or back to the original $n = 1$ exciton state. Thus a two-body interaction will lead to transitions in which the change in the exciton number $\Delta n = \pm 2,0$.

The transition rates are proportional to the level density of the, final accessible states (Fermi's Golden Rule). A simple expression for the partial level density at exciton number *n* for a nucleus with excitation energy E_C, is given by Williams [127] as,

$$\rho_n(E_c) = \frac{g^n E_c^{n-1}}{p!\,h!\,(n-1)!} \tag{2.20}$$

where, g is the single particle level density and p and h are the number of excited particles and holes, respectively. As can be seen from (2.20) the partial level density is a rapidly increasing function of *n* for small values of *n*. Thus the transition with $\Delta n = 2$ is far more probable than the transitions corresponding to $\Delta n = -2\ or\ 0$ when *n* is small. As *n* increases the partial state densities gradually level-off. Finally when equilibrium is reached there are as many $\Delta n = 2$ transitions as $\Delta n = -2$ and the exciton number becomes constant at $n = \bar{n}$.

During the transition from $n = 3$ to $n = \bar{n}$ state particle emission is possible from every exciton state if a particle has energy greater than its separation energy. The energy differential pre-equilibrium cross-section $\sigma_{PEQ}(\varepsilon)$, is the sum of the cross-sections from each exciton state:

$$\sigma_{PEQ}(\varepsilon) = \sigma_{abs} \sum_{\substack{n = n_0 \\ \Delta n = 2}}^{\bar{n}} D_n . P_n(\varepsilon) \tag{2.21}$$

where, σ_{abs} is the absorption cross-section of the projectile by the target. D_n is the probability of reaching the n exciton state without prior emissions (the depletion factor). $P_n(\varepsilon)$ is the emission probability of the ejectile with energy ε from the n exciton state. The summation starts from the initial exciton number n_0 which is 3 if the projectile is a nucleon. In the case of cluster projectiles n_0 is often assumed to be equal to the number of nucleons making up the projectile plus 2 (1 excited particle + 1 hole).

The depletion factor D_n is given by [109],

$$D_n = \prod_{\substack{n' = n_0 \\ \Delta n = 2}}^{n} \left[1 - \int d\varepsilon \, P_{n'}(\varepsilon) \right] \tag{2.22}$$

The exciton model assumes that every partition of energy occurs with equal a priori probability. The emission probability, $P_n(\varepsilon)$, is then the ratio of the emission rate with energy ε from exciton state *n* to the rates of all transitions (collision + emission) from *n* at all energies. If $\lambda_c^n(\varepsilon)$ be the emission rate with energy ε from the *n* exciton state and λ_+^n , λ_-^n , and λ_0^n be the rates of $\Delta n = 2, -2, 0$ transitions, respectively, then

$$P_n(\varepsilon) = \frac{\lambda_c^n(\varepsilon)}{\lambda_+^n + \lambda_-^n + \lambda_0^n + \int d\varepsilon . \lambda_c^n(\varepsilon)} \tag{2.23}$$

Hence, the emission rates are summed over all ε in the denominator to obtain $P_n(\varepsilon)$. The emission rate is obtained from the principle of detailed balance as,

$$\lambda_c^n(\varepsilon) = \frac{\rho_{n'}(U)}{\rho_n(E_c\ )} . \frac{(2s+1)m\ \varepsilon\ \sigma_{inv}(\varepsilon)}{\pi^2\ \hbar^3} \tag{2.24}$$

where, n' is the exciton number after emission of the ejectile with v nucleons: $n' = n\ -\ v$ .U is the residual excitation energy given by $U = E_c - B - \varepsilon$ with B the ejectile separation energy. s and m are the intrinsic spin and the reduced mass of the ejectile and $\sigma_{inv}(\varepsilon)$ is the inverse cross-section, i.e., the cross-section of the time-reversed process of absorption of the ejectile by the residual nucleus. The evaluation of the inter-nuclear transition rates $\lambda_{\pm,0}^n$ are discussed in **Appendix-A**.

2.4.2 Hybrid Model

The hybrid model [128-129 and references therein] calculates PEQ energy-differential cross-section $\sigma_{PEQ}(a; x, \varepsilon)$ of a nucleon x (x: proton or neutron) as sum of energy-differential cross-sections from each exciton state n:

$$\sigma_{PEQ}(a; x, \varepsilon) = \sigma_{abs}(a) . \sum_{\substack{n = n_0 \\ \Delta n = 2}}^{\bar{n}} D_n P_n^x(\varepsilon)\ =\ \sum_{\substack{n = n_0 \\ \Delta n = 2}}^{\bar{n}} D_n . \sigma_n(a; x, \varepsilon) \tag{2.25}$$

$P_n^x(\varepsilon)$ is the probability of emission of x-type ejectile from n-exciton state with energy ε. $\bar{n}$ is the average number of excitons once statistical equilibrium is reached.

$P_n^x(\varepsilon)$ can be written as,

$$P_n^x(\varepsilon) = [f_n^x . P_n(x, \varepsilon)] . P_c^n(x, \varepsilon) \tag{2.26}$$

where, f_n^x is the number of x excited per absorbed 'a' in the n-exciton state, $P_n(x, \varepsilon)$ is the probability of x having energy ε in the n-exciton state, $P_c^n(x, \varepsilon)$ is the emission probability of x with energy ε from the n-exciton state. The hybrid model evaluates the probability $P_n(x, \varepsilon)$ from the ratio of the number of states available to the system of n-excitons at excitation E_c, where one particle is at energy ε to the total number of states available to the system when there is no such restriction.

$$P_n(x,\varepsilon) = \frac{\rho_n(U,E)}{\rho_n(E_c)} \tag{2.27}$$

$\rho_n(E_c)$ is the density of states when all n-excitons (particles and holes) share the energy E_c. $\rho_n(U,E)$ is the density of states available to the n-excitons under the constraint that one particle-exciton has energy E and the rest (n-1) excitons share the energy $U = E_c - E$. E is the energy of the ejectile x inside the nucleus and is related to ε as $E = \varepsilon + S_x$, S_x being the separation energy of x. The relations between ε, E, U and E_c are shown schematically in the adjoining figure where V stands for the potential depth.

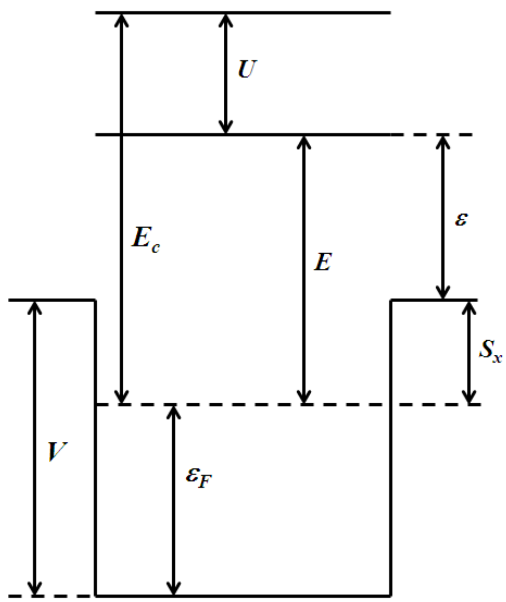

Figure 2.4 The schematic of energy levels used for Hybrid model description [109, p-319]

We then write as, $\sigma_n(a;x,\varepsilon) = \sigma_{abs}(a).\left[f_n^x.\frac{\rho_n(U,E)}{\rho_n(E_c)}\right].P_c^n(x,\varepsilon)$ (2.28)

The quantity in the square bracket of (2.28) is the probability of x having energy E (corresponding to the emission energy ε) in the n- exciton state. There are now only two possibilities available to x – it can either be emitted with the rate $\lambda_c^n(x,\varepsilon)$ or it can undergo a two-body interaction with another nucleon with the rate $\lambda_t^n(\varepsilon)$. Thus the emission probability $P_c^n(x,\varepsilon)$ is,

$$P_c^n(x,\varepsilon) = \frac{\lambda_c^n(x,\varepsilon)}{\lambda_c^n(x,\varepsilon) + \ \lambda_t^n(\varepsilon)} \tag{2.29}$$

Substituting (2.29) in (2.28), $\sigma_n(a;x,\varepsilon) = \sigma_{abs}(a).\left[f_n^x.\frac{\rho_n(U,E)}{\rho_n(E_c)}\right].\frac{\lambda_c^n(x,\varepsilon)}{\lambda_c^n(x,\varepsilon)+\ \lambda_t^n(\varepsilon)}$ (2.30)

Substituting (2.30) in (2.25) we have the familiar hybrid model expression [109]:

$$\sigma_{PEQ}(a;x,\varepsilon) = \sigma_{abs}(a)\sum_{\substack{n=n_0\\ \Delta n=2}}^{\bar{n}} D_n.\left[f_n^x.\frac{\rho_n(U,E)}{\rho_n(E_c)}\right].\frac{\lambda_c^n(x,\varepsilon)}{\lambda_c^n(x,\varepsilon) + \ \lambda_t^n(\varepsilon)} \tag{2.31}$$

The emission rate $\lambda_c^n(x,\varepsilon)$ is evaluated from principle of detailed balance, assuming initial level density available to *x* inside nucleus is single particle level density *g* and final density of state is the number of states per unit energy interval available to a free nucleon moving with energy ε. So, the emission rate can be expressed as,

$$\lambda_c^n(x,\varepsilon) = \frac{2m\varepsilon\sigma_{inv}(\varepsilon)}{g\pi^2\hbar^3} \tag{2.32}$$

The two body interaction or collision rates are related to nucleon mean free path and is given by the empirical relation of Blann [85].

$$\lambda_t^n(\varepsilon) = [1.4\times10^{21}(\varepsilon+S_x) - 6\times10^{18}(\varepsilon+S_x)^2]k^{-1}\ \ sec^{-1} \tag{2.33}$$

For the complete information regarding the PEQ cross-sections using hybrid model, the only unknown quantities remaining is to evaluate $\rho_n(U,E)$ and $\rho_n(E_c)$ and the required ratio $\rho_n(U,E)/\rho_n(E_c)$ there from. This can be found in detail at **Appendix - B**.

2.4.3 Master Equation model

In the master equation exciton model the occupation probability, $P(n,t)$, of the exciton state n at time t is obtained from the time-dependent master equation developed by Cline and Blann [91] :

$$\frac{d}{dt}P(n,t) = \lambda_{+}^{n-2}P(n-2,t) + \lambda_{-}^{n-2}P(n+2,t) - P(n,t)\left[\lambda_{+}^{n} + \lambda_{-}^{n} + \int d\varepsilon.\lambda_{c}^{n}(\varepsilon)\right] \qquad (2.34)$$

The equation is similar to the radioactive decay equation. The first two terms give the growth rate of the n-exciton state by creation and annihilation of a particle-hole pair from $(n-2)$ and $(n+2)$ states respectively. The terms in the square bracket give the decay rate of the n-exciton state by $\Delta n = \pm 2$ transitions and particle emission. The master equation is solved numerically. Having obtained $P(n,t)$ the mean life τ_n of the n-exciton state is obtained from

$$\tau_n = \int_0^{\infty} dtP(n,t) = \int_0^{t_{eq}} dtP(n,t) \qquad (2.35)$$

t_{eq} is the time taken to reach compound nuclear equilibrium. The emission probability $P_n(\varepsilon)$ is obtained from

$$P_n(\varepsilon) = D_n.\tau_n.\lambda_c^n(\varepsilon) \qquad (2.36)$$

and effectively $\tau_n$can be represented as,

$$\tau_n = \frac{1}{\lambda_{+}^{n} + \lambda_{-}^{n} + \lambda_{0}^{n} + \int d\varepsilon.\lambda_{c}^{n}(\varepsilon)} \qquad (2.37)$$

$$\sigma_{PEQ}(\varepsilon) = \sigma_{abs} \sum_{\substack{n=n_0 \\ \Delta n=2}}^{\bar{n}} D_n.\lambda_c^n(\varepsilon).T_n(p,h) \qquad (2.38)$$

2.4.4 The Harp-Miller-Berne model

Both exciton model and master equation model assume that all energy partitions between particles and holes in a given exciton state have equal a priori probability. But in reality '*equal a priori probability*' does not hold for the energy distribution of the excitons which influences the PEQ particle emission spectrum. This aspect of the pre-equilibrium phenomenon was first studied by Harp, Miller and Berne [88,111] and taken into account in the model developed by the authors. The nuclear single particle states are grouped into energy bins of some constant size $\Delta\varepsilon$. The model calculates the occupation probability of an average state in the i-th bin as a function of time. At the onset of the reaction all levels below the Fermi energy are filled up (since the target is in its ground state) and the projectile is in an excited state. This gives the bin occupation probabilities at time $\tau = \tau_0$. Consequently, two-body interactions lead to a redistribution of probabilities and the system proceeds towards equilibrium. This goes on until a steady state configuration is reached. At each time during the equilibration process the energy spectrum of emitted nucleons are calculated. A net spectrum is obtained by summing the spectra over the total interaction time.

The basic assumptions of the model are:

(1) Interactions within the nucleus arise from scattering between two nucleons;

(2) The transition probabilities are dependent only on the energies of the particles involved in the scattering;

(3) The transition probabilities vary slowly with energy over the energy interval $\Delta\varepsilon$ so that a constant value of the transition probability may be used for all levels within the bin.

The HMB model gives the time evolution of the equilibration process. Secondly it calculates the transition rates from nucleon-nucleon scattering cross-sections. It avoids the uncertainties involved in the calculation of the transition matrix probability $|M|^2$ of the exciton model.

2.4.5 Multistep direct/compound mechanisms

The break-up of the pre-equilibrium emission spectra into multi-step direct (MSD) and multi-step compound (MSC) components was suggested by Feshbach, Kerman and Koonin (FKK) in their quantum mechanical theory of pre-equilibrium reactions [92]. At initial stages of relaxation process only a few degrees of freedom are excited and the excitation energy per particle is large enough for one or more particle to be unbound with a finite probability of being emitted. These emissions from configurations of the composite nucleus where there is ***at least one unbound particle at each stage of the cascade of two-body interactions (P chain)*** are termed as MSD emissions.

After several two-body interactions enough number of particles get excited so that the excitation energy per particle is insufficient for any particle to become unbound. At this stage all excited particles in the composite nucleus remain bound. Emissions can take place from any of these bound configurations if a particle acquires sufficient energy as a result of statistical fluctuation. Such emissions which take place from ***those configurations of the composite nucleus where all excited particles are bound (Q chain)*** but the system is still in a non-equilibrated state contributes to the MSC component of the pre-equilibrium spectra.

The MSD and MSC components are distinguished by their angular distributions. During MSD emissions, since fewer two-body interactions have taken place, correlations exist between the entrance and the exit channels. As a result the emissions have a forward peaked angular distribution. For MSC emissions this correlation is washed out and the angular distributions are symmetric about 90° centre-of-mass angles as in the case of purely compound nucleus emissions.

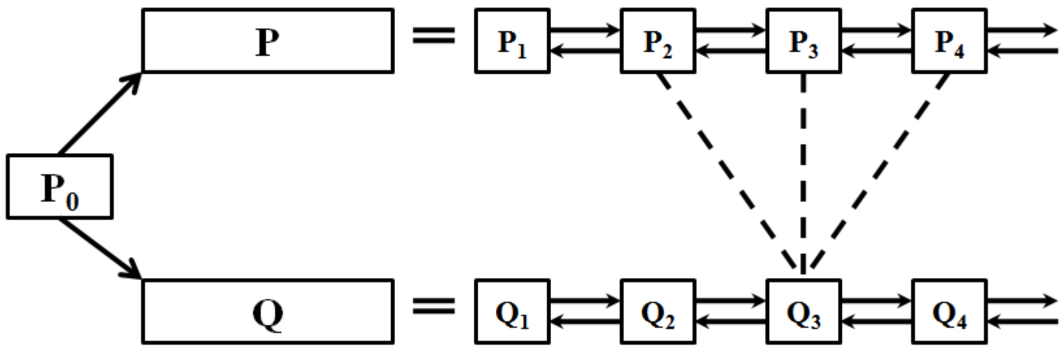

Figure 2.5 Multistep description of nuclear reaction using FKK theory [109, p-322].

The FKK theory of pre-equilibrium reactions considers that the P-chain and the Q-chain are non-interfering chains. In Figure 2.5 P_0 is the initial configuration with the projectile in the continuum and the two-body interactions are yet to begin. After the initial two-body interaction relaxation may proceed through either the P-chain or the Q-chain. The following are the important physical considerations in the FKK theory.

(1) Transitions can take place only between neighboring stages through two-body interactions. This is known as the chaining hypothesis.

(2) There is no interference between the P-chain and the Q-chain. Transitions from the Q-chain to the P-chain can take place only through statistical fluctuations in energy which may lead to emission.

(3) At low projectile energies the Q-chain interactions dominate giving the MSC emissions. As the energy increases the P-chain interactions become increasingly important giving MSD emissions.

(4) Since there is no interference between the P-chain and the Q-chain, the MSD and MSC components can be evaluated separately. Their sum is the total pre-equilibrium cross-section:

$$\sigma_{PEQ}(\varepsilon) = \sigma_{MSD}(\varepsilon) + \sigma_{MSC}(\varepsilon) \tag{2.39}$$

In the FKK theory, $\sigma_{MSD}(\varepsilon)$ and $\sigma_{MSC}(\varepsilon)$ are calculated quantum mechanically. In an extension of the exciton model [122,124] $\sigma_{MSD}(\varepsilon)$ is calculated by partitioning the partial level densities into densities of bound and unbound states. The exciton model calculates $\sigma_{PEQ}(\varepsilon)$ and after calculating $\sigma_{MSD}(\varepsilon)$ the MSC component is obtained by subtracting $\sigma_{MSD}(\varepsilon)$ from $\sigma_{PEQ}(\varepsilon)$.

In calculating $\sigma_{PEQ}(\varepsilon)$ we have defined D_n as the probability of reaching the n-exciton state without any prior particle emission. But same n can be obtained from different combinations of excited particles and holes ($n = 5$ can be obtained from $3p - 2h$ or $4p - 1h$ states). Therefore instead of D_n, $S_u(p, h)$ is used which is the probability of reaching a (*p*,*h*) configuration with at least one excited particle in the unbound state (denoted by the subscript u). D_n is given by, $D_n = S_u(p, h) + S_b(p, h)$ [109] where $S_b(p, h)$ is the probability of reaching a (*p*,*h*) configuration when all excited particles are bound.

Similar considerations apply to the emission rate $\lambda_c^n(\varepsilon)$ and the partial density of states $\rho_n(E_c)$ which take into account both bound and unbound states. These are replaced by $\lambda_c^{\langle u\rangle}(p, h, \varepsilon)$ and $\rho^{\langle u\rangle}(p, h, E_c)$, respectively representing unbound states only. Writing $\rho_{n'}(U) = \rho(p - \nu, h, U)$ where ν is the number of nucleons in the ejectile

$$\lambda_c^{\langle u\rangle}(p, h, \varepsilon) = \lambda_c^n(\varepsilon) \frac{\rho(p - \nu, h, U)}{\rho^{\langle u\rangle}(p, h, E_c)} \tag{2.40}$$

With these modifications (2.38) is written as

$$\sigma_{PEQ}(\varepsilon) = \sigma_{abs} \sum_{\substack{p=p_0 \\ \Delta p=1}}^{\bar{p}} S_u(p,h).T_u(p,h).\lambda_c^{\langle u\rangle}(p,h,\varepsilon) \tag{2.41}$$

where, the summation over n in (2.38) is replaced by a summation over p with $\bar{p}$ the number of excited particles in the equilibrated compound nucleus.

Now, MSD emissions occur from the P-chain where there should be at least one unbound particle at each stage of the relaxation process prior to emission. $S_u(p,h)$ is the probability of finding the composite nucleus in the (p,h) configuration with at least one unbound particle but it is not ensured that there was an unbound particle at each stage of the relaxation process prior to the formation of the (p,h) configuration. To make sure that the unbound state has not been populated through statistical fluctuations from the Q-chain, $S_u(p,h)$ in (2.56) is replaced by, $S_d(p,h)$, the probability of formation of the (p,h) configuration with at least one unbound particle such that the state has evolved from configurations which all had at least one particle in the continuum. This ensures that the system has always been in the P-chain prior to the emission - the condition for MSD emission. We then have

$$\sigma_{MSD}(\varepsilon) = \sigma_{abs} \sum_{p=p_0}^{\bar{p}} S_d(p,h).T_u(p,h).\lambda_c^{\langle u\rangle}(p,h,\varepsilon) \tag{2.42}$$

Derivations and details of evaluating $S_u(p,h), S_d(p,h), T_u(p,h)$ and $\lambda_c^{\langle u\rangle}(p,h,\varepsilon)$ are discussed in [123].

2.4.6 Multiple two-body scattering kinematics

The pre-equilibrium cross-section for the emission of a particle of type ν can be written as,

$$\frac{d^2\sigma}{d\varepsilon.d\Omega} = \sigma_{abs} \sum_N P_N^\nu(\varepsilon,\Omega) = \sigma_{abs} \sum_N D_N f_N^\nu P_N(\varepsilon,\Omega) \frac{\lambda_C^\nu(\varepsilon)}{\lambda_C^\nu(\varepsilon) + \lambda_t^\nu} \tag{2.43}$$

where $P_N^\nu(\varepsilon,\Omega)$ is the probability of emission ν type particle with energy ε in the direction Ω after Nth interaction. All other symbols have the same meaning as in eqn. 2.31. Eqn. (2.43) is a reformulation of the hybrid model. When integrated over all emission angles it reduces to the hybrid model for the angle integrated energy spectrum. In writing (2.43) the hybrid model has been reformulated in the following aspects. First ejectile emissions are considered after each representative two-body interaction instead of a given exciton state $'n'$ as is done in the hybrid model. Secondly, $P_N(\varepsilon,\Omega)$ and consequently the probability $P_N(\varepsilon) = \int P_N(\varepsilon,\Omega)d\Omega$ are obtained from the kinematics of multiple nucleon-nucleon scattering while the corresponding hybrid model probability of a nucleon having energy ε in the n-exciton state is expressed as the ratio of the partial level densities. The probability $P_N(\varepsilon,\Omega)$ is related to $P_N(E,\omega)$ --- the probability of the particle of type ν of having energy E moving in the direction ω inside the nucleus where $\varepsilon = E - E_0 - S_\nu(C)$ and Ω is related to ω through the effect of refraction. E_0 is the Fermi energy and $S_\nu(C)$ is the separation energy of ν in the composite nucleus.

To obtain $P_N(E,\omega)$ from nucleon-nucleon scattering kinematics we use, for convenience, the equivalence $P_N(E,\omega)dE.d\omega = P(k)dk$, the probability of a particle having momentum between k and $k + dk$, after N two-body interactions. After the first two-body interaction between the projectile and the target nucleon with momentum k_t , the probability that one of the scattered particles has momentum k is $P_{N=1}\,(k) = P(k_1 \rightarrow k)$, the transition probability from initial momentum $k_1$to final momentum k, being the projectile momentum inside the nucleus.

The differential cross-section, $\sigma(k_1 \rightarrow k)dk$, for this transition is given by

$$\sigma(k_1 \rightarrow k)dk = \int_{k_t} \frac{2k_r}{k_1}.\sigma(k_r\,,k_r')\frac{d\Omega'}{dk}.dk.P(k_t)dk_t \qquad (2.44)$$

where k_r and $k_r^{'}$ are the relative momenta of the nucleons before and after scattering, respectively. $\sigma(k_r\,, k_r^{'})d\Omega'$ is the scattering cross-section in the centre-o,f-mass frame of the two nucleons, Ω' being the solid angle containing $k_r^{'}$. $2k_r/k_1$ is the ratio of the relative to the incident velocity (needed for transformation from the centre-of-mass to the laboratory frame) and $P(k_t)dk_t$ gives the probability of the target nucleon having momentum between k_t and $(k_t + dk_t)$. The integration is over k_t only.

In (2.44) $\sigma(k_r\,, k_r')d\Omega'$ is in the centre-of-mass frame of the interacting nucleons while k_1, k and k_t are in the laboratory frame. $k_r\,, k_r^{'}$ are the same in the two frames. If $d\Omega'/dk$is expressed as a function of k_r and k_r' then $\sigma(k_r\,, k_r^{'})\frac{d\Omega'}{dk}$ becomes invariant in the two reference frames and (2.44) can be solved in the laboratory frame. After doing the necessary algebra [130] we have,

$$\sigma(k_1 \;\to\; k)dk = \frac{4dk}{k_1}\int \delta\left({k_r'}^2 - {k_r}^2\right).\,\sigma(k_r\,, k_r')P(k_t)dk_t \tag{2.45}$$

where the δ -function ensures energy and momentum conservation. Since the transition probability $P(k_1 \;\to\; k)dk$ is proportional to the cross-section $\sigma(k_1 \;\to\; k)dk$ we have,

$$P(k_1 \;\to\; k)dk = \frac{4dk}{k_1}\int \delta\left({k_r'}^2 - {k_r}^2\right).\,P(k_r\,, k_r')P(k_t)dk_t \tag{2.46}$$

where $P(k_r\,, k_r^{'})$ is the transition probability fromk_r to $k_r^{'}$ and corresponds to the nucleon-nucleon differential scattering cross-section $\sigma(k_r\,, k_r^{'})$.

Once $P_{N=1}\,(k)$ is known $P_N(k)$ for all subsequent two-body interactions can be obtained from the recursion relation,

$$P_N(k) = \int P_{N-1}(k')\,P(k^{'} \to k)dk^{'} \tag{2.47}$$

where the scattering kernel $P(k' \to k)$ is defined with k' replacing k_1.

To solve (2.46) it is necessary to define $P(k_r, k'_r)$ and $P(k_t)dk_t$. For $P(k_r, k'_r)$ the following assumptions are made. Since free nucleon-nucleon scattering cross-sections are nearly isotropic in the CM frame of the two nucleons $P(k_r, k'_r) = P(k_1)/4\pi$. The target nucleon momentum distribution $P(k_t)dk_t$ is given by the Fermi distribution function. Since the nucleus is in the ground state at the time of the first interaction it is assumed that $P(k_t)dk_t$ is given by the zero-temperature Fermi distribution:

$$P(k_t)dk_t = \frac{3dk_t}{4\pi k_F^3} \tag{2.48}$$

where, k_F is the Fermi momentum. With these assumptions Kikuchi and Kawai [130] have obtained the following solutions of (2.46)

$$P(k_1 \to k) = \frac{3P(k_1)}{4\pi k_1 k_F^3 q}\{k_1^2 k^2 \sin^2\varphi - kq^2(k^2 - k_F^2)\} \tag{2.49}$$

$$P(k_1 \to k) = \frac{3P(k_1)}{4\pi k_1 k_F^3 q}(k_1^2 - k^2) \tag{2.50}$$

Here φ is the scattering angle and q is the magnitude of the momentum transfer:

$q^2 = k_1^2 + k^2 - 2k_1 k\cos\varphi$. The different kinematic conditions under which (2.49) and (2.50) are to be used are

$$\begin{aligned}
&If\ k^2 \le k_1^2 - k_F^2 \quad and \quad \alpha_2 \le \cos\varphi \le \beta_2 \quad use \qquad Eqn.\,(2.49)\\
&If\ k^2 \ge k_1^2 - k_F^2 \quad and \quad \alpha_2 \le \cos\varphi \le \alpha_1 \quad use \qquad Eqn.\,(2.49)\\
&\qquad\qquad\qquad\qquad\qquad\ \ \alpha_1 \le \cos\varphi \le \beta_1 \quad use \qquad Eqn.\,(2.50)\\
&\qquad\qquad\qquad\qquad\qquad\ \ \beta_1 \le \cos\varphi \le \beta_2 \quad use \qquad Eqn.\,(2.49)
\end{aligned}$$

where,

$$\alpha_2 = \frac{k^2 - k_F^2 - k_F(k_F^2 + k_1^2 - k^2)^{1/2}}{k_1 k}$$

$$\beta_2 = \frac{k^2 - k_F^2 + k_F(k_F^2 + k_1^2 - k^2)^{1/2}}{k_1 k}$$

$$\alpha_1 = \frac{k_1^2 - k_F^2 - k_F(k_F^2 + k^2 - k_1^2)^{1/2}}{k_1 k}$$

$$\beta_1 = \frac{k_1^2 - k_F^2 + k_F(k_F^2 + k^2 - k_1^2)^{1/2}}{k_1 k}$$

Using the Kikuchi-Kawai solutions for $P(k_1 \rightarrow k)$ the angular distribution of pre-compound emissions can be obtained. The detail of the kinematical conditions with specific constraints can be found in **Appendix - C**.

This is the brief overview of the existing pre-equilibrium models but all these models have their own merits and demerits based on the incident particle energy, shape of the composite system, density distribution geometry with respect to the axis of rotation (spherical/ prolate/ oblate) etc. The model developed in this work along with the theoretical validation of the same will be discussed in the next chapter. In the next subsections we will discuss about the existing computer codes available for evaluating the emission contribution from direct, pre-compound and compound nuclear with a very brief discussion about the codes been used in this work.

2.5 Nuclear reaction model codes

The nuclear reaction model codes based on the type of reactions can be classified in same three categories, viz. direct, pre-compound and compound nuclear reactions codes. Among these, in the present work we have not considered the direct reaction components in the emission yield studies and the associated model codes will not be discussed here. There is a number of nuclear reaction codes available to describe compound and pre-compound nuclear reactions based on different formalisms. The reaction codes ECIS88[131], STAPRE [132], GNASH [133], HAUSER-V [134], PERINNI [135], TNG [136] etc. use the exciton model for PEQ reactions coupled with Hauser-Feshbach (HF) formalism to estimate evaporation contribution. The second one uses the same exciton model for the pre-compound calculations but the low energy evaporations are calculated using the Weisskopf-Ewing (WE) model. Example of such codes are PRECO [137], PRECO-D2 [138], PREM [139], PREANG-1 [140], PEQGM [141], AMAPRE etc. The third category uses the geometry dependent hybrid model (GDH) for calculation of the pre-compound emission. ALICE [142], HAFKA [143-144] are among the codes which uses the GDH model along with WE for obtaining the particle spectrum. In the code EMPIRE [79, 145] either exciton model or the hybrid model can be employed to calculate the PEQ emission. The details of the physical model and the basic structure of the codes can be found in the reference and references therein. In this work, we have used the statistical model code EMPIRE and the Monte Carlo based code PACE [77-78] to calculate the compound nuclear emissions. We shall discuss briefly about these two.

2.5.1 The EMPIRE code

EMPIRE is a flexible and adaptive set of nuclear reaction code, comprising of various nuclear models for different kind of projectiles viz. photon, neutron, proton or heavy ions, in a large energy range starting from a few keV for neutron induced reactions to a few hundreds of MeV for heavy ion reactions [79]. The models provide complete set of nuclear reaction channels involving the major nuclear reaction mechanisms with direct, pre-equilibrium and compound nuclear reactions along with observables like particle emission spectra, cross-section, angular distribution and double differential cross-section. At higher energies, the Distorted-Wave Born

Approximation (DWBA) and Coupled-Channel (CC) approaches are employed for dealing with the classical and quantum mechanical pre-equilibrium models for prediction of particles, clusters and γ-emissions from the composite nucleus before the thermal equilibrium of the compound nucleus is attained. Once the thermal equilibration is reached, the compound nucleus decay is described by the Hauser-Feshbach theory incorporating γ-decay and width fluctuations with angular momentum and parity coupling using *l*-dependent transmission coefficients. The angular distribution of the particles is assumed to be isotropic in the center of mass frame. Neutron, proton and other light ion emissions are taken into account with the competing fission channel. To account for correlation between the entrance and exit channel in the case of elastic scattering, the Hofmann, Richert, Teple and Weidenmuller (HRTW) model is used. Photon emissions are taken into account by statistical Hauser-Feshbach model with E1, E2 and M1 transitions using the giant multi-pole resonance model. The fission formalism involved in the code induced by photons and light particles work in the range from sub-barrier excitation energies to up to 200 MeV. It describes the transmission through the multi-humped fission barrier and makes use of the optical models to account for the fission mechanism associated with the full or partial damping of different degrees of vibrational states. EMPIRE also accounts for different nuclear models, extensively dependent on the level densities and the choice of different systematics. The evaluation of the level density parameters depend on the type of nucleon induced reaction, range of energy and collective enhancement of the level densities due to rotation and nuclear vibrations. In the present study, the dynamic EMPIRE specific level density approach has been used with super fluid model below the critical excitation energy and the Fermi-gas model at higher energies for a proper accounting of the spin-dependent rotation-induced deformation of the nucleus at higher energies. Finally, the recoil energy spectra are calculated considering the correlation between the compound nucleus excitation and the emission energy of the emitted particles by following throughout the de-excitation cascade. A particle emission depletes the spectrum bin of the parent and accumulates in the bin of daughter nucleus. Associated γ-emissions lower the effective excitation energy of the same nucleus without producing any recoil particle.

2.5.2 The PACE code

The code PACE (Projection Angular-momentum Coupled Evaporation)is a modified version of JULIAN, the Hillman-Eyal evaporation code with angular momentum coupling at each stage of de-excitation [77]. The formation of the compound nucleus is calculated using the Bass Model and for systems reported to de-excite solely by evaporation residues are determined by the height of the fission barrier and the ratio of level densities at saddle point to ground state. Transmission coefficients for the light particle emissions are calculated based on the optical model potentials till the energy regime where fission surpasses particle emission. The mode of de-excitation is calculated from the excited compound nucleus after normalization of the initial spin distributions using a Monte-Carlo random sampling with all possible decay channels according to their respective probabilities. The angular momentum projections are calculated at every stage of de-excitation for individually generated random emitted particles as functions of effective energy and angle around the recoil axis. In the present version of PACE2 a few modifications has been incorporated compared to the JULIAN code like incorporation of a fission decay mode using a rotating liquid drop fission barrier routine, level density information is taken from Gilbert-Cameron formalism. Further inclusions are like, artificial gamma cascade decay to simulate gamma multiplicity and photon energy when level density table cannot accommodate further decay due to spin inhibition.

These two model codes have been used in the present study to calculate the evaporation contribution from the thin or thick target systems. The estimated pre-compound emission contributions were then added with the evaporations to compare with the experimental emission spectrum of the ejectile (neutrons in the present case). Both the evaporation codes and the presently developed pre-compound code (HION) provides the emission spectrum from the thin targets, EMPIRE in the centre of mass frame whereas PACE and HION in the lab frame. So to estimate the emission spectrum from a thin target, the outputs of HION and PACE can be added together to compare with the experimental observations. Whereas in case of thick target neutron emissions, the codes need to run at different degrading energies considering a superimposition from projectiles of gradually reducing energies, starting from the incident energy up to the neutron emission threshold. A brief description of this superimposition is discussed in the following section.

2.6 Thin to thick target neutron yield

The neutron yield estimation is of prime importance in terms of the safety of personnel, installation and environment. From the perspective of radiation safety in a nuclear installation, the primary need is the shielding which can reduce the energy of the emitted particles through large number of interactions. So for safety purposes, the thick target yield is more important than the thin target neutron yields. In case of a nuclear reaction after projectile interacts with a stopping target, the emitted neutron spectra with angular distribution and associated dose can be estimated assuming it to be a superimposition from projectiles of gradually reducing energies, starting from the incident energy up to the neutron emission threshold of the compound nucleus or the Coulomb barrier. The estimations from the statistical model codes have been carried out in the same manner in the lab frame of reference for estimating the evaporation contribution. For the ease of calculation, the slowing down of the projectile is considered in small discrete energy steps and the thick target is divided in a number of thin slabs where the particle loses a specified amount of energy ΔE MeV in each of the slabs. In a given slab, the particle is assumed to interact with all the target nuclei with an average energy while ignoring the slowing down due to multiple scattering and straggling. After obtaining the neutron energy distributions at specified projectile energies through individual thicknesses, the effective thick target neutron spectra were generated. During the process of superimposition of thin target neutron spectra, the flux removal at individual target thicknesses and the respective fusion cross-sections at those energies were considered for the calculation of generated neutrons after each thickness grid, as discussed in the following part. The projectile energy E_p^i incident on i-th thin slab and the average energy $\bar{E}_p^i$ at this slab is computed for the incident projectile energy E_p^0 by,

$$\begin{aligned} E_p^i &= E_p^0 - (i-1)\Delta E \\ \bar{E}_p^i &= \left(E_p^i + E_p^{i+1}\right)/2 \end{aligned} \tag{2.51}$$

The slab thickness x_i was estimated from the stopping power of the projectile dE/dx as,

$$x_i = \int_{E_p^i}^{E_p^{i+1}} \frac{dE}{-dE/dx} \tag{2.52}$$

The total thick target emission neutron yield $Y(\epsilon,\theta)d\epsilon d\theta$ at energy ϵ and direction θ with respect to the initial projectile direction is computed using the relation

$$Y(\epsilon,\theta)d\epsilon d\theta = \sum_{i=1}^{n} \sigma\left(\bar{E}_p^i,\epsilon,\theta\right)d\epsilon d\theta N_T\, x_i \times exp\left[-N_T\left\{\sum_{k=1}^{i-1}\sigma_{fus}\left(\bar{E}_p^k\right)x_k\right\}\right] \tag{2.53}$$

Where, the $\sigma(\bar{E}_p^i, \epsilon, \theta)$ is the emission cross section of neutrons with energy ϵ emitted at an angle θ upon bombarded with a projectile of energy$\bar{E}_p^i$ and the exponential factor for the first slice is considered to be unity. The running index n represents the number of thin slices depending upon the discrete energy decrement, $n = (E_p^0 - E_p^{Th})/\Delta E$ where, E_p^{Th} is the projectile neutron emission threshold. The other parameters like, σ_{fus} is the fusion cross-section of the projectile with the target material and N_T represents the total number of target atoms per unit volume.

So in this chapter, the basic nuclear physics models were discussed with a few derivations used in the compound or pre-compound emission cross-sections and yield estimations. In the next chapter we will discuss about the development and modifications of the pre-equilibrium nuclear reaction model code (HION) with validation of the emission yields with some literature available experimental data.

Chapter 3

Development of the PEQ Model and Validation with existing data

3.1 The basic Pre-Equilibrium Model (HION)
- 3.1.1 Nucleon-Nucleon Scattering in the composite system
- 3.1.2 Hot and cold spot
- 3.1.3 Initial number of excited particles
- 3.1.4 Angular distribution at initial stage
- 3.1.5 Emission/Collision rate and emission probability

3.2 Literature Data for multiplicity (Ne/C +Ho at different energies)

3.3 Comparison with primary version of HION code and requirement of modifications

3.4 Present work involving HION model: Emission probability from Density dependent collision rates
- 3.4.1 Mean free path and nucleon density distribution
  - 3.4.1.1 Uniform density distribution and free nucleon- nucleon scattering
  - 3.4.1.2 Non-uniform density distribution and nucleon- nucleon scattering inside nucleus
  - 3.4.1.3 The semiphenomenological Approach
  - 3.4.1.4 The Relativistic mean field (RMF) Approach
- 3.4.2 Multiple pre-equilibrium (MPEQ)
  - 3.4.2.1 Simultaneous MPEQ
  - 3.4.2.2 Sequential MPEQ

3.5 Spatial Density profile of composite systems
- 3.5.1 Semiphenomenological approach
- 3.5.2 Relativistic Mean Field Approach

3.6 Modified Emission probability

3.7 Comparison with modified version of HION code

3.8 Comparison with multiple pre-equilibrium module at higher beam energies

3.9 Comparison of total Neutron Multiplicity data with experiment

The basic pre-equilibrium emission processes have already been discussed in the previous chapter using both closed form analytical solutions as well as quantum mechanical formalisms. Some other available phenomenological and theoretical proposals like moving source parameterization [146-147], Fermi-jet model [148-149] or quantum molecular dynamics (QMD) [62-64] approach have also been used widely to estimate the emission yield and angular distribution of the PEQ neutrons in heavy ion nuclear reactions. There are some shortcomings of these approaches as well. As for example, the moving source parameterization uses a number of fitting parameters to match the emission spectrum and does not explain the exact physical processes involved. The Fermi-jet model explains the pre-equilibrium (PEQ) emission spectra well at forward angle with respect to the incident beam direction but fails to predict the same in the backward direction. This model at higher incident projectile energies, predicts the total PEQ yield with a near linear increase, whereas the experimental yield increases in a power relationship, so it under-predicts the emissions compared to the experimental observations. The QMD approach predicts the yield fairly well, but this is a Monte-Carlo based simulation approach where the nucleons are represented as wave packets and the estimates are constrained by the Newtonian equation of motion. The QMD approach is computer intensive, time consuming and associates a large amount of statistical uncertainty even in case of light composite systems. The complexity involved restricts its use in the domain of heavy ion nuclear reactions. In order to overcome the shortcomings of these models, a two body scattering kinematics based pre-equilibrium model was developed by Ghosh et al [100-101] to estimate the pre-equilibrium emission spectra and angular distribution of neutrons.

3.1 The basic Pre-Equilibrium Model (HION)

In earlier works the heavy ion reaction model developed by Ghosh et al [100-101] energy angle distribution of nucleons in the target + projectile composite system was determined from the kinematics of two-body scattering. Excitation of the composite system was taken into account by dividing the composite system into two subsystems – a) a hot spot in which the nucleons are in Fermi motion at finite temperature and b) a cold spot where the nucleons are at zero temperature. Relaxation of the composite system proceeds through two-body scattering. Two body scattering between a nucleon in the hot spot and one in the cold spot leads to production of an excited particle-hole pair. Scattering between two nucleons in the hot spot results either in annihilation of a particle-hole pair or redistribution of the energies of the interacting particles. At any stage of the relaxation process nucleons may be emitted or take part in further binary interactions. Different stages of the relaxation process is described in terms of the number of two body interactions (N) that has taken place by then within the fused system till an equilibrium is reached. The PEQ double differential cross-section can be expressed as,

$$\frac{d^2\sigma^\nu}{d\varepsilon\, d\Omega} = \sigma_{fus} \sum_N f_N^\nu \left[\frac{\lambda_C^\nu(\varepsilon)}{\lambda_C^\nu(\varepsilon) + \lambda_t^\nu(\varepsilon)}\right] P_N(\varepsilon, \Omega) \tag{3.1}$$

where σ_{fus} is the fusion cross section of the projectile with the target nucleus and f_N^ν is the number of excited particles of type ν after N two-body interactions. $\lambda_C^\nu(\varepsilon)$ and $\lambda_t^\nu(\varepsilon)$ are the emission rate and two-body interactions rate with other nucleons of ν -type particle with energy ε respectively. $P_N(\varepsilon, \Omega) d\varepsilon d\Omega$ is the probability that the ejectile has energy between ε and $\varepsilon + d\varepsilon$ and is moving in the direction between the solid angles between Ω and $\Omega + d\Omega$ outside the composite nucleus. The probability $P_N(\varepsilon, \Omega) d\varepsilon d\Omega$ is determined from the probability $P_N(E, \omega) dE d\omega$ of a particle moving inside the composite system with energy between E and $E + dE$ in the direction between ω and $\omega + d\omega$ after N two-body interactions. The energy correlation can be represented as, $\varepsilon = E - E_F - S_\nu(C)$, where E_F and $S_\nu(C)$ are the Fermi energy and separation energy of ν-type particle in the composite nucleus respectively. The direction Ω outside the composite nucleus is related to the direction ω inside through the effects of refraction at the nuclear surface [101]. So, for estimation of the emission probability in the lab frame of reference, we initially need to calculate the probability $P_N(E, \omega) dE d\omega$ inside the nucleus and this can be obtained from the kinematics of two-body scattering inside the excited composite nucleus. In the next subsection we will discuss the methodology of estimating this.

For nucleon-induced reactions the summation in equation (3.1) starts from $N = 1$ as the projectile nucleon is removed from the entrance channel (particle gets absorbed in the target nuclei) through a two-body interaction with a target particle. In the case of fusion between two heavy ions, the process begins through the free flow of nucleons between the reacting nuclei as a result of the lowering of the interaction barrier between the two. The summation for heavy-ion reactions, thus, starts from $N = 0$. The upper limit of the summation should, in principle, extend up to infinity or at least to a very large number. However, since we are interested in pre-equilibrium emissions the summation is terminated when equilibrium is reached. In the process of calculating the emission probability, the most important point need to be considered is, the emission of neutrons taking place from the composite system and after emission of one particle the residual composite system is of no importance as far as the calculation is concerned. So at successive stages, one non-emission probability term needs to be introduced in the multiple two-body kinematics approach.

3.1.1 Nucleon-Nucleon Scattering in the composite system

The energy and angular distribution of the excited particles in the laboratory frame of reference remains incorporated within $P_N(E, \omega) dE d\omega$ and evolves through a sequence of two-body interactions in the composite nuclei. In the work of De et. al. [100] the interaction process within the composite system is considered to take place between the nucleons in two different subsystems, a hot spot and another cold spot. Considering partial equilibrium in the two sub-systems, the emission probability $P_N(E,\omega)dEd\omega$ within the nucleus will be governed by the two body kinematics in these sub-systems. The brief description and estimation of hot and cold spot fractions will be discussed in the next section. In the next part particle emission probability using the scattering kernels will be estimated .

The nucleons in cold spot does not contain the nuclear excitation carried in the incoming projectile, so interaction between two nucleons within the cold spot will not contribute to particle emission. So there are only two possibilities for particles emission: either interaction between two nucleons both from the hot spot or one in the hot spot interacting with the second one in the cold spot can lead to emission. The former process can be described by the scattering kernel at N −th stage of two body interaction by, $P_N(E', \omega' \rightarrow E, \omega)$ for scattering from the initial state of (E', ω') to the final state (E, ω). This interaction can lead to all possible processes, viz. the creation, annihilation or re-distribution of the energies of the excited particles. The energy-angle distribution probability at the N −th interaction $P_N(E', \omega' \rightarrow E, \omega)$ will consist of the components of creation, annihilation and redistribution of energy among the involved excitons which are denoted as $P_N^+(E', \omega' \rightarrow E, \omega)$, $P_N^-(E', \omega' \rightarrow E, \omega)$ and $P_N^0(E', \omega' \rightarrow E, \omega)$ respectively in the laboratory frame of reference.

$$P_N(E', \omega' \rightarrow E, \omega) = P_N^+(E', \omega' \rightarrow E, \omega) + P_N^-(E', \omega' \rightarrow E, \omega) + P_N^0(E', \omega' \rightarrow E, \omega) \qquad (3.2)$$

A short derivation of the transition probabilities for a multiple two body scattering is discussed in earlier and kinematical conditions with specific constraints are presented in Appendix -D and the more detail analysis can be found in [100].

For the latter kind of interaction responsible for a particle emission, the scattering kernels $P_{K-K}(E', \omega' \to E, \omega)$ are calculated using the standard Kikuchi-Kawai formalism [21]. In this scattering process, only a particle-hole pair is created as all energy levels below the Fermi energy are filled up. The probability $P_N(E, \omega)dEd\omega$ through these two processes can be estimated using the recursion relation,

$$P_N(E, \omega)dEd\omega$$

$$= \Big[\xi_{N-1} \iint D(E')P_{N-1}(E', \omega') \times P_{N-1}(E', \omega' \to E, \omega)dE'd\omega'$$

$$+ (1 - \xi_{N-1}) \iint D(E')P_{N-1}(E', \omega') \times P_{K-K}(E', \omega' \to E, \omega)dE'd\omega'\Big] dEd\omega \quad (3.3)$$

where, ξ_{N-1} is the hot spot fraction at the N −th set of scattering. In this cascade of interactions, the number of particles in the hot spot reflects the measure of the effective temperature at each step. In eqn. 3.3, the first term denotes the interactions in the hot spot at N −th scattering. $D(E')$ is the non-emission probability till (N-1)th interaction introduced to preserve the identity of the composite system. This can be expressed as,

$$D(E) = 1 - \sum_{\nu} \frac{\lambda_C^{\nu}(\varepsilon)}{\lambda_C^{\nu}(\varepsilon) + \lambda_t^{\nu}(\varepsilon)} \quad (3.4)$$

The basic PEQ process does not consider the residual nucleus for further emissions, but multi-nucleon emissions can occur from any stage of two-body interactions. In the later stage we will introduce the emissions from the residual composite systems while discussing the modifications in the calculation of emission probability.

3.1.2 Hot and cold spot

The hot spot fraction of the composite nucleus and its defining temperature progressively varies as the system evolves through the number of scattering interactions. The hot spot fraction

(ξ_N) available for $(N+1)$-th scattering interaction can be considered as the ratio of number of particles in the hot spot (A_N) to the total number of particles in the composite system (A). As described in [21] the hot spot fraction with excited particles(p_N) and the chemical potential μ can be represented as:

$$\xi_N = \frac{A_N}{A} = \frac{p_N}{A}\frac{A_N}{p_N} = \frac{p_N \int_0^\infty F(E,\beta)dE}{A\int_\mu^\infty F(E,\beta)dE} \tag{3.5}$$

where, excited particles can be described using Fermi distribution at temperature $T = 1/\beta$;

$$F(E,\beta) = \frac{\sqrt{E}dE}{1+e^{[\beta(E-\mu)]}};\ \beta = \frac{1}{kT} \tag{3.6}$$

The number of excited particles(p_N) after N-th interaction can be represented as, $p_N = \sum_\nu f_N^\nu$. And is obtained through a recursion relation,

$$f_N^\nu = f_{N-1}^\nu + p_{N-1}P_N^{creation}\left[\frac{A^\nu - f_{N-1}^\nu}{A - p_{N-1}}\right] \tag{3.7}$$

$P_N^{creation}$ is the net creation probability at the N-th interaction and the total number of available ν-type particle in the composite system is denoted as A^ν. $P_N^{creation}$ is obtained from the probability of creation (P_N^+) and annihilation (P_N^-) of exciton at N-th level.

$$P_N^{creation} = P_N^+ - P_N^- \tag{3.8}$$

3.1.3 Initial number of excited particles

The initial numbers of the excitons (n_0) available within the composite system is important for estimating the hot spot temperature at the first stage and the net emission at $N = 0$ in heavy ion reactions. The simplest is the formalism used by Blann [21,150] where the total projectile mass number is considered to be the initial numbers of exciton at $N = 0$ state i.e., $n_0 = A_P$.

A more realistic approach is estimation of the number of ν-type excited particles at the initial stage of relaxation through the Fermi momentum sphere consideration. In this approach, the

Fermi sphere of the composite system in momentum space is assumed to be in the centre of mass (C.M.) frame where the Fermi motions of the projectile and target nucleons are coupled with their respective C.M. motions [151]. A typical heavy-ion reaction using Fermi sphere model [152] is described in the Figure 3.1 where centers of the Fermi spheres of the projectile and target are separated from the composite by their respective center-of-mass momentum per particle.

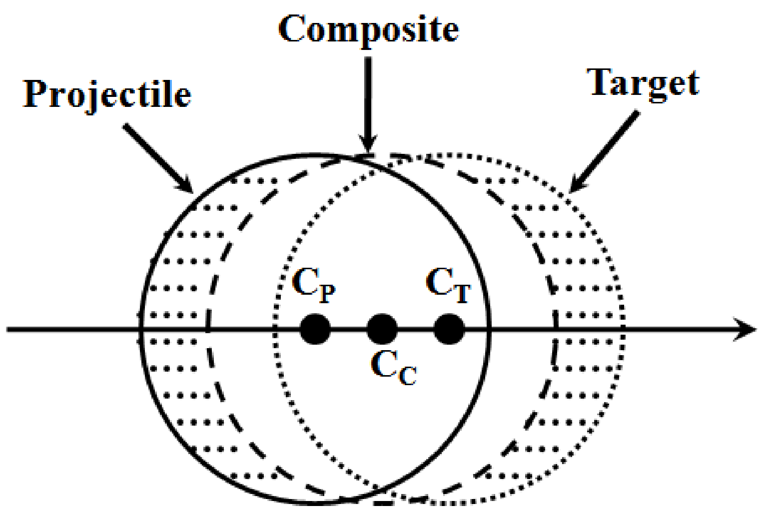

Figure 3.1: A typical Fermi momentum sphere for heavy-ion reaction leading to the formation of the composite nucleus is shown with Fermi sphere centered at C_P, C_C, C_T for projectile, composite and target nuclei respectively [21].

The volume outside the composite system represents the momentum states above the Fermi level. The number of these states can be estimated from the density of the momentum states $(\overline{n_\iota})$ for i-type particle folded by the total volume obtained from integrating the momentum vector p over appropriate limits. The total number of excited particles of type ν at the initial stage is given by [21],

$$f_{N=0}^{\nu} = \frac{A_P^{\nu}}{A_P} n_{0P} + \frac{A_T^{\nu}}{A_T} n_{0T} \tag{3.9}$$

3.1.4 Angular distribution at initial stage

The information regarding the distribution of the excited particles at the initial stage, $P_{N=0}(E,\omega)dEd\omega$ serves as the input for estimating the $P_N(E,\omega)dEd\omega$ in relation (3.3) at $N > 0$. For nucleons of the projectile, the effective velocity can be obtained by adding the Fermi velocity to the incident velocity of the constituent nucleons, as $v = v_{inc} + v_F$. If E, E_F are the energies corresponding to v, v_F respectively with ω and ω_F being the solid angles defining their direction with respect to the projectile, then one can write the following relation,

$$E_F = E + E_{inc} - 2\sqrt{EE_{inc}}\cos\eta \tag{3.10}$$

where, η is the polar angle of v with respect to v_{inc}. During the fusion of projectile in the target nuclei, it forms an excited nuclei but the initial direction of emission depends on the probability of particle having energy E_F and direction ω_F prior to the coupling of projectile velocity. This probability can be represented in terms of the finite temperature Fermi distribution [21]:

$$P_{0P}(E_F,\omega_F) = \left(\frac{3}{8\pi E_0^{3/2}}\right)\frac{1}{1+e^{[\beta(E_F-\mu)]}} \tag{3.11}$$

where, $\mu, \beta = \left(1/_T\right)$ are the corresponding chemical potential and excitation parameter respectively. The Jacobian of the transformation from (E_F,ω_F) to (E,ω) being unity, using relation (3.10) in (3.11), we get

$$P_{0P}(E,\omega)dEd\omega$$

$$= \left(\frac{3}{8\pi E_0^{3/2}}\right)\frac{\sqrt{E}}{\sqrt{E + E_{inc} - 2\sqrt{EE_{inc}}\cos\eta}}$$

$$\times \frac{dEd\omega}{1 + exp\left[\beta\left\{E + E_{inc} - 2\sqrt{EE_{inc}}\cos\eta - \mu\right\}\right]} \tag{3.12}$$

The excitation parameter β can be calculated from the entropy of the system with a knowledge of the partial density of states $\rho_N(E_C)$ after N-binary interactions at an excitation energy of E_C, $\beta = \frac{dS_N}{dE_C} = \frac{d}{dE_C}[\ln \rho_N(E_C)]$, $\rho_N(E_C)$ is the statistically weighted average of the partial level densities $\rho_n(E_C)$ of all possible n exciton states that may be formed after N two-body interactions. The average number of excitons after N collisions, $\bar{n}_N$, can be presented as $\rho_N(E_C) = \rho_{\bar{n}_N}(E_C)$. At the initial stage of fusion $N = 0$, the $\bar{n}_N = n_0$. For $N > 0$, at progressive stages, the average number of excitons can be calculated using a recursion relation (3.13).

$$\bar{n}_N = \bar{n}_{N-1} + \Delta\bar{n}_N \,; \quad \Delta\bar{n}_N = \bar{n}_{N-1} P_N^{creation} \tag{3.13}$$

Using the Blann prescription of $n_0 = A_P$, one achieves $P_{N=0}(E,\omega)dEd\omega = P_{0P}(E,\omega)d\omega$.

For the second formalism $n_0 = n_{0\,P} + n_{0\,T}$, where a part of both target and projectile is considered to be excited due to interaction and part of the target nucleons are supposed to gain the forward velocity due to forward motion of the composite system. For this choice, the forward velocity ($v_{C.M.}$) corresponding to the centre of mass energy of the target nucleons should be coupled with the Fermi velocity to obtain the initial distribution of the target nucleons. So using the similar approach used for the projectile distribution, one achieves the initial distribution of the target nucleons by [21],

$$P_{0T}(E,\omega)dEd\omega = \left(\frac{3}{8\pi E_0^{3/2}}\right)\frac{\sqrt{E}}{\sqrt{E + E_{c.m.} - 2\sqrt{EE_{c.m}}\cos\eta}}\,\frac{dEd\omega}{1 + exp\left[\beta\left\{E + E_{c.m} - 2\sqrt{EE_{c.m.}}\cos\eta - \mu\right\}\right]} \tag{3.14}$$

So, the total probability distribution of the excited particles in the hot spot at energy E within a solid angle ω at $N = 0$, can be represented as the

$$P_{N=0}(E,\omega)dEd\omega = \frac{1}{n_0}[n_{0P}P_{0P}(E,\omega) + n_{0T}P_{0T}(E,\omega)]dEd\omega \tag{3.15}$$

3.1.5 Emission/Collision rate and emission probability

In the early version of the pre-equilibrium reaction model for heavy ion (HION), the hybrid model has been used for the calculation of the emission probability of the neutrons emitted from heavy ion reactions upto few tens of MeV per nucleon. The respective emission and collision rates were calculated based on the hybrid model formalism. The emission rate [$\lambda_c^n(\varepsilon)$], is calculated using the relation (2.24) whereas the collision rates [$\lambda_t^n(\varepsilon)$] were calculated using the Blann formalism [85] presented as the relation (2.34)

$$\lambda_c^n(\varepsilon) = \frac{(2s+1)m\,\varepsilon\,\sigma_{inv}(\varepsilon)}{\pi^2\,\hbar^3} \tag{3.16a}$$

$$\lambda_t^n(\varepsilon) = [1.4\times 10^{21}(\varepsilon + B_v) - 6\times 10^{18}(\varepsilon + B_v)^2]k^{-1}\ \ sec^{-1} \tag{3.16b}$$

The symbols used in the earlier two relations carry their usual meaning. The cross-section for the reverse reaction $\sigma_{inv}(\varepsilon)$ is estimated using the method of Chatterjee et. al. [153]. From the emission and the collision rates the emission probability of the emitted particle can be calculated as;

$$P_c^n(x,\varepsilon) = \frac{\lambda_c^n(x,\varepsilon)}{\lambda_c^n(x,\varepsilon) + \ \lambda_t^n(\varepsilon)} \tag{3.17}$$

3.2 Literature Data for multiplicity (Ne/C +Ho at different energies)

The HION model discussed till now [21], has been tested with the experimental multiplicity data obtained from Holub et. al., Hilscher et al. [106-108] using ^{20}Ne and ^{12}C on ^{165}Ho target at different energies. A total of four different projectile energies for ^{20}Ne viz. 11, 14.6, 20.1 and 30 MeV/nucleon and 25 MeV ^{12}C on ^{165}Ho target have been studied. The multiplicity data obtained from the experiment were compared with the previously developed HION code (old HION/HION1) estimates at higher neutron emission energies considering it as majorly contributed by the PEQ neutrons. The comparisons are presented in the next subsection.

3.3 Comparison with primary version of HION code and requirement of modifications

The comparison of estimates from primary version of the HION code (now onwards will be considered as old HION) with the experiments are presented in the following figures [21].

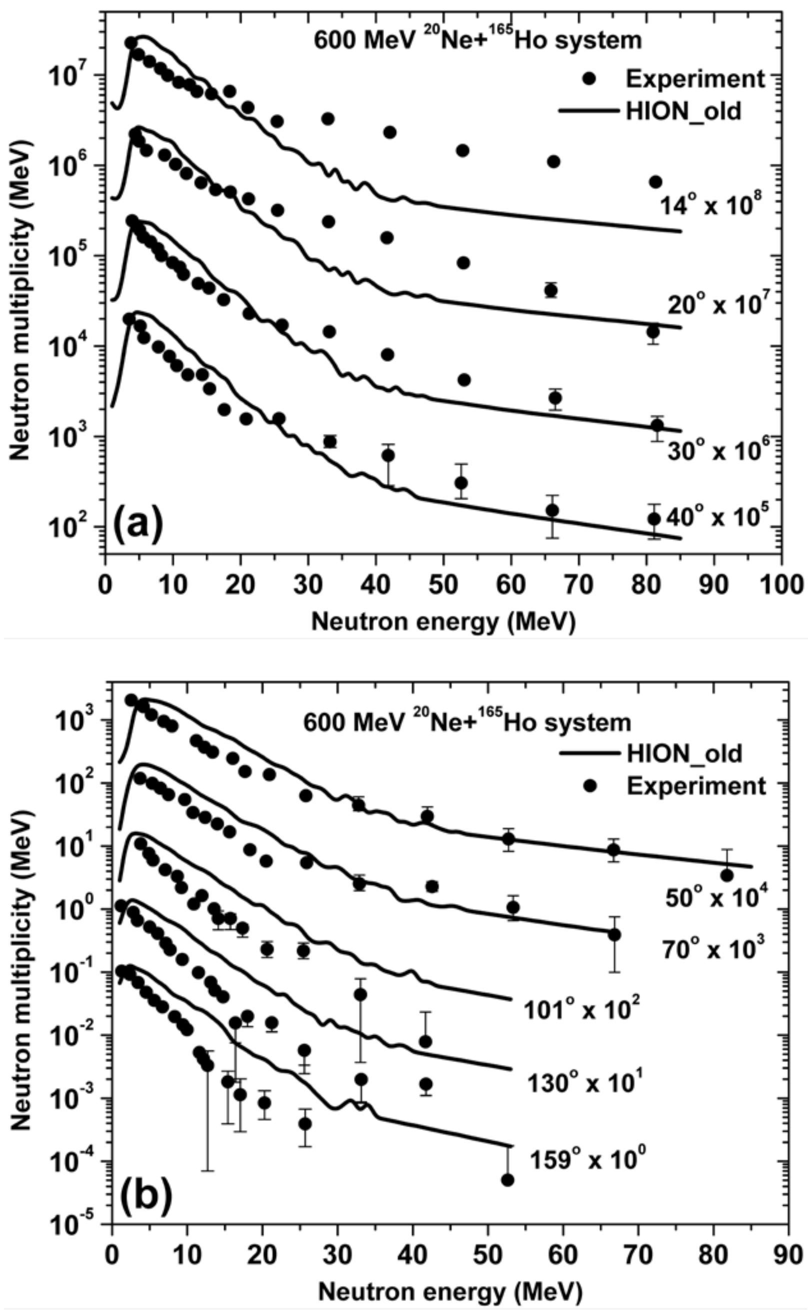

Figure 3.2: Comparison between the experimentally obtained (black circles with error bars) and theoretically calculated neutron multiplicities (evaporation from PACE4, PEQ from old HION model) for ^{20}Ne+^{165}Ho reaction at 600 MeV.

The evaporation contributions were calculated using the PACE4 nuclear reaction model code and the PEQ contributions from the old HION code. After obtaining the two estimates, the additive estimates were compared with the experimental observations. For the maximum projectile energy of 30 MeV/A, comparison at higher emission energies clearly shows a large underprediction at the forward angles as shown in Fig. 3.2(a). In the extreme forward angles, 14° and 20°, the multiplicity values underestimates drastically after 30 MeV of emission neutrons to the maximum. Whereas at other angles the underestimation is restricted to the intermediate energy regions (30° and 40°) showing relatively better match at the higher energies. Similarly at larger emission angles, presented in Fig. 3.2(b), angles 70° and beyond showed overprediction at higher emission energies for $^{20}Ne+^{165}Ho$ reaction at 600 MeV. Similarly for decreasing projectile energies of 402, 292 and 220 MeV ^{20}Ne target on the ^{165}Ho target are presented in the following figures.

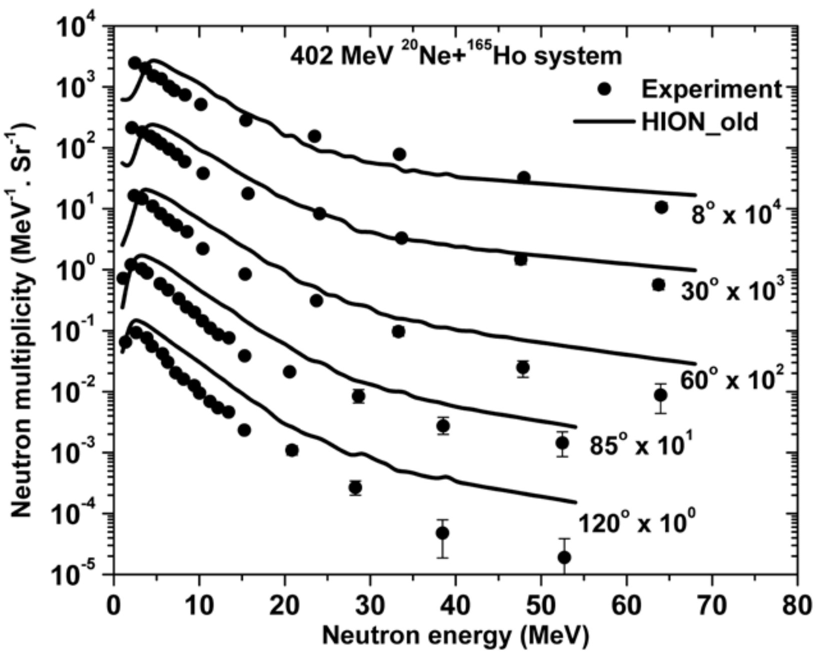

Figure 3.3: Comparison between the experiment and theoretically estimated neutron multiplicities for $^{20}Ne+^{165}Ho$ reaction at 402 MeV.

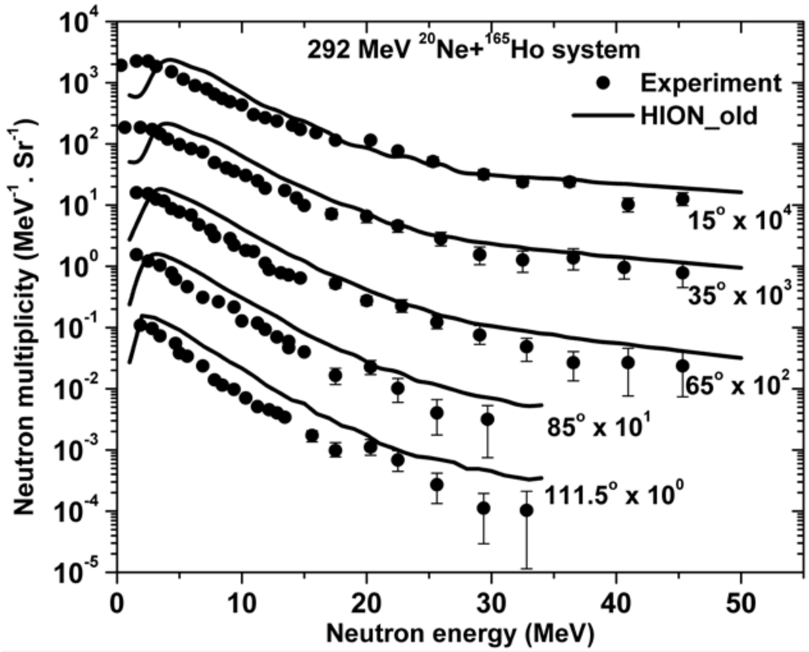

Figure 3.4: Comparison between the experiment and theoretically estimated neutron multiplicities for ^{20}Ne+^{165}Ho reaction at 292 MeV.

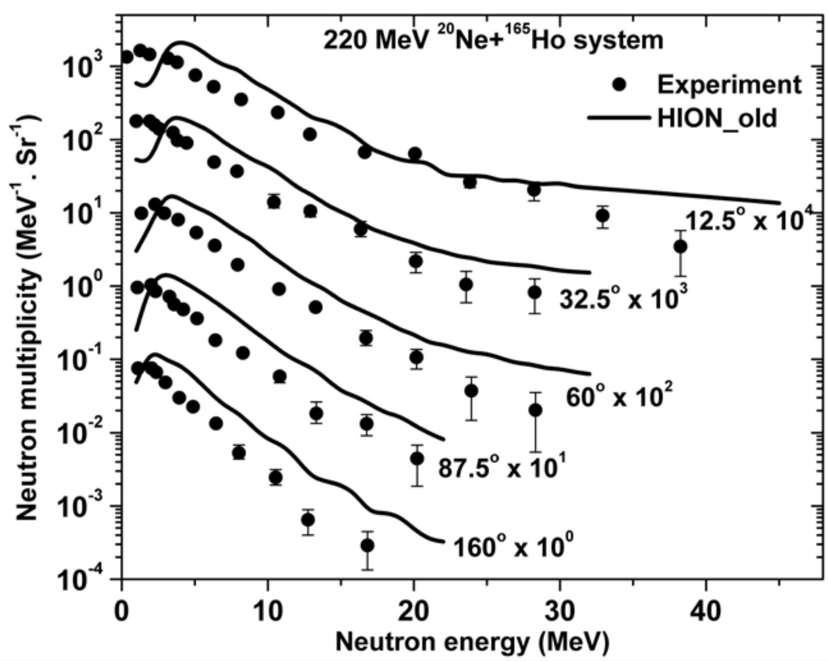

Figure 3.5: Comparison between the experiment and theoretically estimated neutron multiplicities for ^{20}Ne+^{165}Ho reaction at 220 MeV.

The comparison shows that, for 402 MeV the initial underestimation at the intermediate energies were present whereas at backward angles, the code overestimates and the observations are in line with earlier. At the same time from Figure 3.4 and 3.5 indicates no such underprediction in the forward angle estimates but backward angle over-predictions still persists at back angles. The similar behavior is found in case of $^{12}C+^{165}Ho$ system at 25 MeV/A projectile energy shown in figure 3.6. In this case also, model under-predicted at forward angles and over-predicted at back angles, similar to Figure 3.2 and 3.3.

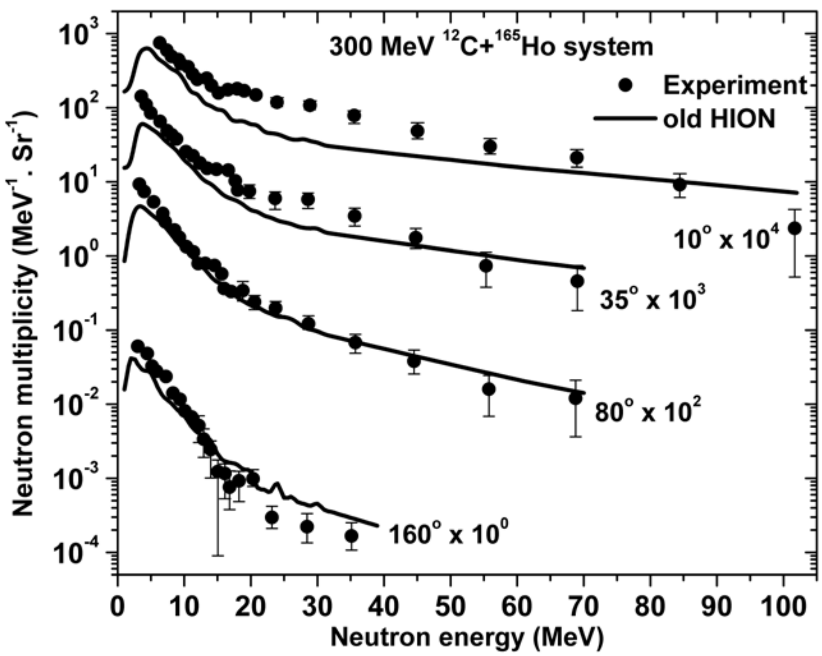

Figure 3.6: Comparison between the experiment and theoretically estimated neutron multiplicities for $^{12}C+^{165}Ho$ reaction at 300 MeV.

The trend found from Figure 3.2-3.3 and 3.6 clearly shows that as projectile energy increases beyond 20 MeV/A, the difference between the estimated and experiment also increases. This indicates the presence of some physical process whose accounting has not been considered at the forward angles in the old model for projectile energies more than 20 MeV/A. based on the observations, a possibility of secondary emissions or multiple particle emissions can be considered over and above the single particle emission consideration of the HION code. So in the next subsection, while discussing the modifications incorporated, we will discuss the effect of multiple particle emissions. Secondly a common feature leading to the overprediction in the back angles for all projectile energies need to be imposed in the present model to reduce the emission probabilities in the higher energies to make it more physically realistic. As a part of this exercise, there are two basic possibilities exist, firstly modifying the collision rates based on spatial nucleon distribution profile around the composite system to calculate a more realistic emission probability. Secondly, we need to review the effective excitation of the composite system, from which the emissions are taking place and possibly to reduce it by correcting the rotational energy contributions at different contributing azimuthal quantum numbers (*l*-values).

3.4 *Present work involving HION model: Emission probability from Density dependent collision rates*

In the present work, the emission rate has been kept same as earlier but the collision rate calculations have modified. In place of the Blann formalism, which uses an empirical relation depending solely on the separation energy of the emitted particle with respect to the composite system, a more realistic approach has been introduced in the present calculation based on the spatial nucleon density distribution and mean free path based collision rate calculation within the composite nucleus [96]. In the case of a heavy in reaction at energies up from a few tens of MeV/u to a few hundreds of MeV/u, the de-excitation is predominantly through the nucleon-nucleon interactions and the spatial distribution of the nucleons largely influences the total interaction/collision rate during the de-excitation phase of the nuclear reactions. Initially considering the over-predictions at backward angles as mentioned in the section 3.3, the effective nuclear excitations of the composite nuclei has been modified by accounting the rotational energy losses. The basic rotational energy relation has been used in the present work as expressed below,

$$E_{rot} = \frac{l(l+1)\hbar^2}{2\mu R^2}; R = 1.2A^{1/3} \tag{3.18}$$

$$E^*_{eff} = E_{CM} - SE - E_{rot} \tag{3.19}$$

where, the μ is the reduced mass and l is the azimuthal quantum number. So finally the effective excitation energy $\left(E^*_{eff}\right)$ of the composite system is calculated after subtracting the separation energy of the ejectile and its of the axis rotational contribution from the centre of mass energy(E_{CM}). As the contribution of the rotational energy is very small compared to the E_{CM}, so effective reduction in the emission neutron yield at backward angles were found to be vary between 2-4% of the total neutron yield and separately is not shown here. In the next subsections we will discuss about the modifications carried out in the earlier formalism in terms of the collision rates and how the nucleon density distribution affects the emission probability of the ejectiles.

3.4.1 Mean free path and nucleon density distribution

The calculation of the collision rates within the composite system calculated based on relation (3.16b) does not consider the prevalent nuclear fields as well as spatial nucleon density distribution and calculates a gross behavior of the system. This formalism assumes that the nuclear matter to be uniformly distributed throughout the nuclear volume whereas in reality the matter density is less in the surface region. This reduced matter density will have the following effects.

The reduced matter density at the surface will increase the mean free path (MFP) and thereby reduce the two-body interaction rate $\lambda^n_t(\varepsilon)$. Since, $\lambda^n_t(\varepsilon)$ competes with the emission rate, $\lambda^n_c(x,\varepsilon)$, reduction of $\lambda^n_t(\varepsilon)$ at the surface will enhance the emission probability, according to relation (3.17). Secondly, nuclear potential results from the sum of two-body nucleon-nucleon interactions. A lower matter density at the surface will, therefore, results in a potential of shallower depth at the surface. This will set a limit on the hole-excitation energy in the surface region. As a result, the ratio $\{\rho_n(U,E)/\rho_n(E_c)\}$ will differ in the surface region leading to a variation in the emission probability. So to make it more practical, a spatial nucleon density distribution around the centre of the composite system can give us a relatively better estimate of the emission neutrons. Before discussing the formalisms of density estimates a brief description of calculating the collision rate from MFP approach will be presented.

3.4.1.1 Uniform density distribution and free nucleon- nucleon scattering

The nucleon mean free path (MFP), L, is by definition,

$$L = \frac{1}{\rho\langle\sigma\rangle} \tag{3.20}$$

where, $\langle\sigma\rangle$ is the average two-body interaction cross-section and ρ is the matter density.

The two-body collision rate for a particle having velocity v and MFP, L can be expressed as,

$$\lambda_t^n(\varepsilon) = \frac{v}{L} = \frac{\sqrt{2E/m}}{L} = \rho\langle\sigma\rangle\sqrt{\frac{2E}{m}} \tag{3.21}$$

This simply refers that lesser the value of ρ, the larger is L leading to lower values of $\lambda_t^n(\varepsilon)$.

To evaluate (3.21), it is necessary to define $\langle\sigma\rangle$. This has done by Kikuchi and Kawai [130] formalism using the free nucleon-nucleon scattering cross-sections. The measured nucleon-nucleon (free) interaction cross-sections are fairly well-reproduced by an empirical expressions [154]:

$$\begin{gathered}\sigma_{nn} = \sigma_{pp} = \left(\frac{10.63}{\beta^2} - \frac{29.92}{\beta} + 42.9\right) mb \\ \sigma_{np} = \left(\frac{34.10}{\beta^2} - \frac{82.20}{\beta} + 82.2\right) mb\end{gathered} \tag{3.22}$$

Where, σ_{nn} , σ_{pp} and σ_{np} denote the neutron-neutron, proton-proton and neutron-proton cross-sections and $\beta = v/c$, c being the velocity of light in vacuum. Representing the nucleon motion inside the nucleus by a zero-temperature Fermi distribution function and applying constraints of energy and momentum conservation between the interacting nucleons, Kikuchi and Kawai obtain the average nucleon-nucleon interaction cross-section between a nucleon of type $i-$ and that of type $j-$ inside the nuclear matter as,

$$\overline{\sigma_{ij}} = \sigma_{ij} P(\varepsilon_F/E) \tag{3.23}$$

Where, σ_{ij} is given by (3.22) and

$$P(\varepsilon_F/E) = 1 - \frac{7}{5}\left(\frac{\varepsilon_F}{E}\right) + \frac{2}{5}\left(\frac{\varepsilon_F}{E}\right)\left(2 - \frac{E}{\varepsilon_F}\right)^{5/2} \; when, \qquad E \leq 2\varepsilon_F$$

$$= 1 - \frac{7}{5}\left(\frac{\varepsilon_F}{E}\right) \qquad when, \qquad E \geq 2\varepsilon_F$$

$\overline{\sigma_{ij}}$ is the scattering cross-section between a given nucleon $i-$ and given nucleon j. There are N neutrons and Z protons in the nucleus with which the i^{th} nucleon can interact. The average interaction cross-section of the i-type nucleon using the cross-section $\langle\sigma\rangle$ as,

$$\langle\sigma(E)\rangle_i = \frac{N}{A}\overline{\sigma_{ni}}(E) + \frac{Z}{A}\overline{\sigma_{pi}}(E) \tag{3.24}$$

Once no surface effects are considered and the density ρ is a constant, using an appropriate value of ρ with an assumption of free nucleon-nucleon scattering one can obtain the relation (3.16b), i.e., Kikuchi-Kawai value of $\lambda_t^n(\varepsilon)$.

3.4.1.2 Non-uniform density distribution and nucleon- nucleon scattering inside nucleus

In case of scattering inside the nucleus, angular momentum and parity conservation as well as constraint imposed by the Pauli principle would reduce the number of scattering events, thereby increasing the MFP with consequent decrease in $\lambda_t^n(\varepsilon)$. These may be included by dividing (3.21) by an arbitrary constant $\kappa > 1$.

$$\lambda_t^n(\varepsilon) = \frac{\rho\langle\sigma(E)\rangle_i}{\kappa}\sqrt{\frac{2E}{m}} \tag{3.25}$$

Blann [85] accounted for the effect of lower matter density in surface region by redefining κ as, $\kappa = C\kappa', \kappa'$ being the value of the arbitrary constant in the region of uniform density. The constant C is related inversely to the density [The larger the value of C, the smaller is the value of $\lambda_t^n(\varepsilon)$, with values of ρ we get smaller values of $\lambda_t^n(\varepsilon)$; hence $C \propto 1/\rho$]. In order to explicitly account for surface effects the nucleus needs to be divided into different zones characterized by the classical impact parameter, r_l, corresponding to each orbital angular momentum, l, in the entrance channel:$r_l = l\lambda$ where, λ is the reduced de Broglie wavelength of the projectile. Then the PEQ cross-sections can be calculated for each reaction zone as,

$$\sigma_{PEQ}^l(a; x, \varepsilon) = \pi\lambda^2(2l+1)T_l(\varepsilon_a)\sum_{\substack{n=n_0 \\ \Delta n=2}}^{\bar{n}} D_n \cdot \left[f_n^x \cdot \frac{\rho_n(U,E)}{\rho_n(E_c)}\right] \cdot \frac{\lambda_c^n(x,\varepsilon)}{\lambda_c^n(x,\varepsilon) + \lambda_t^n(\varepsilon)} \tag{3.26}$$

Where, $T_l(\varepsilon_a)$ is the transmission co-efficient of the $l^{th}-$partial wave of the projectile having energy ε_a and the rest of the notations carry their usual meaning. The absorption cross section is $\sigma_{abs}(a) = \pi\lambda^2 \sum_{l=0}^{\infty}(2l+1)T_l(\varepsilon_a)$ and PEQ energy spectrum of ejectile x is, $\sigma_{PEQ}(a; x, \varepsilon) = \sum_{l=0}^{\infty} \sigma_{PEQ}^l(a; x, \varepsilon)$. According to Blann (1972) the nuclear matter distribution can be represented by a two-parameter Fermi distribution function,

$$\rho(r_l) = \frac{\rho_0}{1 + e^{(r_l - R)/\alpha}} \tag{3.27}$$

with half-density radius R and diffusivity α. ρ_0 is the saturation density. The average $\langle\rho(r_l)\rangle$ can be evaluated between the impact parameters $r_l = l\lambda$ and, $r_{l+1} = (l+1)\lambda$, as

$$\langle\rho(r_l)\rangle = \frac{1}{r_{l+1} - r_l}\int_{r_l}^{r_{l+1}} \rho(r_l)\, dr_l \tag{3.28}$$

In a later paper, Blann [128] replaced the upper limit r_{l+1}, by the arbitrarily chosen limit, $R_S = R + S\alpha$, being that point, where the density falls to $(1/150)$ of saturation density ρ_0. The average was then evaluated between r_l and, r_{l+1}. The reason given is that with, r_{l+1}, the upper limit of the s- or p-wave, will show lesser surface absorption with (3.28), in spite of the fact, that all partial waves do have to pass through the surface region as shown in the figures below. The inadequacy of model to include possible surface interaction of low l −waves arises from the limitation of representing the three-dimensional nucleus by a single-dimension line divide in to segments by single-dimension impact parameter as shown in the left figure. The right one is more realistic, with a two-dimensional view of nucleus. The third dimension can be disregarded since the incident plane wave has azimuthal symmetry.

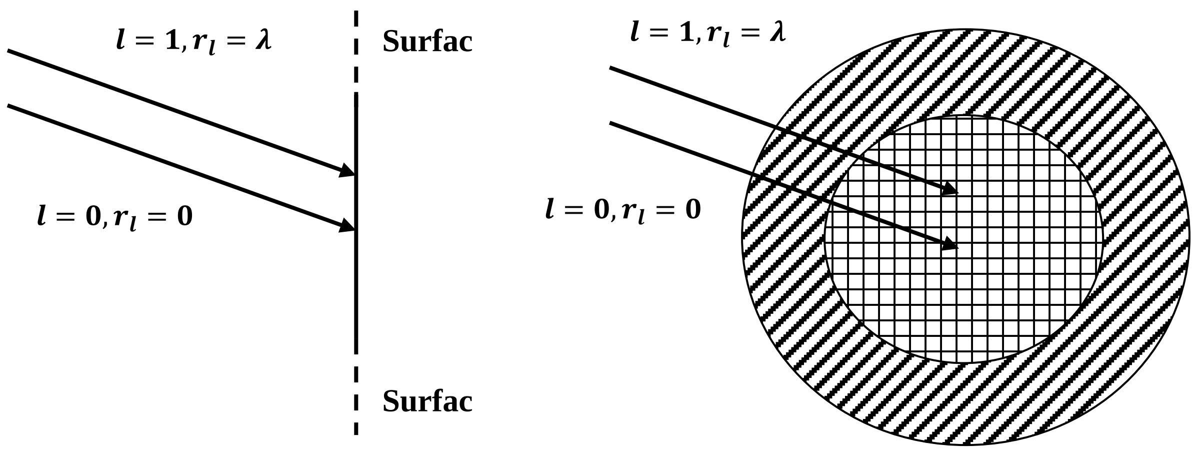

Geometrical situation of Eqn.(3.28). The solid line represents the section of bulk region and the dashed line that of the surface region

Actual situation shows the l-waves have to pass through the surface, even when l-is small. The heavily hatched area is the bulk region and the lightly hatched area is the surface region.

Figure.3.7 A proposition for nucleon- nucleon scattering inside nucleus

To compensate for the shortcoming, Blann [128] replaced (3.28) by evaluating $\langle \rho(r_l) \rangle$ between r_l and a sufficiently large impact parameter R_S where, the density is small enough

$(\rho_0/150)$ so that the surface region is covered in the average, $\langle\rho(r_l)\rangle = \frac{1}{R_S - r_l}\int_{r_l}^{R_S}\rho(r_l)\,dr_l$, which gives,

$$\frac{1}{C} = \frac{\langle\rho(r_l)\rangle}{\rho_0} = 1 + \frac{\alpha}{R_S - r_l}\ln\left\{\frac{1 + e^{(r_l - R_S)/\alpha}}{1 + e^{(R_S - R)/\alpha}}\right\} \tag{3.29}$$

Eqn. (3.29) is used to evaluate C for $r_l \leq R_S$. For, $r_l > R_S$, Blann uses the, straight forward arithmetic mean of $\rho(r_l)$ and $\rho(r_{l+1})$,

$$\frac{1}{C} = \frac{\langle\rho(r_l)\rangle}{\rho_0} = \frac{1}{2}\left[\frac{1}{1 + e^{(r_l - R)/\alpha}} + \frac{1}{1 + e^{(r_{l+1} - R)/\alpha}}\right] \tag{3.30}$$

So this is one of the relations for calculating the spatial nucleon density distribution in a composite nucleus. In the next sub-section we will discuss two other approaches of calculating the spatial nuclear density distribution using a semi-phenomenological and a relativistic mean field approach.

3.4.1.3 The semiphenomenological Approach

The semiphenomenological approach proposed by Gambhir and Patil [103], provides a relatively simpler expression for the nucleon densities which satisfactorily brings out the nuclear properties like shell effects, approximate global consistency of neutron central densities, large surface thickness and root mean square radius for neutron densities compared to that of protons etc. So considering these advantages over the earlier approach, the semi-phenomenological approach has been introduced in the present work. This approach serves as a simple and meaningful description which satisfies two general requirements, firstly the asymptotic behavior of the density and the central behavior. The constraints used for the density of particles were governed by the asymptotic nature, this in a nucleus is given by

$$\rho_i(r) \to r^{-2\alpha_i}e^{-r/a_i} \quad for \quad r \to \infty; \quad a_i = \frac{\hbar}{2(2mE_i)^{1/2}};\ \alpha_i = \frac{q}{\hbar}\left(\frac{m}{2E_i}\right)^{1/2} + 1 \tag{3.31}$$

Here, $i = n, p$, E_i is the separation energy of the last neutron or proton and $q = 0$ for neutrons and $q = Z - 1$ for protons, where Z is the atomic number of the composite system. Based on these parameters, the neutron and proton densities based on the semiphenomenological approach is represented as;

$$\rho_i(r) = \frac{\rho_i}{1 + \beta_i \left[1 + \left(\frac{r}{R}\right)^2\right] [e^{(r-R)/a_i} + e^{-(r+R)/a_i}]} \tag{3.32}$$

where, $i = n, p$ and R is the nucleus size. The expression ensures the asymptotic behavior for $r \gg R$ and includes significant corrections in the intermediate values of r as well. The second exponential term in the denominator is very small and this makes the expression different than a Fermi distribution. To identify the half density radius R, the term β_i is taken as $\beta_i = 2^{-\alpha_i}$. There are a total of 3 unknown quantities to be evaluated ρ_n, ρ_p, R in the present study using the physical constraints and normalizations. The first two of these were estimated using the normalization over the total number of protons (Z) and neutrons (N) as follows;

$$\begin{gathered} 4\pi \int \rho_n(r) r^2 dr = N \\ 4\pi \int \rho_p(r) r^2 dr = Z \end{gathered} \tag{3.33}$$

The remaining parameter, R for protons R_p can be predicted from the experimental rms charge density radius R_c (Angeli, 2013) for proton density by using the relation, $R_p \approx (R_c^2 - 0.6)^{1/2}$. This 0.6 is the small correction used for accounting the finite size of proton and the neutron. The analytical expression for the relation (3.33) near $r \approx R$ can be approximated as:

$$\beta_i \left[1 + \left(\frac{r}{R}\right)^2\right] \approx e^{[\alpha_i (r-R)/R]}$$

By placing it in (3.32), integrations reduces to standard one involving Fermi distributions;

$$4\pi \int \rho_i(r) r^2 dr \approx \frac{4\pi R^3}{3} \rho_i (1 + x_i^2)$$
$$\langle r_i^2 \rangle \approx R^2 (0.6 + 1.4 x_i^2)\ ;\ x_i = \frac{\pi a_i}{R + a_i \alpha_i} \tag{3.34}$$

So, finally all the parameters can be evaluated from the relation (3.33-34) to estimate the spatial density distribution relation (3.32).

In the semi-phenomenological approach, the spatial density distribution provides the density based on two basic patterns, firstly a central nucleon density behavior and an asymptotic behavior outside. The second important feature is that, the simplicity of the model provides a scope to readily use it for various calculations related to the nuclear scattering or heavy ion interactions, but individual nucleon interactions and the effect of nuclear potentials on the spatial nucleon distribution has not been considered in this formalism. But for an accurate estimation of the densities, these parameters need to be included in the estimation of density. So, a relativistic mean field based nucleon density distribution approach also has been introduced in the next subsection.

3.4.1.4 The Relativistic mean field (RMF) Approach

The theory of nuclear structure at low energies, treats the nucleus as quantum mechanical many body problem of Fermions through a non-relativistic two-body problem. After the understanding of exchange forces, a concept of relativistic Lagrangian has been introduced describing point-like nucleons interacting through the exchange of different types of mesons. In the RMF theory [104], the nucleus is described as a system of point like nucleons, Dirac spinors coupled to mesons and to photons. The mesons considered are the scalar σ, the vector ω and the iso-vector-vector ρ. The σ - meson provides a strong attraction whereas ω -meson provides strong repulsion, such that the sum (attraction + repulsion) of σ and ω contributions roughly adds up to around 50 MeV, the value consistent with the accepted non relativistic value of the average nucleon potential inside the nucleus. The inclusion of ρ meson accounts for the small iso-spin dependence. The variation principle yields the equations of motion. There are three basic assumptions in the model: (a) nucleons are point particles; (b) theory is fully Lorentz invariant and (c) it strictly follows causality. The starting point of relativistic mean field theory is the well known local Lagrangian density:

$$\mathcal{L} = \bar{\psi}\left(i\gamma^{\mu}\partial_{\mu} - m\right)\psi - m_{\sigma}^{2}\sigma^{2} - \frac{1}{3}g_{2}\sigma^{3} - \frac{1}{4}g_{3}\sigma^{4} - \frac{1}{4}\Omega_{\mu\nu}\Omega^{\mu\nu} + \frac{1}{2}m_{\omega}^{2}\omega_{\mu}\omega^{\mu} - \frac{1}{4}\vec{\mathrm{R}}_{\mu\nu}\vec{\mathrm{R}}^{\mu\nu}$$
$$+ \frac{1}{2}m_{\rho}^{2}\vec{\rho}_{\mu}\vec{\rho}^{\mu} - \frac{1}{4}\mathrm{F}_{\mu\nu}\mathrm{F}^{\mu\nu} - g_{\sigma}\bar{\psi}\sigma\psi - g_{\omega}\bar{\psi}\gamma^{\mu}\omega_{\mu}\psi - g_{\rho}\bar{\psi}\gamma^{\mu}\vec{\tau}\vec{\rho}_{\mu}\psi$$
$$- e\bar{\psi}\gamma^{\mu}\frac{1+\tau_{3}}{2}\psi \tag{3.35}$$

At this stage the mean field approximation is introduced. The fields are not quantized and so are replaced by the expectation values. Considering the time reversal invariance along with this we obtain the Dirac type equation. Here the potentials involving the meson fields describe the nucleons. Additionally, the Klein – Gordon type equations describe the sources involving nucleon currents and densities for mesons [96]. These nonlinear set of coupled equations known as RMF equations, are to be solved self-consistently. The required set of parameters is determined through the χ^2 - fit to reproduce the observed ground state properties of a spherical nucleus. Several sets of parameters exist - some of which include additional coupling terms and/or additional mesons. The most widely used set is NL3 [155]. The calculation yields the nucleon spinors, total binding energy (BE) and the deformation. Other observables like the proton and neutron rms radii, neutron skin, nucleon density distributions, quadrupole moments etc. can also be calculated. The resulting axially deformed (function of r and θ) density distributions are expanded in terms of multipoles and the L=0 (the spherical) part is projected out. This spherical part with correct normalization is used in the present work [96].

3.4.2 Multiple pre-equilibrium (MPEQ)

The discussions and plots considered in the earlier subsection 3.3 clearly indicate that at forward direction the underestimation in the PEQ estimates with respect to the experimental observations increases with increase in the projectile energy. The probability of multiple emissions is only significant at relatively high excitation energies and can only be found at energies higher than 20 MeV/A projectile energies. This signifies a possibility of multiple particle emission contribution which has not been considered in the old formalism of the model. Along with that as the particles emits out, it shares a part of the excitation energy of composite system, the most probable energy of the particles will lie between both the extremities, the lower energy end will be dominated by the evaporation neutrons and the higher emission energies by the single particle emissions. So the pattern observed specifies the MPEQ contribution in the experimental measurements. So in the present work, an effort has been made to introduce the energy dependent multi-particle emission probability in the PEQ stage. In an earlier work Blann and Vonach [90] introduced a geometry dependent hybrid model approach to encounter the multi-particle emissions in the PEQ stages based on simple probability arguments. The similar approach has been adopted in this work also.

The multiple pre-equilibrium emissions from the composite system exciton hierarchy, can follow two different pathways depending upon the time scale of interactions and energy sharing processes. If we consider a particle-hole formalism, then multiple particle emission possibility exist from any of the configurations beyond a two particle - one hole system and both particles can be emitted at a time. In that case based on the recoil of the system, the particle energies and directions can be estimated and the process can be named as simultaneous MPEQ. The second possibility is emission of one particle from the composite system, leading to a recoil nucleus with sufficiently excess energy beyond the particle separation energy. This excited residual nucleus, at later stages can de-excite via further single or multiple emission pathways based on the available excitation energy and is known as sequential MPEQ.

3.4.2.1 Simultaneous MPEQ

In case of a simultaneous emission, the particle emissions are taking from the un-equilibrated (target + projectile) composite system as a whole and the source nucleus behaves as a reservoir from which both nucleons gets emitted. So in this case the physical constraints for estimating the particle emission probabilities and the kinetic energy distributions were estimated considering the system excitation energy of the initial nucleus. In the present study, the former option has been incorporated following the idea proposed by Blann and Vonach [90]. The probability $P_{nn}(\varepsilon,\omega)$ of emission of two neutrons with energy ε in the direction ω from the same exciton hierarchy is taken as $P_{nn}(\varepsilon,\omega) = P_n(\varepsilon,\omega).P_n(\varepsilon,\omega)$ where, $P_n(\varepsilon,\omega)$ is the probability of single neutron emission.

3.4.2.2 Sequential MPEQ

In case of the Sequential multi-particle emissions, it is assumed that only the residual nucleus will be considered for tracking in the next exciton hierarchy where neutron has been emitted as the initial particle. The emission probability and the associated kinetic energy of the emitted neutron defines the residual nucleus excitation energy and the other kinematical conditions. The residual nucleus is then considered as a potential excited nucleus for a single or a multi-particle emission. For single particle emission the same set of constraints and conditions discussed earlier is used and the process continues till the system energy reduces effectively below the multi-particle emission threshold. So for the multi-particle emission through a "sequential" pathway needs even higher projectile energy compared to the "simultaneous" one for generation of similar kinetic energy distribution of the emitted particles, due to the reduction in the system energy after initial particle emission.

Initially at energies starting from 20 MeV/A, the contribution from the simultaneous emission is found to be higher than the sequential emissions as the probability of a particle emission from the residual reduces due to the insufficient available energy in the later stages. As the projectile energy increases, the contribution from sequential emissions increases. The second important aspect in terms of the emission energies from these two types are, the simultaneous emissions are mostly restricted in the intermediate energy range of the emissions, whereas the sequential emissions tend to populate the higher energy regime and drastically reduces at larger angles and with projectile energy. In the next sections we will discuss about the implementation of the modifications mentioned in the HION code and its effect on the same systems discussed in section 3.3.

3.5 Spatial Density profile of composite systems

The spatial nucleon density distribution of the composite systems under study are ^{185}Ir and ^{177}Ta generated from the bombardment of ^{20}Ne and ^{12}C bombardment on the ^{165}Ho target respectively. In this subsection we will try to analyse the distribution pattern with both the formalisms, viz. semiphenomenological and RMF.

3.5.1 Semiphenomenological approach

The nucleon density distributions for both the composite systems using semiphenomenological approach are presented in the figure 3.8. The assumption considered in this calculation is that during the fusion process between the target and projectile during the evolution of the composite system, the nucleon density distributions remains unchanged throughout the fusion process. This is not a strict realistic representation of the microscopic behavior within the nucleus in the true sense but by far a better assumption that an empirical relation presented by Blann [85]. Considering the time invariance of the density distributions to hold good, formalism shows a near consistent nucleon distribution in the central region and the nucleon density is found to be ~0.09 nucleon.fm^{-3} for neutrons and 0.07 nucleon.fm^{-3} for protons.

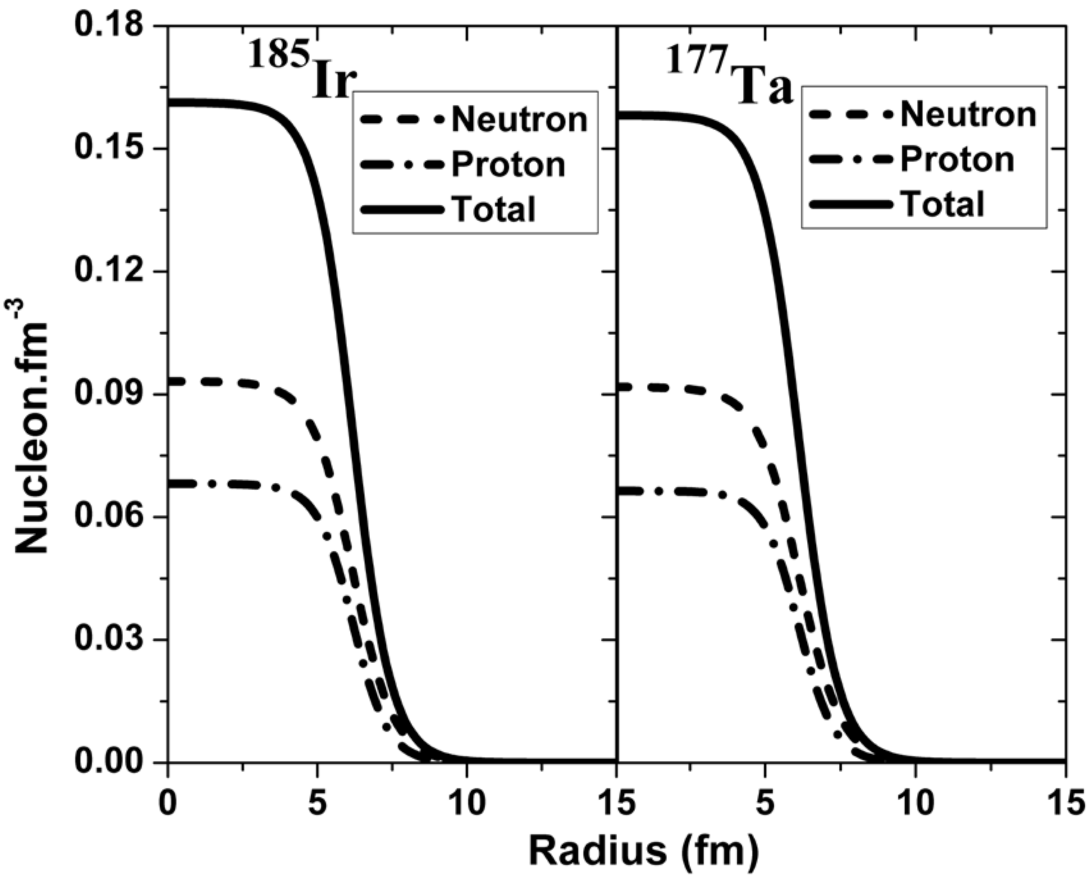

Figure 3.8: The nucleon density distribution of composite systems (^{185}Ir and ^{177}Ta) using semiphenomenological approach.

The variation in the nucleon density values for both the systems are due to the experimental r.m.s. charge density radius values of the composite system. The ^{185}Ir system generated from the ^{20}Ne+^{165}Ho system, shows a central neutron density of 0.93 fm^{-3} and almost remains the same till 4 fm from centre of nucleus and then falls 0.0061 fm^{-3} by 8 fm whereas similar trends with a reduced nucleon density values were found for the proton densities. The proton density is found to be 0.068 fm^{-3} at the central point and reduces to 0.003 fm^{-3} at 8 fm from the centre core. A larger value of the neutron density compared to the protons is basically attributed to the repulsive Coulomb forces present within the nucleus. Similarly for ^{177}Ta composite system, the density distribution value obtained from the semiphenomenological approach shows a value of 0.917 and 0.664 fm^{-3} respectively for neutron and proton respectively at the nucleus core.

3.5.2 Relativistic Mean Field (RMF) Approach

The relativistic theory of nuclear forces generally starts with a density dependent form of energy functional to be used for variational calculations of Hartree-Fock type and fitted with the experimentally obtained data of nuclear matter and nuclei using Gogny [ref] or Skryme [ref] forces [Ref: Ring et al]. As discussed earlier about the RMF approach, here the fields are represented by the wave functions of nucleons with several different kinds of interacting meson fields and electromagnetic potentials. Nucleons interact only by meson fields and the extent of interaction depends on the type of meson characterized by the angular momentum, isospin and parity. Among these, the exchange of scalar mesons (pion) lead to attractive and the vector mesons (ω-meson) to repulsive nature whereas the δ-mesons lead to scalar nuclear potentials leading to a different interaction for neutrons and protons within the nucleus. An interplay between all these forces deforms the spatial nuclear density distribution pattern in the RMF field. Both the composite systems under study, shows a depression in the total nucleon density distributions and among the two types, the protons have a much reduced nucleon density at centre due to the presence of short range repulsive exchange mesons and Coulomb repulsion. In case of neutrons the only repulsive nature is present so density profile shows a depression compared to the intermediate range densities. In both cases it was found to have a double hump nature in the composite system spatial densities and the central density is found to be less than the semiphenomenological density profile.

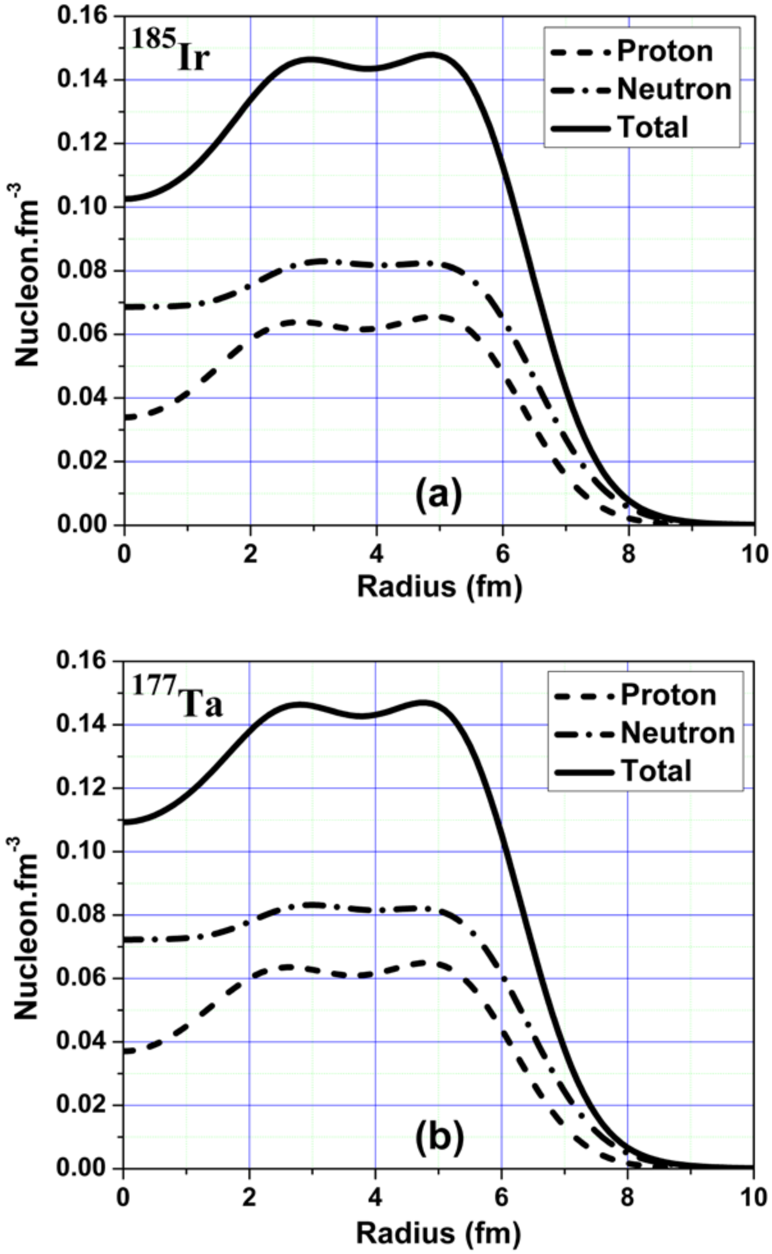

Figure 3.9: The nucleon density distribution of composite systems (^{185}Ir and ^{177}Ta) using Relativistic mean field approach.

The skin thickness in the RMF case is also found to be less than the earlier one. The calculated density profiles for ^{185}Ir and ^{177}Ta systems are shown in Figure 3.9. In case of ^{185}Ir system the central core density is found to be ~35% less compared at 5 fm and reduces to almost zero by 9 fm. Similar trend is found in case of ^{177}Ta system as well.

For neutron densities, the central values are found to be ~83% of the maximum density and nucleon density appears as a double hump in the range of 3–5 fm with a dip at 4 fm. For protons densities a similar but more pronounced trend is found. The collective nucleon density distribution shows, at the center a density of 70% that of the maximum value at 5.0 fm.

3.6 Modified Emission probability

The modified emission probability based on collision rates from the density variation within the nuclei of the composite system is shown below. In the figure, all three formalisms (Empirical, semiphenomenological and relativistic mean field) were compared for the ^{20}Ne+^{165}Ho system. From the calculated density profile and associated in medium N-N interaction cross-sections as obtained from [153-154], the two-body collision rates and subsequently the emission probabilities of neutrons are calculated as a function of neutron energy for different values of ℓ for both the composite systems. These emission probabilities for ℓ = 10 are shown in figure 3.10 along with that calculated using the N-N collision rate. The variation is energy dependent and increases with increase in the emission energy of the neutrons. As the density of the composite system is assumed to be time independent, so it became independent of the projectile energy as well. So the density value in the relation 3.31 will remain valid for all energies from 220 to 600 MeV of projectile energy. In the figure, the maximum neutron energy theoretically has been calculated till 480 MeV considering the theoretical limit of neutron energy derived from the excitation energy of the composite systems although the effective yield at this energy will be negligible from the scattering kinematics. The figure clearly indicates that the empirical relation (blue dash dot line) sharply increases after 100 MeV and after 150 MeV sharply increases to 0.5. Beyond 200 MeV, the emission probability values become unphysical. In contrary, for semiphenomenological and RMF cases the emission probability steadily increases till 300 MeV and after that retains a steady probability value till 350 MeV and further reduces.

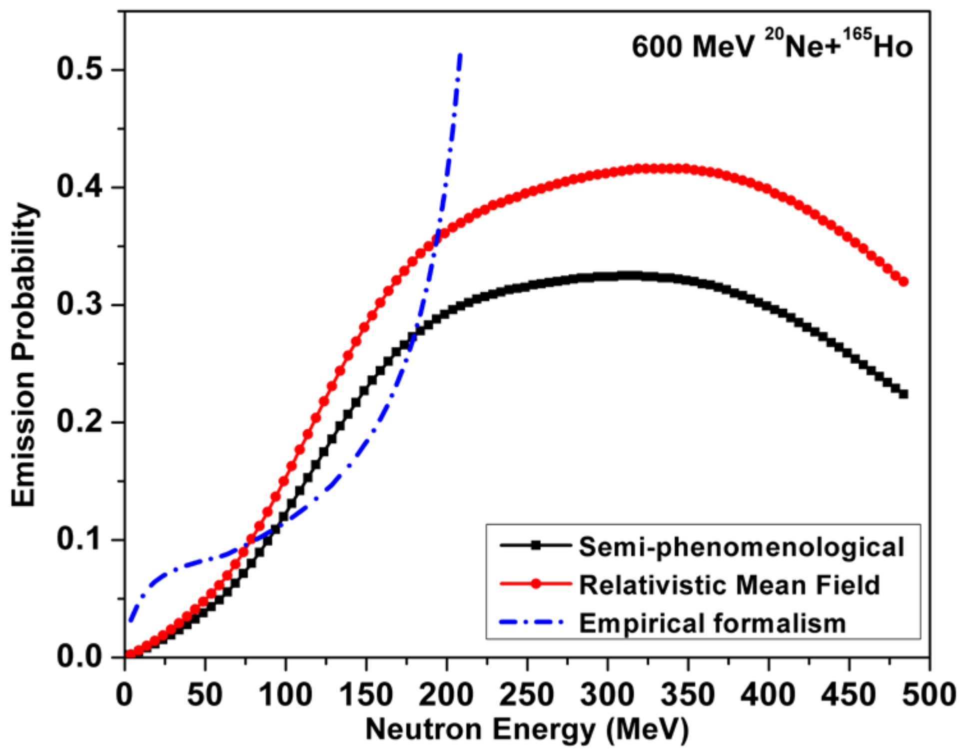

Figure 3.10: The modified emission probability of ^{185}Ir composite systems using Empirical, semiphenomenological and Relativistic mean field approach [96].

The semiphenomenological densities are found to be higher compared to RMF one in the central part but the total effect of the collision rate reflects that the emission probability from RMF formalism will estimate a higher neutron yield compared to the semiphenomenological approach. The close view till the emission probability values up to 150 MeV, clearly shows that the empirical relation provides a higher neutron yield till 75 MeV of emission energies and beyond this energy both the modified formalism showed a greater yield till 175 MeV of emission energy. This clearly supports the experimental observations discussed in section 3.3, where at lower projectile energies forward angle yield are overestimated and at higher energy is was underestimated with the older version of the HION code [21]. Similar trends were also observed for the ^{177}Ta system shown in Figure 3.11. In this case also till 75 MeV and beyond 175 MeV of emission neutron energy, the empirical relation shows a higher probability whereas in the energy range of 75-175 MeV, the density dependent models showed a greater yield. In the next section we will discuss the effect of modified emission probability values in the pre-equilibrium neuron yield. The emission yields will be compared with the older formalism along with the modified ones.

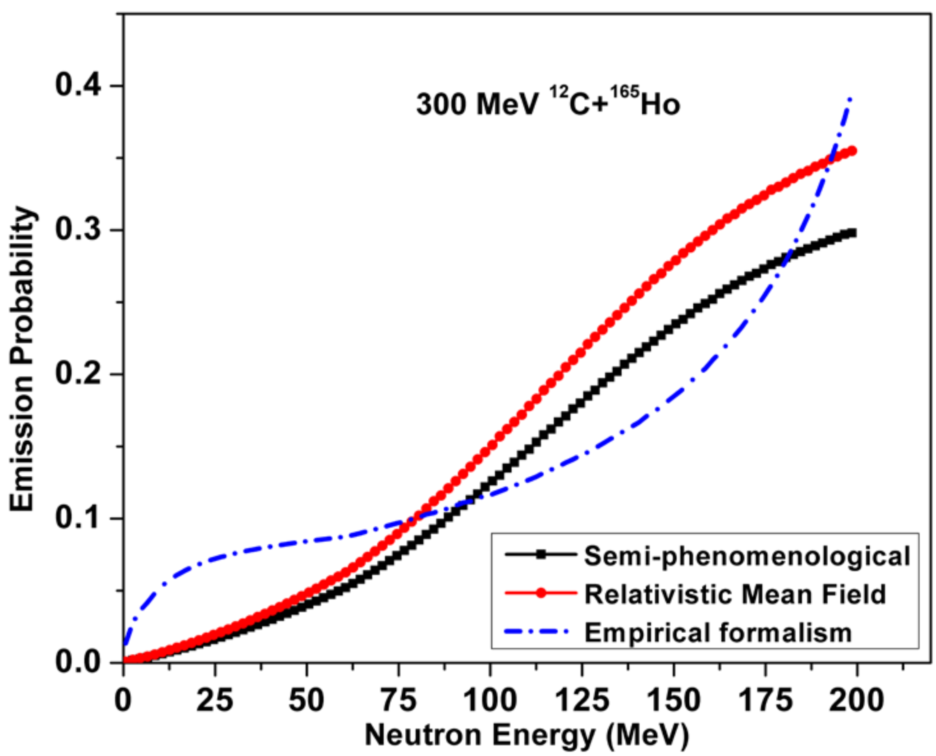

Figure 3.11: The modified emission probability of ^{177}Ta composite systems using Empirical, semiphenomenological and Relativistic mean field approach.

3.7 Comparison with modified version of HION code

In this section the experimental neutron multiplicities will be compared with the modified emission probability calculation based on the modification of the density dependent collision rates. In the present comparison, only the PEQ component will be compared for all available energies of $^{20}Ne+^{165}Ho$ and $^{12}C+^{165}Ho$ system. In the figures, the old HION formalism will be denoted as the HION1 and the RMF and semiphenomenological modifications as HION2 and HION3 respectively [96].

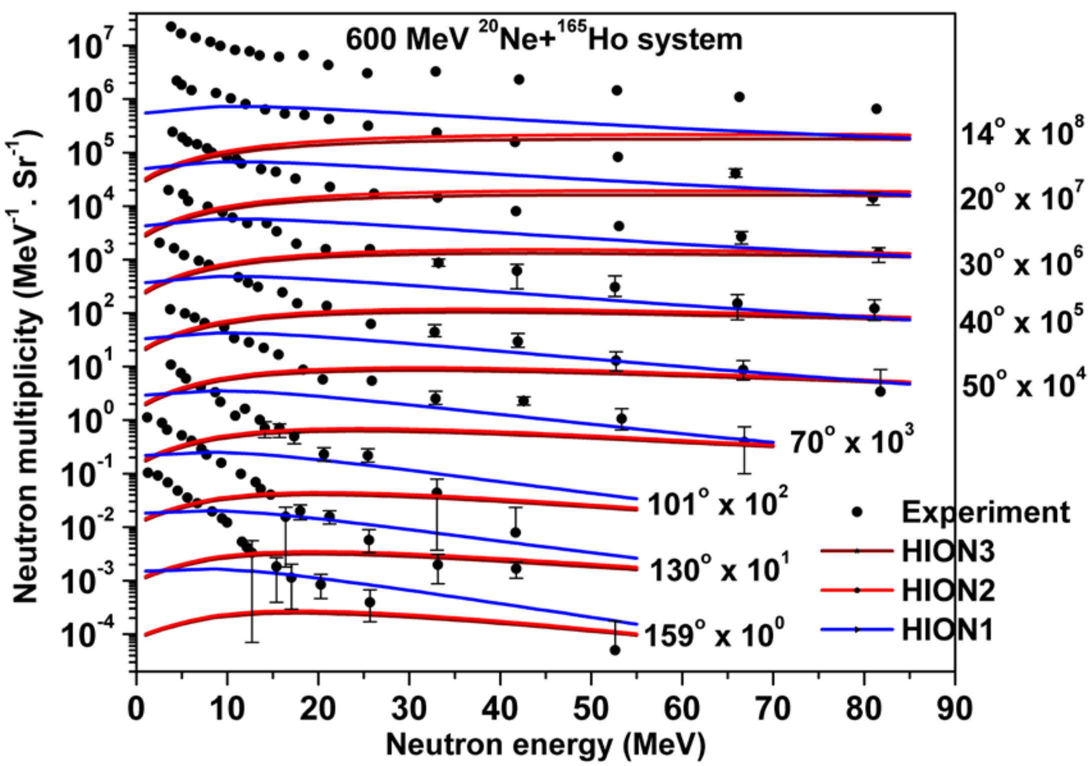

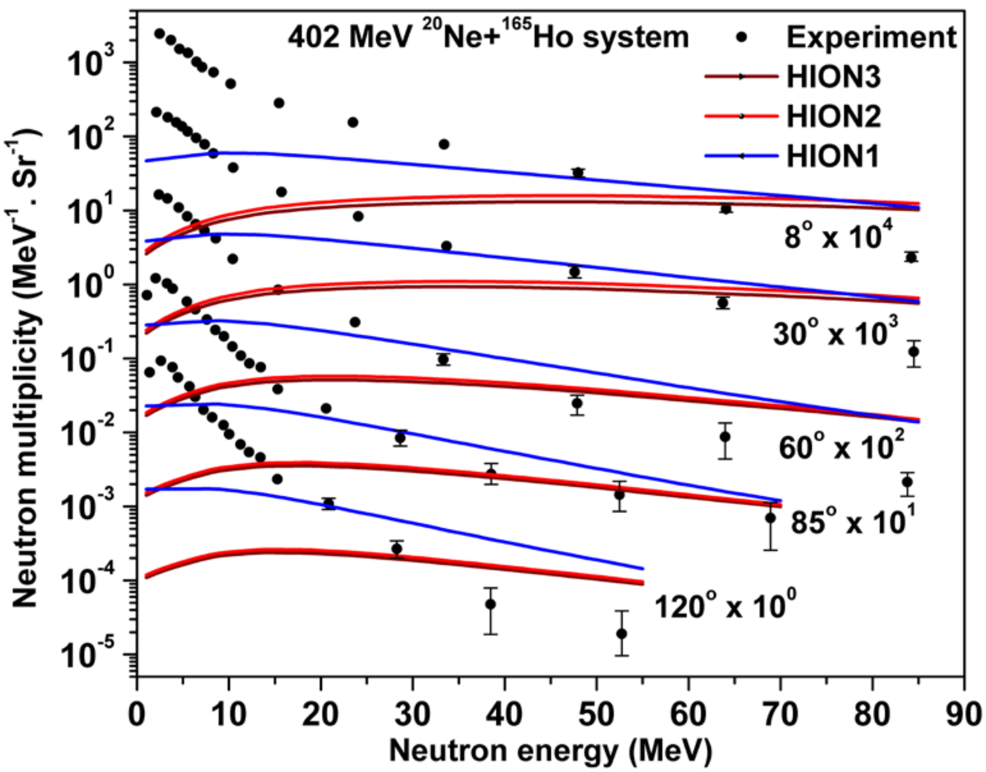

Figure 3.12: Comparison between the experiment and theoretically estimated neutron multiplicities for ^{20}Ne+^{165}Ho reaction at 600 and 402 MeV.

At 600 MeV projectile energies, the neutron multiplicity was found to be underestimated largely at forward angle and at backward angles the yield is reduced compared to the HION1. This is as per the discussion of section 3.6, related to the higher emission probability estimated with HION1 till an energy of 75 MeV. The blue line indicating the HION1 formalism is found to be consistently overestimating the PEQ yield compared to HION2 and HION3. Among the two modified formalisms, the HION2 (with the RMF approach) is found to have comparatively higher yield. But for 600 MeV, the first four forward angle (14°, 20°, 30° and 40°) yields were still found to be underestimated largely by the modified HION code as well. So for this energy, being an energy of more than 25MeV/A projectile energy, the possibility of the multiple emission needs to be investigated as discussed in sub-section 3.4.2. The neutron yields at the backward angles were found to be in close agreement with the experimental observations. On the other hand, for 402 MeV projectile energy, in both forward and back angles the multiplicity yields obtained from HION2 and HION3 is found to be in good agreement. The overprediction at the backward angles with HION1 got reduced due to the reduction in the emission probability due to the modification in the collision rate. The similar trend was also found in other two projectile energies, viz. 292 and 220 MeV. In both cases, the overprediction of the estimated neutron yield at all the angles got resolved by the modified collision rate as shown in Figure 3.13. Similarly for $^{12}C+^{165}Ho$ system at 300 MeV projectile energy shown in Figure 3.14, the forward angle neutron multiplicities were found to be underestimated compared to the experimental observations and a further improvement through the multiple PEQ emission formalism needs to be incorporated. At neutron energies higher than 20 MeV, in the emission spectra shows a drastic reduction in the PEQ yields compared to the experimental observations for both 10° and 35° angles. Whereas at the two backward angles (80° and 160°), the estimated neutron multiplicity is found to be in good corroboration with the experimental measurements. In the next subsection, an effort will be made to match the forward angle experimental multiplicities for large projectile energies ≥25 MeV/A with the multiple pre-equilibrium prescription.

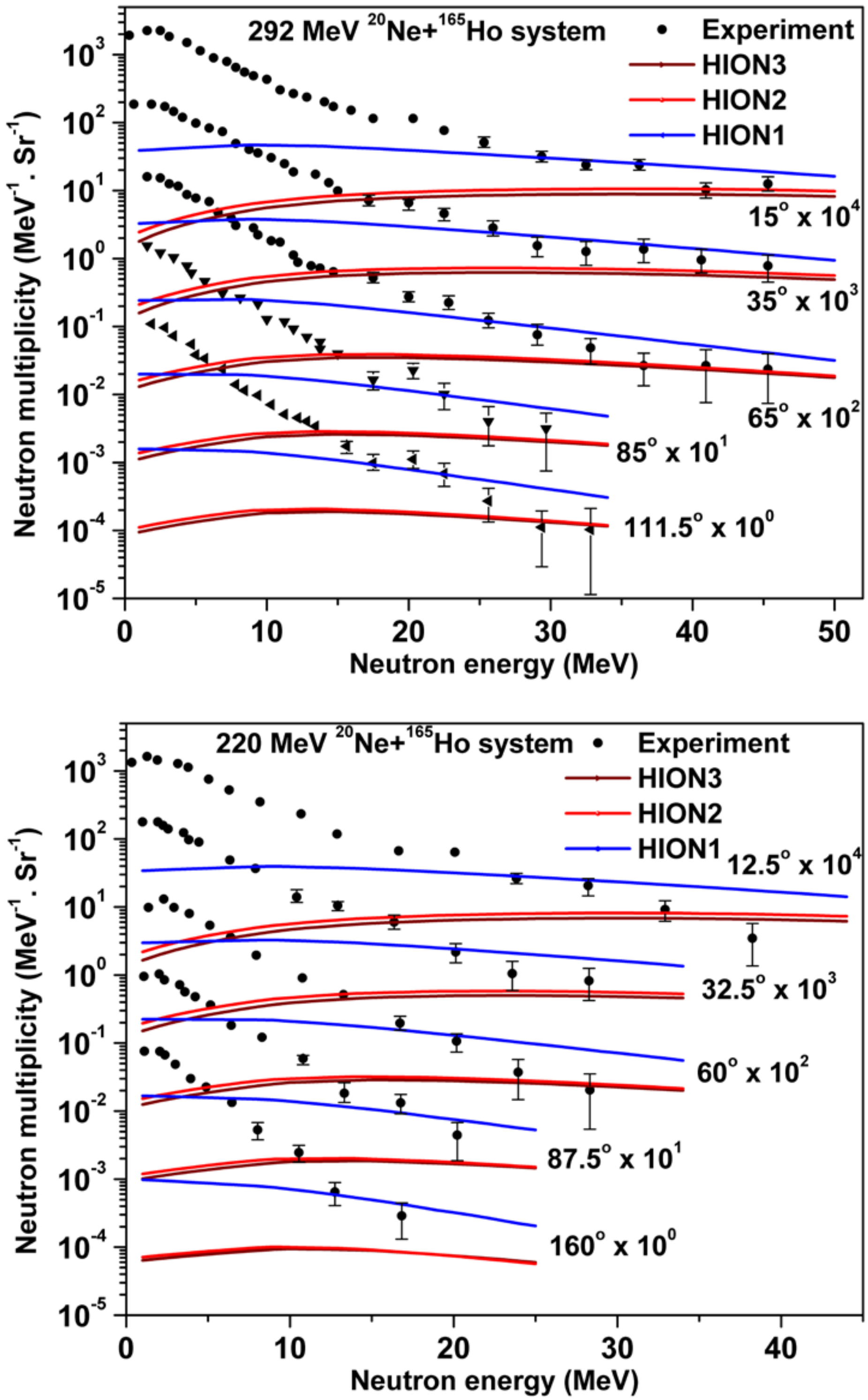

Figure 3.13: Comparison between the experiment and theoretically estimated neutron multiplicities for ^{20}Ne+^{165}Ho reaction at 292 and 220 MeV.

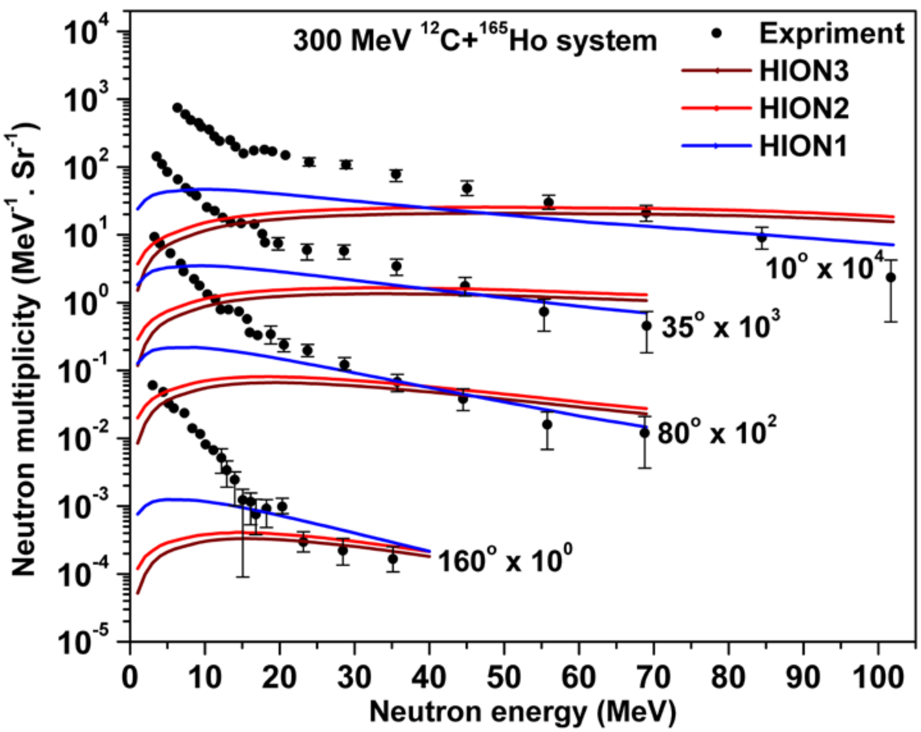

Figure 3.14: Comparison between the experiment and theoretically estimated neutron multiplicities for $^{12}C+^{165}Ho$ reaction at 300 MeV.

3.8 Comparison with multiple pre-equilibrium module at higher beam energies

The variation in the forward angle neutron multiplicities at higher projectile energies were not reproduced completely by the density dependent collision rate modification and the results found to be largely underestimating the experimental observations. To account this, the multiple pre-equilibrium module has been incorporated in the study. The result shows a large increase in the neutron multiplicities for projectile energies higher than 25 MeV/A through a sequential MPEQ formalism discussed in subsection 3.4.2.2. As in case of other energies also, there is a finite chance of the neutron emissions through the multiple pre equilibrium, either simultaneous (both neutrons are emitted from the composite system at the same time) or sequential (one neutron emission from the composite system and further emissions from the residual state), so the MPEQ formalism is applied for both the systems at all energies. The result showed that, the MPEQ contribution is found to be only 2-3% at forward angle from the sequential MPEQ for both composite systems. Although the yield is projectile energy dependent, but not much variation is there from this component but at higher projectile energies, the sequential MPEQ contribution is large compared to the earlier formalism and found to contribute as high as 47% of the PEQ contribution. Both the PEQ and MPEQ contributions and comparison with the experimental measurements for both composite systems will be discussed in the next section and presently we will discuss the MPEQ contribution (sequential and simultaneous) for 600 MeV $^{20}Ne+^{165}Ho$ and 300 MeV $^{12}C+^{165}Ho$ systems. In both the cases, the experimental neutron multiplicities were found to be largely underestimated by the modified HION (HION2 and HION3) codes. The comparison of the neutron multiplicity with MPEQ for the above two energies are given in Figure 3.15. The HION estimated MPEQ neutron yield is represented as HION4 (simultaneous + sequential) in the figure and all other nomenclature follows as earlier. The figure clearly depicts that at large projectile energies, the contribution from multiple PEQ plays a significant role. The HION2 and HION3 considers in the present case both modified emission probability with only the simultaneous multi-particle emission only and HION4 gives the addition of sequential MPEQ contribution over the HION2. The simultaneous MPEQ considers the probability of emission at the same time whereas sequential MPEQ considers a neutron emission and further residual systems emits further a single neutron or simultaneously more than one neutrons, so total emission probability increases by many folds in the sequential case if the incoming particle retains higher energy. The same is found in Figure 3.15(a), where the sequential MPEQ increased the yield by 4 times in the forward angle. The increase in the lower neutron energies specifies the multi-particle emissions from the residual systems.

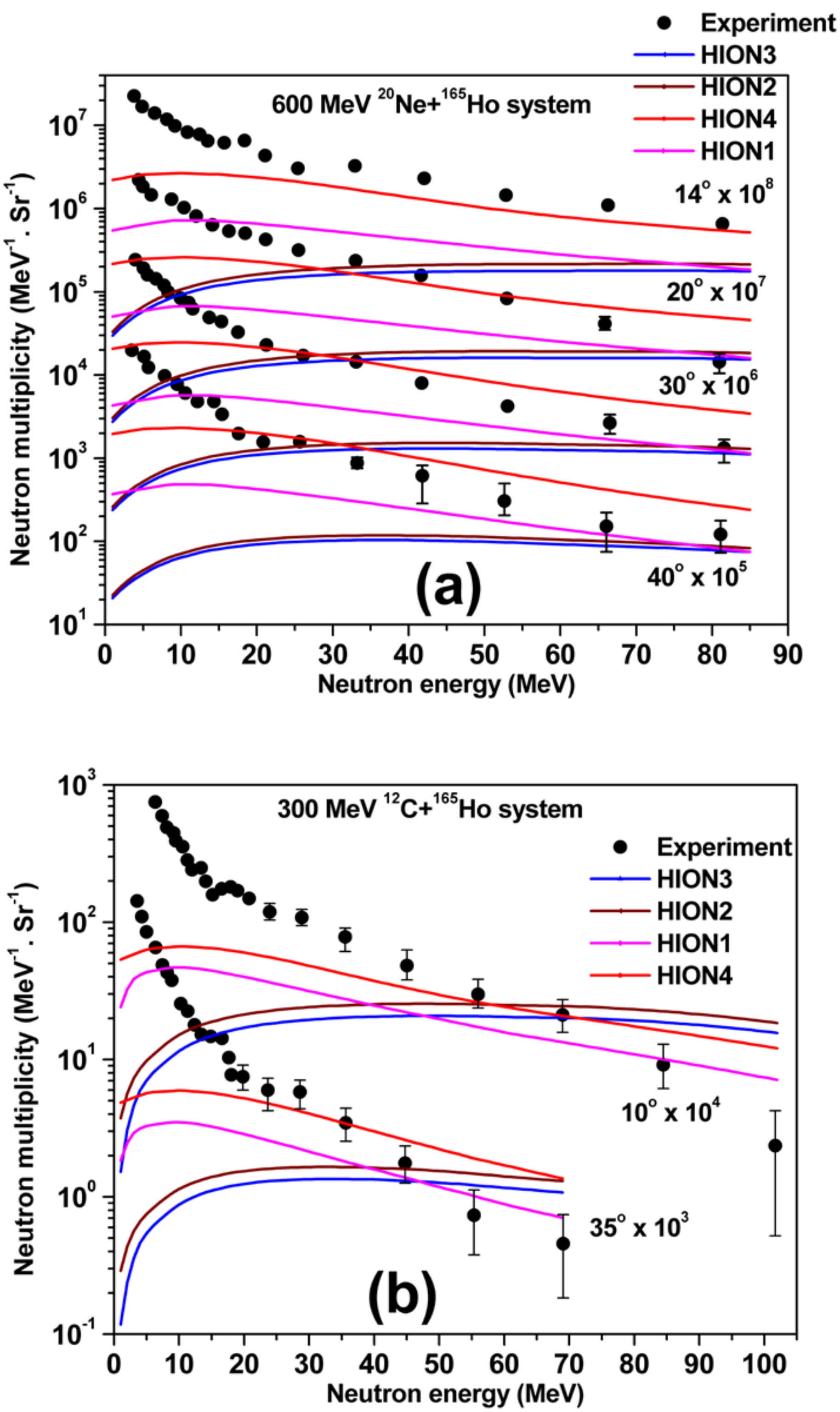

Figure 3.15: Comparison between the experiment and theoretically estimated neutron PEQ multiplicities for (a) ^{20}Ne+^{165}Ho at 600 MeV and (b) ^{12}C+^{165}Ho system at 300 MeV.

A similar trend was found in case of ^{12}C+^{165}Ho system at 300 MeV. In this system the neutron multiplicity values increased by almost three times in the energy range of 20-30 MeV of emission neutrons but at higher emission energies the yield reduced compared to the older formalisms to conserve the number of total emission neutrons. The same trend is found in case of earlier system as well at higher emission energies. For ^{12}C+^{165}Ho system at 300 MeV projectile energy, due to relatively lower excitation of the composite system the crossover of the neutron multiplicities took place at 55 MeV emission neutron energy in the extreme forward angle. At larger emission angles, the increase due to MPEQ formalism is found to be less and consequently, the conservation of the total neutron in turn reflects by a crossover at relatively larger emission energies. This figure clearly shows that by introducing the MPEQ formalism (simultaneous and sequential), the experimental neutron multiplicities are fairly well reproduced by the theory. The sequential MPEQ contributions in percentage to the total neutron multiplicity for both the systems are given in the Table 3.1.

Table 3.1. Percentage contribution of PEQ emission at different angles

Reaction	**Beam Energy (MeV)**	**Angle (degree)**	PEQ emission (%)
^{20}Ne + ^{165}Ho	600	14	**33.9**
		20	**33.0**
		30	**32.7**
		40	**31.9**
		50	**3.18**
		70	**2.22**
		101	**1.51**
		130	**1.47**
		159	**1.23**
^{12}C+^{165}Ho	300	10	**47.7**
		35	**40.4**
		80	**12.4**
		160	**6.0**

3.9 Comparison of total Neutron Multiplicity data with experiment

In the earlier sections, only the higher energy neutron multiplicities using the PEQ component has been discussed. For a complete comparison of the neutron multiplicity, the lower energy evaporation also need to be estimated. In the present work, the evaporation contribution was estimated using the Monte Carlo based evaporation code PACE4 [78]. The thin target results obtained by the PACE4 yields were converted to the neutron multiplicity and then compared with the experimental data. The lower energy neutron part is fairly well represented by the PACE4 code for all energy and angles for both the systems. The experimental neutron multiplicity compared with the estimated one from PACE4 and different formalisms of the HION code are presented as separate contributions in the following figures. The comparison of the ^{20}Ne+^{165}Ho reaction at 600 MeV with the PACE4 contribution marked in red in shown in the Figure 3.16.

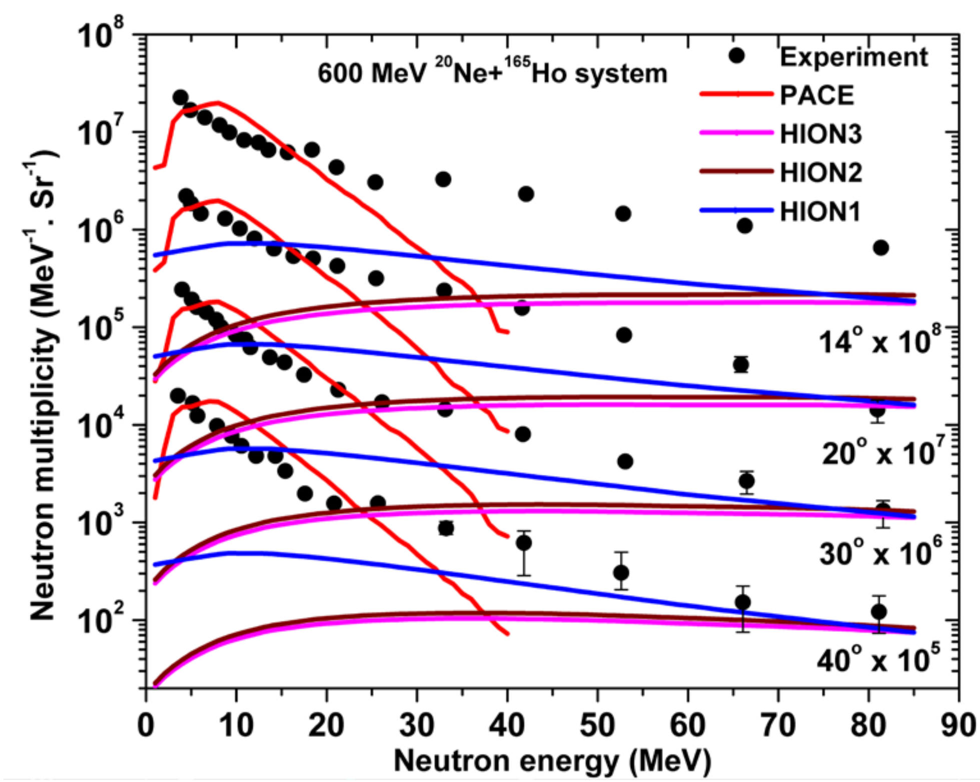

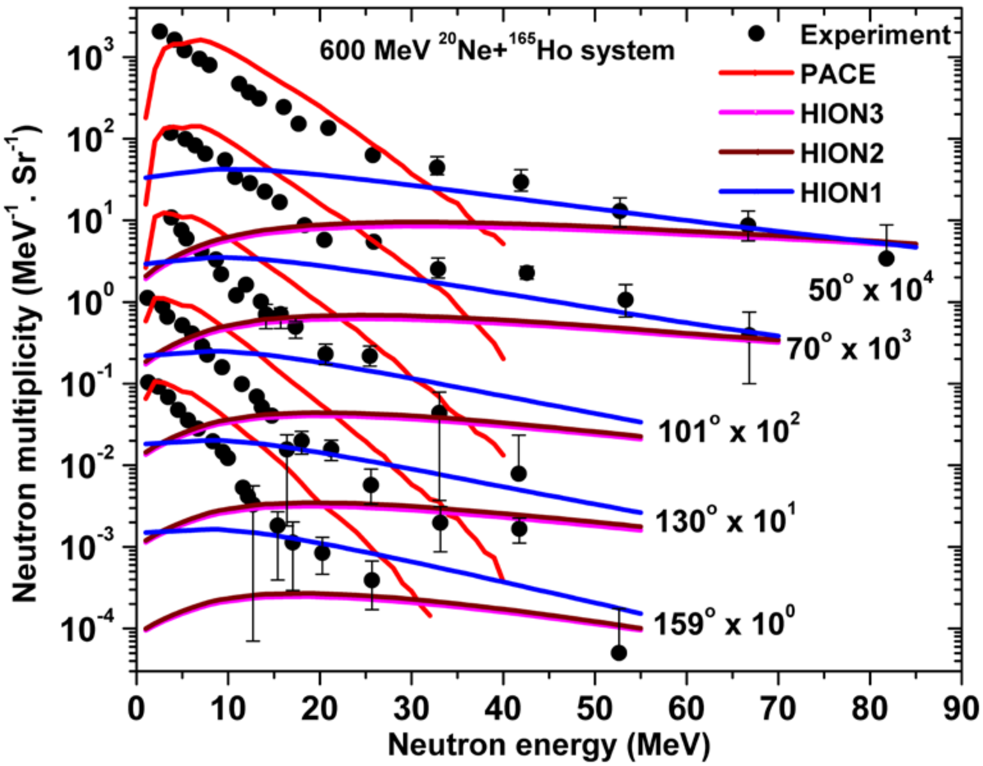

Figure 3.16: Comparison between the experimentally obtained (black circles with error bars) and theoretically calculated neutron multiplicities (evaporation from PACE4, PEQ from HION model): a) red line: PACE4, b) blue line: HION1, c) brown line: HION with RMF approach (HION2) d) pink line: HION with semi-phenomenological approach (HION3) for ^{20}Ne+^{165}Ho reaction at 600 MeV.

Similarly for other energies viz. 402, 292 and 220 MeV neutron multiplicities for ^{20}Ne+^{165}Ho system is represented in Figure 3.17. In all cases it was found to have a reasonably well match in the lower energy part of the neutron multiplicity spectra using PACE4 and at higher energies with the HION2 and HION3. As the RMF formalism is more closure to the realistic nucleus-nucleus interactions compared to the semiphenomenological approach, the former is favored over the two formalisms. The comparison for ^{12}C+^{165}Ho reaction at 300 MeV is shown in Figure 3.18. The comparison of the neutron multiplicity at the forward angles of higher projectile energies viz., 600 MeV ^{12}Ne and 300 MeV ^{12}C are presented separately in Figure 3.19.

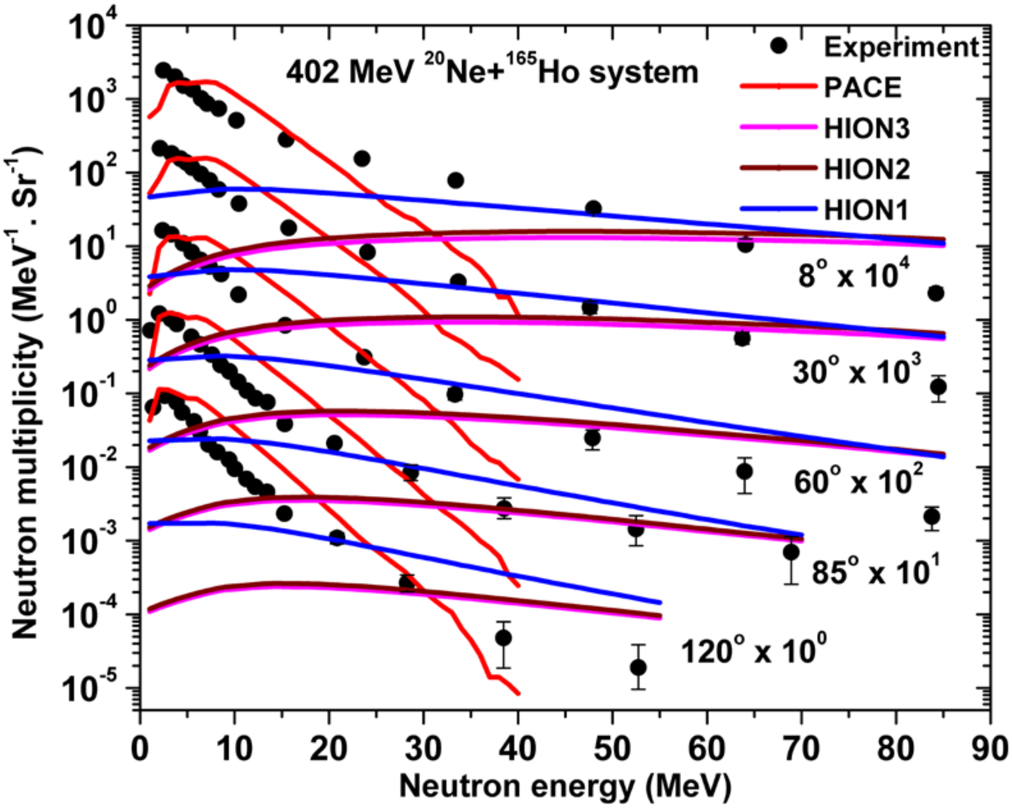

402 MeV ^{20}Ne+^{165}Ho system
Experiment
PACE
HION3
HION2
HION1
8° x 10^4
30° x 10^3
60° x 10^2
85° x 10^1
120° x 10^0
Neutron multiplicity (MeV^{-1} . Sr^{-1})
Neutron energy (MeV)

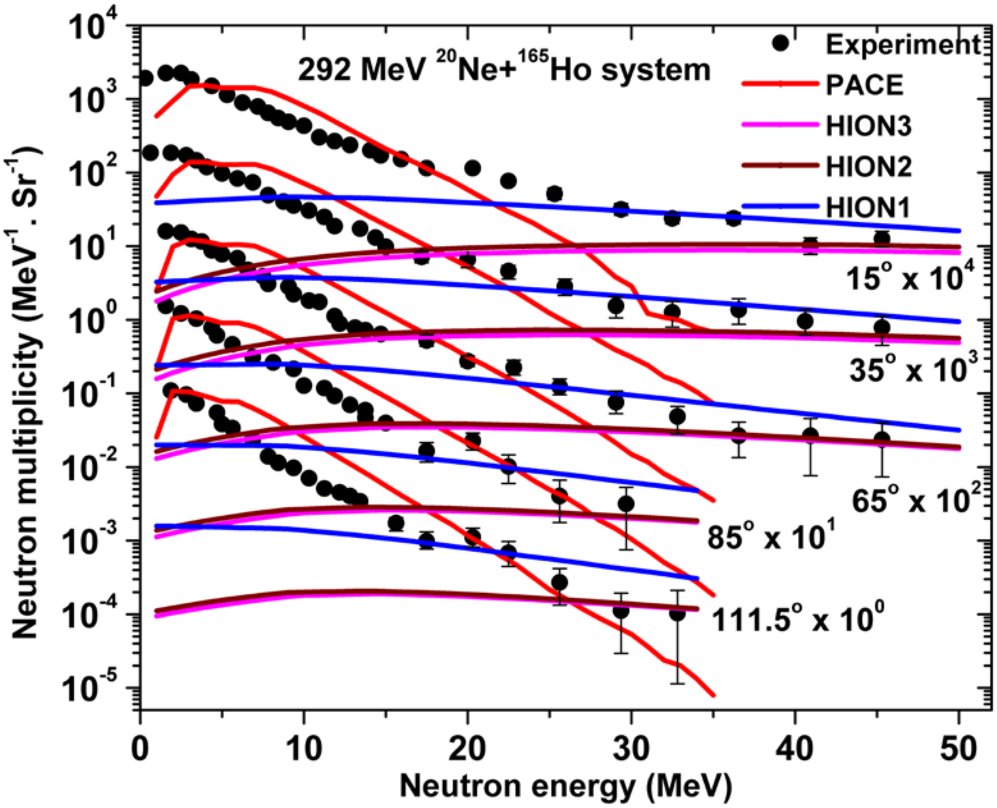

292 MeV ^{20}Ne+^{165}Ho system
Experiment
PACE
HION3
HION2
HION1
15° x 10^4
35° x 10^3
65° x 10^2
85° x 10^1
111.5° x 10^0
Neutron multiplicity (MeV^{-1} . Sr^{-1})
Neutron energy (MeV)

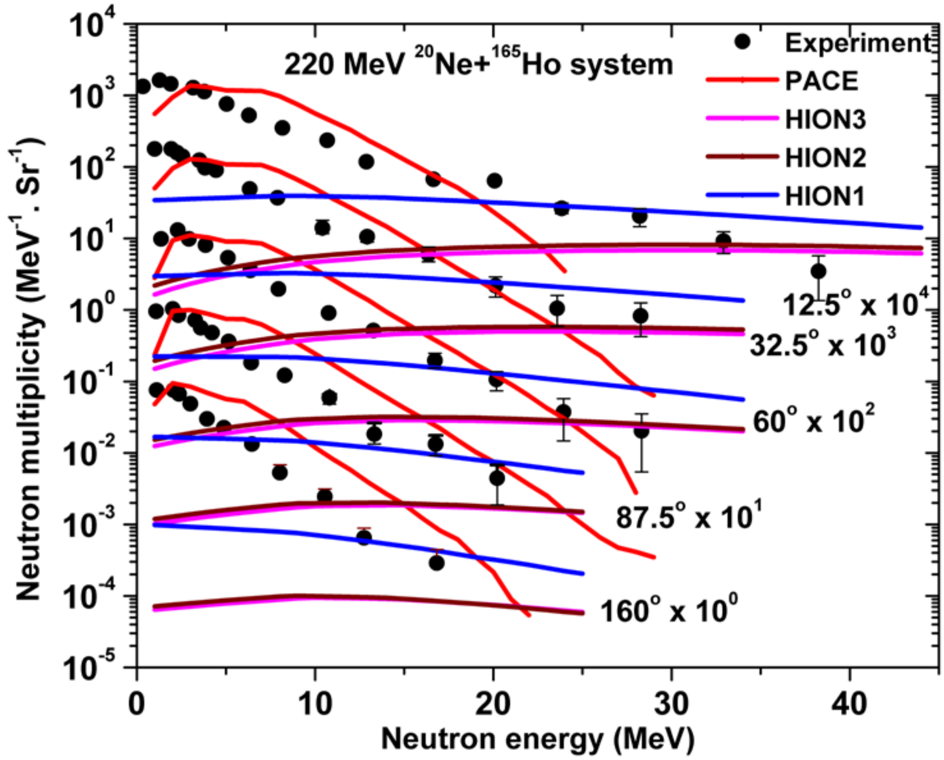

Figure 3.17: Same as figure 3.16 for ^{20}Ne+^{165}Ho reaction at a) 402 MeV, b) 292 MeV, c) 220 MeV.

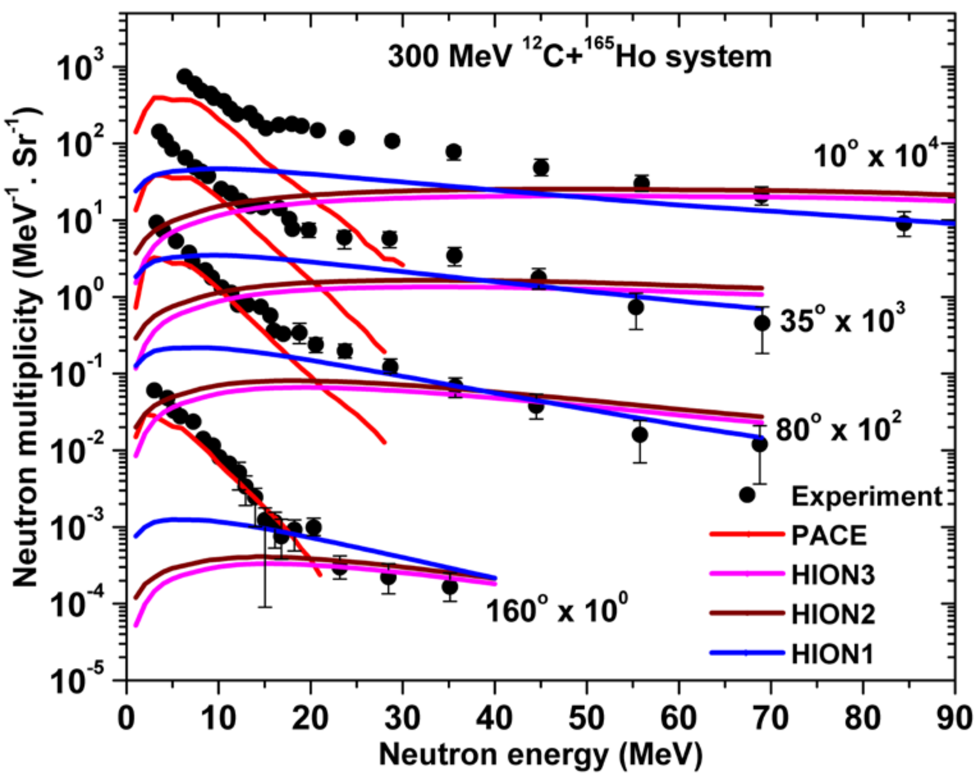

Figure 3.18: Same as figure 3.16 for ^{12}C+^{165}Ho reaction at 300 MeV.

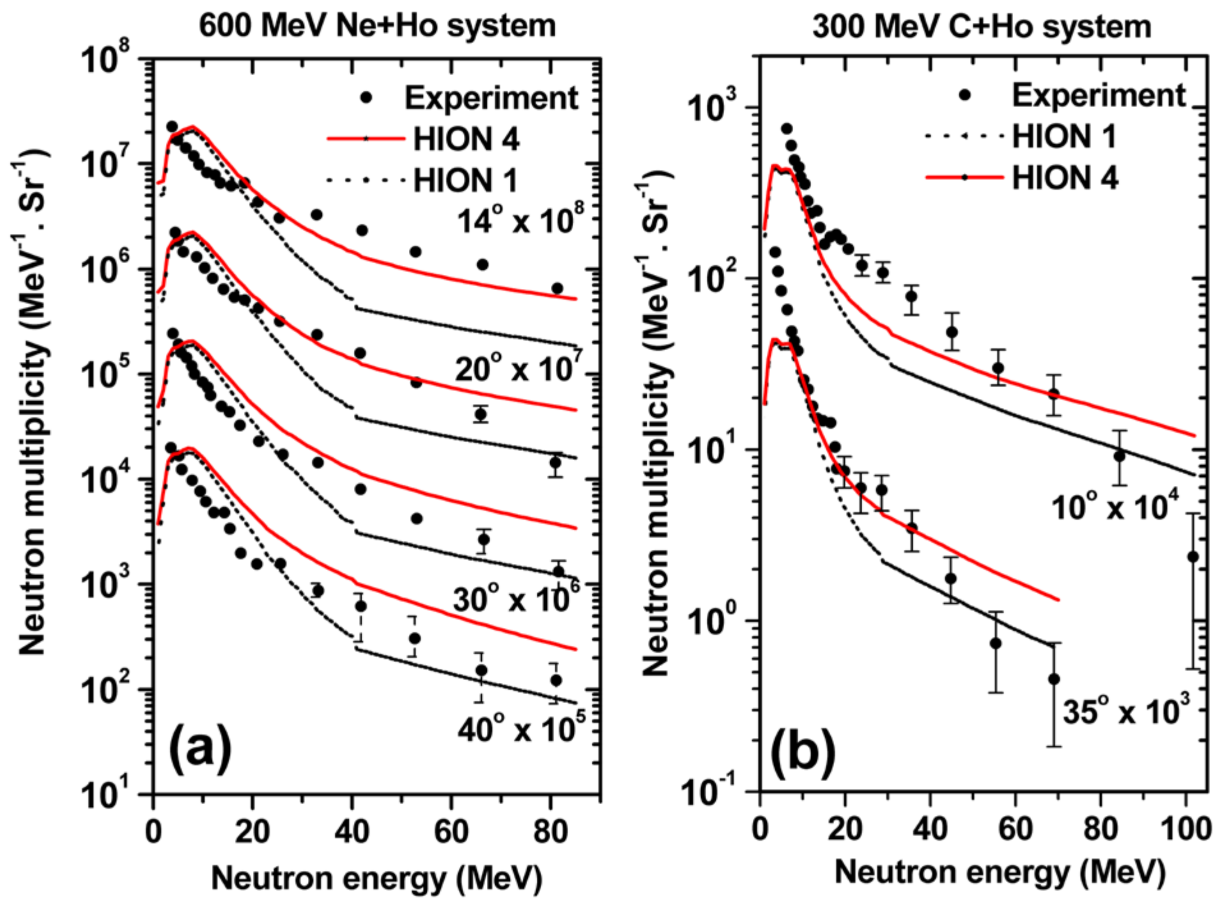

Figure 3.19: Comparison between the experimental and theoretically obtained [evaporation contribution from the PACE4 code, pre-equilibrium from (i) HION1 model (black dash), (ii)HION2+simultaneous and sequential (from successive stages) multi-particle emission (HION4) (red solid line)] neutron multiplicities at different angles at (a) 600 MeV for ^{20}Ne+^{165}Ho system and (b) 300 MeV for ^{12}C+^{165}Ho system.

The MPEQ contribution along with the PACE4 shows a better agreement with the experimental data as shown in the Figure 3.19. So from this work it can be concluded that for neutron yield studies at different neutron energies, one need to consider slightly different prescriptions to reproduce the experimental observations. The modified collision rates represents a more realistic physics approach of the nucleon-nucleon collision than the Blann formalism. Secondly, for relatively lower projectile energies till 20 MeV/A, single particle pre-equilibrium emission is sufficient to reproduce the neutron yields from a nuclear reaction and at higher energy till 25 MeV/A, simultaneous multi-particle emissions can be used. In energies higher than this, one needs to account for the neutron emissions from the residual systems as well, considering a large residual energy left to the residual nucleus even after one neutron emission as shown in the discussions of the present work. As a concluding remark, it can be considered that, the present model works satisfactorily well to reproduce the emission neutron multiplicity spectra till an energy range of 30 MeV/A and in the next chapter we will try to compare the thick target neutron yields from this code at higher neutron energy region.

Chapter 4

Experimental Validation of PEQ estimates from HION code

The objective of the present chapter is the validation of theoretical estimates obtained from the HION code and comparison with high energy emission neutrons emitted from experiment. For this purpose, neutron energy spectra were measured for ^{16}O + ^{27}Al reaction at two different projectile energies of 120 and 142 MeV. The experiments were carried out at BARC-TIFR Pelletron-LINAC Facility (PLF) [156], Mumbai, India. This is a tandem type two stage accelerator with a maximum terminal voltage of 14 MeV. Further the acceleration is provided through the superconducting LINAC boosters. During the experiment, the neutron energy spectra have been measured using the time of flight (ToF) technique. The ^{16}O beam from the SNICS (source of negative ion through Cs-sputtering) source was made pulsed using the buncher facility available just after the ion source. The energies of the projectile were chosen to attain an excitation of the fused system to facilitate pre-equilibrium neutron emission. A theoretical dosimetric estimate of the relative contribution from the pre-equilibrium neutrons to those from evaporation neutrons has also been presented here. For comparison of the measured to estimated dose, a conventional dose equivalent meter has been exposed in the similar set up as the liquid scintillator for all five angles from 0° to 120°.

4.1 Experimental system and its characteristics

The ^{16}O beam was extracted using the analyzing magnet at a charge state of $^{16}O^{6+}$ in the experiment and bombarded on a 3 mm thick hemispherical Al target. The neutrons emitted were measured using EJ301 detectors. The details of the experimental setup and detectors will be discussed in the next section. The system under study goes through the formation of ^{43}Sc composite system. The evaporation residue from the composite system are estimated with the statistical model codes PACE, EMPIRE using the Houser-Feshbach model. The high energy emissions from the pre-compound state are estimated using the HION code. The system has a Coulomb barrier [157] of 15.99 MeV and the Q-value for single neutron emission is 2.115 MeV having the neutron separation energy of -12.14 MeV. The centre of mass energies for the compound system for 120 and 142 MeV of projectile energies are found to be 75.35 and 89.16 MeV respectively. The compound nuclear excitations are 89.6 and 103.42 MeV respectively for the above mentioned ^{16}O beam energies. The PACE estimated fusion cross sections using the Bass model [157] for ^{16}O + ^{27}Al system at increasing energies are shown in Figure 4.1.

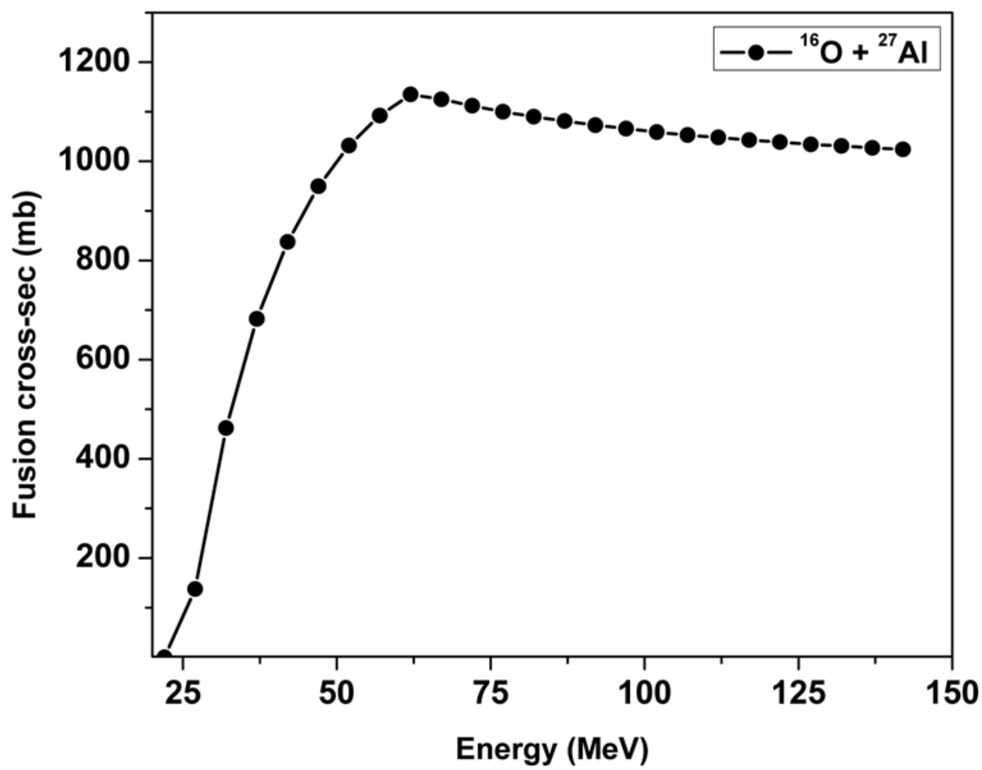

Figure 4.1: The fusion cross-section for the ^{16}O + ^{27}Al at different projectile energies.

The figure clearly shows that, the cross-section initially increases beyond 20 MeV and reaches a maximum value of 1135 mill barn at 62 MeV and then gradually decreases to 1024 mb at 142 MeV. The study emphasizes the thick target neutron emission study, so the cross-section variation will be used for the generation of the thick emission spectra by enveloping all thin target results by appropriate folding with the residual yield at each successive hypothetical fixed energy thin slabs and corresponding decreased projectile energies.

4.2 Experimental setup

In the present study, double differential neutron distribution has been measured out using the neutron ToF technique, with the help of five 5cm × 5 cm EJ301 (make Scionix, Holland) proton recoil liquid scintillator [56] detectors. Angular distribution of neutrons and corresponding thick target yields (TTNY) were measured at five different angles with respect to the incoming projectile beam direction.

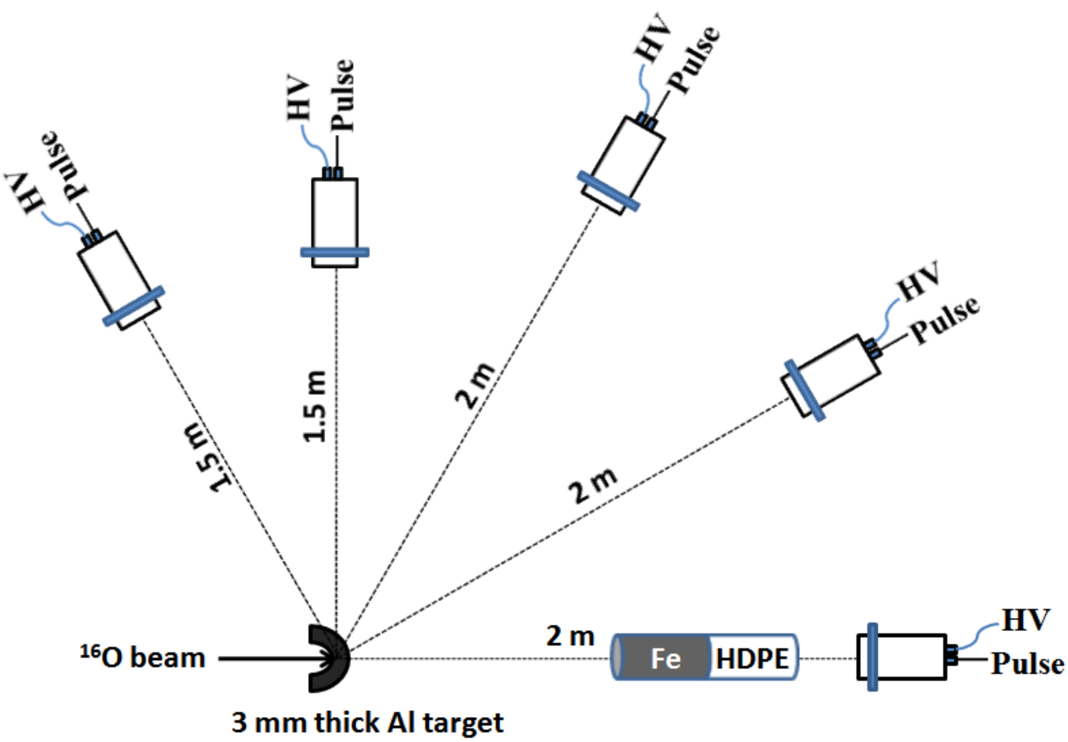

Figure 4.2: A Schematic of the experimental setup for $^{16}O+^{27}Al$ system

For 0°, 30°and 60° angles, the detectors were kept at a distance of 2 m from the source. The rest of the two detectors at 90° and 120° angles were kept at a distance of 1.5 m. The schematic of the experimental arrangement is shown in figure 4.2. The two different sets of distances for neutron spectrometry was chosen to obtain better energy resolution at higher emission energies (for forward angles) and good statistics at backward angles. A longer flight path provides a better resolution for detection of higher energy neutrons. The contribution of the pre-equilibrium (higher energy) neutrons was expected to be significant in the forward directions with respect to the incoming beam and the source to detector distance was kept 2 m to ensure efficient energy determination. At backward angles, the major contributor is the evaporation neutrons (lower energy) and secondly total yield is lesser. So for backward angles the distance was kept at 1.5 m. During the experiment, the measured full width at half maximum (FWHM) of the beam was ~ 0.8-1.0 ns inclusive of detector resolution. ^{27}Al target was made in the form of a hemisphere of 40 mm diameter and 3 mm thickness, to reduce unwanted scattering and attenuation of emitted neutrons [158-159] during the experiment. The range of ^{16}O particles in ^{27}Al medium was calculated to be 110 μm and 142 μm for 120 and 142 MeV energies, respectively, using the range-energy code SRIM [160]. This confirms the complete stopping of the incoming particle flux within the target thickness. The neutrons measured by this technique consist both of direct neutrons as well as neutrons scattered from structural and shielding materials. In order to estimate the neutron distribution from the reaction, the shadow bar technique was used which is pictorially depicted for the extreme forward angle in fig. 4.2. Two 30 cm long cylindrical bars, one of iron and the other made of high density polyethylene were placed end-to-end between the target and detector. The iron cylinder will eliminate the gamma rays produced in the reaction. Any photoneutron generated in the iron bar and the neutrons emitted from the reaction will be absorbed by the high density polyethylene (HDPE) cylinder. So these two cylinders will completely screen all the direct neutrons emitted from the reactions. In this setup, the neutrons detected by a EJ301 detector represent the background neutrons scattered from other directions. So subtracting it from the total neutron spectra at that specified angle will provide the net neutron spectra solely from the reaction. Background neutron measurement was carried out at all the five angles.

4.3 Detector and Electronics

The detection of the neutrons were carried out with the EJ-301 proton recoil scintillator [56] in these accelerator environment experiments due to its very good pulse shape discrimination (PSD) properties for fast neutron counting and spectrometry in presence of gamma radiation. The basic properties of the scintillator material are shown in table 4.1.

Table 4.1: The properties of EJ-301 Scintillator

Light Output (% Anthracene)	78
Scintillation Efficiency (photons/1 MeV e^-)	12,000
Wavelength of Maximum Emission (nm)	425
Decay Time, Short Component (ns)	3.2
Mean Decay Times of First 3 Components (ns)	3.16 32.3 270
Bulk Light Attenuation Length (m)	2.5-3
Specific Gravity	0.874
Refractive Index	1.505
Flash Point (°C)	26
Boiling Point (°C at 1 atm)	141
No. of H Atoms per cm^3 ($x10^{22}$)	4.82
No. of C Atoms per cm^3 ($x10^{22}$)	3.98
No. of Electrons per cm^3 ($x10^{23}$)	2.27

The detectors provides both anode and dynode pulse for the acquisition purpose, in the present work the anode negative pulse was taken for the analysis. The block diagram of the electronic set up used in the present work is shown in figure 4.3. The anode output of the photo multiplier tube (PMT) was input to a 4 channel pulse shape discriminator (PSD) (MPD-4, make Mesytec) for distinguishing neutrons over the gamma ray photons. The MPD-4 output was taken for estimating 3 different parameters - flight time of the particle, pulse height and pulse shape. The electronic set-up for the measurement is schematically shown below in figure 4.3. For the design of the master gate, the detector signals were combined in an OR logic through a quad 4-fold logic unit (Philips, 755) and a level translator (Philips, 726) and transmitted to the data acquisition system VME analog to digital converter (ADC) (CAEN-V785) with proper impedance matching.

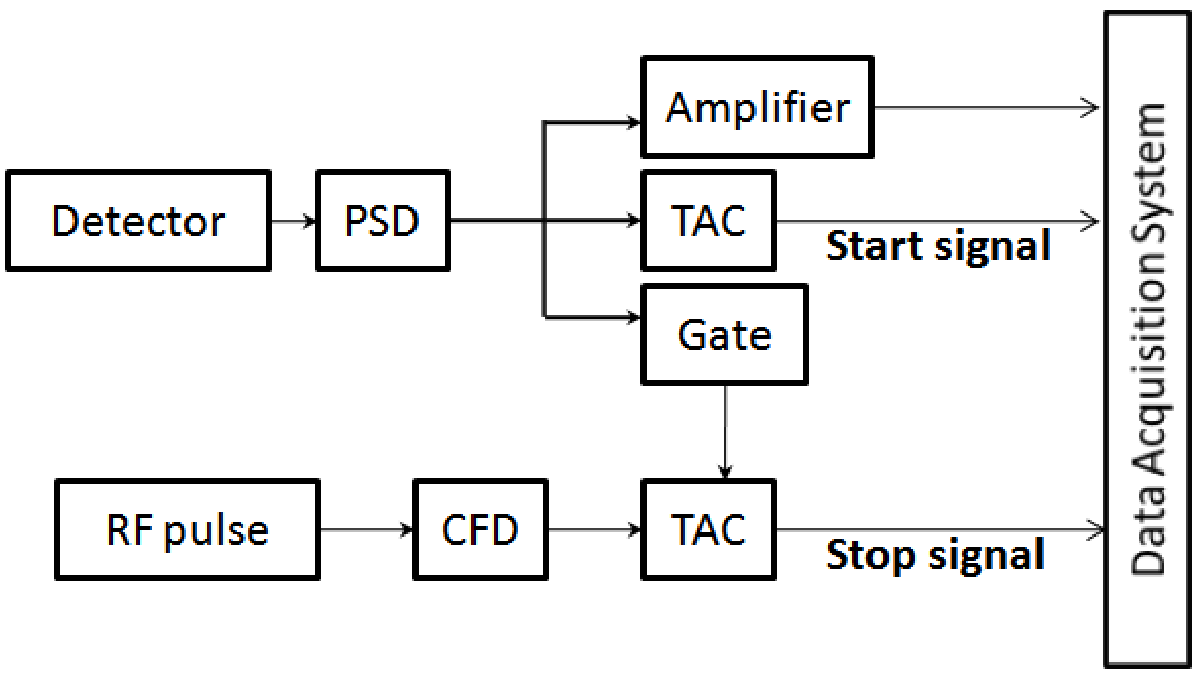

Figure 4.3: Block diagram of the electronic setup for signal acquisition for $^{16}O+^{27}Al$ system.

The particle energy is measured through the flight time between the source to detector and the time difference is calculated using the TAC module (Canberra) with proper tagging with respect to the initial burst of the gamma ray photons. The RF signal was acquired from a BaF_2 detector through a constant fraction discriminator (CFD, 454) with an appropriate delay and a logic unit (LF 4000). Finally the RF feed goes to the TAC unit and the neutron detection time was recorded with respect to the initial gamma burst. The chopped beam reappear in an interval of 107.3 ns and the generated neutrons within this time difference is collected as a signature of the reaction corresponding to the initial burst of the projectile pulse. Once the second gamma pulses appear, the low energy delayed neutrons may get superimposed with fast counterparts of the second pulse, necessitating a detection threshold for neutron spectrometry. The TAC module has been calibrated using a TAC calibrator with known set of signal widths. The difference in the channel numbers for the set difference in time is the time calibration factor. During measurement neutron energies are determined from the time differences acquired through the TAC unit and the corresponding target to detector distance. The offline analysis has been carried out using the Linux advanced multi-parameter system (LAMPS) [161] software and the neutron spectra were generated after appropriately folding by the detector efficiency.

4.4 Detector efficiency

The EJ-301 measured pulse height distribution and TAC data was converted to the energy differential neutron yield distribution per projectile per unit solid angle at different angles, corrected for background and intrinsic efficiency of the detectors. Efficiency of the proton recoil detectors can be approximated as,

$$\varepsilon = 1 - e^{-N\sigma_s L} \tag{4.1}$$

where, σ_s is the scattering cross section of hydrogen, N is the number density of target nuclei, and L is the path length for the neutrons in the detector medium. In EJ-301 the H/C (atomic ratio) is 1.211, and hence recoil of carbon nuclei also need to be considered for efficiency calculations. In such cases, equation 4.1 gets a bit modified and the efficiency can be expressed as given in relation 4.2, where the subscript C and H stand for carbon and hydrogen respectively. Although the number densities are of similar order but the cross-sections vary largely leading to a small change in the effective efficiency;

$$\varepsilon = \frac{N_H \sigma_H}{N_H \sigma_H + N_C \sigma_C}\left[1 - e^{-(N_H \sigma_H + N_C \sigma_C)L}\right] \tag{4.2}$$

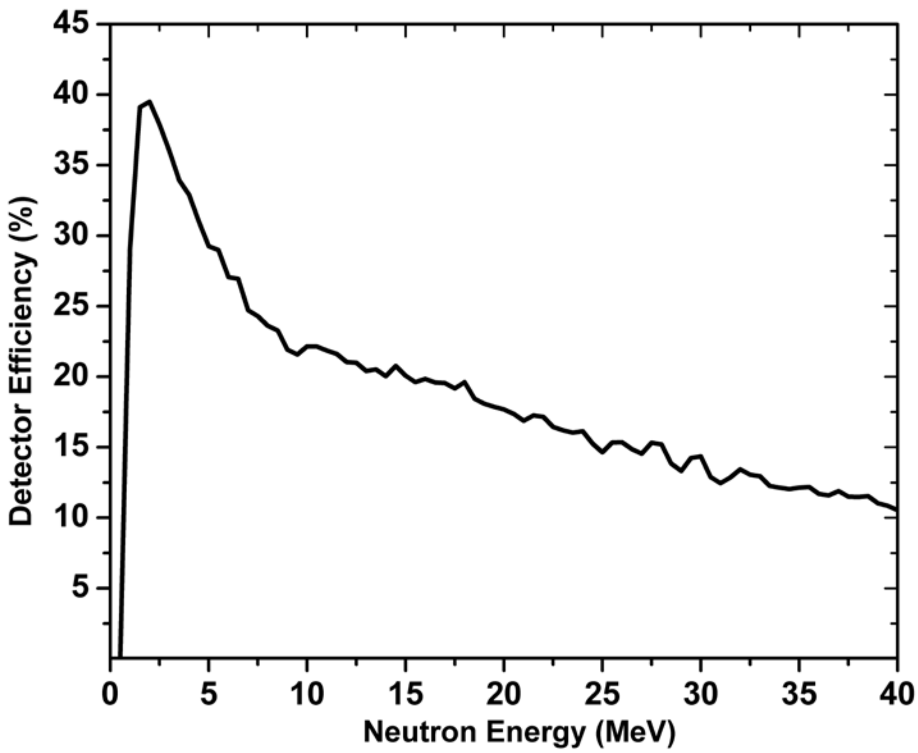

Figure 4.4: Efficiency plot for EJ-301 detector (from Monte Carlo simulations).

The efficiency of a liquid scintillator can be calculated theoretically using a scoring algorithm (Monte Carlo method). It can also be determined by experimental methods using monoenergetic neutron source and counting the corresponding yields at different energy bins. The EJ-301 detector efficiency in the energy range of 1 – 40 MeV is presented in Figure 4.4. The efficiencies at 0-40 MeV energies was calculated by Sunil et. al. using a FLUKA Monte Carlo code [159].

4.5 Neutron pulse height extraction

In the present experiment, the gamma-neutron separation has been achieved by the pulse shape discrimination and ToF information, as shown in figure 4.5. The figure shows a two dimensional plot, pulse height at the y-axis and pulse height discrimination being at the x-axis. The figure clearly indicates a wide separation between the two types of signals. The left one indicates the photon signals and the right one, the corresponding neutrons. The

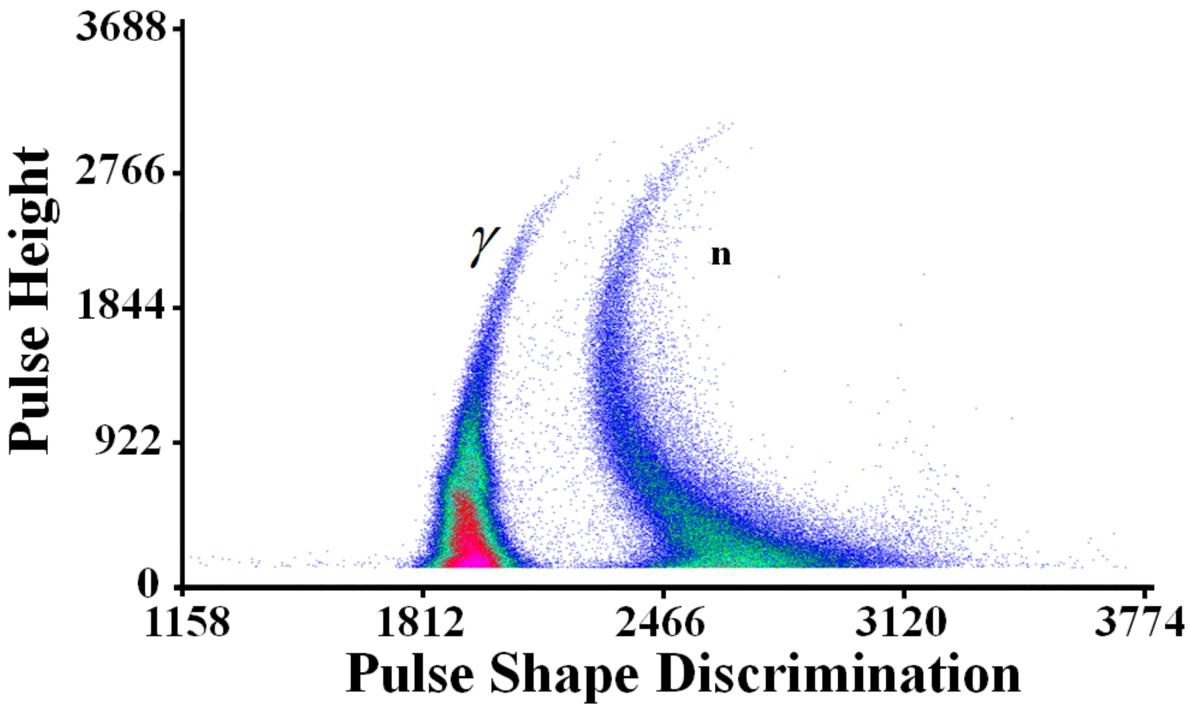

Figure 4.5: The pulse height vs. PSD spectra for $^{16}O+^{27}Al$ system

The color code represents the counts and a typical projection in one of the axis provides an one dimensional PSD spectrum with clear separation between the photons and neutrons as shown in figure 4.6. At the TAC the gamma pulses should ideally appear as a sharp line but due to practical constraints like electronic noise, time walk jitters and statistical fluctuations etc. effectively appear with a finite spread. For the neutrons, the flight time is dependent on the energy of the neutrons and time spectra become very wide as shown in the inset of figure 4.6.

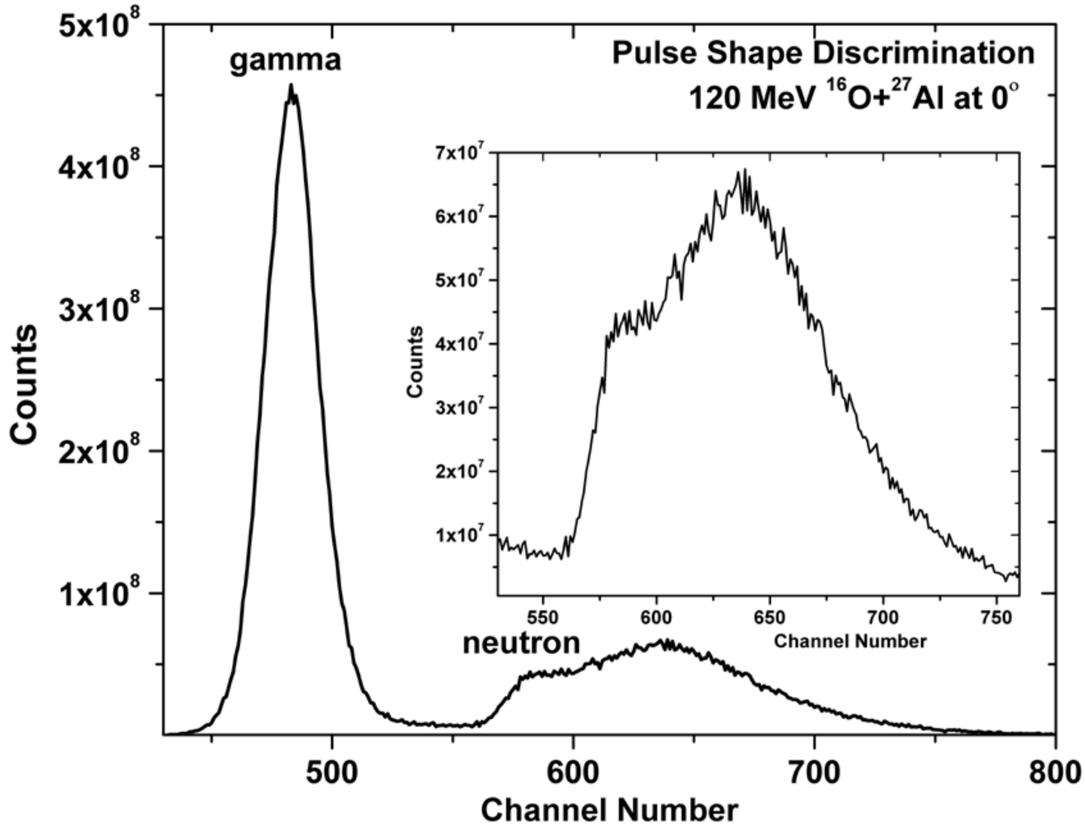

Figure 4.6: A typical pulse height vs. PSD spectra for $^{16}O+^{27}Al$ system at 0° for 120 MeV energy

Similarly a two dimensional spectrum with two bunches of gamma and neutrons is presented in figure 4.7. This indicates the PSD vs. ToF spectra and the two gamma lines are separated by 107.3 ns. The neutrons appear between the two gamma lines and correspond to one bunch of neutrons generated from a projectile flash on the ^{27}Al thick target. The left gamma line represents the flash of projectile on the target. The neutrons generated from the reaction were acquired by the proton recoil detectors till the second bunch of projectile hit the target which is signaled by the second flash of gamma line.

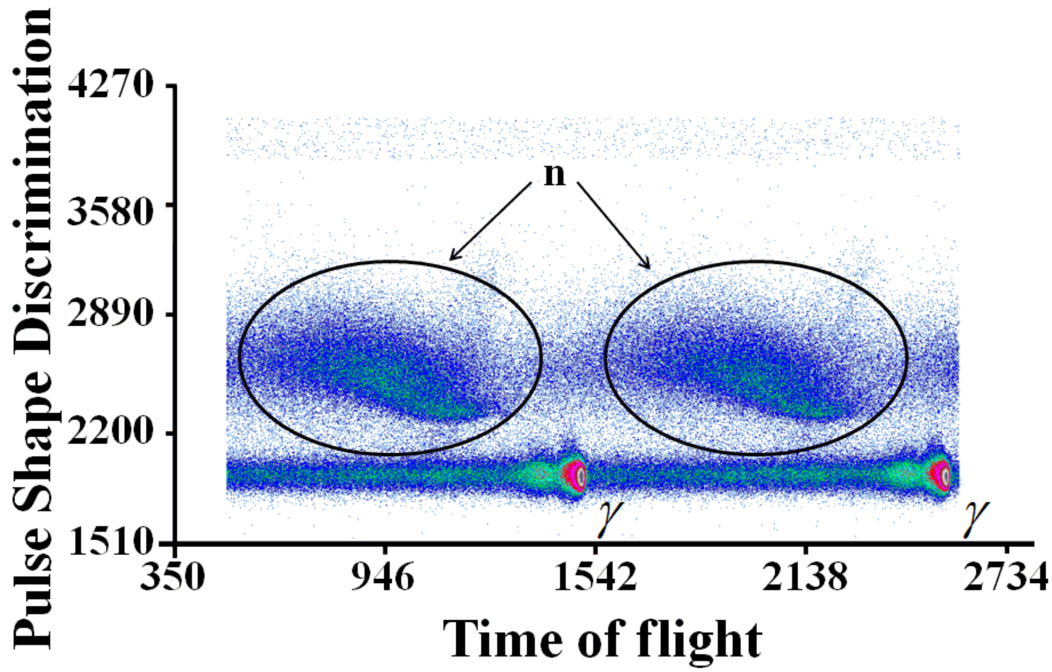

Figure 4.7: A contour plot of PSD and TOF spectra showing n-γ separation for ^{16}O+^{27}Al system.

4.6 Neutron spectra generation

The neutron spectra are recorded using appropriate gates to choose regions mentioned in figure 4.7. The area marked as neutrons can be extracted by a software gate generated to extract neutrons with minimum contamination of gamma photons. For proper estimation of neutron flight time from the onset of the reaction, the photon time distribution was fitted to a Gaussian peak by the least square minimization. The centre point of this Gaussian was chosen as the start time. The two gamma lines are separated by a time difference of 107.3 ns, so from this the calibration factor for the channel to time conversion can be achieved. Further using the same calibration factor, the neutron energy spectra and the corresponding yields at different energy bins can be calculated. In the present work, this is done using the Linux Advanced Multi-Parameter System (LAMPS) software in an offline mode of analysis [161]. The neutron energy spectra was then folded with the efficiency distribution given in figure 4.4 to get the experimental neutron distribution for $^{16}O+^{27}Al$ system at two different energies 120 MeV and 142 MeV. These are shown in figure 4.8 below. The measured spectra at five angles 0°, 30°, 60°, 90° and 120° have been plotted with multiplication factors of 10^4, 10^3,10^2, 10^1 and 10^0 respectively to accommodate all data it in a single plot.

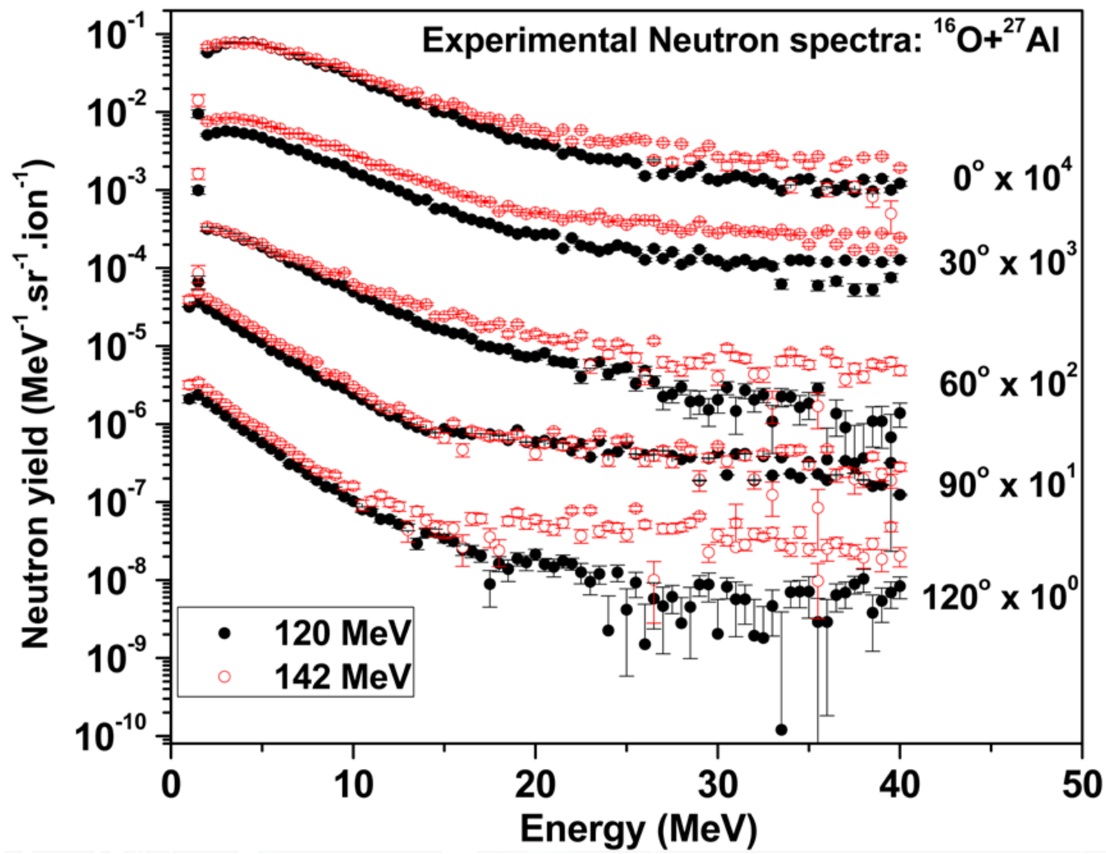

Figure 4.8: A comparison between the experimental neutron yield at 120 and 142 MeV.

The red open circles represent the yield for 120 MeV projectile energy and the black closed circles correspondingly the 142 MeV projectile yields. The statistical uncertainties associated with the measurements are represented in terms of error bars for both measurements.

The corresponding background measurements at all five angles are shown in figure 4.8a for (i) 120 and (ii) 142 MeV projectile energies respectively, obtained with the shadow shield technique discussed in section 4.2.

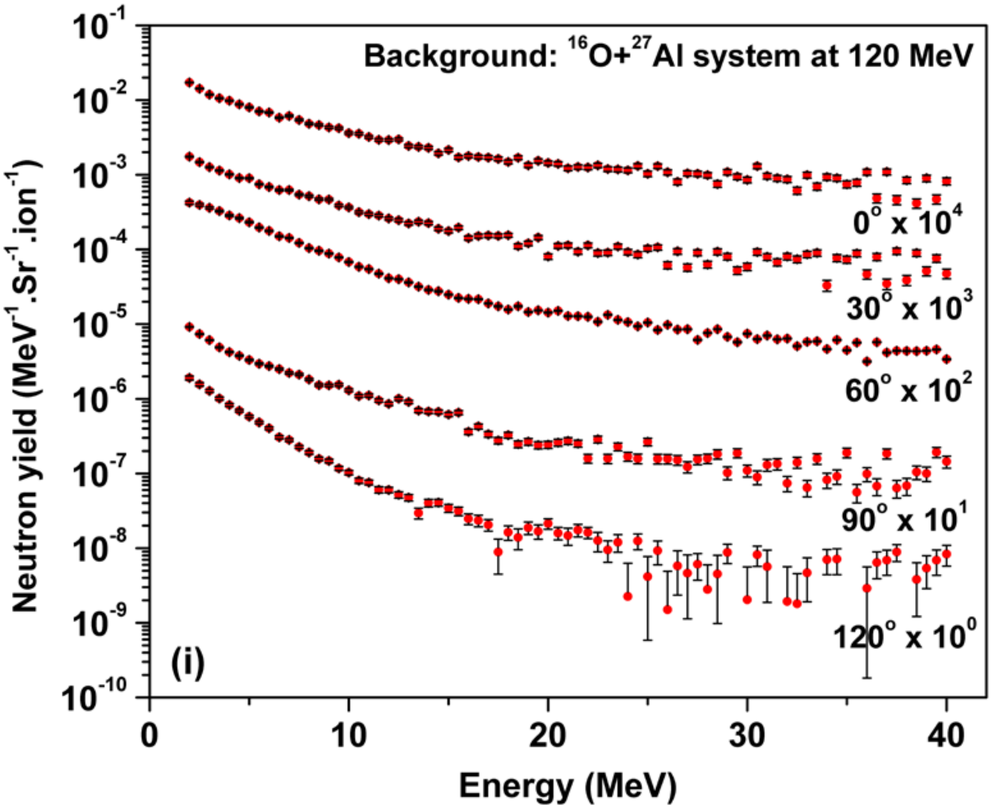

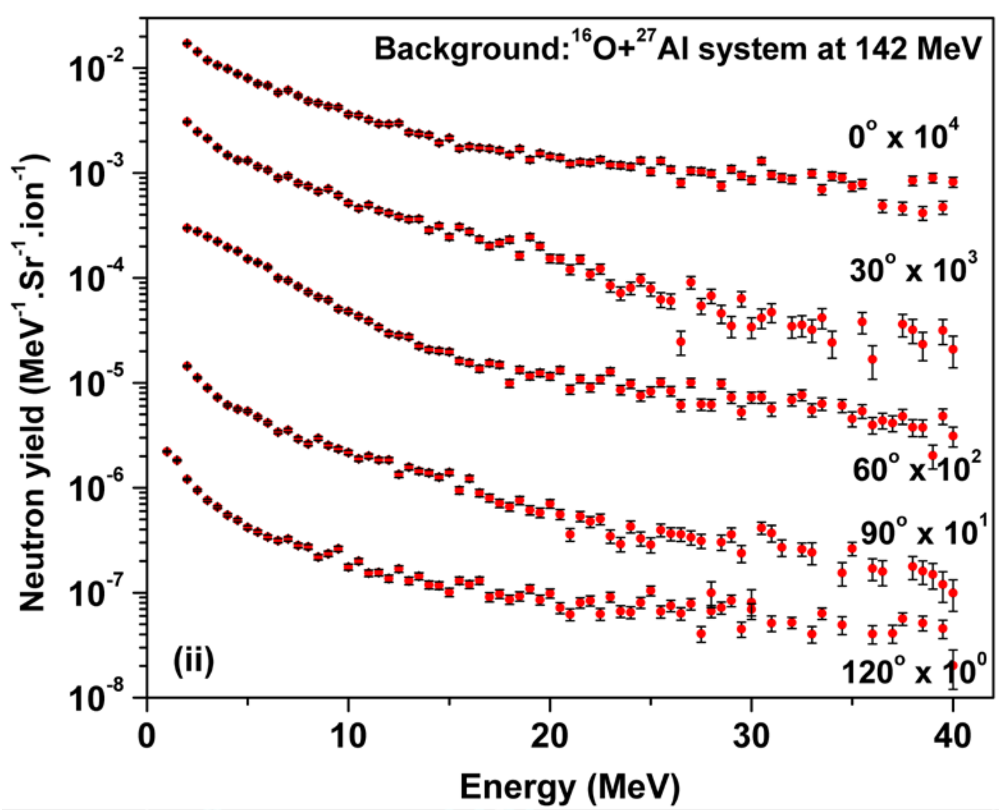

Figure 4.8a: A comparison between the experimental neutron yield at (i) 120 and (ii) 142 MeV.

The variation between the measured total and background spectra of the neutron yield at two different angles, 0° and 90° for both the energies are shown in the figure 4.8b and c.

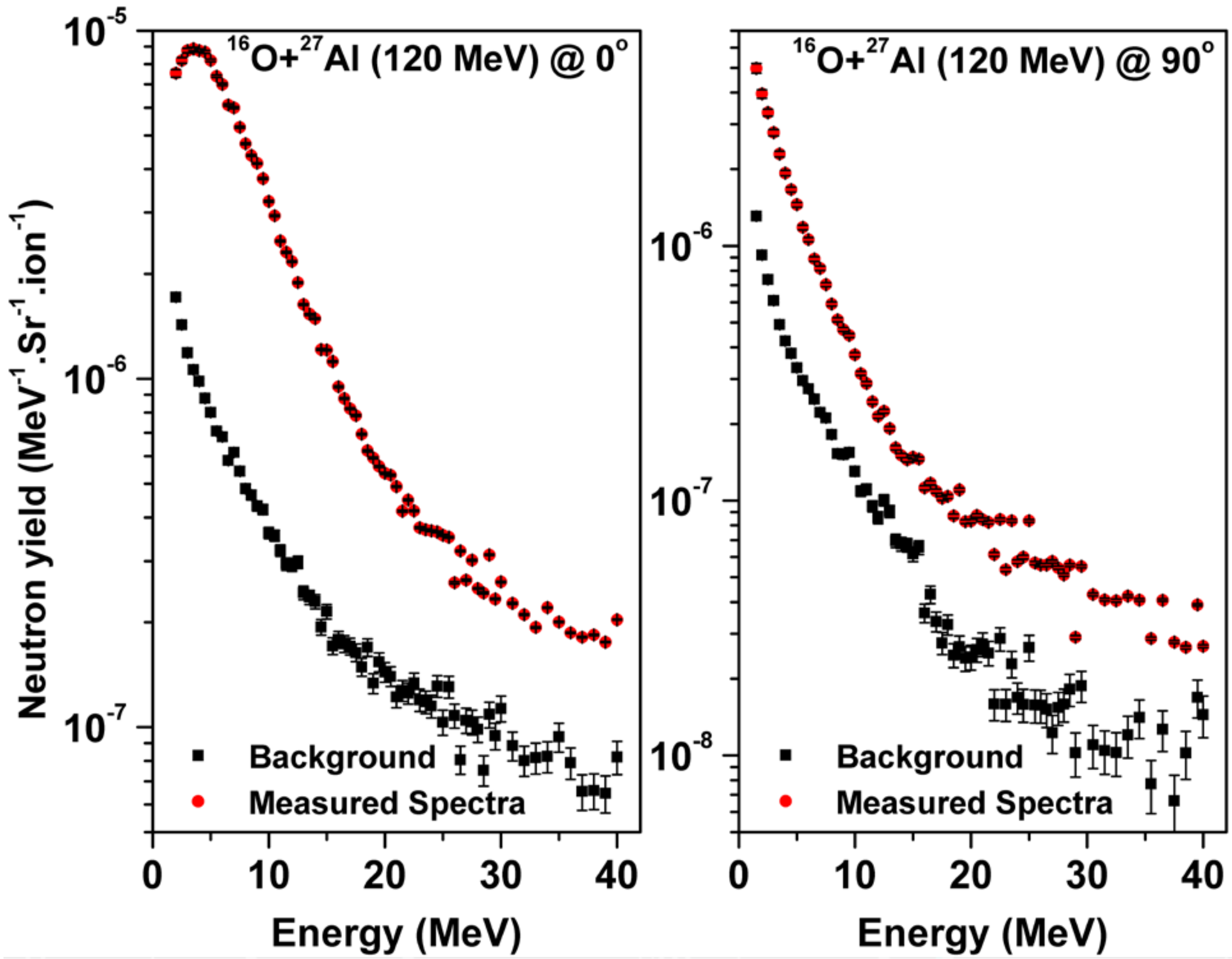

Figure 4.8b: Comparison between the background to the total measured neutron yield at 0° and 90° for projectile energy of 120 MeV.

The plots clearly show that a significant contribution of the measured neutron yield over background exists at higher neutron emission energies. For the 0° angle, the neutron yields were found to be more than five times higher than the corresponding background measurements in the lower energy evaporation region and two to three times at the higher emission energy region beyond 20 MeV. Similarly, at backward angle 90°, significant increase can be observed though the relative increase in the yield values were found to be less. This signifies the higher contribution of the high energy neutrons at forward angles compared to the backward. The similar comparison at 142 MeV projectile energy shows a very similar trend shown in the figure below. In this case the difference between the background to measured neutron spectra at higher emission energies are found be separated by a factor of more than six times in the lower energy evaporation dominated emission region and three to four times in the higher emission energy region. This clearly indicates that the higher energy contribution increases as the projectile energy increases.

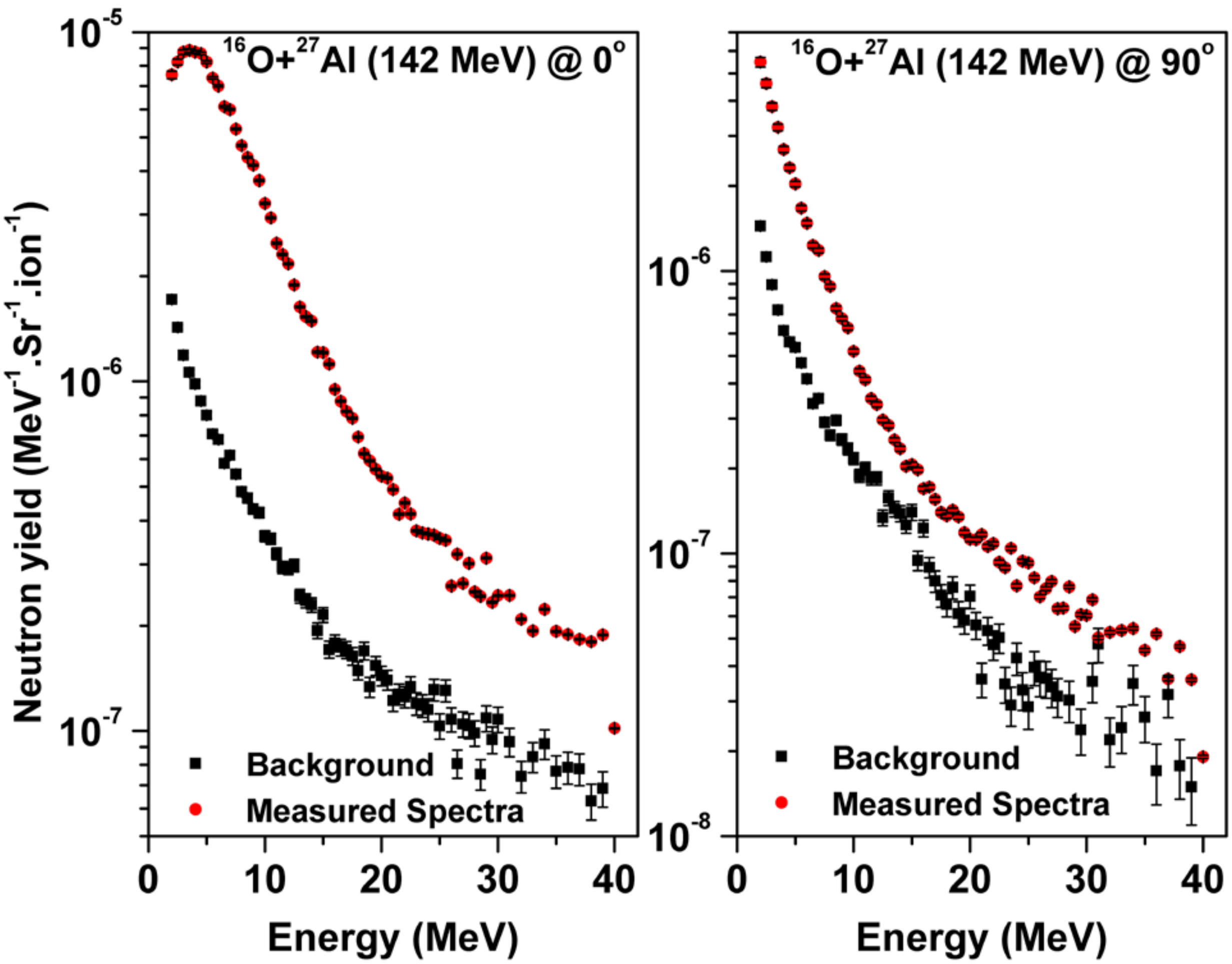

Figure 4.8c: Comparison between the background to the total measured neutron yield at 0° and 90° for projectile energy of 142 MeV.

4.7 Errors and uncertainties

The errors and associated uncertainties for the ToF measurements using EJ-301 liquid scintillator may originate from different sources like the variation in the projectile energy resolution, beam current normalization, time resolutions etc. Among these, the most predominant factor is the time resolution, as they can appear from different sources, viz. the intrinsic time resolution of the detector, spread in the photon pulse and determination of the centroid, self attenuation and energy reduction in the target itself and time spread resulting from the finite thickness of the detector.

4.7.1 Energy Resolution

The relative energy resolution in this method can be represented as,

$$\frac{\Delta E}{E} = \gamma(\gamma + 1)\left(\frac{\Delta t}{t}\right); \quad \gamma = 1 + \frac{E}{Mc^2} \tag{4.3}$$

Here the kinetic energy of neutron is represented by E, M being the rest mass and $t, \Delta t$ are the neutron flight time and overall time resolution respectively. This includes the error in the beam current normalization and found to be less that 2% of the measured values.

4.7.2 Time Resolution

The factors contributing to the time resolution includes the experimental gamma photon energy spread, thickness of target and small uncertainty in the target to detector distance and angular correction. The rest of the important factors are detector resolution and finite thickness of the detector. Considering these factors, overall time resolution can be estimated using relation,

$$\Delta t = \left((\Delta\tau)^2 + \left(\frac{\Delta x}{\mathrm{v}}\right)^2\right)^{1/2} \tag{4.4}$$

where, $\Delta\tau$ is the time spread in the detector, v is the velocity of the neutrons and the Δx is the detector thickness. Considering these factors, the energy resolution $\left(\frac{\Delta E}{E}\right)$ of the ToF measurements for 2 m and 1.5 m distance, the estimated resolution can go up to 15% for 40 MeV of neutrons. As neutron energy decreases, the energy resolution deteriorates. As mentioned earlier the time interval between two bunches of the projectiles was 107.3 ns. As a result the neutrons energy lower than 0.5 MeV reached the detector at the same time as that of the faster neutrons and the photon pulses of the next generation. This has put a constraint on the lower limit of the neutron energy detection and the low energy neutron identification in the present ToF set up was restricted up to 0.5 MeV. The statistical uncertainties in the measurements were minimized by providing a large counting time and varies from 0.01% for low energy (1 MeV) to a maximum of 4% for the high energy (40 MeV) region of spectra. The scattered component subtraction for estimating the net counts also adds to the uncertainty. The scattered contribution increases at the backward angles. These were found to be 1% for (0°, 30°), ~2% for 60° and up to 5% for 90° and 120°. The variation in the flight path due to error in source to detector measurements, solid angle corrections for a detector type of (5 cm×5 cm) and the pulse pile up effects at the detector were collectively found to pose an uncertainty of <1%.

4.8 Results and Discussions

In the present study, the emission neutron yield has been estimated for $^{16}O^{+6}+^{27}Al$ system at two different energies. The corresponding pre-equilibrium (PEQ) neutron contributions has been estimated using the HION model with spatial density distribution. In order to identify the high energy PEQ contribution in the experimental data, the evaporation contribution for the reaction system has been estimated from statistical model calculations. Here we have used the code Empire ver. 3.2 (Malta) for estimating the evaporation neutron yields from heavy ion reaction and the Monte Carlo code PACE4 as discussed in section 2.5. The comparison of the estimated neutron yields from both the statistical model codes and the experiment is shown in the next subsections.

4.8.1 Experimental comparisons with evaporation code

Experimental emission neutron yields with the corresponding evaporation estimates are shown in figure 4.9 for 120 MeV ^{16}O projectiles on a thick Al target. Here the thin target neutron yields with degraded incoming projectile energies were calculated using the PACE and EMPIRE codes and finally superimposed to convert to corresponding thick target yields using the steps discussed in section 2.6. In this calculation, the thin slabs having the fixed energy degradation is chosen to decrease by 5 MeV in energy. Further the particle is assumed to interact with all the target nuclei and there is no slowing down taking place due to multiple scattering and straggling.

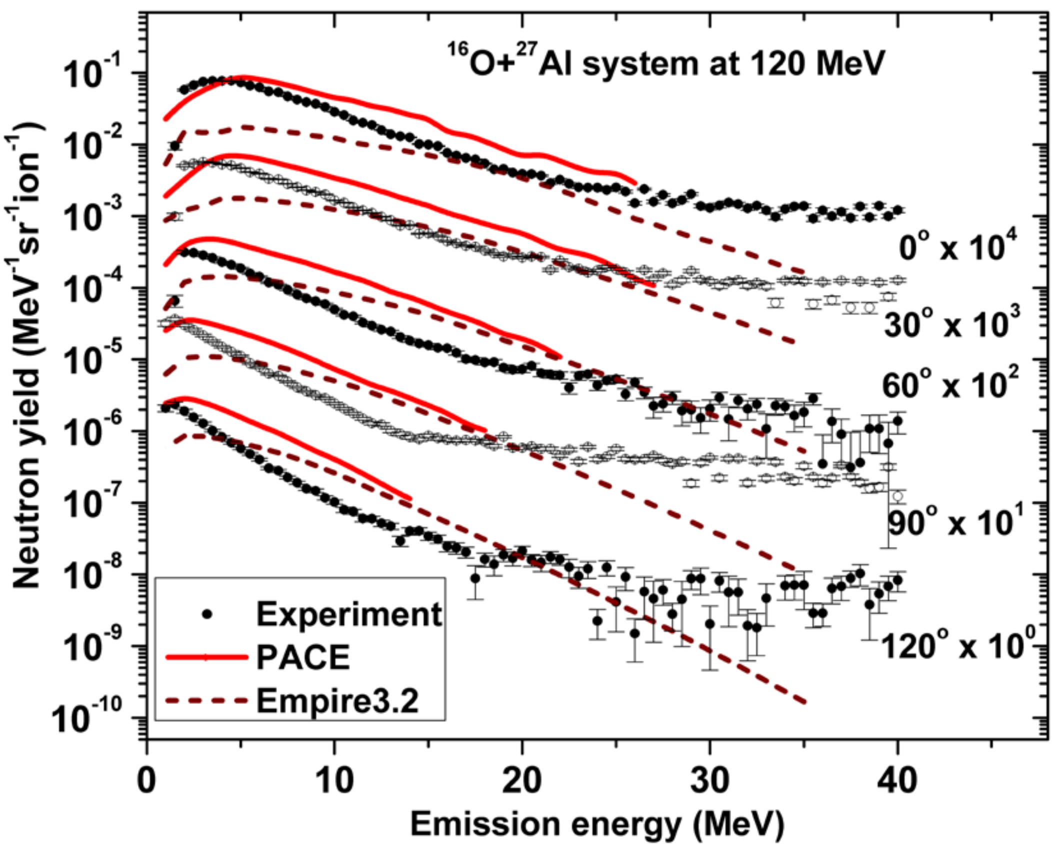

Figure 4.9: A comparison between the experimental to statistical code estimates for thick target neutron yield at 120 MeV (black dots: experiment, solid red: PACE and brown dots: EMPIRE)

The PACE is found to have a good agreement with the experimental neutron yield at 0^o and 30^o, whereas at large backward angles, the estimates are found to be largely overestimated compared to the experimental ones. In contrary, the EMPIRE estimates are found to be initially underestimated at forward angles, whereas at backward angles, this also over-predictions the experimental yields. In the figure, the experimental yields for alternate angles were marked in solid and open circles for a better understanding. The high energy neutron contributions and the multiplication factors associated with the measurements and estimates are mentioned in the figure. The statistical uncertainties for the experimental measurements are indicated in term of the error bars for 120 MeV projectile energy. The similar results for the 142 MeV projectile energy is shown in figure 4.10.

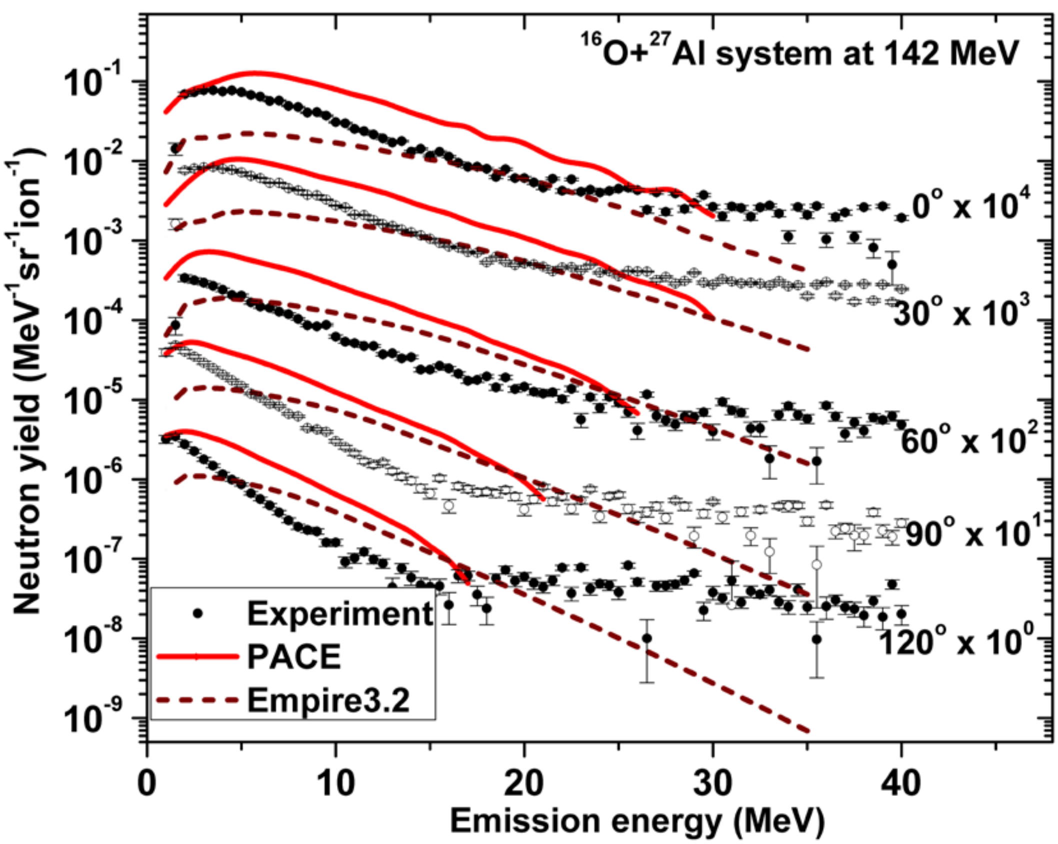

Figure 4.10: A comparison between the experimental to statistical code estimates for thick target neutron yield at 142 MeV (black dots: experiment, solid red: PACE and brown dots: EMPIRE)

The PACE over-predictions at all angles in comparison to the measured evaporation neutron yield may be attributed to the overestimation of the fusion cross sections. The variation in emission probabilities resulting from the choice of level density parameters (A/10) for PACE also give higher neutron yield compared to Empire 3.2 predictions. In both the projectile energies, the PACE calculations were trimmed at higher emission neutron energies considering a sharp decrease in the population of neutrons leading to large calculation uncertainties.

In both the cases, the high energy neutrons are largely underestimated by both models. The difference in the yields between theory and the experiment is highest at 0^{o} for both the measurements and decreases at wide angles. This clearly indicates a contribution from the pre-equilibrium emissions along with the evaporation contributions. In order to account for this higher neutron yields, an attempt has been made to include the contribution of the PEQ neutrons at higher emission energies using the HION code and will be discussed in the next section. In the next subsection the angular distribution of the emission neutrons from the models and experiment will be discussed.

4.8.2 Angular distributions of Neutron emission

The angular distribution clearly shows that the Empire results largely underestimates the experimental measurements at all angles and the similar with the PACE estimates (~20-40% underestimation) in the forward angles. This underestimation at the forward angles indicates the presence of another contributor in the emission neutron yield apart from the evaporation. The PEQ contribution and the associated increase in the total yield at different emission angles will be discussed in the next section. The angular distributions at back angles between 60^{o} to 120^{o} matches well with the PACE estimates for 120 MeV projectile energy, as shown in figure 4.11. In this angle range, evaporation is the major contributing factor and due to anisotropic nature of the PEQ angular distribution, the effects will be very less and the variation from the PACE results vary by 8-12 %. In the calculation procedure, as the Empire calculation provides the energy differential neutron emission cross sections in the centre of mass frame, so it has been converted to the corresponding lab frame using the centre of mass to lab frame conversion relations. Further the thick target conversion using different equal energy degradation slices at various degrading projectile energies were assumed and the cross-sections were converted to double differential neutron yield distributions.

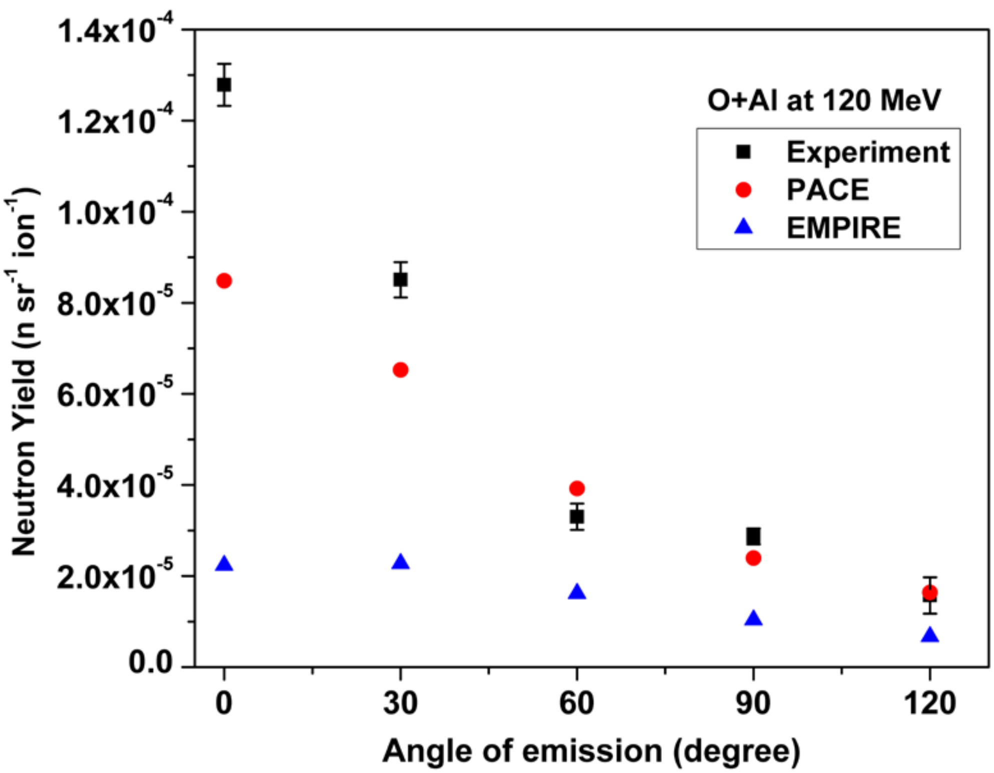

Figure 4.11: Angular distribution of the emission neutrons at for thick target neutron yield at 120 MeV (black square: experiment, red circle: PACE and blue triangle: EMPIRE)

Angular distributions of neutron yield are tabulated in Table 4.2 for both the ^{16}O energies on thick Al target. Trends of emission neutron angular distributions for 142 MeV projectile energy are shown in figure 4.12. This also shows a similar trend to the earlier estimates. In this case, the PACE estimates showed a closer corroboration. In this case also the experimental yields are found to be higher that the corresponding model calculations at the forward angles and the experimental yields at 30 ^{o} is found to comparatively higher than other angles. The Empire estimates are found to be still large underestimated with respect to the experimental yields.

Table 4.2: Angular distribution of neutron yields from 120, 142 MeV ^{16}O on thick Al target

Angle (degree)	Neutron Yield from 120MeV ^{16}O ($n.Sr^{-1}.ion^{-1}$)			Neutron Yield from 142 MeV ^{16}O ($n.Sr^{-1}.ion^{-1}$)		
	ToF	PACE	EMPIRE	ToF	PACE	EMPIRE
0	1.279×10^{-4}	8.482×10^{-5}	2.234×10^{-5}	1.428×10^{-4}	1.388×10^{-4}	3.205×10^{-5}
30	8.506×10^{-5}	6.527×10^{-5}	2.274×10^{-5}	1.390×10^{-4}	1.061×10^{-4}	3.241×10^{-5}
60	3.302×10^{-5}	3.920×10^{-5}	1.618×10^{-5}	3.942×10^{-5}	6.253×10^{-5}	2.282×10^{-5}
90	2.872×10^{-5}	2.395×10^{-5}	1.040×10^{-5}	3.748×10^{-5}	3.687×10^{-5}	1.448×10^{-5}
120	1.573×10^{-5}	1.637×10^{-5}	6.713×10^{-6}	2.305×10^{-5}	2.433×10^{-5}	9.262×10^{-6}

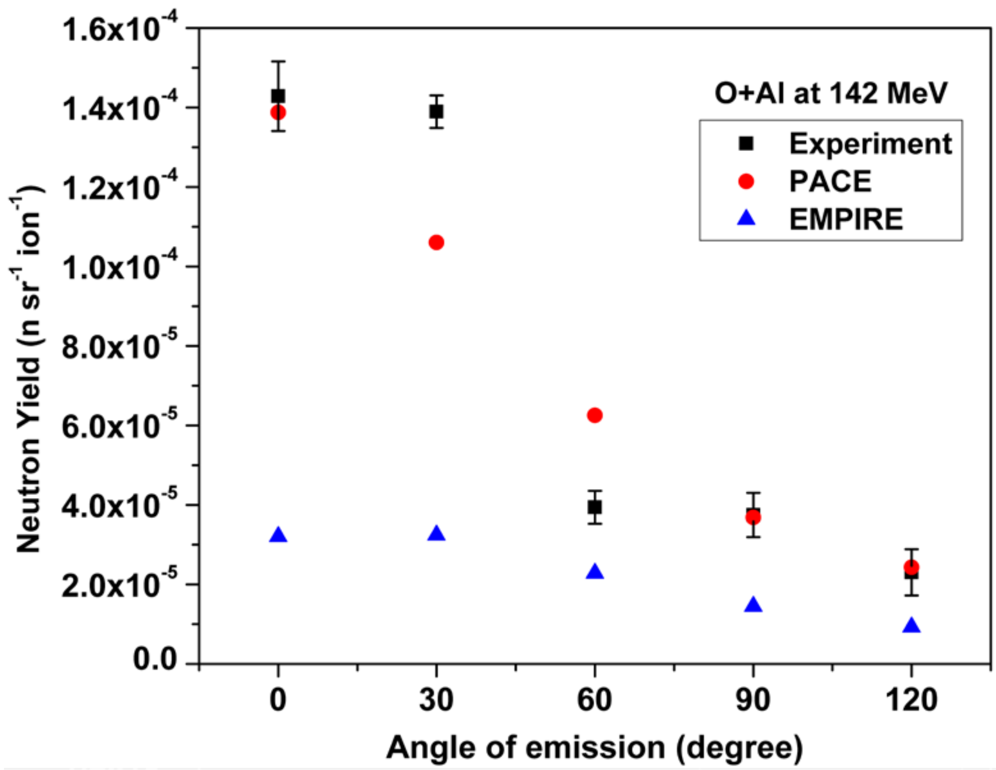

Figure 4.12: Angular distribution of the emission neutrons at for thick target neutron yield at 142 MeV (black square: experiment, red circle: PACE and blue triangle: EMPIRE)

4.9 Study of the PEQ contribution

Emission neutron yield in the present study shows an underprediction by the model calculations, specifically in the forward angles with respect to the incoming beam directions, as shown in the earlier section. In this regard, the possibility of pre-equilibrium emissions has been investigated using the in house developed HION code [96]. This code have already showed the applicability in the energy range of 10 - 30 MeV/nucleon, in the earlier chapter and there are a number of evidences [162-168] regarding the contribution of PEQ emissions below 10 MeV/nucleon also. So considering that, this HION code has been used in the present work and the yield of high energy neutrons were compared with the code estimates.

For HION code, the neutron yields are largely dependent on the spatial nucleon distribution within the nucleus and the emission probability and the collision rates are calculated based on this distribution.

4.9.1 Nucleon density distribution

In the present work the density distributions has been calculated using both the semi-phenomenological of Gambhir and Patil [103] and the relativistic mean field (RMF) [104] approach. The density profiles for composite system ^{43}Sc using both the models are shown in figure 4.13. The density profile shows a larger neutron density compared to the corresponding neutron density considering the proton-proton repulsion to exist for both the formalisms. The semiphenomenological approach shows a near constant density values for both neutrons and protons till 2.5 fm and then the density values fall sharply to become almost zero by 6 fm. The central neutron density is found to be 0.11 fm^{-3} and corresponding proton one is 0.1 fm^{-3}. The RMF estimated spatial density distribution also shows a steady decrease in the density values at larger distances from the centre of the nucleus.

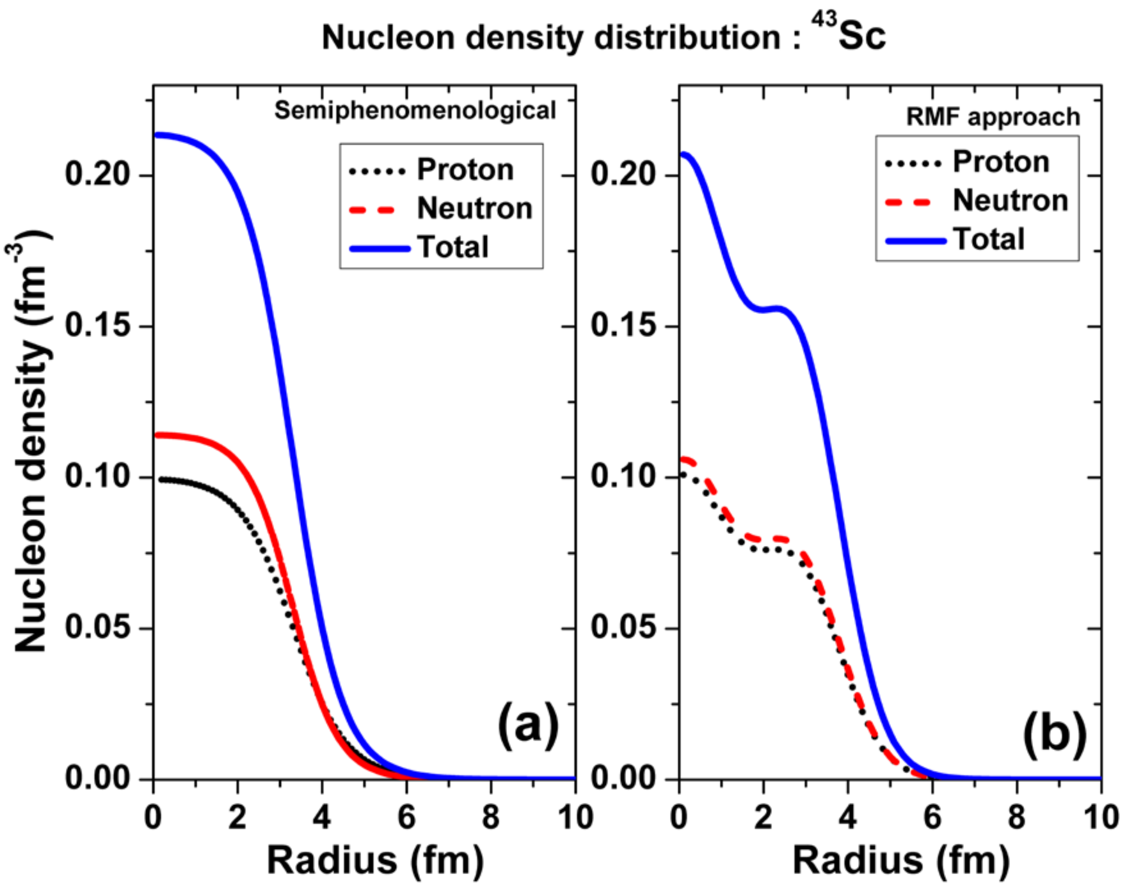

Figure 4.13: Nucleon density distribution for compound nucleus ^{43}Sc (^{16}O + ^{27}Al) system using (a) semiphenomenological and (b) RMF approach

The density values for both proton and neutron steadily decreases by 25% of the central value till 2 fm and then becomes almost steady till 3 fm. Further the density values decreases after 3 fm and reduces to zero by 6 fm. So apart from the core part density variation, the density profile remains almost similar at the external part of the nucleus.

4.9.2 Study of the high energy neutron yield

Using both the spatial distributions, further particle emission, collision rates and emission probability calculations were done as discussed in chapter 3. In the present work, considering the projectile energy to be less than 10 MeV/nucleon, only the single neutron emission possibility has been included for HION calculations and both the simultaneous and sequential multiple pre-equilibrium modules were not used during the calculations. The neutron emissions obtained from the emission probability calculations for 142 and 120 MeV projectile energies using both the density values (semiphenomenological and RMF), showed only a 5% variation in the thin target yields. For the thick target neutron yield calculations, at lower energies, the variation becomes even lesser and the weighted sum of all the gradually decreasing energies makes the total integrated yield difference to be negligible. So, in the present study only the emission probability and neutron yields from semiphenomenological approach and the corresponding experimental counterpart is shown. The experimentally obtained neutron spectra for 120 and 142 MeV ^{16}O energies on a thick ^{27}Al target and the corresponding PEQ neutron yields at different angles estimated from HION code are presented in Fig. 4.14 and 4.15 respectively.

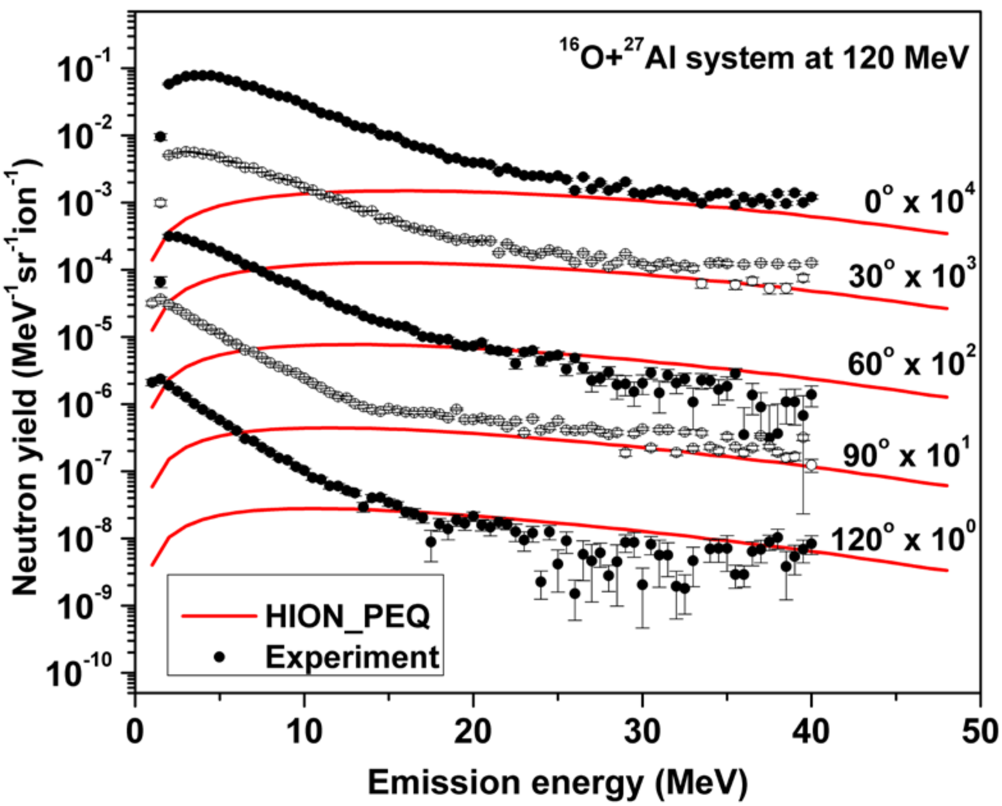

Figure 4.14: Comparison of experimental neutron yield with HION estimated PEQ contribution at 120 MeV ^{16}O beam on a thick ^{27}Al target.

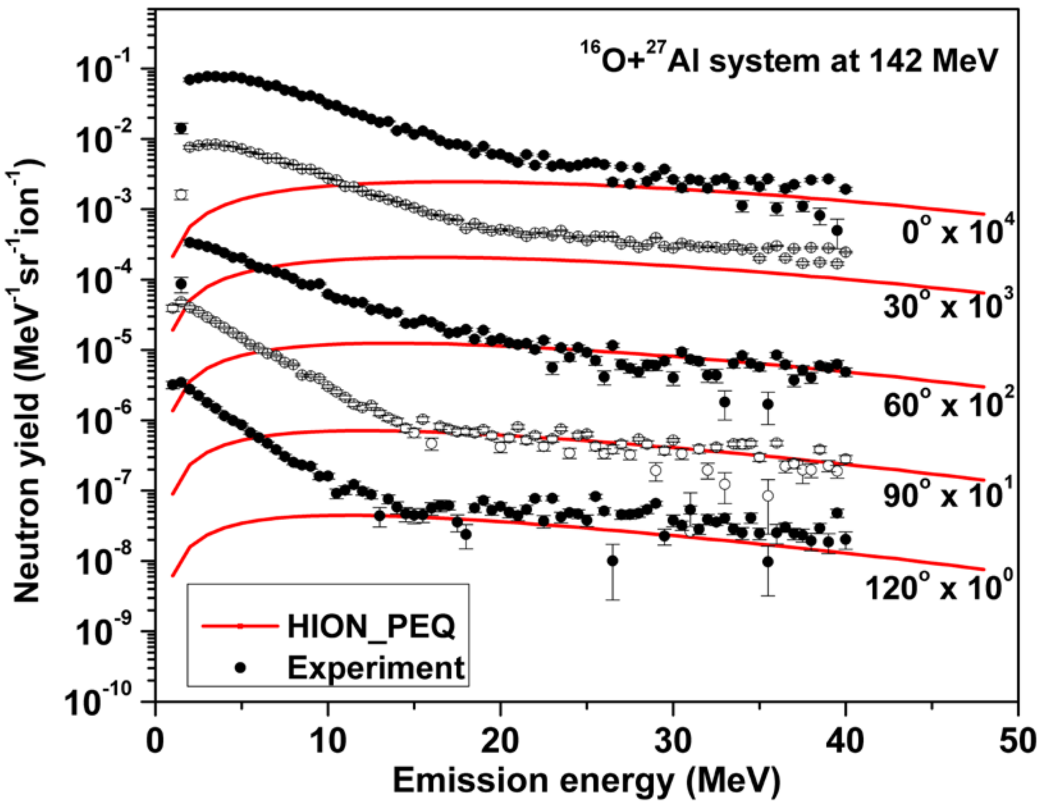

Figure 4.15: Comparison of experimental neutron yield with HION estimated PEQ contribution at 142 MeV ^{16}O beam on a thick ^{27}Al target

At lower energies, the HION results are found to have a low yields and at higher emission energies, the PEQ estimates obtained from the HION code shows a very good corroboration. For a better estimation of the sole PEQ contribution, the evaporation estimates calculated from the PACE were subtracted from the experimental measurements and the resulting spectra were compared with the HION. At forward angles, the subtraction was done above 25 MeV and for 90^{o} and 120^{o} angles above 20 MeV. Figure 4.16 and 4.17 shows that HION estimates reproduces the experimental data at higher energies and for both 142 and 120 MeV beam energies and the PEQ contribution is found to be 3.3% and 2.3% of evaporation contribution respectively at 0^{o} emission angle.

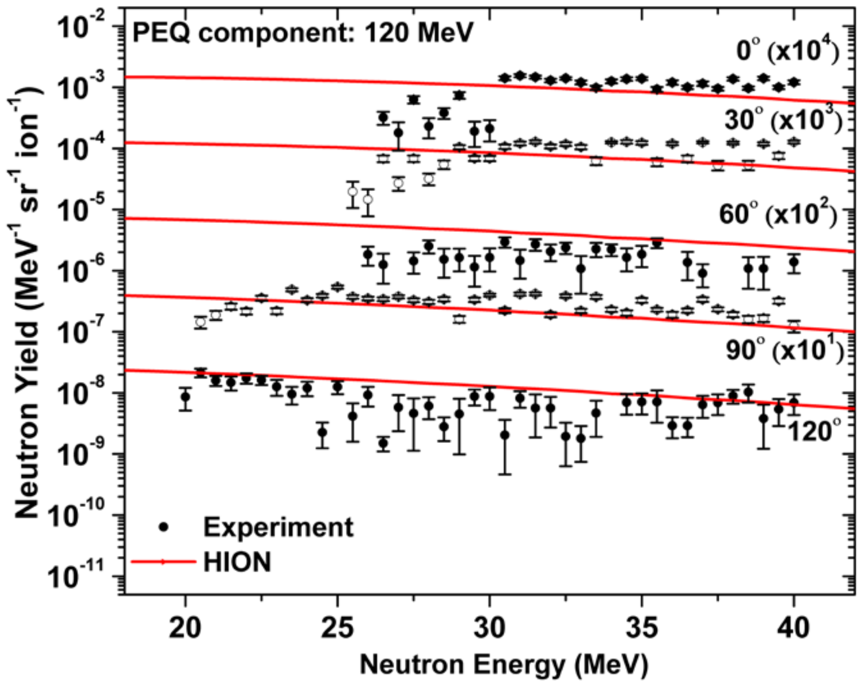

Figure 4.16: Comparison of evaporation subtracted experimental neutron yield with HION estimated PEQ contribution at 120 MeV ^{16}O beam on a thick ^{27}Al target

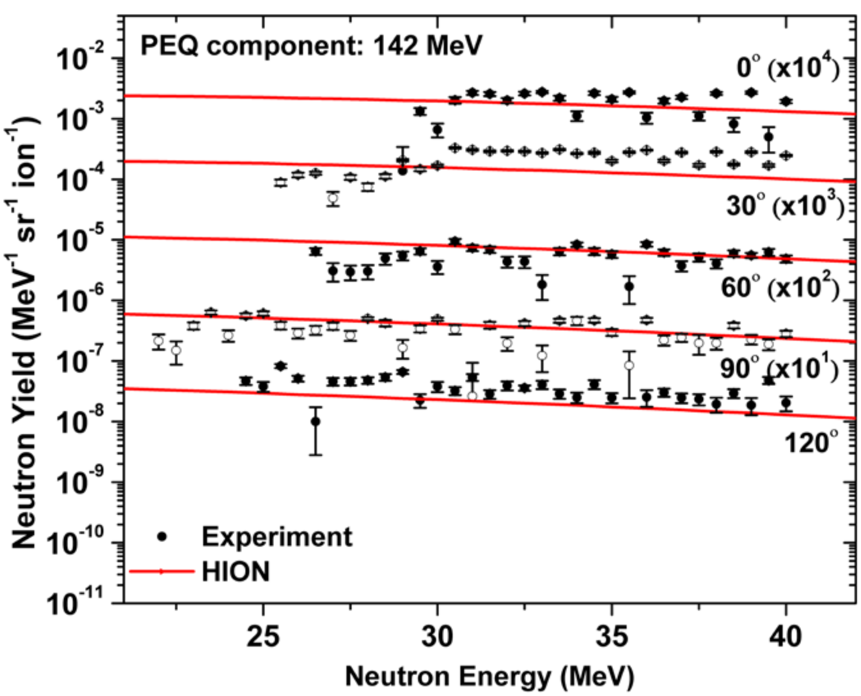

Figure 4.17: Comparison of evaporation subtracted experimental neutron yield with HION estimated PEQ contribution at 142 MeV ^{16}O beam on a thick ^{27}Al target

The percentage particle variation for the PEQ range at forward angles may not appear to be large as we are considering the PACE estimates till the 25 MeV at forward angles and 20 MeV till the backward angles. But if a comparison from the dosimetric point of view is considered using a conventional neutron dose equivalent (NDE) meter, the total estimated dose variation becomes very significant. It is because the maximum possible measurable energy range for a NDE meter is restricted up to 17-20 MeV, so the variation in estimated dose arising from the large energy neutrons can be significantly large. This problem needs to be addressed and for this purpose, the estimate of the high energy neutron dose contributions has been carried out in the next section.

4.10 Dosimetric estimates with experiment and NDE meter

In the present work the neutron dose estimates from the nuclear reaction has been carried out using the dose conversion coefficients (DCC) as published in ICRP publication number 74 [12]. The fluence to dose conversion coefficients [ICRP74] were calculated from the figure 4.18 for the energy range 0.5 to 40 MeV. For the dosimetric estimations, a LB6411 (make Berthold) type NDE meter has been used in the present work and the meter has been kept at all five measurement angles. The NDE meter has been kept at 1 m and 0.5 m distances from the target depending on the measurement angle. For 0° to 60°, the NDE meter was kept at a distance of 1 m and for rest two backward angles, it was kept at 50 cm distance. The variation in the distance has been adjusted to acquire a greater neutron yield by increasing the solid angle covered. The results were then normalized with appropriate corrections for solid angle, current integrator (CI) readings and associated CI-scales, i.e., the total accumulated charge at the target. Finally the results were converted in the unit of mSv.μC^{-1} of the projectile charge. The comparison of dose equivalents from ToF technique and corresponding evaporation estimates are given in table 4.3.

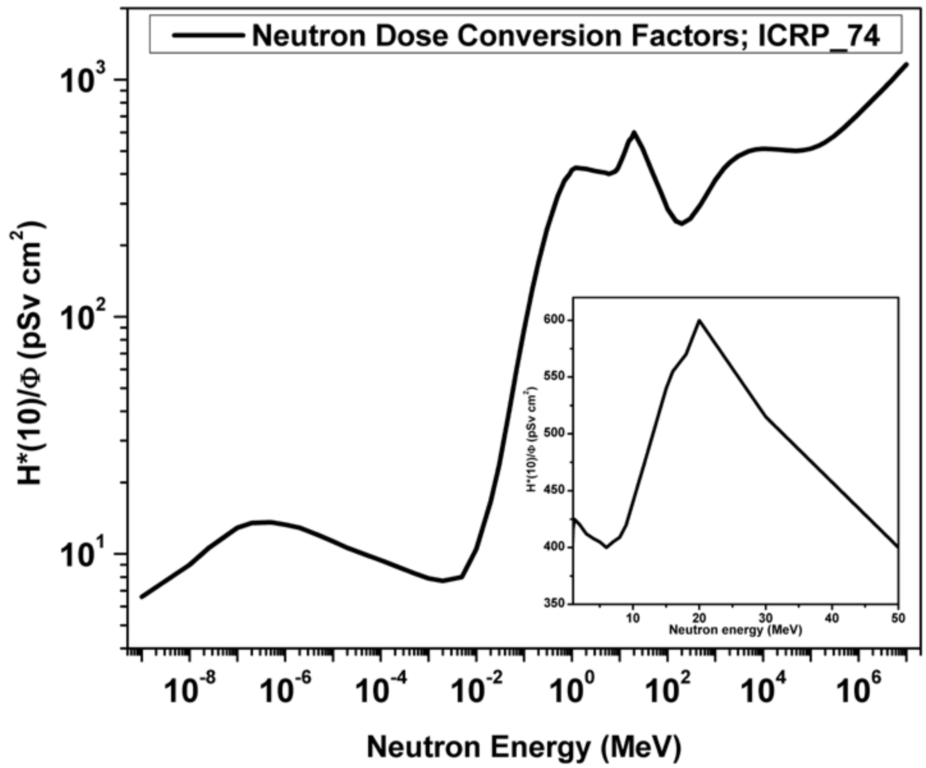

Figure 4.18: The flux to dose conversion coefficients for neutrons as given by ICRP; close look at the 1-50 MeV region in linear scale (inset)

Table 4.3: Angular distribution of dose equivalent from 120 and 142 MeV ^{16}O on thick Al target.

Angle (degree)	Dose Equivalent from 120MeV ^{16}O (mSv.μC^{-1})				Dose Equivalent from 142 MeV ^{16}O (mSv.μC^{-1})			
	ToF	EMPIRE	PACE	NDE	ToF	EMPIRE	PACE	NDE
0	57.8	10.6	39.1	38.1±2.7	65.5	15.4	64.5	58.6±2.3
30	38.4	10.7	29.8	29.3±2.3	63.4	15.5	48.9	46.4±2.3
60	14.7	7.5	17.5	14.1±1.3	17.8	10.7	28.2	21.3±1.3
90	12.7	4.7	10.5	6.3±0.8	16.5	6.6	16.3	12.4±1.1
120	6.9	3.0	7.1	3.7±0.6	10.1	4.1	10.6	7.7±0.9

Measured neutron doses using the NDE meter for both projectile energies are shown in figure 4.19 with associated measurement errors. A comparison of measured to estimated neutron equivalent dose with ToF and model predictions are shown in figure 4.20 and 4.21.

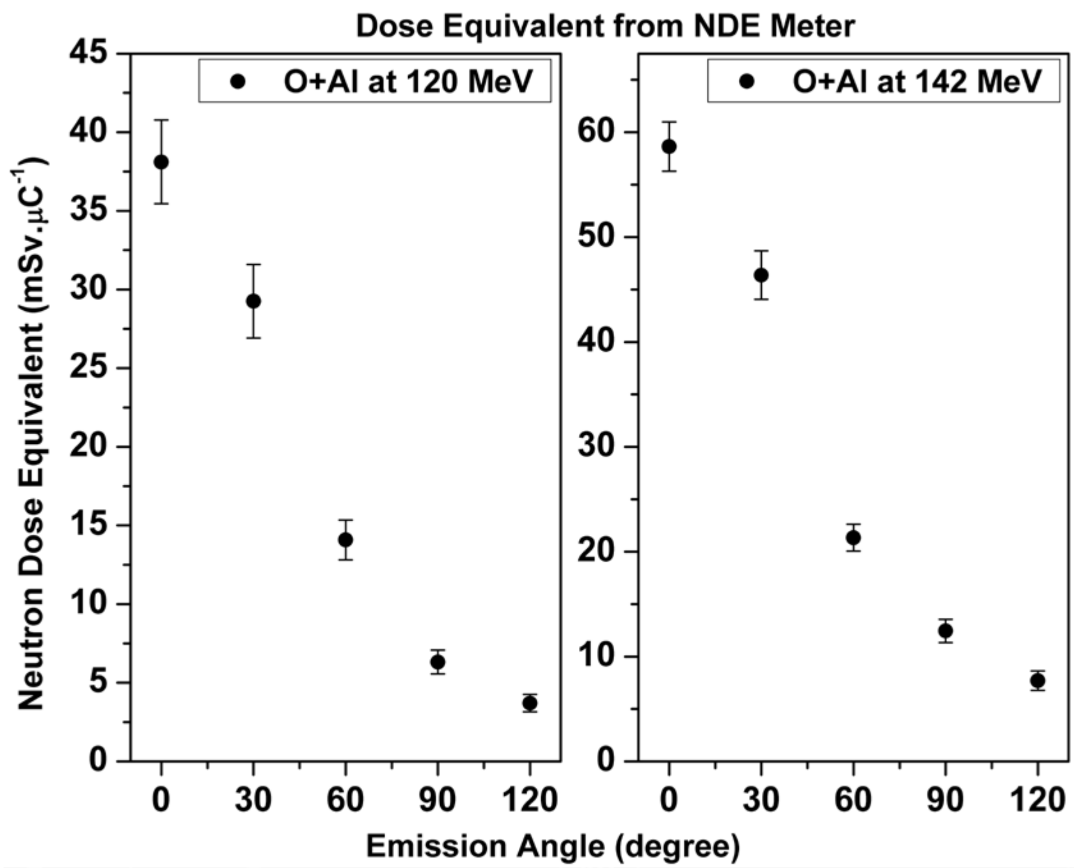

Figure 4.19: Measured Neutron doses using NDE meter for ^{16}O beam on a thick ^{27}Al target

For 120 MeV projectile energy, the measured equivalent dose with NDE meter is found to be close to the PACE measurements for the angles 0° to 60° but underestimates largely compared to the ToF measured ones. This is because the high energy emitted neutrons cannot be detected by the NDE meter. At backward angles the measured dose are found to be less than the PACE estimated one, as seen in fig. 4.20.

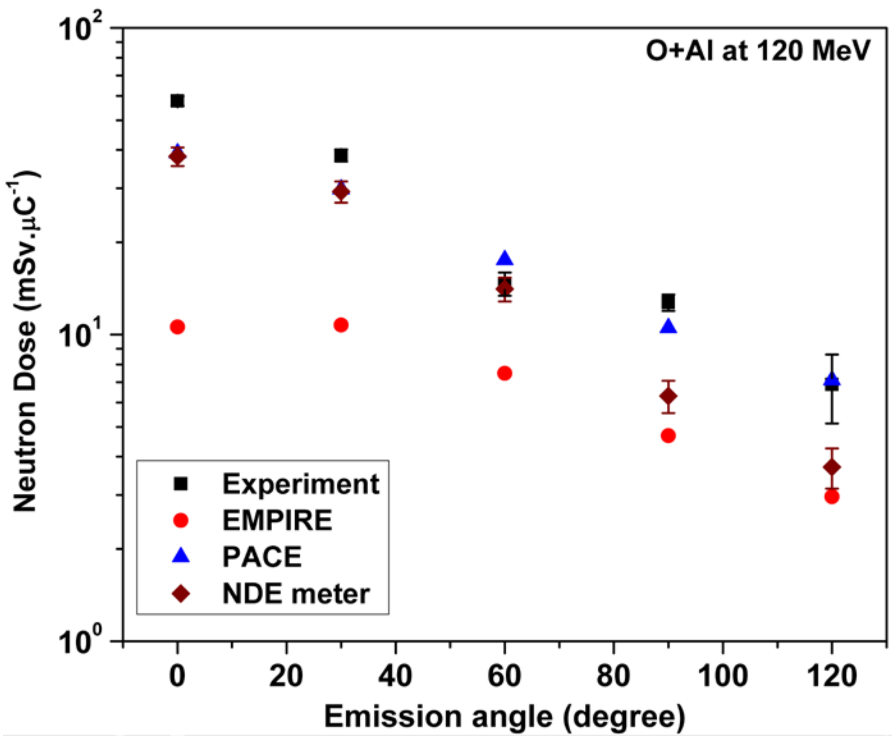

Figure 4.20: Estimated neutron dose at 120 MeV ^{16}O beam on a thick ^{27}Al target.

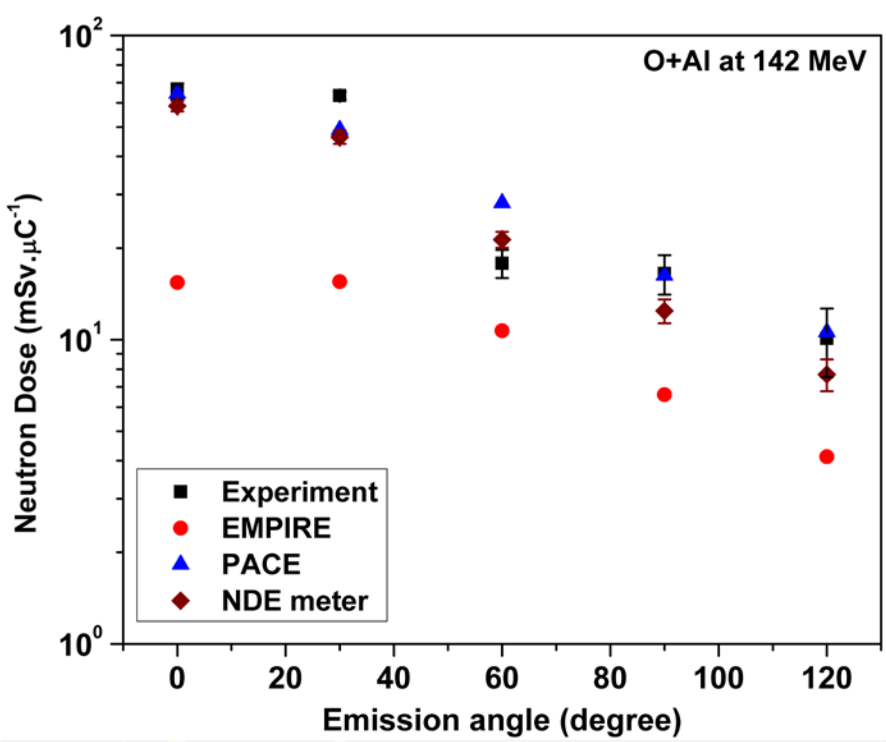

Figure 4.21: Estimated neutron dose at 142 MeV ^{16}O beam on a thick ^{27}Al target.

Similar results are found for 142 MeV projectiles as well. A separate estimation for the PEQ neutrons estimated from the HION code has been done in this work and found to have almost 6-10% of the evaporation contribution in the forward angle, and at backward angles, contribution reduces due to reduction in the large energy neutron contents. The PEQ estimated dose for both the energies are shown in figure 4.22.

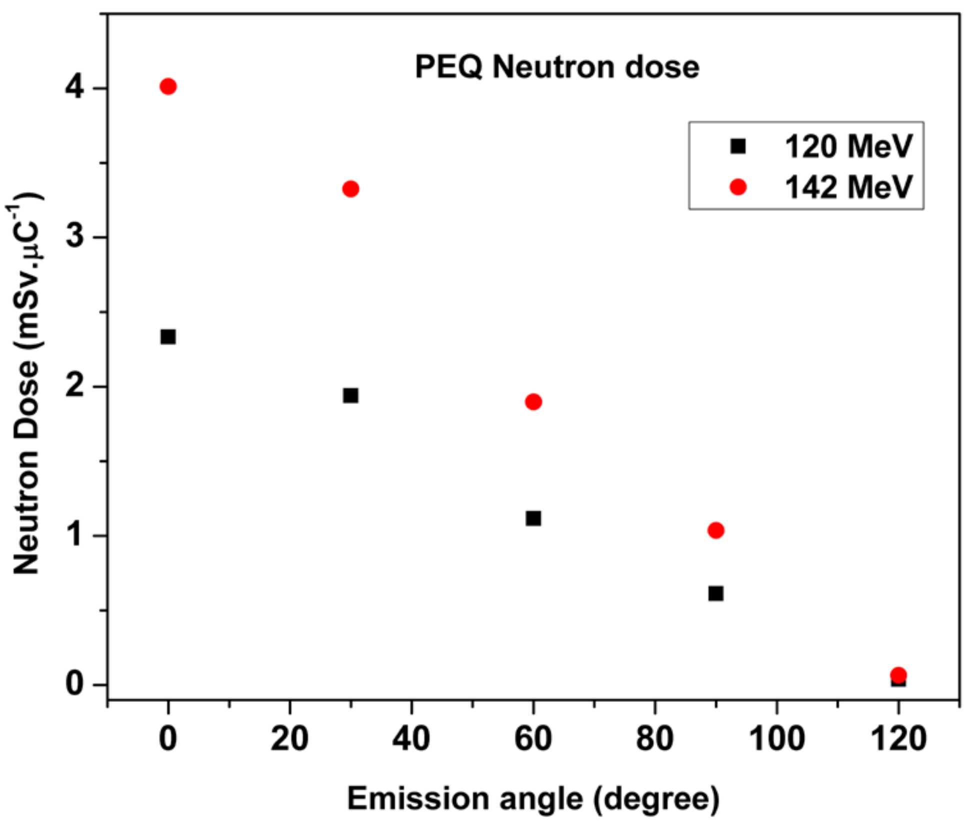

Figure 4.22: HION estimated PEQ neutron dose from 120 and 142 MeV ^{16}O beam.

So in the present work it has been found that the HION code can estimate the high energy neutrons from thick target emissions for projectile energies even at less than 10 MeV/A. The reproduction of the experimental data at higher emission energies for all angles with the code estimates also validates the applicability of the code at low energies as well. Calculations also showed that for 7.5 and 8.8 MeV/A cases the PEQ contributions at 0° are 2.3% and 3.3% of the evaporation contribution respectively in terms of the neutron yield. Whereas the estimated dose using the dose conversion coefficients of ICRP74, for the PEQ neutrons can go up to 6-10 % at forward angles, due to large DCC values at higher neutron energies as shown in fig 4.18. The contributions increase significantly at larger projectile energies beyond 17 MeV. In the next chapter a theoretical estimate of the neutron yields and the corresponding dose equivalents for various target projectile system at increasing energies will be estimated to get an estimate of the dosimetric corrections to be incorporated due to large energy emissions in an accelerator environment.

Chapter 5

Estimation of Preequilibrium component for heavy ion reactions at large projectile energies

The present chapter deals with the determination of PEQ neutron yield from different target projectile combinations, which can serve as an additional support for the yield and dose estimation from PEQ neutrons. These estimates are very important from the radiological protection purposes, the design of shielding or estimation of equivalent doses for radiation workers. In a radiation installation, prior to commencement of construction, a detailed shielding and dose apportionment analysis is carried out. The shielding thickness is decided based on the available source term and the consequences in case of incidents or accidents due to some wrong practices or otherwise. In such calculations, for an accelerator installation, neutron distribution from different elements need to be studied, as the beam interactions can take place with the structural materials, machine components, air or water. So yield studies need to be carried out with a wide range of target elements in order to have a proper idea about the shield design and dose profiles inside or outside the accelerator hall. To obtain such information, the possible ways are, firstly to carry out some experiments with the known set of commonly used target and particle beams. Other options are careful examination of possible yield and angular distributions from available literature data or carrying out some model calculations to obtain the respective yields. In most of the cases, the experimental validation is difficult considering the complexities in neutron spectra measurements with a large setup of detectors and electronics and is time consuming. The second constraint appears from the available particle fluence (current) and beam energies in different facilities. With available experimental facilities, at times the desired energies and target projectile combinations are not available. so one of the most effective option is to look for one or more model codes for estimation of the neutron spectra, angle or energy integrated yield and total yield. These parameters are used as the source term for designing an optimized shielding for the facility or estimation of the dose levels at different locations of the facility. The dose distribution study allows an accurate zoning to facilitate the administrative control and to minimize the radiation exposure to the workers.

With the motivation to enforce the radiological safety in a nuclear installation, the present work can provide a good estimate of the doses from the PEQ and evaporation neutron components originating from the heavy ion nuclear reactions in the projectile energies between few MeV to tens of MeV. This energy range regime a very limited number of codes are available, though heavy ion accelerators at these projectile energies are widely used for basic studies and isotope production. As discussed earlier in chapter 2, most reaction model codes dealing with heavy ion reactions like PACE [77-78], EMPIRE [79], GEMINI [169], The GEM code [170], restricts its usage till 7-10 MeV per nucleon. Monte Carlo based codes like FLUKA [171] which uses relativistic quantum molecular dynamics [172-173] at higher energies between 0.1 to 5 GeV per nucleon and Boltzmann master equation at lower energies at lower energies or fluid dynamics based models using the Vlasov or Vlasov-Uhlenbeck-Uhling (VUU) models [73-76] provide a better estimate at energies of 100 MeV per nucleon or more. So with an aim to calculate the neutron energy and angular distributions in the intermediate gap area of the incoming projectile energy, this part of the work has been carried out. In the present work a total of seven different elements have been chosen as the target material and five different projectiles were used to estimate the effective neutron yield from the concerned heavy ion reaction at energies between 10-50 MeV per nucleon. In the following sections, we will discuss about the choice of projectile and target elements and increase in the neutron yields and associated doses evaluated from the PEQ code.

5.1 Choice of target and projectiles

The five different projectile beams were chosen for the theoretical estimation of neutron yields based on the experiences gained from PLF operations during last 25 years. The projectile beams operated most frequently in the facility have been chosen for evaluation of the neutron yields from PEQ process. These beams are ^{7}Li, ^{12}C, ^{16}O, ^{19}F and ^{28}Si and all calculations are carried out at projectile energies between 10-50 MeV per nucleon. Choosing the target materials in an accelerator domain for the study of yields are very difficult considering the variety of elements available in different shielding materials, beam line assembly and beam dump. Among these, the dump is the prominent source of radiation during the accelerator operation. Mostly Ta and Cu are used for fabrication of the dump assembly. So yields from ^{63}Cu, ^{65}Cu and ^{181}Ta are chosen for the evaluation studies. ^{12}C and ^{56}Fe are chosen as C and Fe are the constituents of the components of beam line assembly. Cu is also extensively used in electrical and cryogenic components. In most of the cases stainless steel, which contains Fe and C along with many other elememts, is primarily used for the beam housing. ^{107}Ag and ^{197}Au are widely used in basic research as scattering or stopping target in experiments, so evaluations involving these two elements have also been carried out. All the projectile-target combinations were studied with both PACE4 and HION codes to estimate the evaporation and the PEQ contributions at different energies. The estimated results are discussed in the next sections.

5.2 Study of yield and angular distributions

As mentioned in the last section, reaction systems formed from the combination of five beams and seven different targets were chosen for study of neutron yields. But some of the composite systems under study involving ^{107}Ag target or ^{28}Si projectile form highly unstable systems with limited knowledge of the level density. Those systems were not considered for the present work. In Figure 5.1 the angular distribution of the evaporation and PEQ contributions for ^{12}C projectile on ^{65}Cu target at 20 MeV per nucleon projectile energy is shown.

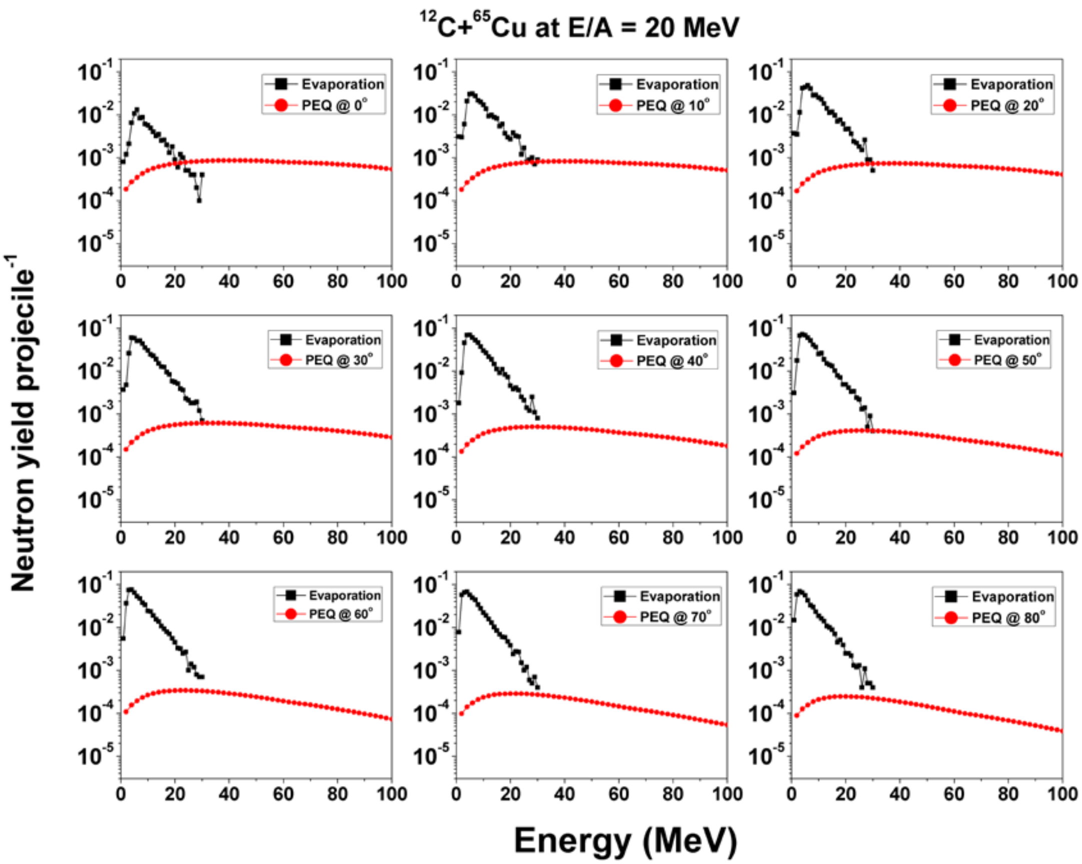

Figure 5.1: A typical evaporation to PEQ neutron yield distribution pattern for (^{12}C + ^{65}Cu) at 20 MeV per nucleon projectile energy

The figure depicts the evaporation and PEQ neutron energy spectra at different emission angles, calculated using the PACE and HION codes respectively. For evaporation calculations, a significant particle yield is found till 30 MeV of emission energy. At energies beyond this point the yield reduces drastically incorporating large estimated uncertainties. To overcome the issue for all sets of estimation, the evaporation data are trimmed beyond 30 MeV. For the PEQ contribution, the lower energy component is small, it reaches a maximum and then the yield gradually reduces over a long range of energies. The maximum of the PEQ yield is dependent on the emission angle and at angles closer to the beam direction appears to have a large energy component compared to corresponding backward angle spectra.

The total multiplicity distributions for both the processes for available set of composite systems with variation in energy are shown in the following figures.

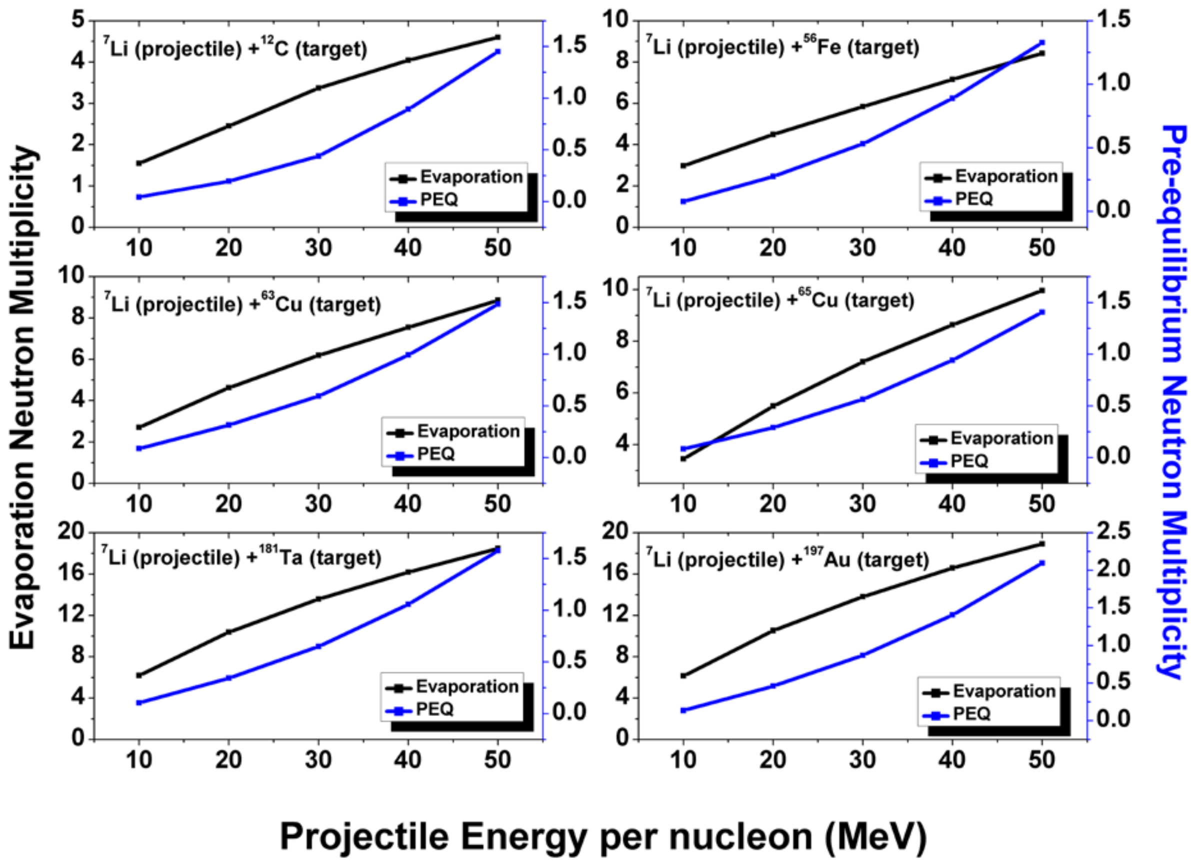

Figure 5.2: Evaporation and PEQ neutron multiplicities with ^{7}Li beam at different targets.

All results are calculated considering a thin target scenario and the emission multiplicities are calculated considering the total 4π geometry. The figures are represented in a double Y-axis format. The left y-axis indicates the evaporation multiplicities marked in back and the corresponding PEQ contributions are shown in blue in the right y-axis. The set of composite systems, not calculated due to lack of availability of input data regarding the density of states or separation energies include the ^{28}Si beam on all three high Z targets (^{107}Ag, ^{181}Ta and ^{197}Au). The rest of the systems are the yields from ^{107}Ag target with all beam particles, except ^{16}O. The plot of the neutron multiplicities using a beam with all available target elements at all five projectile energies are shown in figure 5.2 to 5.6.

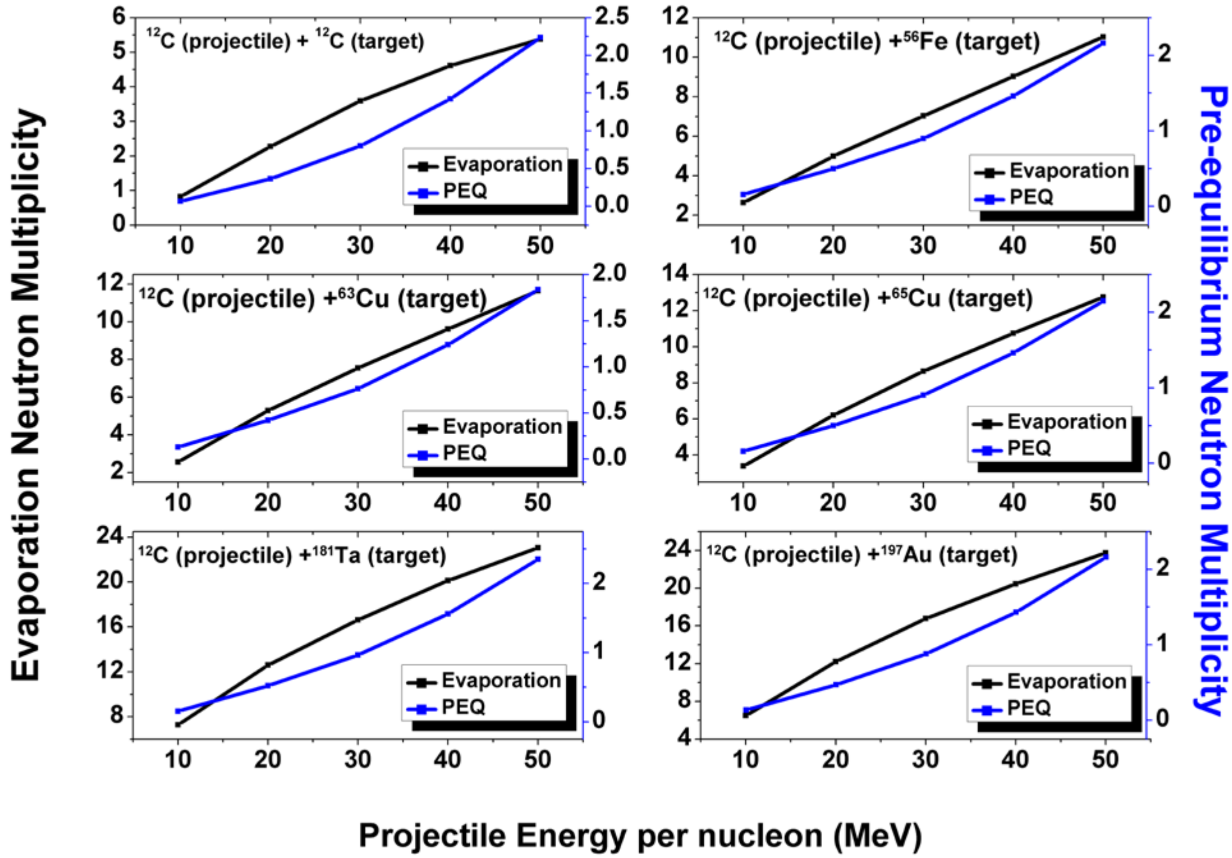

Figure 5.3: Evaporation and PEQ neutron multiplicities with ^{12}C beam at different targets.

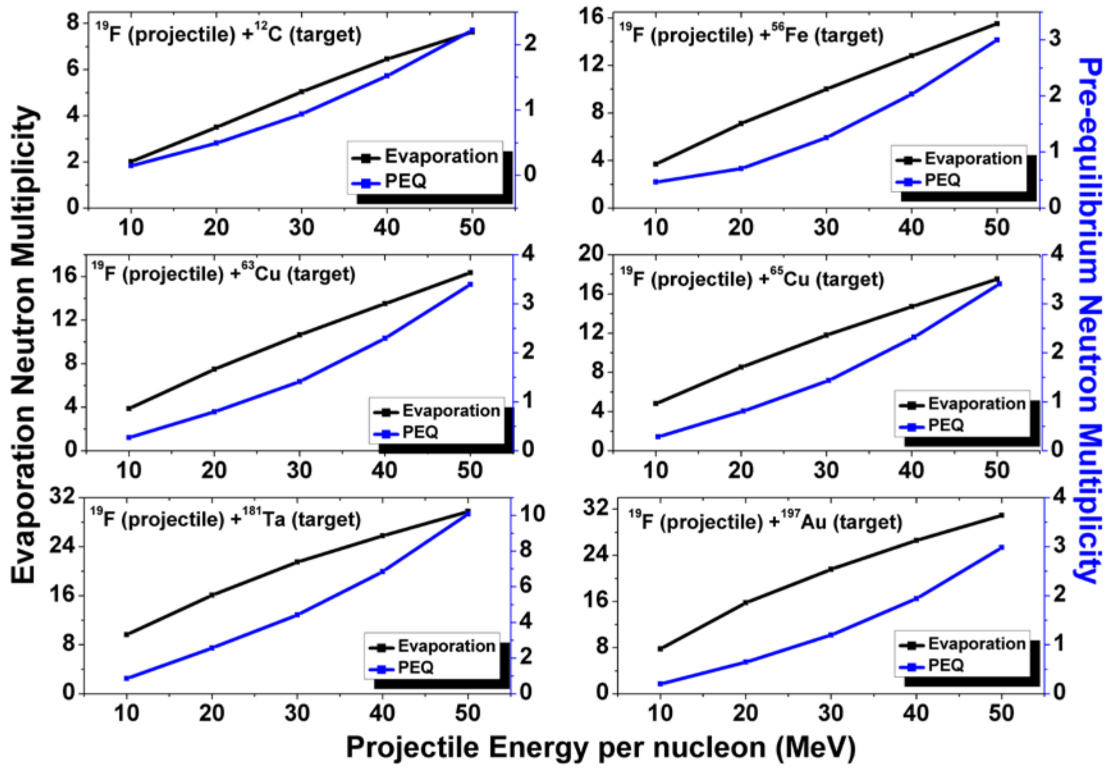

Figure 5.4: Evaporation and PEQ neutron multiplicities with ^{19}F beam at different targets.

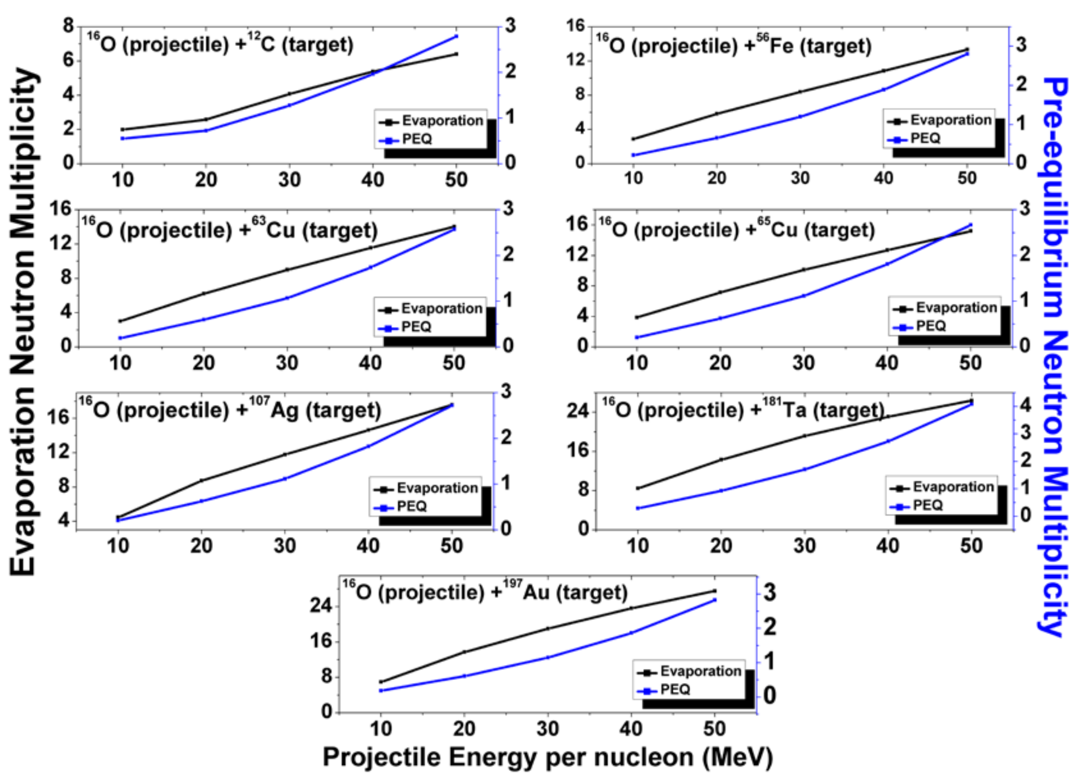

Figure 5.5: Evaporation and PEQ neutron multiplicities with ^{16}O beam at different targets.

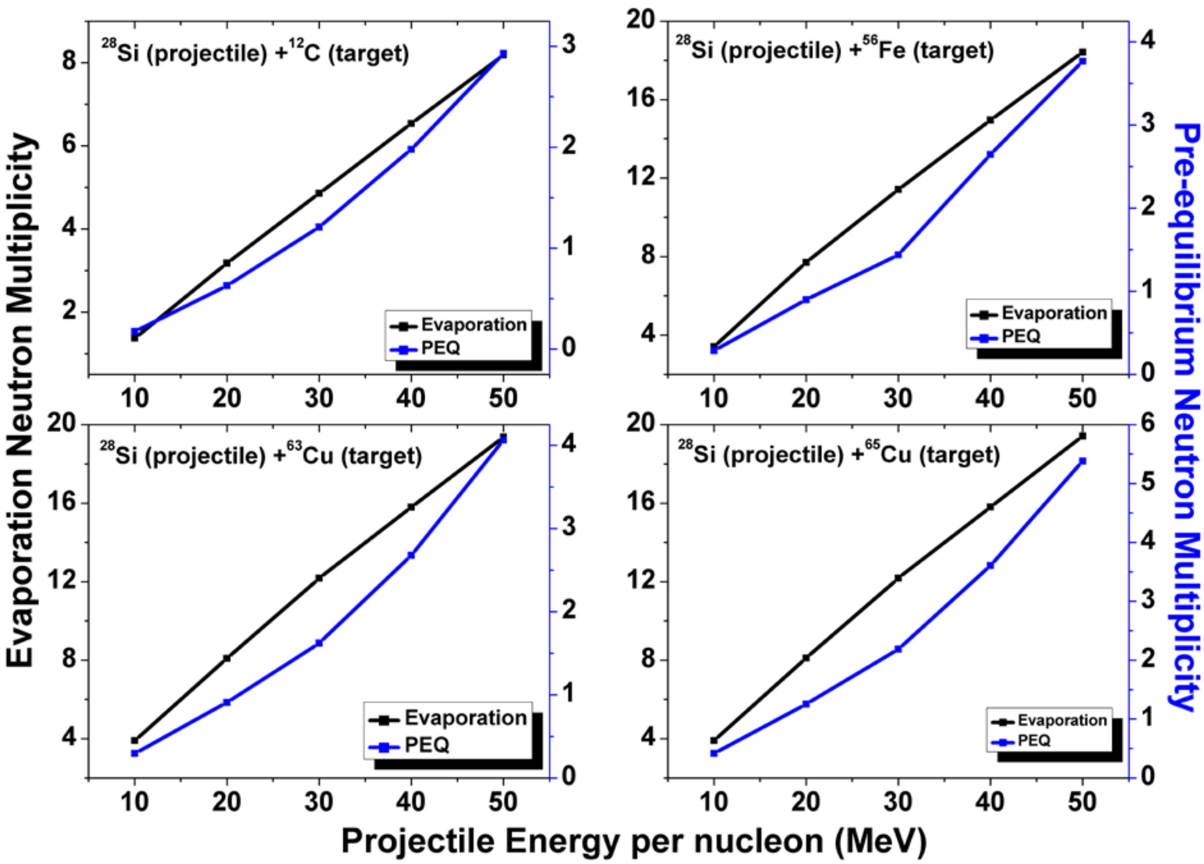

Figure 5.6: Evaporation and PEQ neutron multiplicities with ^{28}Si beam at different targets.

In all the figures, it's evident that both the evaporation and the PEQ multiplicity values increases with increase in the beam energies, but the slope of the curves are different. The effective sharing of the evaporation to PEQ multiplicity fractions vary between 3-40% depending upon the energy and the composite system mass and density of states available at the effective excitations. The yield percentages with different beam target combinations are shown in the figure 5.7 to 5.11.

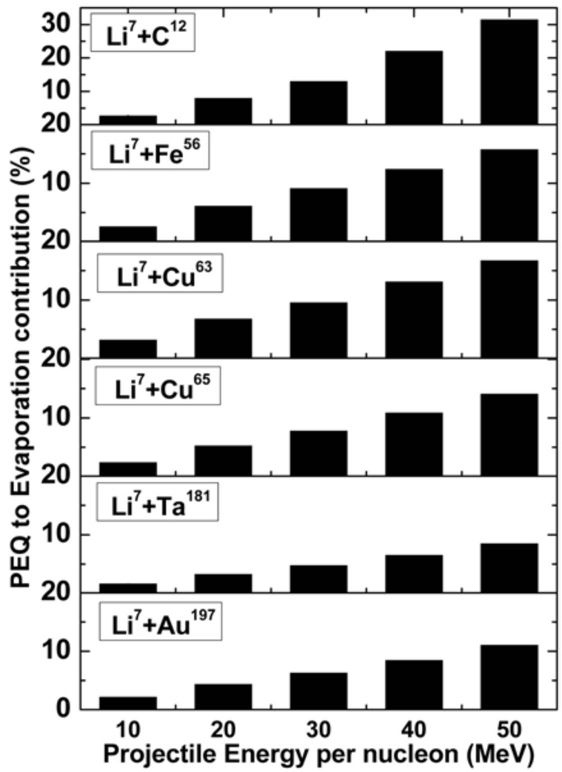

Figure 5.7: Yield percentages from PEQ to Evaporation with ^{7}Li beam at different targets.

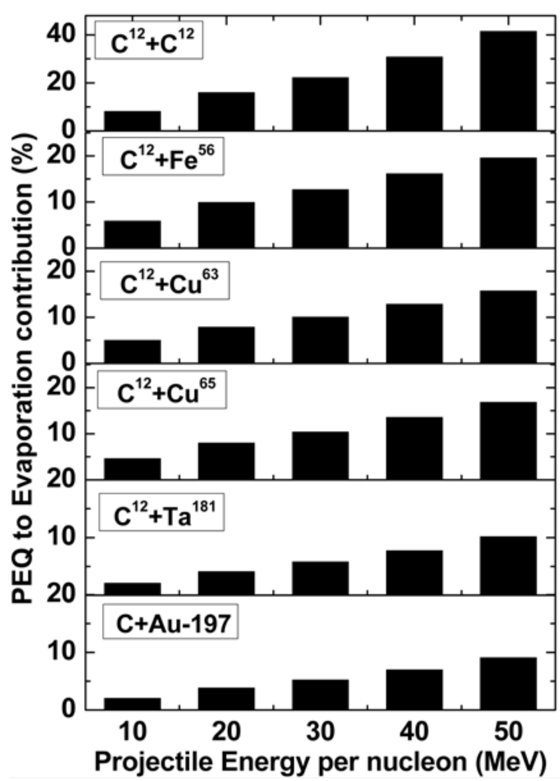

Figure 5.8: Yield percentages from PEQ to Evaporation with ^{12}C beam at different targets.

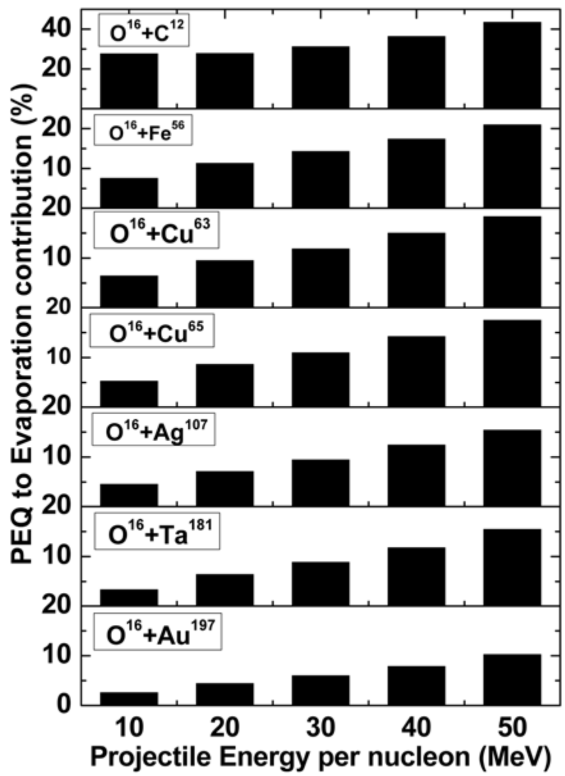

Figure 5.9: Yield percentages from PEQ to Evaporation with ^{16}O beam at different targets.

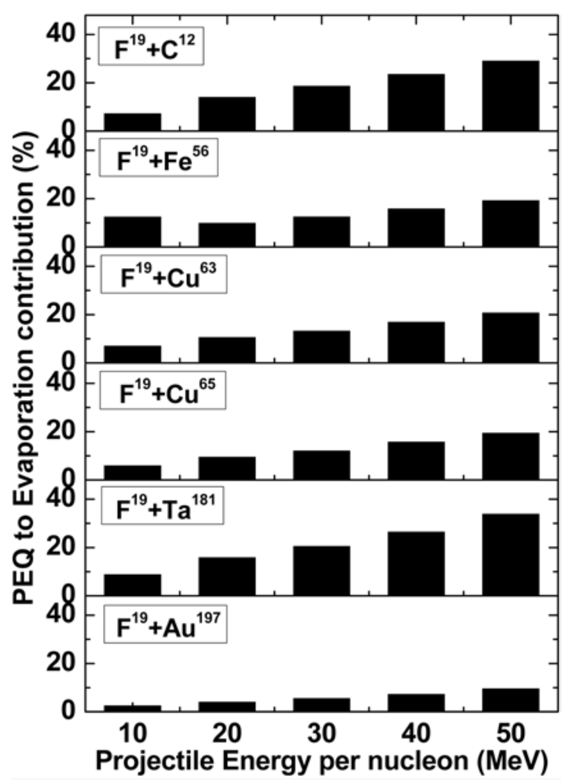

Figure 5.10: Yield percentages from PEQ to Evaporation with ^{19}F beam at different targets.

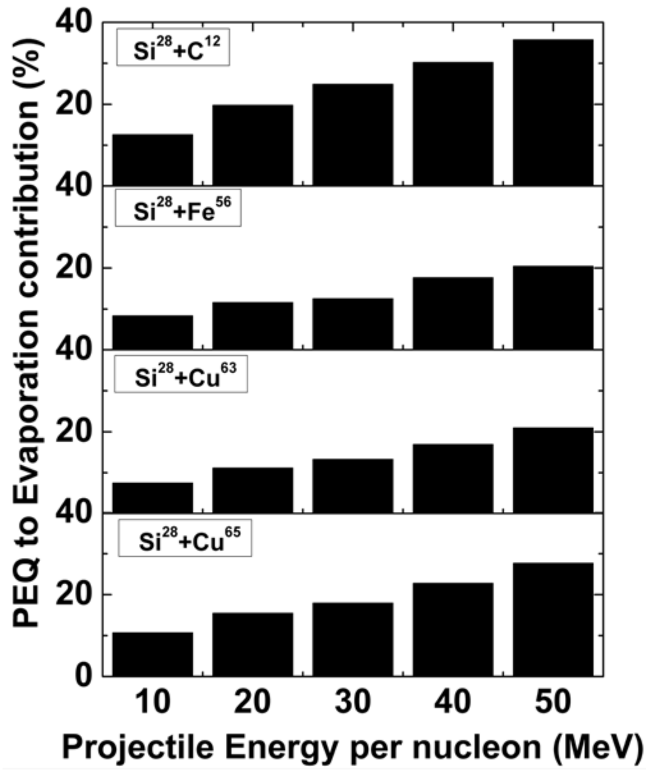

Figure 5.11: Yield percentages from PEQ to Evaporation with ^{28}Si beam at different targets.

The maximum contribution of the PEQ multiplicities was found for cases where the low mass projectiles are bombarded on a low mass target atom. In the case of ^{12}C target, almost all low mass projectile beams showed a large contribution from the PEQ and the contributions are found to be as high as more than 40% for 50 MeV per nucleon (^{12}C projectile). The contribution reduces to 15-20 % at 50 MeV per nucleon energy for the rest of the projectile beams. This is attributed to a lower emission probability due to high collision rates and lower excitation energy per particle for the higher number of nucleons in a heavy target. This PEQ contribution remains unaccounted for in the evaporation codes and in the case of results obtained from conventional NDE meter leading to a large underestimation of the total doses. It would be helpful to find out an empirical relation to give a conservative estimate of these PEQ contributions. With an approach to estimate this yield, an empirical relation has been proposed and compared with the HION estimates in the next section.

5.3 Empirical relation for Pre-equilibrium neutron yield

In this section, a simplified empirical relation to reproduce the integral yield of PEQ neutrons from most of the target-projectile systems mentioned earlier has been proposed. The relation is developed by fitting the PEQ yield distribution obtained from HION code. HION results are obtained using both single and multiple PEQ formalisms. For projectile energy of 10 MeV per nucleon, only single PEQ emission has been considered and for energies of 20 – 50 MeV per nucleon, both simultaneous and sequential MPEQ are used. The empirical relation is based on the simplified geometrical consideration and the neutron excess in the composite system. This empirical relation calculates the total yield of neutrons in the projectile energy range of 10 - 50 MeV/nucleon in complete 4π geometry. The simplified relation can be presented as;

$$Yield_{Sim} = \begin{cases} \frac{5\times10^{-3}}{A_C^2}\left(\frac{E_P}{A_P}\right)^2 \left[A_P^{1/3} + A_T^{1/3}\right]^2 N_P(N_T - Z_T) & for \quad n_T > z_T \\ \\ \frac{5\times10^{-3}}{A_C^2}\left(\frac{E_P}{A_P}\right)^2 \left[A_P^{1/3} + A_T^{1/3}\right]^2 N_P & for \quad n_T = z_T \end{cases} \tag{5.1}$$

where the subscripts P,T and C denote the projectile, target and composite systems respectively. The incoming projectile energy is designated as E_P and the ratio $\left(\frac{E_P}{A_P}\right)$ is the projectile kinetic energy in MeV-amu^{-1}. This formula describes data generally within factors of two for ions from Li to Si incident ions interacting with the thin targets ranging from C to Au over the specific energy domain 10 to 50 MeV amu^{-1}. The results obtained using this formalism have been compared with the HION estimated neutron multiplicities. The comparison is shown in figures 5.12 to 5.16 for all five projectiles with different target elements.

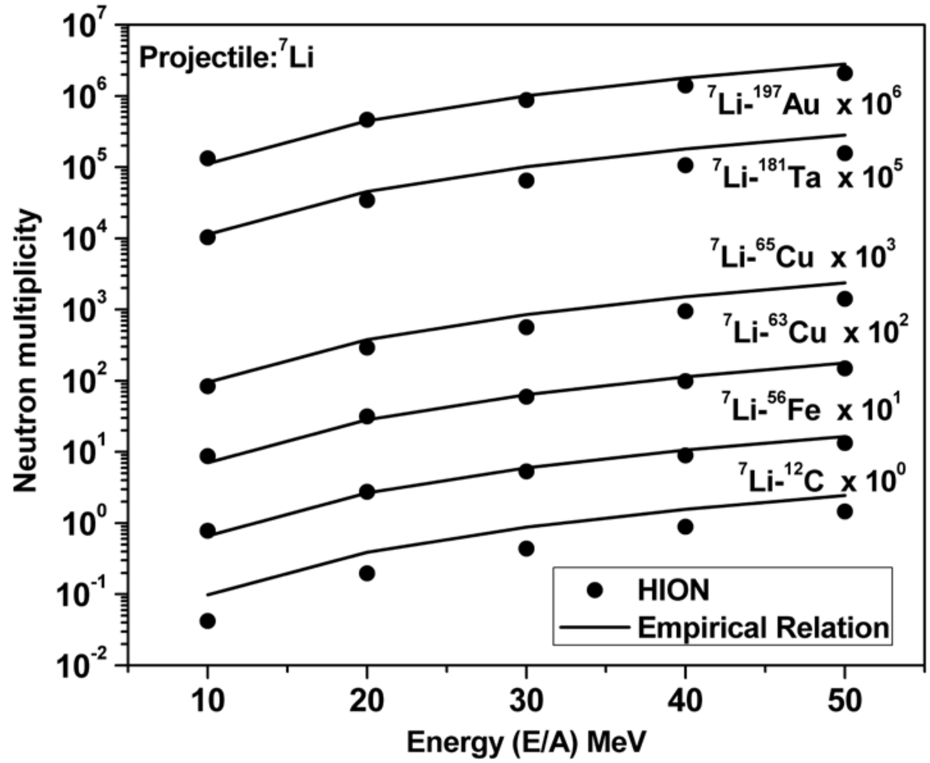

Figure 5.12: Comparison of integral yield from HION with empirical relation for ^{7}Li beam.

The closed circles represent the HION estimates at different projectile energies and the solid lines represent the simplified empirical relation estimates. In the case of ^{7}Li projectiles, the neutron yield for carbon target is overestimated (compared to HION results) at lower projectile energies, whereas for all other targets, the relation has reproduced the HION estimated yield within a factor of 2. Estimated yield for ^{12}C projectile also shows a small overestimation compared to the HION estimates at 10 MeV per nucleon for ^{12}C target. A small overestimation has also reported at ~50 MeV/nucleon for high Z targets but the estimates are within a factor of 2 and mostly conservative in nature.

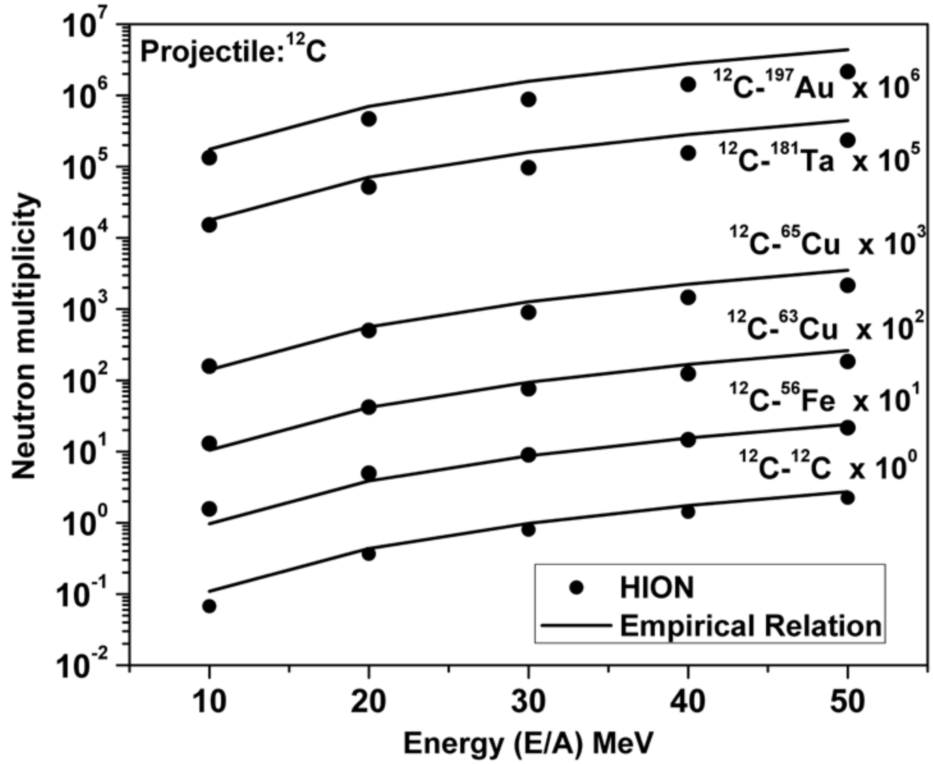

Figure 5.13: Comparison of integral yield from HION with empirical relation for ^{12}C beam.

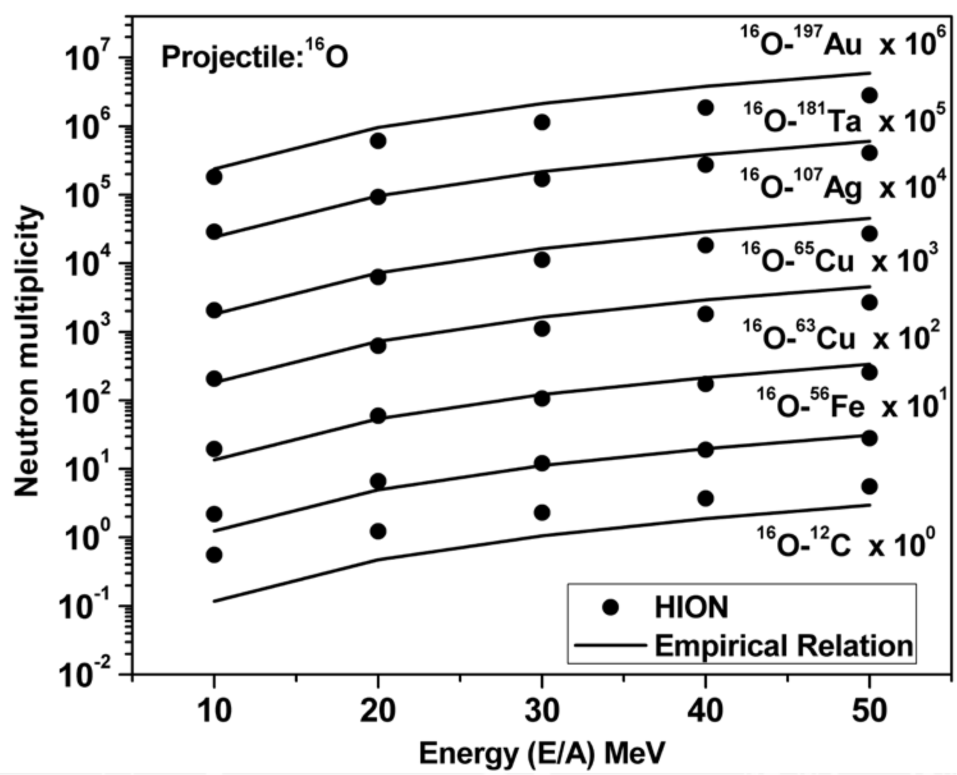

Figure 5.14: Comparison of integral yield from HION with empirical relation for ^{16}O beam.

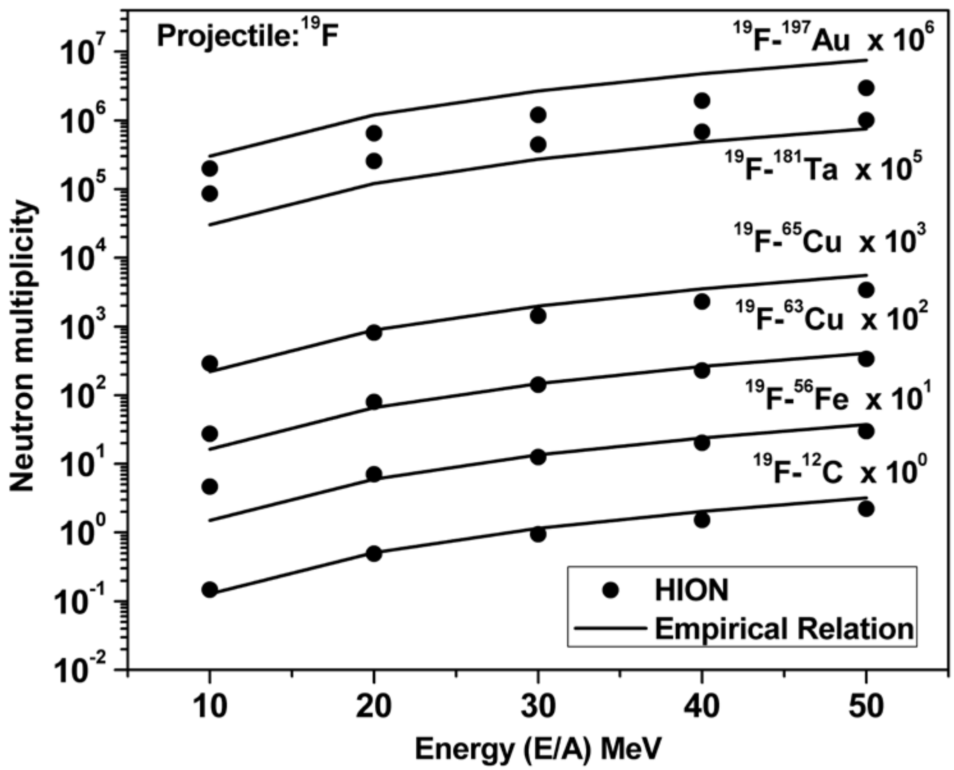

Figure 5.15: Comparison of integral yield from HION with empirical relation for ^{19}F beam.

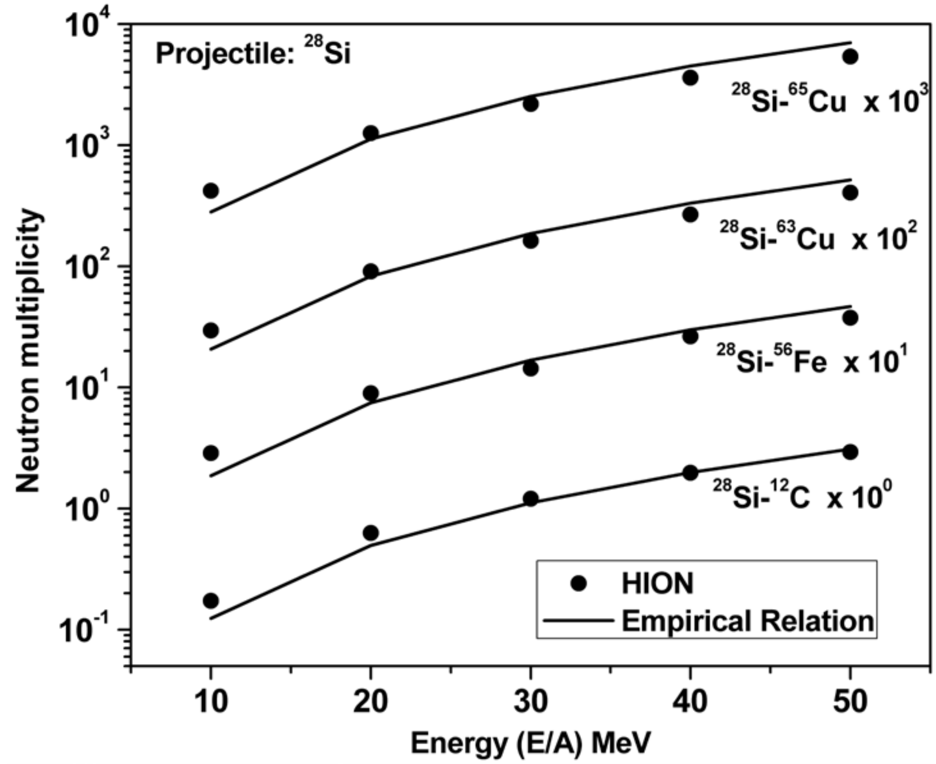

Figure 5.16: Comparison of integral yield from HION with empirical relation for ^{28}Si beam.

For most of the reaction systems considered the empirical relation has reproduced the HION data fairly well. In the case of ^{19}F beam induced reaction on heavy mass targets and for ^{16}O beam on ^{12}C target the agreement is not very good.

These empirical relation estimates can be highly beneficial for the estimation of the shielding calculations around heavy ion accelerator in this energy range. In the next section the variation in the estimated doses beyond 20 MeV of emission neutron energies is estimated.

5.4 Estimation of dose from neutron beyond 20 MeV

The study of different target projectile combinations at intermediate energies have shown an increase in the total neutron multiplicities as discussed in the earlier sections. Presently, based on the ICRP-74 DCC values, an effort has been made to estimate the doses from the high energy neutrons for these target-projectile combinations. In this part of the calculation, the effective doses are calculated based on the thick target assumption, considering the thickness of the target to be sufficient to stop the projectile beam. In this process, the thick yield has been calculated based on the formalism described in section 2.6. These estimates are calculated beyond neutron emission energies of 20 MeV, assuming these neutrons will not be accounted properly with a conventional NDE meter. So the overall variation in the dose estimates from the higher energy neutrons calculated using the HION code can be added to the NDE meter reading for a better estimate of the equivalent doses. The result for different projectile-target combinations are presented in Table 5.1 and 5.2.

Table 5.1: Evaporation and PEQ estimated doses for ^{7}Li, ^{12}C and ^{19}F projectiles

Projectile	Target	Energy (E/A)	Evaporation ($pSv.ion^{-1}$)	PEQ ($pSv.ion^{-1}$)	Target	Evaporation ($pSv.ion^{-1}$)	PEQ ($pSv.ion^{-1}$)
^{7}Li	^{12}C	10	1.37218	0.04168	^{56}Fe	2.23993	0.06598
		20	2.21837	0.18004		3.45558	0.19829
		30	2.97203	0.37198		4.58575	0.34603
		40	3.43685	0.70124		5.67747	0.54111
		50	3.65495	1.04908		6.72902	0.76752
	^{63}Cu	10	1.7898	0.06129	^{65}Cu	2.36534	0.06498
		20	3.82884	0.18814		3.85142	0.19165
		30	5.62091	0.31964		5.14004	0.33583
		40	7.22541	0.50074		6.25683	0.52598
		50	8.69538	0.71273		7.26605	0.74743
	^{181}Ta	10	2.14207	0.04126	^{197}Au	2.14207	0.0487
		20	3.62822	0.11823		3.62822	0.14367
		30	4.70513	0.20006		4.70513	0.24673
		40	5.61557	0.30507		5.61557	0.37514
		50	6.4384	0.43247		6.4384	0.5328
^{12}C	^{12}C	10	0.33519	0.01329	^{56}Fe	0.55983	0.0147
		20	0.92874	0.06499		1.09414	0.04216
		30	1.38297	0.1257		1.56991	0.07083
		40	1.61137	0.20603		2.02509	0.11084
		50	1.67188	0.30686		2.46836	0.15733
	^{63}Cu	10	0.79339	0.02014	^{65}Cu	0.51989	0.01222
		20	1.49528	0.05862		1.10624	0.03559
		30	2.12118	0.09876		1.60957	0.06027
		40	2.65341	0.1538		2.06808	0.09428
		50	3.15899	0.2171		2.50602	0.13364
	^{181}Ta	10	0.74808	0.00712	^{197}Au	0.35236	0.008
		20	1.26793	0.02159		0.61869	0.02477
		30	1.64601	0.03802		0.83012	0.04385
		40	2.02107	0.05854		0.99784	0.06788
		50	2.27567	0.08279		1.16927	0.09816
^{19}F	^{12}C	10	1.02	0.09873	^{56}Fe	0.54497	0.06364
		20	1.6864	0.14727		1.0796	0.07444
		30	2.13257	0.2544		1.52933	0.12473
		40	2.32392	0.39057		1.93882	0.19453
		50	2.34079	0.54474		2.29268	0.27458
	^{63}Cu	10	0.36	0.01568	^{65}Cu	0.3924	0.01786
		20	0.71442	0.04452		0.71346	0.04994
		30	1.02661	0.07651		0.99763	0.08348
		40	1.29715	0.11943		1.23716	0.12975
		50	1.54329	0.16911		1.44951	0.18267

^{19}F	^{181}Ta	10	0.36823	0.00427	^{197}Au	0.16782	0.00372
		20	0.58578	0.01224		0.32617	0.01121
		30	0.75596	0.01983		0.45425	0.01926
		40	0.89167	0.02965		0.5642	0.02967
		50	1.02263	0.04191		0.65912	0.04361

Table 5.2: Evaporation and PEQ estimated doses for ^{16}O and ^{28}Si projectiles

Projectile	Target	Energy (E/A)	Evaporation ($pSv.ion^{-1}$)	PEQ ($pSv.ion^{-1}$)	Target	Evaporation ($pSv.ion^{-1}$)	PEQ ($pSv.ion^{-1}$)
^{16}O	^{12}C	10	0.36577	0.01291	^{56}Fe	0.44052	0.00974
		20	0.84208	0.05067		0.92135	0.02769
		30	1.19488	0.08525		1.3422	0.04859
		40	1.38289	0.13067		1.72814	0.07304
		50	1.40971	0.18711		2.10355	0.10344
	^{63}Cu	10	0.4779	0.01128	^{65}Cu	0.66396	0.01683
		20	1.02236	0.03239		1.27083	0.04919
		30	1.50086	0.05514		1.82107	0.08286
		40	1.92929	0.08634		2.28857	0.12937
		50	2.32179	0.1223		2.72156	0.18275
	^{107}Ag	10	0.53682	0.0169	^{181}Ta	0.42264	0.0036
		20	1.07622	0.04967		0.68685	0.01075
		30	1.47777	0.08377		0.90218	0.01884
		40	1.866	0.13178		1.06991	0.02874
		50	2.23765	0.18791		1.2057	0.04115
	^{197}Au	10	0.14558	0.004			
		20	0.2884	0.00616			
		30	0.40182	0.01093			
		40	0.50305	0.01689			
		50	0.57572	0.02444			
^{28}Si	^{12}C	10	0.3732	0.01198	^{56}Fe	0.44	0.01326
		20	0.80742	0.03749		1.01849	0.0262
		30	1.02346	0.06633		1.49418	0.04047
		40	1.10086	0.10325		1.89135	0.06985
		50	1.11892	0.14635		2.22531	0.05909
	^{63}Cu	10	0.45	0.00997	^{65}Cu	0.49	0.01299
		20	0.95766	0.02927		1.04733	0.03757
		30	1.43099	0.04963		1.56207	0.0629
		40	1.80781	0.07835		1.96987	0.09927
		50	2.13523	0.11378		2.33517	0.14089

The first table represents both evaporation and PEQ doses over the complete 4π geometry for ^{7}Li, ^{12}C and ^{19}F projectiles on available target and the table 5.2 for ^{16}O and ^{28}Si projectiles.

Estimated values clearly shows that for low Z projectile interaction with Low Z targets at higher energy has contributed up to 30% additional dose from PEQ process for (Li+C) composite system. In case of high Z target elements, the doses are found to vary between 3-20% for energies between 10 to 50 MeV per nucleon. All the doses are calculated based on the total thick target neutron yield values at complete 4π geometry.

5.5 PEQ estimates at higher projectile energies

The high energy PEQ estimates at higher projectile energies up to 50 MeV per nucleon has been studied in the present work. In this section, an extension in the higher projectile energy of 100 MeV per nucleon has been tested. In the present work, the estimated HION estimated high energy neutron component is compared with an experimentally measured emission from ^{12}C projectile beam bombarded on a stopping natural C target (98.93% ^{12}C and 1.07% ^{13}C) [174]. The experimental yield variations at different angles were compared with the HION code including both Simultaneous and sequential multiple PEQ processes with single particle emission probabilities. The resulting lower energy neutron components are estimated using the PACE4 code and the comparison with the experimental observations are shown in figure 5.17. The experimental data (black dots) [175] has been scaled with a factor of 10 for the extreme forward angle with respect to the beam direction, considering a very large contribution from the high energy neutrons in the range of 80-200 MeV of emission neutron energies. For rest of the angles, the data is presented in the measured form. The comparison with the evaporation estimates clearly shows that the emission estimates largely underestimates the experimental yield even at energies less than 10 MeV. At larger emission energies, the extent of underestimation increases up to a factor of 10 for all emission angles. The higher energy neutron multiplicities were then estimated using the HION code with single and multiple (simultaneous and sequential) pre-equilibrium formalisms to estimate the high energy neutron yields, as shown in figure 5.18.

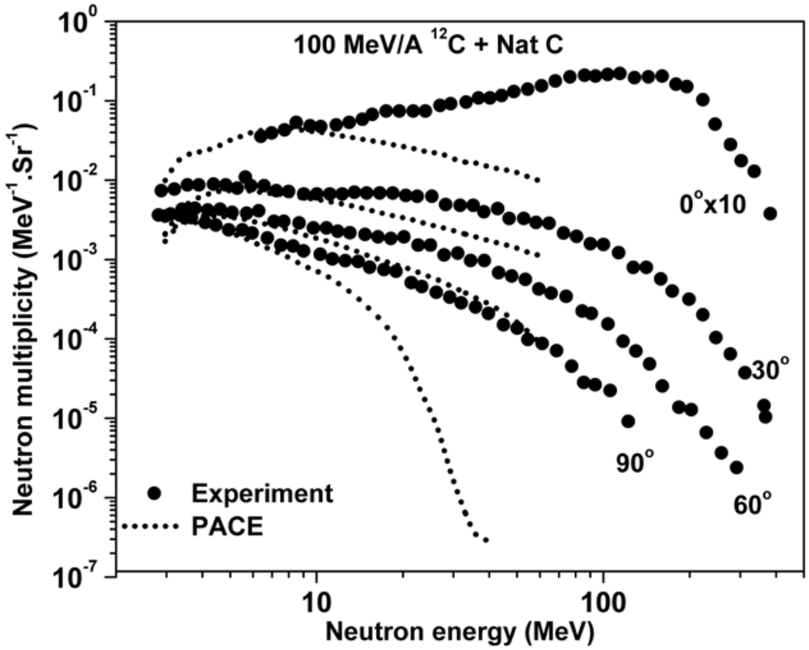

Figure 5.17: Experimental yield vs. evaporation estimates for ^{12}C beam on a thick C target.

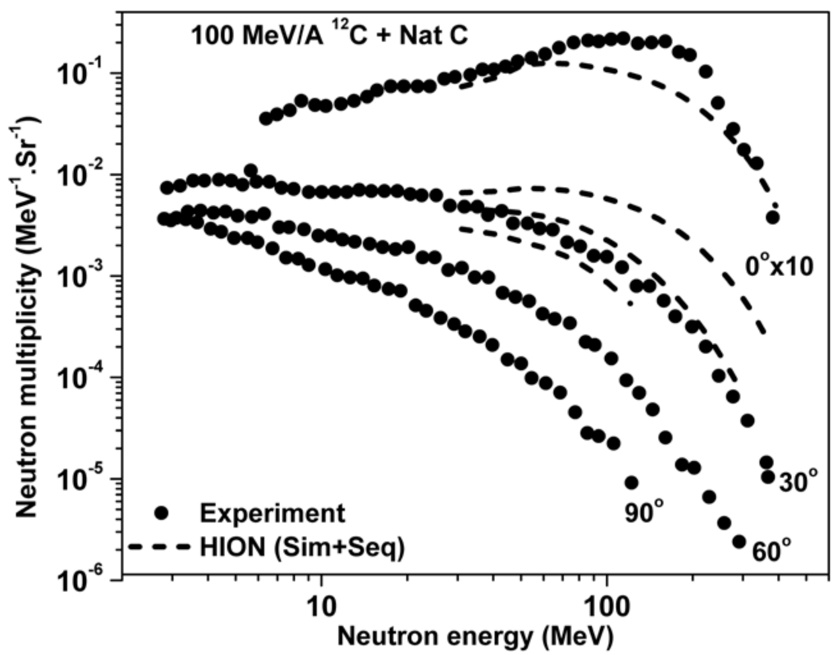

Figure 5.18: Experimental yield vs. PEQ from HION (simultaneous + sequential) estimate for ^{12}C beam on a thick C target.

The figure clearly shows a relatively good match at the forward angle neutron spectra with HION estimates and for the rest of the angles, the yields are found to be significantly higher than the corresponding experimental observations. At forward direction the PEQ formalism reproduces the neutron yields up to 70 MeV emission energies. The underestimations in the range of 80-200 MeV of emission neutron energies at extreme forward angle measurement may be attributed to a significant contribution from the direct reaction processes taking over at very large projectile energy of 1200 MeV. Secondly, large over-predictions at other angles indicate a partial contribution from the multiple PEQ at backward angles. The overestimations were tried to standardize at 100 MeV of emission energy to check the emission pattern from the HION codes for 30° to 90° angles. The variation in the standardized emission pattern with the experimental observations are shown in figure 5.19.

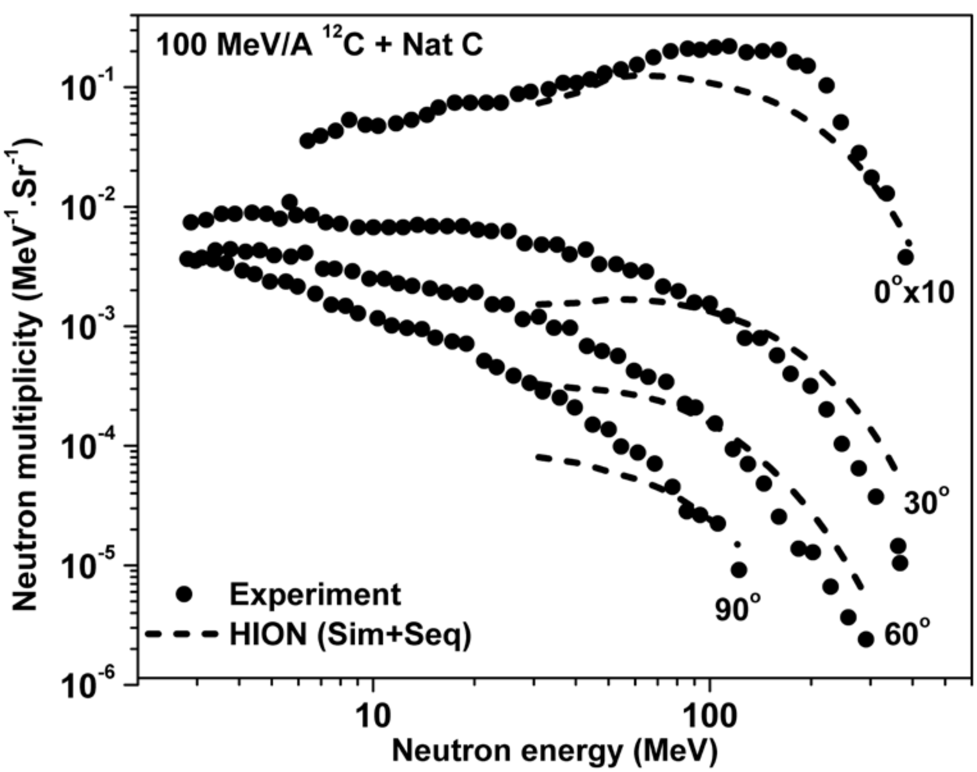

Figure 5.19: Experimental yield vs. PEQ from HION (Simultaneous + Sequential) normalized at 100 MeV for 30°,60° and 90°.

The figures indicates that the pattern of the neutron emissions from HION estimates at larger energies matches well with the experimental observations. The variations from the multiple PEQ needs further correction based on the angular distributions and upon standardization, it has been found that 27%, 6.9% and 2.6% MPEQ contributions have reproduced the experimental data effectively with HION code. So further study involving the contributions of direct reaction components and the effective fraction leading to the multiple particle emissions at wider angles or the effective angular distribution of the multiple PEQ process needs to revisited for estimating the higher energy emission beyond 50 MeV per nucleon projectile energies.

Chapter 6
Conclusions and Future Scope

6.1 Summary

The present dissertation focuses on the estimation of high energy neutrons from heavy ion nuclear reactions using the pre-equilibrium model. Emissions at intermediate energies of few tens of MeV per nucleon are very important considering the possibility of emissions from equilibrated as well as non-equilibrated systems. In this work, an improved version of the pre-equilibrium model HION has been proposed with a set of modifications to estimate neutrons with emission energies higher than 20 MeV. HION model uses a series of two body scattering interactions and associated kernels to estimate the energy angle distribution of pre-equilibrium neutrons. The emission of neutrons from the composite system with excitation energies of few MeV to few tens of MeV and different target-projectile masses were investigated. This model helps us to understand the significance of PEQ mechanism in heavy ion reactions and can serve as an estimator for high energy neutron emission for intermediate particle beam energies for most of the target elements beyond the evaporation limits. This study is important for various academic and material science studies for understanding of reaction mechanism, material characterization and shielding designs in radiation facilities. This study will provide a strong support for estimation of the equivalent doses from neutrons above 20 MeV energy to ensure proper radiological protection for upcoming intermediate energy particle accelerators. The code will also help in minimizing the doses from shielding compositions based on the prior estimation of neutron yields and induced activity from the structural and construction materials. The experimental validation of the code in estimating the yield of pre-equilibrium neutrons from heavy ion reactions in the projectile energy range of less than ten MeV per nucleon extends its applicability manifold in the area of radiation protections. The limitations of conventional neutron dose equivalent meters in estimation of the equivalent doses beyond 20 MeV, can also be supplemented with the neutron spectra calculated from this model. With a proper accounting of the ICRP-74 dose conversion coefficients, for various target-projectile combinations, it has been shown both experimentally and theoretically that an underestimation up to 40% with respect to the conventional NDE meters can be corrected based on the model code calculations. This will provide a reliable estimate of the pre-equilibrium neutron contributions from heavy ion nuclear reactions and ensure proper radiation protection practices at low to intermediate energy heavy ion accelerators facilities.

6.2 Conclusions

The present work serves the need of a nuclear reaction model code capable of estimating the neutron yields at intermediate projectile energies using a pre-equilibrium model framework. A number of nuclear reaction codes available for heavy ion reactions in the lower projectile energies till 8 MeV per nucleon and for energies beyond ~100 MeV per nucleon but there is a lack of efficient reaction model in the intermediate energies. So this work complements both the upper limit of the lower energy regime and the lower limit of the high energy range by serving in the range of few MeV to few tens of MeV.

To estimate the higher energy emission neutrons from a heavy ion nuclear reaction, the modified version of the PEQ nuclear reaction model HION is used. The primary interaction phenomena are based on the two body scattering kinematics and the emission probabilities are calculated using the exciton model framework. The major improvements to estimate the neutron emission probabilities from excited nuclear system include the modifications in the collision rates within the nuclei based on the spatial nucleon density distributions. The second modification is the consideration of the rotational energy at large values of rotational quantum numbers (ℓ) (which effectively provides an off centre rotational motion of the composite nuclei) in calculating the nuclear excitations. The calculations showed that the effect of the second factor is less than 2-3% at large ℓ values. Collision rates calculated from spatial density distribution provides a better estimate compared to that obtained from the empirical formalism [85] based on excitation energy the fused system and binding energy of the nucleons. In the present work, the nucleon density distributions are calculated using two formalisms, semiphenomenological and relativistic mean field approach. Both showed significant differences in the density distribution patterns of the composite system. Although final emission probabilities in case of single PEQ emission formalism showed a variation of only 3-5%, but at higher projectile energies the emission probabilities differed significantly compared to the older formalism. At neutron emission energies beyond 15 MeV per nucleon, HION model with a single particle PEQ emission failed to predict the neutron multiplicities at the forward angles and underestimated the experimental findings.

In order to account for the underestimations multi-particle PEQ emissions from the composite system is further proposed in this work. Two basic formalisms for the multiple PEQ emissions are considered: i) simultaneous multiple pre-equilibrium emission where both the particles are ejected out of the composite system simultaneously from a single exciton hierarchy and ii) sequential PEQ emission where the second PEQ neutron is emitted from the residual system after one neutron PEQ emission from the composite nucleus. In the latter process, emission from the second stage is strongly dependent on the effective excitation energy retained by the residual system after emission from the first stage. Calculations showed that at higher projectile energies, the emissions from the sequential process are higher compared to the simultaneous multiple PEQ. This modification reproduced the forward angle neutron yields significantly well, above energies of 15 MeV per nucleon for heavy ion interactions.

An experimental validation of the model has also been carried out to compare the yield estimations and angular distributions at higher emission energies. $^{16}O^{6+}$ beam at two different energies (120 and 142 MeV) is bombarded on a thick Al target and the yields are measured using the ToF technique with proton recoil scintillator detectors. Measurements are carried out for neutron emission energies up to 40 MeV. The higher energy neutrons beyond 20 MeV are estimated using the PEQ model. Comparison with the experimental data showed a good agreement with the measured neutron distribution. This work provides a strong support to estimate doses from neutron energies beyond 20 MeV from low energy heavy ion reactions. In such facilities the equivalent doses measured with a conventional NDE meter are underestimated as the operating range of such meters are between thermal to less than 20 MeV. So this work can complement the measurement of a conventional NDE meter. The doses recorded by folding the ToF yield data with ICRP-74 DCC values are compared with the estimated doses from NDE meter readings for ^{16}O projectile on thick Al target. The results showed an underestimation by the NDE meter readings. Equivalent doses obtained from the HION estimated yields and added to NDE meter readings agree fairly well with the dose estimated from the ToF measurements.

In the present work a theoretical estimate of neutron yield and dose for different target-projectile systems at various incoming energies has been carried out. This work will be helpful in planning the shielding design for facilities with sources of low to intermediate energy neutrons and to estimate the neutron doses from the structural, construction and dump materials in an accelerator. The study with different projectile beams at incident energies between 10 to 50 MeV per nucleon showed that for low Z target-projectile combinations the PEQ doses can be as large as 60% of its evaporation contributions at 50 MeV per nucleon. For targets with higher atomic number, the PEQ contribution varies between 5-20% of the corresponding evaporation estimates.

An empirical relation has also been proposed for estimating the energy integrated yields for the PEQ neutrons. This integral value can serve as the source term for different shielding design calculations at various nuclear facilities.

Future Scope

The modified pre-equilibrium nucleon emission model HION has been developed in the present work with realistic emission probabilities to estimate emission neutron energy spectra and angular distributions from heavy ion nuclear reactions in the intermediate projectile energy ranges. The code has reproduced the emission neutron spectra from different experimental systems for both thin and thick targets. However there are scopes of further improvements by extending the range of applicability of the model by incorporating further additional formalisms like association of the direct reaction kernels at high excitation energies or formalisms to understand the emissions from small clusters with the nuclei. The study of the angular variation in the emission probabilities from the multiple PEQ formalisms at energies beyond 100 MeV per nucleon is also a challenging aspect for further work. Another important improvement can be, the incorporation of a step by step interaction mapping for determining the exact evolution of the reaction process using a Monte Carlo based analysis. This will eliminate the approximations enforced in the spatial density measurements of the nuclei assuming the time independent nature of the fused system. In a real time evaluation, the target-projectile fusing together is a time dependent phenomena and the spatial density distributions also evolve through a continuously progressive time dependent structure. So incorporating this physical feature in the present work will provide a more accurate estimation of the higher energy emission neutrons.

References:

1. M. Blann, Phys. Rev. C 31, 1245 (1985).
2. H. Machner, Phys. Rev. C 28, 2173 (1983).
3. J. Pal, S. Saha, C. C. Dey, P. Banerjee, S. Bose, B. K. Sinha, M. B. Chatterjee, and S. K. Basu, Phys. Rev. C 71, 034605 (2005).
4. A. Iwamoto, Phys. Rev. C 35, 984 (1987).
5. K. Hanold, L. G. Moretto, G. F. Peaslee, G. J. Wozniak, D. R. Bowman, M. F. Mohar and D. J. Morrissey, Phys. Rev. C 48, 723 (1993).
6. L. F. Canto, R. Donangelo, Lia M. de Matos, M. S. Hussein, and P. Lotti, Phys. Rev. C 58, 1107 (1998).
7. S. Wald, I. Tserruya, Z. Fraenkel, G. Doukellis, H. Gemmeke and H. L. Harney, Phys. Rev. C 25, 1118 (1982); 28, 1538(1983).
8. D. P. Singh, Unnati, P. P. Singh, A. Yadav, M. K. Sharma, B.P. Singh, K. S. Golda, R. Kumar, A. K. Sinha, and R. Prasad, Phys. Rev. C 80, 014601 (2009)
9. C. Wernli, H. Hoedlmoser, M. Boschung, E. Hohmann, S. Mayer, Indian Journal of Pure and Applied Physics 50 (2012) 757.
10. S. Agosteo, Radiation Measurements 45 (10) (2010) 1171.
11. P.K. Sarkar, Radiation Measurements 45 (2010) 1476.
12. ICRP, 1996. Conversion Coefficients for use in Radiological Protection against External Radiation. ICRP Publication 74. Ann. ICRP 26 (3-4).
13. ICRP. Recommendations of the International Commission on Radiological Protection. Report of Committee II on Permissible Dose for Internal Radiation. ICRP Publication 2. Pergamon Press, Oxford (1959).

14. ICRP/ICRU. Report of the RBE Committee of the International Commissions on Radiological Protection and on Radiation Units and Measurements. Health Phys. 9 357 (1963).
15. ICRP. Relative Biological Effectiveness (RBE), Quality Factor (Q), and Radiation Weighting Factor (wR). ICRP Publication 92. Ann of the ICRP,33 (4). Elsevier Science Ltd, Oxford (2003a)
16. Dietze, G., Harder, D. Proposal for a Modified Radiation Weighting Factor for Neutrons. Proceedings of the 11th International Congress of IRPA (2004)
17. Dietze, G., Siebert, B.R.L. Photon and Neutron Dose Contributions and Mean Quality Factors in Phantom of Different Size Irradiated by Monoenergetic Neutrons. Radiation Research 140,130-133 (1994)
18. Kellerer, A.M., Leuthold, G., Mares, V., Schraube, H. Options for the modified radiation weighting factor of neutrons. Radiat. Prot. Dosim. 109(3), 181-188 (2004)
19. NCRP. The Relative Biological Effectiveness of Radiations of Different Quality. NCRP Report No. 104 (1990).
20. Sasaki, M. S. Primary damage and fixation of chromosomal DNA as probed by monochromatic soft x rays and low-energy neutrons. In: Fielden, E. M., O ´Neil, P. (Eds.). The Early Effects of Radiation on DNA. NATO ASI Series, Vol. H54. Springer Verlag, Berlin, Germany, 369-384 (1991)
21. M. Nandy, S. Ghosh, and P. K. Sarkar, Phys. Rev. C 60, 044607 (1999).
22. S. Paul, M. Nandy, A. K. Mohanty, Y. K. Gambhir, Phys. Rev. C (2016).
23. R. C. Sharma and S. K. Agarwal, BARC Newsletter, 245 (2004).

24. Operation of Dhruva reactor at rated power of 100 Mw on sustained basis, BARC Newsletter, March April (2016)

25. W.J. Drexel, IEEE Trans. Nucl. Sci. NS-29, 123–126 (1982).

26. C.J. Carlile, Physica B 385–386, 961–965 (2006).

27. Fumio Sakurai, Yoji Horiguchi, Shinsho Kobayashi, and Masaji Takayanagi, Physica B, 311, 7–13 (2002)

28. J. Neuhaus and W. Petry, Neutron News 18:2, 13–15 (2007)

29. Shane J. Kennedy, Physica B 385–386, 949–954 (2006).

30. Chang-Hee Lee, Young-Hwan Kang, and Il-Hiun Kuk, ICANS-XV Proceedings of the 15th Meeting of the International Collaboration on Advanced Neutron Sources, Tsukuba, Japan, 146–154 (2000).

31. D.F. Chen, Y.T. Liu, C. Gou, and C.T. Ye, Physica B 385–386, 966–967 (2006).

32. T.E. Mason, et al., Physica B 385–386, 955–960 (2006).

33. Tony A. Gabriel, John R. Haines, and Thomas J. McManamy, J. Nucl Mater. 318, 1–13.

34. J. W. Martin and Japan-Canada, AIP Conference proceedings 1560, 134 (2013).

35. J. Zhang, Q.W. Yan, C. Zhang, P.L. Zhang, S.N. Fu, F.W. Wang, Z. Zhang, and S.X.Fang, J. Neutron Res. 13:1, 11–14 (2005).

36. Q.W. Yan, W. Yin, and B.L. Yu, J. Nucl. Mater. 343, 45–52 (2005).

37. Amaldi, U. The Importance of Particle Accelerators, Europhysics News 2000 , V31, No. 6 - http://www.europhysicsnews.com/full/06/article1.html

38. Alonso, J. Medical Applications of Accelerators in Handbook of Accelerator Physics and Technology, A. Chao, M. Tigner Eds,World Scientific, 2nd printing, 2002

39. Norton, G., Duggan, J.L. Industrial Applications of Electrostatic Accelerators, ibid

40. Livingston, M.S. and Blewett, J.P. Particle Accelerators, McGraw Hill, 1962

41. Tigner, M. Accelerator Science Needs More Brainpower, CERN Courier, May 2002

42. FERDOR code, radiation shielding Information center, RSIC Computer Code Collection, Oak Ridge National Laboratory, PSR-17 (1972).

43. R. Gold, AEC Research and Development Report ANL-6984, Argonne National Laboratory, Argonne, IL, 1964.

44. F.G. Perey, Least-squares dosimetry unfolding: the program STAY'SL, ORNL/TM-6062, ENDF-254, Oak Ridge, 1977.

45. J.T. Routti, J.V. Sandberg, Computer Physics Communications 21 (1980) 119.

46. Keran O'Brien and R.Sanna Nuclear Instruments and Methods 185 (1981) 277.

47. M. Matzke and K. Weise, "Neutron Spectrum Unfolding using the Monte Carlo Method", Nuclear Instruments and Methods A234 (1985) 324.

48. Itoh, S. and T. Tsunoda, "Neutron Spectrum Unfolding with Maximum Entropy and Maximum Likelihood," J. Nuclear Science and Technology, 26[9], 833(1989).

49. M. Reginatto, P. Goldhagen, EML-595, U.S. Department of Energy 1998.

50. M. Reginatto, Radiation Measurements, 45 (2010) 1323.

51. M.R. Kardan, et.al., Neutron spectra unfolding in Bonner spheres spectrometry using neural networks, Radiation Protection Dosimetry, 104 (2003) 27.

52. B. Mukherjee, Radiation Protection Dosimetry 110 (2004) 249.

53. B. Mukherjee, Nuclear Instruments and Methods in Physics Research A 432 (1999) 305.

54. R. Bedogni, C. Domingo, A. Esposito, F. Fernández, Nuclear Instruments and Methods A 580 (2007) 1301.

55. Yu.A. Kaschuck, B. Esposito, L.A. Trykov, V.P. Semenov, Nuclear Instruments and Methods A 476 (2002) 511
56. Eljen Technologies EJ-301 <http://www.eljentechnology.com/index.php/products/liquid-scintillators/71-ej-301>
57. Saint Gobain BC-501 <http://www.detectors.saint-gobain.com/uploadedFiles/SGdetectors/Documents/Product_Data_Sheets/BC501-501A-519-Data-Sheet.pdf>.
58. Bertulani C A, Danielewicz P, 'Introduction to Nuclear Reactions', Institute of Physics Publications 2004, ISBN 0 7503 0932 6.
59. V. F. Weisskopf and D. H. Ewing, 'On the Yield of Nuclear Reactions with Heavy Elements', Physical Review 57, 472 (1940).
60. Walter Hauser and Herman Feshbach, 'The Inelastic Scattering of Neutrons', *Physical Review*, 87, 366 (1952).
61. P E Hodgson, Compound nucleus reactions, Rep. Prog. Phys. 50, 1171-1228 (1987)
62. J. Achelin, Phys. Rep. 202, 233 (1991).
63. K. Niita, S. Chiba, T. Maruyama, T. Maruyama, H. Takada, T. Fukahori, Y. Nakahara, and A. Iwamoto, Phys. Rev. C 52, 2620 (1995);
64. K. Niita, T. Maruyama, T. Maruyama, and A.Iwamoto, Prog. Theor. Phys. 98, 87 (1997).
65. J. Cugnon, T. Mizutani, J. Vandermeulen, Nucl.Phys., A352 ,505 (1981)
66. J. Cugnon, Phys.Rev., C22, 1885 (1980).
67. J.D. Stevenson, Phys.Rev.Lett., 41, 1702 (1978)
68. J.P. Bondorf, H.T. Feldmeier, S. Garpman, E.C. Haibert, Z.Phys., 279, 385 (1976)
69. E.C. Halbert, Phys.Rev., C23, 295 (1981)

70. Y. Yariv, Z. Fraenkel, Phys.Rev., C20, 2227 (1979)
71. K.K. Gudima, H. Iew, V.D. Toneev, J.Phys. G5, 229 (1978)
72. H.W. Bertini, R.T. Santoro, O.W. Hermann, Phys.Rev., C14, 590 (1976)
73. H. Kruse, B.V. Jacak, J. J. Molitoris, G. D. Westfall, and H. Stocker, Phys. Rev. C 31, 1770 (1985).
74. G. Bertsch and S. Dasgupta, Phys. Rep. 160, 189 (1989).
75. C. Gregoire, B. Remand, F. Sebille, L. Vinet, and Y. Raffray, Nucl. Phys. A 465, 317 (1987).
76. A. Bonasera, F. Gulminelli, and J. Molitoris, Phys. Rep. 243, 1 (1994).
77. A. Gavron, Phys. Rev. C 21, 230 (1980).
78. O. B. Tarasov and D. Bazin, Nucl. Instrum. Methods B 204, 174 (2003).
79. M. Herman, R. Capote, B.V. Carlson, P. Oblozinsky, M. Sin, A. Trkov, H. Wienke, V. Zerkin, Nuclear Data Sheets 108 (2007) 2655.
80. K. Hanold, L. G. Moretto, G. F. Peaslee, G. J. Wozniak, D. R. Bowman, M. F. Mohar, and D. J. Morrissey, Phys. Rev. C 48, 723 (1993).
81. L. F. Canto, R. Donangelo, Lia M. de Matos, M. S. Hussein, and P. Lotti, Phys. Rev. C 58, 1107 (1998).
82. S. Wald, I. Tserruya, Z. Fraenkel, G. Doukellis, H. Gemmeke and H. L. Harney, Phys. Rev. C 25, 1118 (1982); 28, 1538 (1983).
83. D. P. Singh, Unnati, P. P. Singh, A. Yadav, M. K. Sharma, B.P. Singh, K. S. Golda, R. Kumar, A. K. Sinha, and R. Prasad, Phys. Rev. C 80, 014601 (2009).
84. J. J. Griffin, Phys. Lett. , 248, 5 (1967)
85. M. Blann, Phys. Rev. Lett. 27, 337 (1971); 27, 700(E) (1971); 27, 1550(E) (1971).
86. Gadioli E, Gadioli-Erba E, Sona P G, Nucl. Phys. A, 217, 589 (1973)

87. K.Chen, Z. Fraenkel, G. Friedlander, J. R. Grover, J. M. Miler and Y. Shimamoto, Phys. Rev. 166, 949 (1968).

88. G. D. Harp, J. M. Miller and B. J. Berne, Phys. Rev., 170, 1174 (1968).

89. K. Chen, G. Friendlander, G. D. Harp and J. M. Miller, Phys Rev. C4, 2234 (1971).

90. M. Blann and H. K. Vonach, Phys Rev C,28, 1475 (1983)

91. C. K. Cline and M. Blann, Nuclear Physics A 172 (1971) 225-259.

92. H. Feshbach, A. Kerman and S. Koonin, Ann. Phys. 125, 429 (1980).

93. H. Nishioka, J. J. M. Verbaarschot, H. A. Weidenmuller, and S.Yoshida, Annals of Physics,172, 67-99 (1986).

94. H. Nishioka, H. A. Weidenmuller, and S. Yoshida, Annals of Physics,183, 166-187 (1988).

95. T. Tamura, T. Udagawa, and H. Lenske, Physical Review C, 26, 379-404 (1982).

96. S. Paul, M. Nandy, A. K. Mohanty, Y. K. Gambhir, Phys. Rev. C,94, 034607 (2016).

97. S. Paul , C. Sunil, Sanjoy Pal , V. Nanal , V. Suman, G. S. Sahoo, A. Shanbhag, S. P. Tripathy, T. Bandyopadhyay, M. Nandy, A. K. Mohanty,Phys. Rev. C 96, 044607 (2017).

98. A. De, S.K. Ray, and S. K. Ghosh, Phys. Rev. C 37, 2441 (1988).

99. A. De, T. Shibata, and H. Ejiri, Phys. Rev. C 45, 774 (1992).

100. A. De, S. Ray, and S.K. Ghosh, J. Phys. G 13, 1047 (1987).

101. A. De, S. Ray, and S.K. Ghosh, J. Phys. G 11, L79 (1985).

102. Y. K. Gambhir and S. H. Patil, Z. Phys. A: At. Nucl. 321, 161 (1985).

103. Y. K. Gambhir and S. H. Patil, Z. Phys. A: At. Nucl. 324, 9 (1986).

104. Y. K. Gambhir, P. Ring, and A. Thimet, Ann. Phys. 198, 132 (1990).

105. P. Ring, Prog. Part. Nucl. Phys. 37, 193 (1996).

106. D. Hilscher, H. Rossner, A. Gamp, U. Jahnke, B. Cheynis, B. Chambon, D. Drain, C. Pastor, A. Giorni, C. Morand, A. Dauchy, P. Stassi, and G. Petitt, Phys. Rev. C 36, 208 (1987).

107. E. Holub, D. Hilscher, G. Ingold, U. Jahnke, H. Orf, and H.Rossner, Phys. Rev. C 28, 252 (1983).

108. E. Holub, D. Hilscher, G. Ingold, U. Jahnke, H. Orf, H. Rossner, W. P. Zank,W. U. Schroder, H. Gemmeke, K. Keller, L. Lassen and W. Lucking, Phys. Rev. C 33, 143 (1986).

109. R. Singh, S. N. Mukherjee, Nuclear Reaction, New Age Publishers (1996)

110. N. Bohr, Nature 137, 344 (1936).

111. G. Breit, E. Wigner, Physical Review, 49, 7 (1936).

112. G. D. Harp, J. M. Miller, Phys. Rev. C3, 1847 (1971).

113. G. M. Braga-Marcazan, E. Erba-Gadioli, L. Milazzo and P. G. Sona, Phys. Rev. C, 6 , 1398 (1972)

114. Kalbach C, Z. Phys. A 283 401 (1977)

115. Kalbach C, Phys. Rev. C 24 819 (1981)

116. Kalbach C, Phys. Rev. C 32 1157 (1985)

117. Kalbach C, Phys. Rev. C 33 818 (1986)

118. Kalbach C, Nucl. Sci. Eng. 95 70 (1987)

119. E. Gadioli, E. Gadioli-Erba, P. Guazzoni, P. E. Hadgson, L. Zetta, Z. Phys. A, 318, 147-155 (1984).

120. R. Madler and R. Reif, Nucl. Phys. A, 27, 373 (1982)

121. K. Sato, Phys. Rev. C, 32, 647 (1985)

122. C. Kalbach and F. M. Mann, Phys. Rev. C, 23, 112 (1981)

123. Kalbach C, Phys. Rev. C 23, 124 (1981)

124. Kalbach C, Phys. Rev. C 37, 2350 (1988)

125. Blann M, Annu. Rev. Nucl. Sci., 25, 123 (1985)

126. H. Gruppelaar , P. Nagel, P. E. Hodgson, Rivista. Nuovo. Cim., 9, 1 (1986)

127. F.C. Williams, Nucl. Phys. A166, 231 (1971).

128. M. Blann, Nucl. Phys. A 213 570 (1973)

129. M. Blann, Annu. Rev. Nucl. Sci. 25 123 (1975)

130. K. Kikuchi and M. Kawai, Nuclear Matter and Nuclear Reactions (North-Holland, Amsterdam), Chap. 2 (1968).

131. J. Raynal, Proceedings of Applied nuclear theory and nuclear model calculations for nuclear technology applications,506 (1988).

132. B. Strohmaier and M. Uhl, Nuclear Theory for Applications IAEA-SMR-43, 313 (1980).

133. P.G. Young et al., “Transport data libraries for incident proton and neutron energies to 100 MeV”, Los Alamos report LA-11753-MS (1990).

134. F.M. Mann, HEDGTME-78-83 (1979).

135. H. Gruppelaar, IAEA advisory group meeting on basic and applied problems of nuclear level densities, brookhaven,, BNL-NCS-51694, 143 (1984)

136. C.Y. Fu, Proc. Int. Cod. on Nuclear Cross-Sections for Technology NBS-Sp 594, 757 (1979); Brookhaven Report BNGNCS-51245, Vol 2, 675 (1980).

137. C. K. Walker, Users manual for PRECO-2006: Exciton model pre-equilibrium nuclear reaction coder with direct reactions, Triangle Universities Nuclear Laboratory report (2001)

138. C. Kalbach, Brookhaven Report BNGNCS-51694, 113 (1983).

139. G. Keeni and S. Yoshida, PREM, Science Report, Tohoku University 8/3, 41 (1982).

140. J.M. Akkermans and H. Gruppelaar, Netherlands Energy Research Foundation Report ECN-60 (1979).

141. E. Betak and J. Dobes, Phys. Lett. 84B, 368 (1979); PEQGM, Bratislava Report (1983).

142. M. Blann, W. Scobel and E. Plachaty, Phys. Rev. C30, 1493 (1984).

143. H. Jahn, C. Broeders and 1. Broeders, Proc. Int. Cod. on Nuclear Cross-Sections and Technology NBS-SP-425, 350 (1975).

144. H. Jahn, Critical Review of Pre-compound Models, KfK 3646 (1984).

145. M. Herman, A. Marcinkowski and K. Stankiewicz, Comp. Phys. Comm. 33, 373 (1984).

146. T.C. Awes, G. Poggi, C.K. Gelbke, B.B. Back, B.G. Glagola, H. Breuer, and V.E. Viola, Phys. Rev. C 24, 89 (1981)

147. T.C. Awes, S. Saini, G. Poggi, C.K. Gelbke, D. Cha, R. Legrain and G.D. Westfall, Phys. Rev. C 25, 2361 (1982).

148. J.P. Bondrof, J.N. De, A.O.T. Karvinen, and B. Jakobsson, Nucl. Phys. A333, 285 (1980).

149. J. Randrup and R. Vandenbosch, Nucl. Phys. A474, 219 (1987).

150. M. Blann, Phys. Rev. C 35, 1581 (1987).

151. E. Fabrici, E. Gadioli, E. Gadioli Erba, M. Galmarini, F. Fabbri, and G. Reffo, Phys. Rev. C. 40, 2548 (1989).

152. A. Iwamoto, Phys. Rev. C 35, 984 (1987);

153. A. Chatterjee, K.H.N. Murthy, and S.K. Gupta, Pramana 16,391 (1981).

154. S. K. Charagi and S. K. Gupta, Phys. Rev. C 41, 1610 (1990).

155. G. A. Lalazissis, J. K¨onig and P. Ring, Phys. Rev. C 55 540 (1997).

156. <http://www.tifr.res.in/~pell/> last accessed on 23.08.2017

157. R. Bass, Nucl. Phys. A 231, 45 (1974)

158. V. Suman, C. Sunil, Soumya Nair, S. Paul et. al., Nucl. Inst. Meth. A, 800 (2015) 29.

159. C. Sunil, T. Bandyopadhyay, M. Nandy et. al., Nucl. Instr. Meth. A 721 (2013) 21.

160. J. F. Ziegler, M. D. Ziegler,J. P. Biersack, Nucl. Ins. Meth. B, 268 (2010) 1818.

161. A. Chatterjee, Priv. comm. (2015); <http://www.tifr.res.in/~pell/lamps.html>

162. M. Blann and A. Mignerey; Nuclear Physics A 186 245-256 (1972)

163. P. E. Hodgson , G. M. Field , H. Gruppelaar & P. Nagel; Radiation Effects, 95:1-4, 27-46 (1986)

164. M B Chadwick, R Bonetti and P E Hodgson; Jour. Phys. G: Nucl. Part. Phys. 15 237- 250 (1989)

165. M. Nandy, T. Bandyaopadhyay, P.K. Sarkar, Phys. Rev. C 63, (2001) 034610.

166. T. Otsuka and K. Harada, Physics Letters 121B (1983) 106.

167. O. V. Fotina, D. O. Eremenko, Yu. L. Parfenova et. al., Int. J. Mod. Phys. E, 19 (2010) 1134.

168. J. Wilczynski et ai., Nucl. Phys. A373 (1982) 109.

169. R.J. Charity, GEMINI: A Code to Simulate the Decay of Compound Nucleus by a Series of Binary Decays, IAEA, Trieste, Italy, 2008, p. 139.

170. S. Furihata et al., The gem code - a simulation program for the evaporation and the fission process of an excited nucleus, JAERI-Data/Code 2001-015, JAERI, Tokai-mura, Naka-gam, Ibarakiken, Japan (2001).

171. A. Ferrari, P.R. Sala, A. Fasso, J. Ranft, FLUKA: a multi-particle transport code, CERN-2005-10 (2005), INFN/TC_05/11, SLAC-R-773, 2005.

172. H. Sorge, H. Stocker, W. Greiner,Poincare invariant Hamiltonian dynamics: Modelling multi-hadronic interactions in a phase-space approach, Ann. of. Phys. 192 , 266 (1989)

173. H. Sorge, H. Stocker, W. Greiner, Relativistic quantum molecular dynamics approach to nuclear collisions at ultrerelativistic energies, Nucl. Phys. A 498, 567 (1989).

174. J. K. Tuli, Nuclear wallet card, National nuclear data centre, October (2011).

175. Tadahiro Kurosawa et. al., Measurements of Thick Target Neutron Yields from 100 to 800 MeV/Nucleon Heavy Ions, Journal of Nuclear Science and Technology,37(1), 135, 2000.

APPENDIX - A

The Intra-nuclear Transition rates

The transition rates are defined as

$$\left.\begin{aligned} \lambda_{+}^{n} &= \frac{2\pi}{\hbar}|M_{+}|^{2}.\rho_{n+2} \\ \lambda_{-}^{n} &= \frac{2\pi}{\hbar}|M_{-}|^{2}.\rho_{n-2} \\ \lambda_{0}^{n} &= \frac{2\pi}{\hbar}|M_{0}|^{2}.\rho_{n} \end{aligned}\right\} \qquad (A.1)$$

$M_{\pm,0}$ are the matrix elements of the respective transitions and ρ_{n+2}, ρ_{n-2} and ρ_n are the density of states available in the $n+2$, $n-2$ and n exciton states after $\Delta n = 2,-2,0$ transitions respectively. A common practice is to assume $M+ = M_- = M_0$ $(= M)$. With this assumption and the consequent restrictions imposed on the final density of states the transition rates are written as:

$$\left.\begin{aligned} \lambda_{+}^{n} &= \frac{2\pi}{\hbar}|M|^{2}.\frac{g^3E_c^2}{2(n+1)} \\ \lambda_{-}^{n} &= \frac{2\pi}{\hbar}|M|^{2}.\frac{g.p.h(n-2)}{2} \\ \lambda_{0}^{n} &= \frac{2\pi}{\hbar}|M|^{2}.\frac{g^2E_c(3n-2)}{4} \end{aligned}\right\} \qquad (A.2)$$

Compound nuclear equilibrium is attained when the rate of creation of particle-hole pairs approximately equals the annihilation rates of such pairs so that the exciton number $\bar{n}$ remains unchanged with two-body interactions. Eqn. (A. 2) give us the value of $\bar{n} \cong (2gE_c)^{1/2}$ from the condition $\lambda_{+}^{\bar{n}} = \lambda_{-}^{\bar{n}}$.

The matrix element M is evaluated empirically by making global fits of calculations with experiment. The most common form of $|M|^2$ is

$$|M|^2 = \frac{K}{E_cA^3}\ MeV^2; \quad K = 190(\pm 32\%)MeV^3 \qquad (A.3)$$

for nucleon-nucleon scattering with A the mass number of the composite nucleus. As can be seen $|M|^2$ is independent of the exciton number. A later empirical expression includes dependence on n:

$$|M|^2 = \left.\begin{matrix} \frac{K}{e.A^3}\left(\frac{e}{7\ MeV}\right)^{1/2}\left(\frac{e}{2\ MeV}\right)^{1/2} \quad , \ for\ \ e < 2\ MeV \\ \frac{K}{e.A^3}\left(\frac{e}{7\ MeV}\right)^{1/2} \qquad ,for\ 2\ MeV \le e \le 7\ MeV \\ \frac{K}{e.A^3} \qquad , \qquad for\ 7MeV \le e \le 15\ MeV \\ \frac{K}{e.A^3}\left(\frac{e}{7\ MeV}\right)^{1/2} \qquad , \qquad for\ e > 15MeV \end{matrix}\right\} \qquad (A.4)$$

Where, $e = E_c/n$ and $K = 135\ MeV^3$.

Eqn. (A.2) are the most widely used expressions for calculating the individual transition rates. The two-body interaction rate, λ_t^n, can be obtained as the, sum of the individual transition rates or directly from a knowledge of the mean free path (mfp) of a particle inside the nucleus. The mfp, L, being the average distance travelled between two successive interactions,

$$\lambda_t^n = v/L = \frac{1}{L}\left(\frac{2E}{m}\right)^{1/2} \qquad (A.5)$$

Where, v and m are the velocity magnitude and mass of the particle, respectively, and E its kinetic energy inside the nucleus. Of the several methods available in literature for calculating L we discuss the two that are most commonly used. The first method is described by Kikuchi and Kawai [130] but is limited to the case of' nucleon mfp only. The mfp is determined by, $L = \frac{1}{\rho.\sigma}$, where ρ is the nuclear matter density and σ the nucleon-nucleon scattering cross-section. The scattering cross-sections between two free nucleons have been measured from a few keV to several hundreds of MeV. Two important features have come out of these experiments. First, the cross-sections are nearly isotropic in the centre-of-mass of the interacting nucleons. Secondly, the cross-sections can be fairly well represented by the empirical relations

$$\left.\begin{aligned}\sigma_{nn} = \sigma_{pp} = \left(\frac{10.63}{\beta^2} - \frac{29.92}{\beta} + 42.9\right)\ mb \\ \sigma_{np} = \left(\frac{34.10}{\beta^2} - \frac{82.20}{\beta} + 82.2\right)\quad mb\end{aligned}\right\} \qquad (A.6)$$

Where, $\sigma_{nn}, \sigma_{pp}, \sigma_{np}$ denote the neutron-neutron, proton-proton and neutron-proton cross-sections, respectively. $\beta = v/c$ with v and c being, respectively, the relative velocity and the velocity of light. From the free nucleon-nucleon scattering cross-sections Kikuchi and Kawai obtained the average two nucleon scattering cross-section inside the nuclear matter as

$$\bar{\sigma}_{ij} = \sigma_{ij}(E).P(E_F/E) \qquad (A.7)$$

Where, $\bar{\sigma}_{ij}$ is the average scattering cross-section between a nucleon of type i and a nucleon of type j. $\sigma_{ij}(E)$ is the free nucleon-nucleon scattering cross-section of (B.6) and $P(E_F/E)$ is the function (E_F being the Fermi energy)

$$P(E_F/E) = \begin{cases} 1 - \frac{7}{5}(E_F/E) + \frac{2}{5}(E_F/E)(2 - E_F/E)^{5/2} & for \quad E_F/E \geq \frac{1}{2} \\ 1 - \frac{7}{5}(E_F/E) & for \ E_F/E \leq \frac{1}{2} \end{cases} \qquad (A.8)$$

Eqn. (A.5) gives the cross-section between a given nucleon i and a given nucleon j. But $'i'$ sees not just one nucleon but A nucleons, Z protons and N neutrons, and it can interact with anyone of these. The average scattering cross-section of nucleon of type i inside the nucleus is

$$\langle\sigma(E)\rangle_i = \left(N\bar{\sigma}_{ni}(E) + Z\bar{\sigma}_{pi}(E)\right).A^{-1} \qquad (A.9)$$

The nuclear matter density is commonly represented by the function, $\rho(r) = \frac{\rho_0}{1+e^{[(r-R_0)/a_0]}}$, where ρ_0 is the saturation density, R_0 is the half-density radius and a_0 the diffusivity. The average density,

$$\langle\rho(r)\rangle = \frac{1}{R}\int \rho(r)dr = \frac{\rho_0.a_0}{R} ln\left(\frac{1 + e^{R_0/a_0}}{1 + e^{(R_0-R)/a_0}}\right);\ R = R_0 + a_0.ln\left(\frac{\rho(r=R)}{\rho_0}\right) \qquad (A.10)$$

One can choose a sufficiently large value of R so that $\rho(r = R)/\rho_0$ is small enough ($\sim 10^{-2}$) to justify the assumption that R represents the nuclear boundary.

It should be noted that the Kikuchi-Kawai expression for the two-body interaction rate is independent of the exciton number n as $\langle\rho(r)\rangle$ and $\langle\sigma(E)\rangle_i$ have no dependence on n. It, however, depends on the particle energy. Eqn. (A.2), on the other hand, is independent of the particle energy but depends on the exciton number as also on the excitation energy. The detailed Kikuchi-Kawai calculations were simplified by Blann [85] through an empirical expression for the two-body interaction rate:

$$\lambda_t^n = [1.4 \times 10^{21}(\varepsilon + B) - 8.0 \times 10^{18}(\varepsilon + B)^2]k^{-1} \qquad (A.11)$$

ε being the particle energy outside the nucleus (the ejectile energy) and B its separation energy. k is an adjustable constant and when $k = 1$, eqn. (A.11) reproduces the Kikuchi-Kawai interaction rates. The adjustable constant k is used considering Kikuchi-Kawai calculations are based upon the free nucleon-nucleon scattering cross-sections and the only restriction imposed to deal with scattering inside the nucleus is that no scattering be allowed into levels below the Fermi energy. There are few restrictions which has not been considered like the presence of well defined quantum states (e.g., states defined by definite spins and parities), which during interactions inside the nucleus must be conserved. The need to conserve the quantum numbers would restrict the scattering events more than the Kikuchi-Kawai calculations. This would result in longer mean free path and consequently lower values of λ_t^n . The adjustable parameter plays an important role in these kind of situations, $k > 1$ adjust λ_t^n to correspond to longer mfp.

The mfp can also be obtained from the imaginary part W of the optical model potential. The mfp is related to W as,

$$L = \hbar^2 \left[E + \sqrt{E^2 + W^2}\right]^{1/2} \cong \frac{\hbar}{W}\sqrt{E/2m} \ ; \quad \lambda_t^n = \frac{2W}{\hbar} \qquad (A.12)$$

APPENDIX - B

Evaluation of Particle level densities

To calculate the PEQ emission cross-section one needs to evaluate partial level densities $\rho_n(U,E)$ and $\rho_n(E_c)$. In this section, the derivation from first principle is presented for the familiar expression: $\rho_n(E_c) = g^n E_c^{n-1}/p!\,h!\,(n-1)!$, with number of excited particles and hole p and h, making up n-exciton system: $n = p + h$.

Considering a simple system of two excitons sharing the excitation energy E_c. The two excitons may be identical, viz., 2 particles ($2p$) or 2 holes ($2h$); or the excitons may be distinguishable, viz., 1-particle and 1-hole ($1p$-$1h$). To start with, we consider the case $1p$-$1h$ sharing the energy E_c.

B.1 Density of states for $1p$-$1h$ system

Suppose either one of the excitons has energy x. This energy can lie anywhere between zero and E_c, i.e., $0 \leq x \leq E_c$. Let us denote the density of states of this single exciton by $\rho_1(x)$. In other words, the number of levels per unit energy interval available to this exciton at energy *x* is $\rho_1(x)$. Consequently, the number of levels available in the energy interval between *x* and (*x*+*dx*) is $\rho_1(x)dx$.

Let *y* be the energy of the other exciton. By energy conservation $x + y = E_c$ or, $y = E_c - x$. Let the density of states of this exciton at energy $y = E_c - x$ be $\rho_2(y) = \rho_2(E_c - x\,)$.

The density of states of the combined system of two excitons when one has density of states $\rho_1(x)$, then density of states available to the two-exciton system is simply, $\rho_2(E_c - x\,)$. If, instead of only one energy level, two energy levels are available to the first exciton in the same energy interval [i.e., $\rho_1(x)dx = 2$], then the density of states for the two-exciton system is $2 \times \rho_2(E_c - x\,)$, for each level of the excitons the density of states for the two-exciton system equals the density of states available to the second exciton. In general, if $\rho_1(x)dx$ number of levels are available to the first exciton (in the energy interval between x and (x+dx)), then the density of states available to the two exciton system is $\rho_1(x)dx\rho_2(E_c - x\,)$.

This is for a given energy interval between x and (x+dx) for the first exciton. But since x can vary as $0 \le x \le E_c$, the total density of states for the two-exciton system must be obtained by summing $\rho_1(x)dx\rho_2(E_c - x\,)$ over all values of x from zero to E_c. We thus have the two-exciton density of states as,

$$\rho_{n=2}(E_c\,) = \int_0^{E_c} \rho_1(x)\rho_2(E_c - x\,)dx \qquad (B.1)$$

To solve (C.1) the actual functional dependence of $\rho_1(x)$ and $\rho_2(E_c - x\,)$ on x should be known. In the present state of knowledge about the nucleus this functional dependence can be described only by invoking an appropriate nuclear model. There are a number of working nuclear models – the shell model, the collective model, the liquid drop model, the free gas model. The model used to solve (B.1) is a simplified version of the free gas model, known as the equidistant spacing free gas model. According to the free gas model, each energy level of the nucleus can accommodate either one particle or one hole. In other words, as nucleons are Fermions the occupancy of a level is either 1 (particle state) or 0 (hole state). The spacing between a level at energy ε and the next level is, from the model, $\frac{2\varepsilon_F}{3A}\sqrt{\frac{\varepsilon_F}{\varepsilon}}$, where ε_F is the Fermi energy and A is the number of nucleons. Thus the spacing between the levels are inversely proportional to $\sqrt{\varepsilon}$. In the equidistant spacing model, it is assumed that the spacing between the levels is constant, say d MeV. This means that in the energy interval of d MeV, there exists only one energy level. Hence, the number of levels in unit energy interval, i.e., the level density, is 1/d MeV^{-1}. We call this, the single particle level density and denote it by $g(= 1/d)$.

Since, according to the equidistant spacing model only one particle or one hole (i.e., one exciton) can occupy a level and since the density of state is g, we have $\rho_1(x) = \rho_2(E_c - x) = g$.

Eqn. (B.1) then reduces to, $\rho_{n=2}(E_c) = \int_0^{E_c} g.g dx = g^2 E_c$ $(B.2)$

And the density of state for 1p-1h system is, $\boldsymbol{\rho_{n=2}(E_c) = g^2 E_c}$ $(B.3)$

B.2 Density of states for 2p or 2h system

Similarly in the case of two identical excitons, this can be treated in the same way as in the 1p-1h system except that the indistinguishability of the two excitons has to be taken into account. The differences between the 1p-1h case and 2p or 2h configurations are illustrated in Figure B-1.

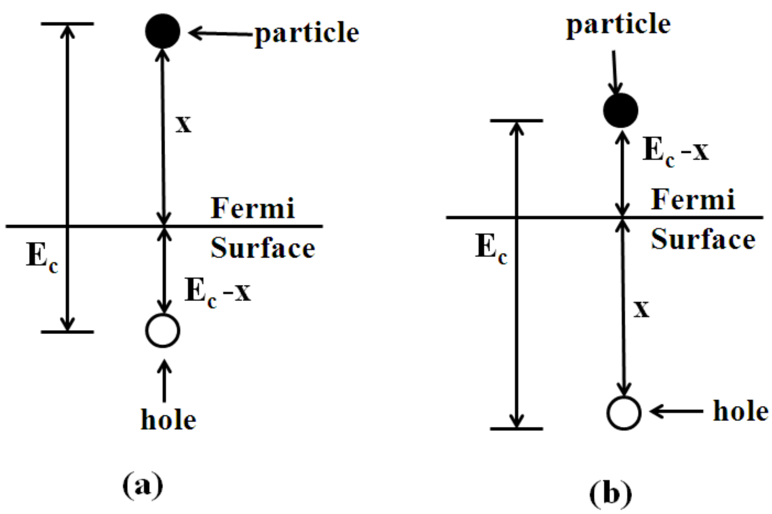

Fig. B1 Possible combinations of two distinguishable exciton system

Fig. B1 shows the different ways in which the energy, E_c can be partitioned between a particle and a hole of the $1p - 1h$ configuration when one exciton (particle or hole) has energy x and the other exciton (hole or particle) has energy $(E_c - x)$. The energies of the excited particles and holes are both measured from the Fermi surface – the excited particle lies above the Fermi surface and the excited hole below it. The energy difference between the particle and hole is E_c. In Fig. B1(a) the particle has energy x and the hole has energy $E_c - x$; in Fig. B1(b) the particle has energy $E_c - x$ and the hole has energy x. Clearly, the two configurations are distinguishable because the excitons are distinguishable.

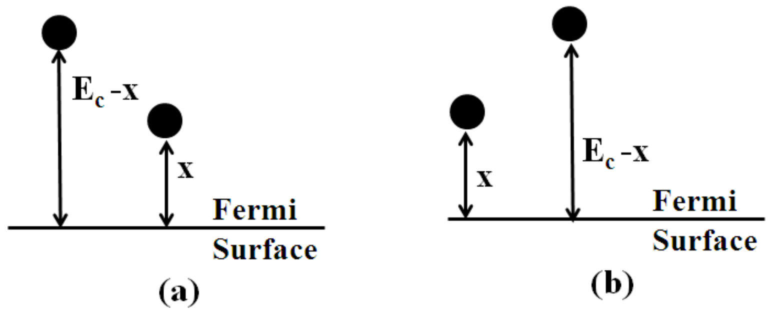

Fig. B2 Possible combinations of two indistinguishable exciton system (particle)

Similarly in Fig. B2 two identical particle-excitons sharing the energy E_c. Fig. B2(a) shows the configuration with one particle having energy x and the second with $E_c - x$ whereas in Fig. B2(b) vice versa. Clearly since the particles are identical, the two configurations are indistinguishable and we really have only one configuration with energies x and $E_c - x$. It means that, if we use Eqn. (B.1) to describe the density of states when two identical particles are sharing the energy E_c then it will lead to counting the same configuration twice and eqn. (B.1), therefore, must be divided by 2 to compensate for this double counting:

$$\rho_{n=2}(E_c) = \frac{1}{2}\int_0^{E_c} \rho_1(x)\rho_2(E_c - x)dx \qquad (B.4)$$

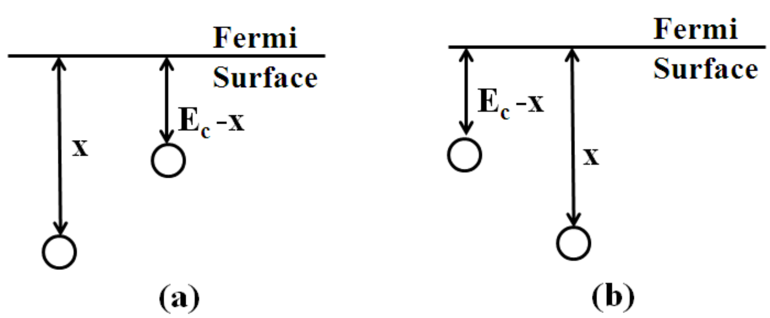

Fig. B3 Possible combinations of two indistinguishable exciton system (hole)

Similarly for two identical holes (Fig. B3), invoking the equidistant spacing model, we have

$$\rho_{n=2}(E_c) = \frac{1}{2}\int_0^{E_c} g.g dx$$

and the density of states for two identical excitons sharing the energy E_c is,

$$\boldsymbol{\rho_{n=2}(E_c) = \frac{g^2 E_c}{2}} \qquad (B.5)$$

B.3 Partial level Densities of system of *n*-excitons

Extending the deduction of partial level densities of two- and three-exciton systems to the general case when the excitation energy E_c is shared among *n*-excitons. We shall consider three cases: (1) When the *n*-excitons are all different; (2) when the *n*-excitons are identical and (3) when there are *p* identical particles and *h* identical holes in the *n*-exciton system.

B.3.1 Density of states of n- different excitons

The energy E_c is shared among *n*-different excitons.

If the first exciton has energy x_1 with $0 \leq x_1 \leq E_c$

and the second exciton has energy x_2 with $0 \leq x_2 \leq E_c - x_1$

and the third exciton has energy x_3 with $0 \leq x_3 \leq E_c - \sum_{i=1}^{2} x_i$

:

and the rth exciton has energy x_r with $0 \leq x_r \leq E_c - \sum_{i=1}^{r-1} x_i$

:

and the (n-1)th exciton has energy x_{n-1} with $0 \leq x_{n-1} \leq E_c - \sum_{i=1}^{n-2} x_i$

the nth exciton has energy x_n with $0 \leq x_n \leq E_c - \sum_{i=1}^{n-1} x_i$.

The partial density of states is then,

$$\rho_n(E_c) = \int_0^{E_c} dx_1 \int_0^{E_c - x_1} dx_2 \int_0^{E_c - \sum_{i=1}^{2} x_i} dx_3 \cdots\cdots\cdots \int_0^{E_c - \sum_{i=1}^{r-1} x_i} dx_r \cdots\cdots \int_0^{E_c - \sum_{i=1}^{n-2} x_i} dx_{n-1}$$

$$\times \rho_1(x_1)\rho_2(x_2)\rho_3(x_3) \cdots\cdots \rho_r(x_r) \cdots\cdots \rho_{n-1}(x_{n-1})\rho_n(x_n) \qquad (B.6)$$

Since, x_n is fixed, there is no integration over dx_n –i.e., for n-different excitons we have (n-1) integrations over $dx_1, dx_2, \cdots\cdots, dx_{n-1}$. Using the equidistantly spaced free gas model,

$$\rho_1(x_1) = \rho_2(x_2) = \cdots\cdots = \rho_r(x_r) = \cdots\cdots = \rho_{n-1}(x_{n-1}) = \rho_n(x_n) = g,$$

And (B.6) reduces to, $\quad \rho_n(E_c) = g^n . I_{n-1}, \qquad (B.7a)$

where, $I_{n-1} = \int_0^{E_c} dx_1 \int_0^{E_c - x_1} dx_2 \int_0^{E_c - \sum_{i=1}^{2} x_i} dx_3 \cdots\cdots\cdots \int_0^{E_c - \sum_{i=1}^{r-1} x_i} dx_r \cdots\cdots \int_0^{E_c - \sum_{i=1}^{n-2} x_i} dx_{n-1}$

It can be shown that, $\quad I_{n-1} = \frac{E_c^{n-1}}{(n-1)!} \qquad (B.7b)$

and

$$\boldsymbol{\rho_n(E_c) = \frac{g^n E_c^{n-1}}{(n-1)!}} \qquad (B.8)$$

B.3.2 Density of states of n- identical excitons

When the n-excitons are identical, there will be multiple counting of identical configurations to define the level density. The number of configurations arising from the permutation of n-different excitons taken all together is $^nP_n = n!$ and when the n-excitons are identical, this reduces to 1, hence (B.8) need to be divided by ^nP_n to obtain the particle level density for n-identical excitons:

$$\boldsymbol{\rho_n(E_c) = \frac{g^n E_c^{n-1}}{n!\,(n-1)!}} \qquad (B.9)$$

B.3.3 Density of states of p- identical particles and h identical holes

The n-excitons are made up of p identical excitons of one kind (say particles) and h identical excitons of another kind (say holes) with $n = p + h$. If eqn. (C.8), is used to calculate the partial level density of such a system, then (B.8) will include the identical configurations arising from (a) the identical particles and (b) the identical holes. The number of configurations arising from the p-particles is equal to the number of permutations of *p*-different object, i.e., $p!$. The number of configurations for *h* holes is $h!$. Therefore, the partial level density is obtained by dividing (B.8) by $p!$ and $h!$ and for *p*-excited particles and *h* excited holes:

$$\boldsymbol{\rho_n(E_c) = \frac{g^n E_c^{n-1}}{p!\,h!\,(n-1)!}} \qquad (B.10)$$

Extending this argument to *n*-excitons made up of *m* -different kinds of excitons:

$$\boldsymbol{\rho_n(E_c) = \frac{g^n E_c^{n-1}}{(n-1)!\prod_{i=1}^{m}(N_i!)}} \qquad (B.11)$$

Where, N_i is the number of *i*th type exciton in the system, i.e., $\sum_{i=1}^{m} N_i = n$

Eqn. (B.11) is the general expression for partial density of states for *n*-excitons sharing the energy E_c. It reduces to (B.10) when $m = 2$ (for two types of excitons: particles and holes) with $N_{i=1} = p$ and $N_{i=2} = h$. When all the excitons are different, we have $m = n$ and $N_{i=1} = 1$ for each *i*. Then, from (B.11), $\rho_n(E_c) = \frac{g^n E_c^{n-1}}{(n-1)!\prod_{i=1}^{n}(1!)} = \frac{g^n E_c^{n-1}}{(n-1)!}$ which is same as (B.8).

In the hybrid model no distinction is made between neutrons and protons and neutron-holes and proton-holes. It considers only two types of excitons – p identical excited particles and h identical excited holes. So (B.10) is the partial level density expression used in the hybrid model.

Evaluation of partial level density $\boldsymbol{\rho_n(U,E)}$

As defined $\rho_n(U,E)$, is the density of the states available to n-excitons under the constraint that one exciton has energy *E* and the rest (*n*-1) excitons share the energy $U = E_c - E$. The n-excitons are made up of *p* identical particles and *h* identical holes. Also, it is a particle-exciton that has energy *E*.

Let us assign the energy *E* to the n^{th} exciton, which is a particle-exciton. The other (*n*-1) excitons then share the energy *U* among these (*n*-1) excitons,

If the first exciton has energy x_1 with $0 \le x_1 \le U$

if the second exciton has energy x_2 with $0 \le x_2 \le U - x_1$

if the third exciton has energy x_3 with $0 \le x_3 \le U - \sum_{i=1}^{2} x_i$

:

if the (n-2)th exciton has energy x_{n-2} with $0 \le x_{n-2} \le U - \sum_{i=1}^{n-3} x_i$

then the (n-1)th exciton has a fixed energy x_{n-1} with $0 \le x_{n-1} \le U - \sum_{i=1}^{n-2} x_i$.

Then as before, the partial density $\rho_n(U,E)$ is given by,

$$\rho_n(U,E) = \frac{1}{p!\,h!} \int_0^U dx_1 \int_0^{U-x_1} dx_2 \int_0^{U-\sum_{i=1}^{2} x_i} dx_3 \cdots\cdots \int_0^{E_c-\sum_{i=1}^{n-3} x_i} dx_{n-2}\, \rho_1(x_1)\rho_2(x_2)\rho_3(x_3)$$

$$\times \cdots\cdots \rho_{n-2}(x_{n-2})\rho_{n-1}(x_{n-1})\rho_n(x_n) \qquad (B.12)$$

Ordinarily, when *n*-excitons share a given energy, the expression for partial level density involves (*n*-1) integrations and not *n* integrations as energy conservation fixes the energy of one exciton, while the other exciton energies are allowed to vary. In (B.12), the n^{th} exciton, has been assigned the fixed energy *E* and the rest (*n*-1)th exciton has a fixed energy (x_{n-1}) on account of energy conservation. A factor $1/h!$ and $1/p!$ comes in to remove the multiple counting of the identical configurations arising from the permutation of *h* holes and *p* particles.

Using equidistant spacing model (B.12) reduces to: $\rho_n(U,E) = \frac{g^n}{p!h!} I_{n-2}$, which finally becomes

$$\boldsymbol{\rho_n(U,E) = \frac{g^n U^{n-2}}{p!\,h!\,(n-2)!}} \tag{B.13}$$

From (B.10) and (B.13) one can evaluate the ratio $\rho_n(U,E)/\rho_n(E_c\,)$ in the hybrid model equation (2.28),

$$\boldsymbol{\frac{\rho_n(U,E)}{\rho_n(E_c\,)} = \frac{g^n U^{n-2}}{p!\,h!\,(n-2)!}.\frac{p!\,h!\,(n-1)!}{g^n E_c^{n-1}} = \frac{n-1}{E_c}\left(\frac{U}{E_c}\right)^{n-2}} \tag{B.14}$$

APPENDIX - C

Quasi-free Nucleon-Nucleon Scattering Inside Nuclear Matter

Consider the elastic scattering between two free and identical nucleons of mass m. Let $\overrightarrow{k_1}, \overrightarrow{k_t}$ with $k_1 > k_t$ be the momenta before scattering and $\overrightarrow{k_1{}'}$ and $\overrightarrow{k_t{}'}$ the momenta after scattering. Since, $\overrightarrow{k_1{}'}$ and $\overrightarrow{k_t{}'}$ are complementary we use $\vec{k}$ to denote either of them.

$\overrightarrow{k_r} = \frac{1}{2}\left(\overrightarrow{k_1} - \overrightarrow{k_t}\right)$ is the relative momentum before scattering of nucleon 1 with respect to nucleon t. $\overrightarrow{k_r{}'} = \frac{1}{2}\left(\overrightarrow{k_1{}'} - \overrightarrow{k_t{}'}\right)$ is the relative momentum of 1 with respect to t after scattering.

$\sigma\left(\overrightarrow{k_r}, \overrightarrow{k_r{}'}\right)$ is the differential scattering cross-section in the C.M. frame of the two nucleons.

$\sigma'\left(\vec{k}\right)$ is the differential scattering cross-section in the laboratory frame.

$$\sigma\left(\overrightarrow{k_r}, \overrightarrow{k_r{}'}\right) = \frac{No. of\ transitions\ from\ \overrightarrow{k_r}\ to\ \overrightarrow{k_r{}'}/time/nucleon}{No. of\ incident\ nucleons\ with\ momentum\ \ \overrightarrow{k_r}\ /time/area} \qquad (C.1)$$

$$\sigma'\left(\vec{k}\right) = \frac{No. of\ transitions\ from\ \overrightarrow{k_1}\ to\ \vec{k}/time/nucleon}{No. of\ incident\ nucleons\ with\ momentum\ \ \overrightarrow{k_1}\ /time/area} \qquad (C.2)$$

From the definition of, $\overrightarrow{k_r{}'} = \frac{1}{2}\left(\overrightarrow{k_1{}'} - \overrightarrow{k_t{}'}\right)$,

$$\overrightarrow{k_1{}'} = \overrightarrow{k_t{}'} + 2.\overrightarrow{k_r{}'}, \qquad \overrightarrow{k_t{}'} = \overrightarrow{k_1{}'} - 2.\overrightarrow{k_r{}'}$$

$$\boldsymbol{\overrightarrow{k_1} + \overrightarrow{k_t} = \overrightarrow{k_1{}'} + \overrightarrow{k_t{}'} = 2\left(\overrightarrow{k_1{}'} - \overrightarrow{k_r{}'}\right) = 2\left(\overrightarrow{k_t{}'} + \overrightarrow{k_r{}'}\right)}$$

Since, from momentum conservation $\overrightarrow{k_1} + \overrightarrow{k_t} = \vec{C}$ a constant, there is a one to one correspondence between $\overrightarrow{k_r{}'}$ and $\vec{k}$ (i.e., $\overrightarrow{k_1{}'}$ or $\overrightarrow{k_t{}'}$), i.e., for each value of $\overrightarrow{k_r{}'}$ there can be one and only one value of $\vec{k}$. Hence the numerators in (C.1) and (C.2) are equal.

To evaluate the denominators consider two cylinders each with unit cross-section but one with length k_1/m and the other k_r/μ, μ-being the reduced mass of the two nucleons. If n_0 is the density of incident nucleons then,

$$No.\,of\ incident\ nucleons\ with\ momentum\ \overrightarrow{k_r}\ /time/area = \frac{n_0 k_r}{\mu}$$

$$No.\,of\ incident\ nucleons\ with\ momentum\ \overrightarrow{k_1}\ /time/area = \frac{n_0 k_1}{m}$$

and,

$$\frac{\sigma'(\vec{k})}{\sigma\left(\overrightarrow{k_r}, \overrightarrow{k_r'}\right)} = \frac{m k_r}{n k_1}$$

Since, $\mu = \frac{m}{2}$

$$\frac{\sigma'(\vec{k})}{\sigma\left(\overrightarrow{k_r}, \overrightarrow{k_r'}\right)} = \frac{2k_r}{k_1}, \quad or,\ \sigma'(\vec{k}) = \frac{2k_r}{k_1}.\sigma\left(\overrightarrow{k_r}, \overrightarrow{k_r'}\right) \qquad (C.3)$$

Equation (C.3) is the conversion of cross-section from C.M. frame to laboratory frame for two-nucleon scattering.

The total cross-section,

$$\sigma_t' = \int \sigma'(\vec{k})\, d\vec{k}$$

If $d\Omega'$ is the solid angle containing the vector $\overrightarrow{k_r'}$, then

$$d\Omega' = \frac{d\Omega'}{d\vec{k}}\, d\vec{k}$$

and,

$$\sigma'(\vec{k}) d\vec{k} = \frac{2k_r}{k_1}.\sigma\left(\overrightarrow{k_r}, \overrightarrow{k_r'}\right).\frac{d\Omega'}{d\vec{k}}\, d\vec{k} \qquad (C.4)$$

These expressions are true, when $\overrightarrow{k_1}$ and $\overrightarrow{k_t}$ have well defined values. For scattering inside nuclear matter the target nucleons have a momentum distribution given by the Fermi distribution and the final momentum $\vec{k}$ may result from scattering with any one of the target nucleons. Hence for quasi-free scattering inside the nuclear matter,

$$\sigma(\vec{k})d\vec{k} = \int_{\overrightarrow{k_t}} \sigma'(\vec{k})d\vec{k}\,.\,P(\overrightarrow{k_t})d\overrightarrow{k_t}$$

Where, $P(\overrightarrow{k_t})d\overrightarrow{k_t}$ is the probability that a target nucleon has momentum between $\overrightarrow{k_t}$ and $\overrightarrow{k_t} + d\overrightarrow{k_t}$.

$$\sigma(\vec{k})d\vec{k} = \int_{\overrightarrow{k_t}} \frac{2k_r}{k_1}.\,\sigma\left(\overrightarrow{k_r}, \overrightarrow{k_r{}'}\right).\frac{d\Omega'}{d\vec{k}}d\vec{k}\,.\,P(\overrightarrow{k_t})d\overrightarrow{k_t} \qquad (C.5)$$

and the total cross-section is,

$$\sigma = \int_{\vec{k}}\int_{\overrightarrow{k_t}} \frac{2k_r}{k_1}.\,\sigma\left(\overrightarrow{k_r}, \overrightarrow{k_r{}'}\right).\frac{d\Omega'}{d\vec{k}}d\vec{k}\,.\,P(\overrightarrow{k_t})d\overrightarrow{k_t} \qquad (C.6)$$

The solid angle element $d\Omega'$ is related to $k_r{}'$ as,

$$dk_r{}' = k_r{}'^2 dk_r{}' d\Omega'$$

The kinetic energy and momentum conservation in elastic scattering require that $k_r{}' = k_r$. To ensure this, the Dirac δ-function: $\delta(k_r{}' - k_r)dk_r{}'$ is used to define,

$$d\Omega' = \frac{\delta(k_r{}' - k_r)dk_r{}'}{k_r{}^2} \qquad (C.7)$$

$$2.\,d\overrightarrow{k_r{}'} = d\overrightarrow{k_t{}'} - d\overrightarrow{k_1{}'}$$

and since from momentum conservation:

$$\overrightarrow{k_1} + \overrightarrow{k_t} = \vec{C}_{const} = \left(\overrightarrow{k_t{}'} + \overrightarrow{k_r{}'}\right)$$

$$d\overrightarrow{k_t}' = -d\overrightarrow{k_1}', \qquad d\overrightarrow{k_r}' = d\vec{k}$$

and,

$$d\Omega' = \frac{\delta(k_r{}' - k_r)d\vec{k}}{k_r{}^2} \qquad (C.8)$$

Using the relation,

$$\delta\left(k_r{}'^2 - k_r{}^2\right) = \frac{\delta(k_r{}' - k_r) + \delta(k_r{}' + k_r)}{2k_r}$$

and noting that $\delta(k_r{}' + k_r) = 0$ as $k_r{}' + k_r \neq 0$ always.

[Note that $k_r{}' + k_r = 0$ only when $k_r = 0$, i.e., $\overrightarrow{k_1} = \overrightarrow{k_t}$. Since the target nucleons have a maximum momentum $= k_F$ and $k_1 = k_F +$ separation energy of incident nucleon + kinetic energy of incident nucleon, $k_1 > k_t$.]

$$\delta(k_r{}' - k_r) = 2k_r\delta\left(k_r{}'^2 - k_r{}^2\right) \qquad (C.9)$$

And substituting (C.9) in (C.5)

$$\sigma(\vec{k})d\vec{k} = \frac{4d\vec{k}}{k_1}\int \delta\left(k_r'^2 - k_r{}^2\right).\sigma\left(\overrightarrow{k_r}, \overrightarrow{k_r'}\right).P\left(\overrightarrow{k_t}\right)d\overrightarrow{k_t} \qquad (C.10)$$